Analysis and Design of Soft-Switching Current-fed Bi-directional Power Conversion for Multifunctional Plug-in EV Charging

Nil Rajeshkumar Patel

A Thesis

in the Department

of

Electrical and Computer Engineering

Presented in Partial Fulfilment of the Requirements

For the Degree of

Doctor of Philosophy (Electrical and Computer Engineering) at

Concordia University

Montréal, Québec, Canada

January 2024

CONCORDIA UNIVERSITY

School of Graduate Studies

This is to certify that the thesis prepared

By: Nil Rajeshkumar Patel

Entitled: Analysis and Design of Soft-Switching Current-fed Bi-directional Power Conversion for Multifunctional Plug-in EV Charging

and submitted in partial fulfillment of the requirements for the degree of

Doctor of Philosophy (Electrical and Computer Engineering)

complies with the regulation of the University and meets the accepted standards with respect to originality and quality.

Signed by the final Examining Committee:

______________________	Chair
Dr. Ciprian Alecsandru	
______________________	External Examiner
Dr. Ambrish Chandra	
______________________	External to Program
Dr. Mohsen Ghafouri	
______________________	Examiner
Dr. Shahin Hashtrudi Zad	
______________________	Examiner
Dr. Chunyan Lai	
______________________	Co-Supervisor
Dr. Akshay Kumar Rathore	
______________________	Supervisor
Dr. Luiz A. C. Lopes	

Approved by ______________________________

Dr. Jun Cai, Graduate Program Director

February 22nd, 2024

Date of Defence ______________________________

Dr. Mourad Debbabi, Dean

Gina Cody School of Engineering and Computer Science

ABSTRACT

Analysis and Design of Soft-Switching Current-fed Bi-directional Power Conversion for Multifunctional Plug-in EV Charging

Nil Rajeshkumar Patel, Ph.D.

Concordia University, 2024

The forefront of EV battery charger research accentuates the imperative of refining power density attributes while concurrently elevating the efficiency standards of power conversion processes. The conventional EV battery chargers are developed with two cascaded power conversion stages. The first stage converts the AC voltage to a DC voltage by employing power factor correction (PFC). The second stage is an isolated DC-DC converter stage. These two-stages are interconnected by DC-link capacitors. This two-stage battery charger suffers from low overall efficiency due to two different power conversion stages. At the same time, the power density is limited due to the inevitable presence of intermediate DC-link capacitors. Generally, high-value electrolytic capacitors are selected for the DC-link. More importantly, the battery charger is placed close to the internal combustion engine under the hood in the case of a plug-in hybrid EV (PHEV), where the ambient temperature is more than 150^{θ}C. The electrolytic capacitors are most susceptible to failure at high ambient temperature, thus the reliability of the conventional two-stage EV battery charger is low in a high-temperature environment. Moreover, the existing research on battery chargers is mainly based on voltage-fed power converter topologies, where the feasibility of current-fed power converter topologies has received very limited attention.

This thesis work proposes and studies a family of novel snubber-less current-fed isolated single-stage bidirectional power converters (AC-DC and DC-DC) for multifunctional EV battery charging (G2V, V2G, and V2V) applications to address the shortcomings of the conventional two-stage battery chargers. The proposed modulation strategy and control technique are demonstrated for promising soft-switching operation of all semiconductor devices with bidirectional power flow capability. These converters enable zero current commutated (ZCC) without any active clamp circuit or passive snubbers, which significantly reduced switching losses, footprints, and cost. The converters steady-state operation and design equations are reported in detail. The simulation results from PSIM 11.04 software and the experimental results from 1.5 kW proof-of-concept laboratory hardware prototypes are provided in order to validate the report analysis, design, and performance.

Acknowledgement

I would like to express my special appreciation, gratefulness, and many thanks to my supervisors *Prof. Akshay Kumar Rathore* and *Prof. Luiz A.C. Lopes*. I got introduced to my field of research and learnt a lot in the field of Power Electronics from *Prof. Akshay Kumar Rathore.* They have been a tremendous mentor for me. I would like to thank them for their esteemed guidance and kind support throughout these years which finally crowned with a lot of knowledge and experience. An advice from *Prof. Luiz A.C. Lopes* on my research has been priceless. I have learned a lot from their scientific knowledge, critical thinking, and punctuality, which are key factors of any success.

I would also like to thank my doctoral committee members, *Prof. Chunyan Lai*, *Prof. Mohsen Ghafouri, Prof. Shahin Hashtrudi Zad* and *Prof. Ambrish Chandra* for serving as my committee members even at hardship.

I gratefully acknowledge Concordia University (CU) for the world-class research facility, and full financial support, which pave way for a successful career.

I extend my gratitude to *Dr. Sivanagaraju*, *Dr. Swati*, *Sukanya Dutta, Dr. Gabriel* and *Dr. Mathews* for their support in building experimental set-up, and for the useful research discussions. Heartfelt thanks to my colleagues *Ying Zuo, Shiva, Ashutosh, Neetusha, Koteswara, Tolga, Sahil, Gael, Gayatri, Qiong, Dwaipayan, Mohanraj, and Tamanwe* for the friendship and moral support.

I am obliged to my *parents (Dr. Rajeshkumar Patel and Mrs. Kokilaben Patel)* for showing me the path to pursue doctoral studies. I am especially grateful to my wife *Bhoomi* for her unconditional love and support throughout my thesis. Also, I would like to thank my sister *Asama* and brother-in-law *Vishal* for always being there and encouraging me throughout this journey.

Most of all I would like to thank the lordships Sri Sri Paramahansa Yogananda, Sri Sri Daya Mata, and Sri Sri Swami Chidananda Giri for giving me the opportunity, intelligence, and ability to carry out this research.

Table of Contents

List of Figures

List of Tables

List of Symbols

V_{in}	Input Voltage
I_{in}	Input Current
L	Input Inductor/Boost Inductor
L_{lk}, L_{lk1}, L_{lk2}	Series Leakage Inductance of HFT
L_{lk_T}	Total Series Leakage Inductance of HFT
V_{bat}	Battery Voltage
C_o	Output Capacitor
d , D	Duty cycle of the switch
f_{line}	Line frequency
f_{sw}	Switching frequency
$d_1,\ d_P$	Duty cycle associate with Primary Side
$d_2,\ d_S$	Duty cycle associate with Secondary Side
I_{bat}	Battery Current
I_L	Boost Inductor Current
I_{LK}	Leakage Inductor Current
DT_s	Switch On-Time
P_{ref}	Reference Active Power
Q_{ref}	Reference Reactive Power
$i_{in,ref}$	Reference Input Current

Φ	Phase Angle
$I_{in,max}$	Maximum Input Current
$V_{o,max}$	Maximum Output Voltage
$V_{o,min}$	Minimum Output Voltage
$V_{in,max}$	Maximum Input Voltage
$d_{1,min}$	Minimum Duty Cycle at Primary Side
d_r	Critical Duty Cycle
$V_{SW,P}$	Maximum Voltage at Primary Switch
ΔI_L	Input Inductor Current Ripple
ΔV_o	Output Voltage Ripple
$I_{P,peak}$	Peak Current at Primary Side Switch
$I_{S,peak}$	Peak Current at Secondary Side Switch
$I_{P,RMS}$	RMS Current at Primary Side Switch
$I_{S,RMS}$	RMS Current at Secondary Side Switch
$I_{PT,peak}$	Peak Current at Primary Side HFT
$I_{PT,RMS}$	RMS Current at Primary Side HFT
$I_{ST,peak}$	Peak Current at Secondary Side HFT
$I_{ST,RMS}$	RMS Current at Secondary Side HFT
N_P	Primary Turns of Transformer
N_S	Secondary Turns of Transformer

B_m	Maximum Magnetic Flux Density
A_C	Cross Sectional Area of Core
A_f	Cross Sectional Area of Frame-Winding
J_f	Frame-Current Density
n	Transformer turns ratio
P_{in}	Converter input power
P_o	Converter output power
I_o	Output Current
T_s	One switching cycle time period
V_{AB}	Terminal Voltage across A and B
V_{CD}	Terminal Voltage across C and D
$1{:}n, 1{:}n{:}n$	Transformer turns ratio
$I_{o,Avg}$	Output Average Current

List of Abbreviations

EVs	Electric Vehicles
ICE	Internal Combustion Engine
BEVs	Battery Electric Vehicles
HEVs	Hybrid Electric Vehicles
FCEVs	Fuel Cell Electric Vehicles
AEVs	All Electric Vehicles
MEVs	More Electric Vehicles
G2V	Grid-to-Vehicle
V2G	Vehicle-to-Grid
V2V	Vehicle-to-Vehicle
V2H	Vehicle-to-Home
V2L	Vehicle-to-Load
V4G	Vehicle for Grid
OBCs	On-board Battery Chargers
BMS	Battery Management System
IC	Integrated Circuit
SPI	Serial Peripheral Interface
EVSE	Electric Vehicle Supply Equipment
UFC	Ultra-Fast Charging
XFC	Extreme-Fast Charging
PFC	Power Factor Correction
AC	Alternating Current
DC	Direct Current
THD	Total Harmonic Distortion

UPF	Unity Power Factor
WBG	Wide Band-Gap
HF	High Frequency
HFT	High Frequency Transformer
EMI	Electromagnetic Interference
CCM	Continuous Conduction Mode
DCM	Discontinuous Conduction Mode
ZCS	Zero Current Switching
ZCC	Zero Current Commuted
ZVS	Zero Voltage Switching
Si	Silicon
SiC	Silicon-Carbide
GaN	Gallium Nitride
HEMT	High Electron Mobility Transistors
MOSFET	Metal Oxide Semiconductor Field-Effect Transistor
IGBT	Insulated Gate Bipolar Transistor
PF	Power Factor
LC	Inductor-Capacitor
LLC	Inductor- Inductor-Capacitor
LCL	Inductor-Capacitor-Inductor
CLLC	Capacitor-Inductor-Inductor-Capacitor
DAB	Dual Active Bridge
PSFB	Phase-Shifted Full Bridge
ASMC	Asymmetrical Secondary Modulated Converter
SoC	State of Charge
UPS	Uninterruptible Power Supply

MPC	Model Predictive Control
AI	Artificial Intelligence
DL	Deep Learning
ML	Machine Learning
WPT	Wireless Power Transfer
IPT	Inductive Power Transfer
RMS	Root Mean Square
RCD	Resistor-Capacitor-Diode
PI	Proportional Integral
PR	Proportional Resonant
P-Q	Active-Reactive
PSM	Phase Shift Modulation
DSP	Digital Signal Processor
CC	Constant Current
CV	Constant Voltage
HFL	High Frequency Link
DBR	Diode Bridge Rectifier
CMA	Control Modelling Approach
CFFB	Current-Fed Full-Bridge
CFPP	Current-Fed Push-Pull
NVC	Natural Voltage Clamping
PCB	Printed Circuit Board
FFDC	Fixed-Frequency Duty-Cycle
PLL	Phase-Locked-Loop
PWM	Pulse Width Modulation

Chapter 1: Introduction

1.1 Introduction

Due to the reduced cost of vehicles, there has been a significant increase in demand for personal vehicles for transportation. The internal combustion engine (ICE) vehicles have been widely used for over 100 years, which has led to a significant rise in oil demand. The emission from these vehicles is a major contributor to global warming. Figure 1.1 displays a comparison between classical internal combustion engine (ICE) vehicles and electric vehicles (EVs) [1]. It is clear that ICE vehicles are not a viable solution due to higher maintenance costs, low fuel efficiency, and more CO2 emissions when compared to classical EVs. Table 1.1 presents the commercial aspects of different vehicle types [2][3]. With the strict restrictions on emissions and fuel economy, there is a pressing need for sustainable and eco-friendly sources of energy, making alternative energy sources highly sought after in the past decades. One of the key requirements to improve the environmental conditions is an alternative, clean, and efficient transportation system. EVs are a viable option to solve the energy crisis issue due to the transportation system. The recent advancements in EV technologies can be considered as a positive step towards clean automobile technology [4][5]. Additionally, there has been a significant increase in the electrification of not only personal vehicles but also local transport vehicles in recent years.

Although the concept of an EV is not new, dating back to the late 1800s and early 1900s, the technology did not gain traction at the time due to high cost, low distance capabilities, and

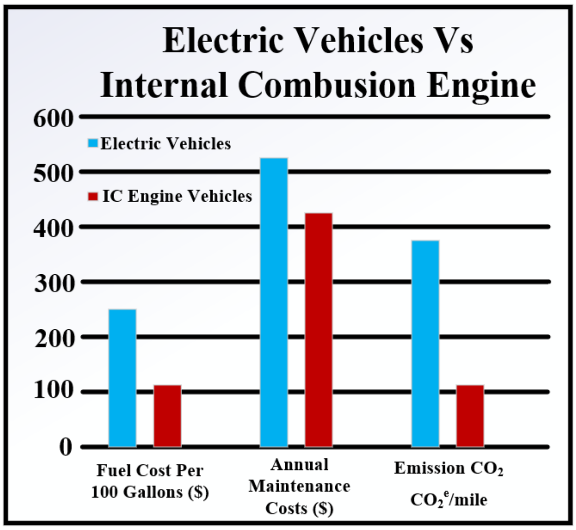

Fig. 1.1. Comparison between EV and IC engines.

Table 1.1: Commercial Aspects

Vehicle	Range	Refuel Time
Hydrogen Fuel Cell Vehicle	**320-405 km/200-250 miles**	**3-4 minutes**
Electric Vehicle	**160-500 km/100-310 miles**	**30 minutes to 12 hours**
Petrol or Diesel Vehicle	**480-640 km/300-400 miles**	**2-3 minutes**

Fig. 1.2. EV evolution.

premature technology. As depicted in Fig. 1.2, various types of EVs have been manufactured in recent years [6]. Global electric vehicle (EV) sales have been increasing rapidly, with analysts predicting that by 2030, global sales will reach 120 million [7]. As of the end of 2022, the global fleet of plug-in light vehicles was 27 million which is described in Fig. 1.3 [7]. Additionally, the contribution of commercial medium and heavy plug-in vehicles to the global stock is 750,000 units [8]. There are several types of EVs available in the market, including battery electric vehicles (BEVs), hybrid electric vehicles (HEVs), and fuel cell

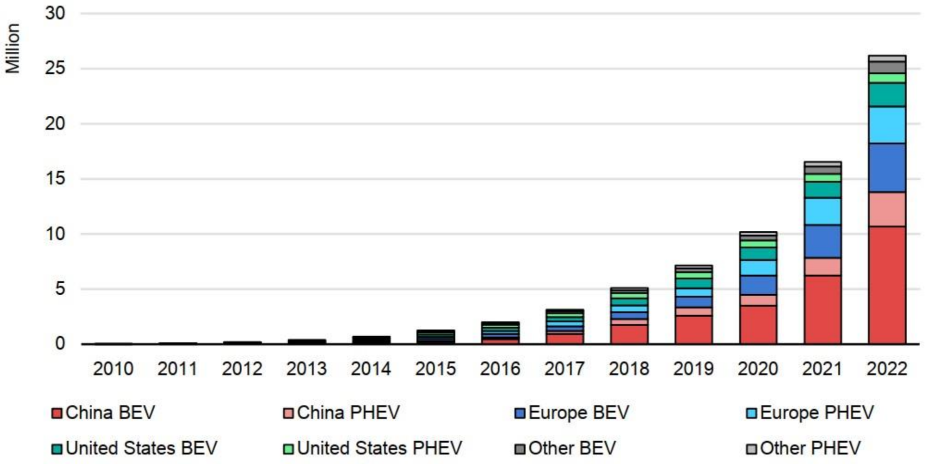

Fig. 1.3. Global electric car stock, 2010-2022.

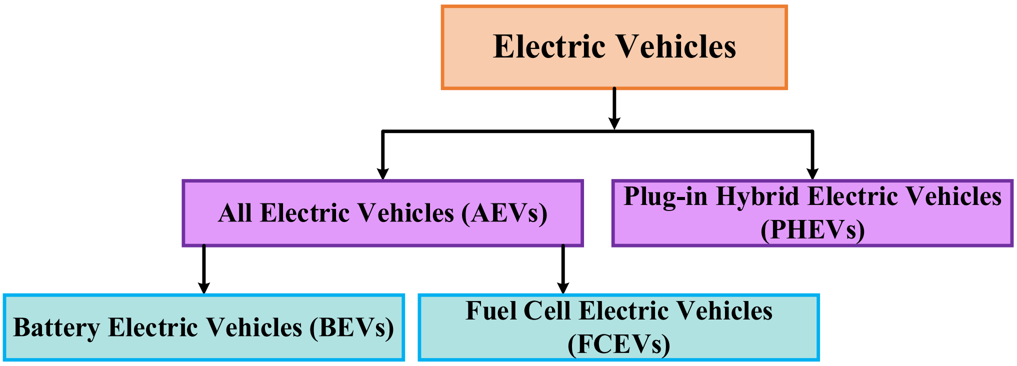

Fig. 1.4. Classification of EVs.

electric vehicles (FCEVs), as shown in Fig 1.4. These EVs can be further classified into two-wheelers, three-wheelers, and four-wheelers. It is important to note that most of these vehicles require batteries as their energy source and a battery charger is necessary to recharge these batteries [9]. Currently, the mass adoption of EVs is hindered by range anxiety, the need for charging infrastructure, and high cost. Therefore, designing a compact and cost-effective plug-in battery charger that enables flexible charging techniques such as grid-to-vehicle (G2V), vehicle-to-grid (V2G), and vehicle-to-vehicle (V2V) while meeting input current harmonic limitations as per standards is crucial [10].

1.2 Classification of All Electric Vehicles

This section provides a description of the EVs namely BEVs and FCEVs which fall in the domain of all electric vehicles (AEVs) [4]. Table 1.2 lists the BEVs and FCEVs attributes.

Table 1.2: FCEVs Vs. BEVs

Attributes	**Fuel Cell Electric Vehicles (FCEVs)**	**Battery Electric Vehicles (BEVs)**
Energy Source and Infrastructure	Hydrogen	Electric grid-based charging
Propulsion System	Electric Motor Drives System	Electric Motor Drives System
Energy System	Fuel cells, batteries, and ultracapacitors	Batteries and ultracapacitors
Basic Characteristics	Ultra-low emission, highly energy efficient, low crude oil dependence, sufficient driving range	Zero emission, highly energy efficient, free from crude oil, commercial availability
Key Issues	Under developed, high cost, reliability, cycle life, hydrogen infrastructure	Initial cost, range anxiety, battery and battery management, charging infrastructure

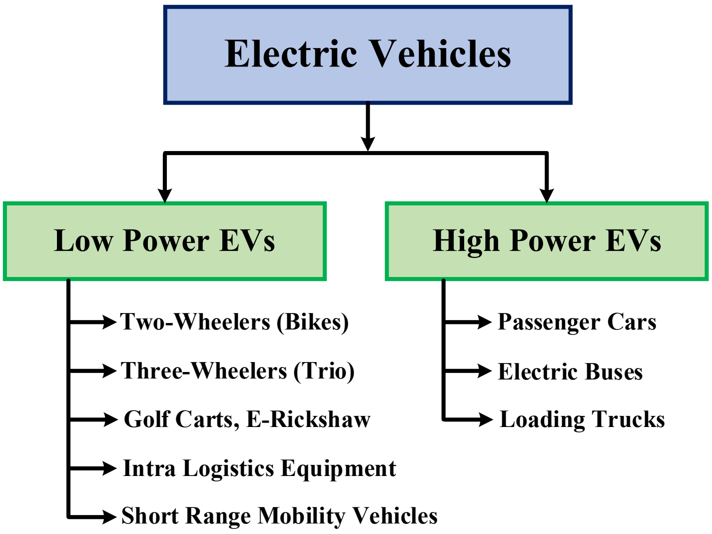

Fig. 1.5. Categories of EVs.

1.2.1 Battery Electric Vehicles (BEVs)

BEVs are a feasible solution to the energy crisis and global warming issue. They use an electric motor drive as their propulsion system, and are powered by batteries or ultracapacitors. Charging facilities and infrastructure on the electric grid are used to recharge the energy source. BEVs have characteristics such as zero emissions, high efficiency, independence from crude oils, and commercial availability. However, they also have disadvantages, including high initial cost and range anxiety. To achieve the desired drive

Table 1.3: Types of EVs with specifications

Electric Vehicle	**2-Wheeler/E-rikshaw/Infra Logistics Equipment**	**Trio/Golf Carts**	**Short Range Mobility Vehicle**	**Passenger cars/ Buses**
Charger Power (kW)	0.5-1	1-3	3.3-7	62-500
Battery Voltage (V)	48	48	120	400-600
Charging Time (hrs)	6-8	3-4	4	0.5

ability at the highest energy efficiency and lowest emissions, automotive and electrical engineering must work together for optimal design. The main components of BEVs include the motor, batteries, converter, controller, and energy management system. The BEVs have the ability to transfer power in various modes, including Grid-to-Vehicle (G2V), where the electric vehicles are charged from the grid, Vehicle-to-Vehicle (V2V), where power is transferred between vehicles, Vehicle-to-Grid (V2G), where power is transferred from the EV to the grid, and Vehicle-to-Home (V2H), where power is transferred from the EV to a home for emergency power backup. These features have contributed to the solution of the range anxiety issue, making the BEVs more commercially viable.

1.2.2. Fuel Cell Electric Vehicles (FCEVs)

FCEVs are emission free due to the fact that they utilize hydrogen for the production of electricity. The electricity thus produced is utilized for driving the vehicle or is preserved in the energy storage device such as batteries or ultracapacitors. The electricity produced here is through chemical reaction thus, there is no fuel burning and no pollutants production. Water and heat are the by-product of the fuel cells. The FCEVs operation is quiet. Similar to BEVs, the electric motor drive based is the propulsion system. The batteries or ultracapacitors are used at the starting for power density enhancement. The prime energy source is hydrogen in FCEVs. The important characteristics of FCEVs are ultra-low emission, high efficiency, low dependence on crude oil, and higher driving range. The disadvantages are high cost, safety, and hydrogen infrastructure. To ensure the efficiency, longevity, reliability, and optimum cost operation of FCEVs, the automotive engineering, electrical engineering, and fuel cell

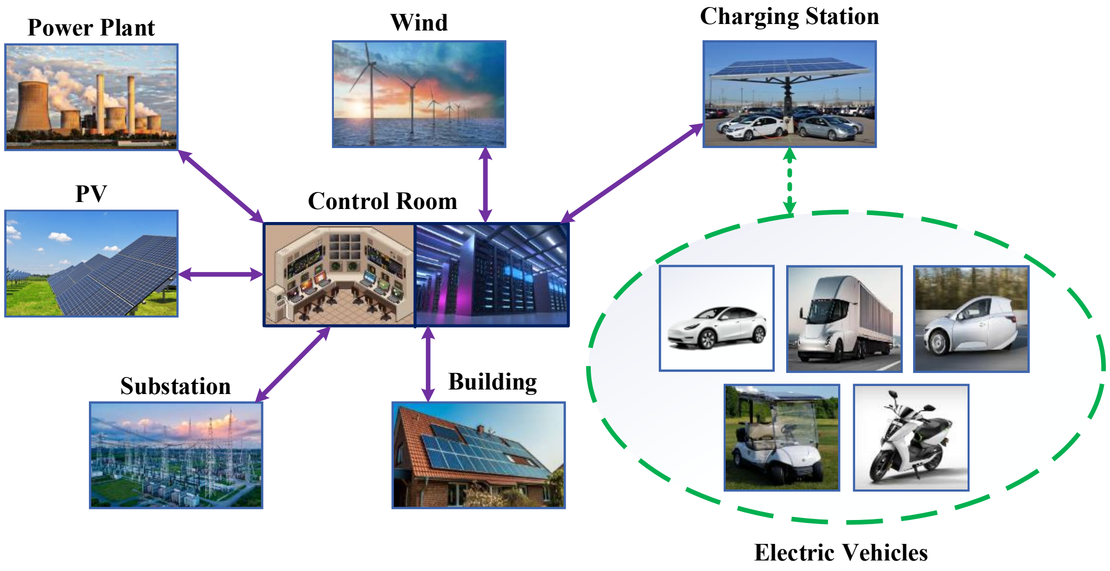

engineering integration are necessary to harness the gasoline and battery dependent new energy device. To achieve the requisite driving range at the highest efficiency and the lowest emission, the electric propulsion and fuel cell system must work very well together.

1.3. Category of EVs

The EVs can be categorized into two groups based on battery voltage, which are low power EVs with a battery voltage of 48V/72V and high power EVs with a battery voltage of 400V/600V, as shown in Fig. 1.5. Low power EVs typically include two-wheelers, three-wheelers, golf carts, e-rickshaws, intra-logistics equipment, and short-range mobility vehicles, while high power EVs include passenger cars and electric buses. Table 1.3 outlines the attributes of various EV categories [11].

1.4. Electric Vehicle Battery Charging Infrastructure

A collection of distributed energy sources and storage devices, used locally by various loads and connected to the grid or operating in islanding mode, form the EV battery charging Infrastructure [12]. Fig. 1.6 illustrates a typical EV charging station as part of a microgrid system. The large capacity penetration of EV charging points increases demand for charging infrastructure, which puts pressure on the utility grid [13]. To alleviate concerns related to power demand, power generated locally from renewable energy sources is combined with appropriate power converter topologies [14]. EV manufacturers also provide charging station facilities as part of their charging infrastructure, such as Tesla's solar city and Nissan's solar

Charging at Home

Charging on Public Networks

Charging at Workplace

Fig. 1.7. Charging station in Different Locations [11]

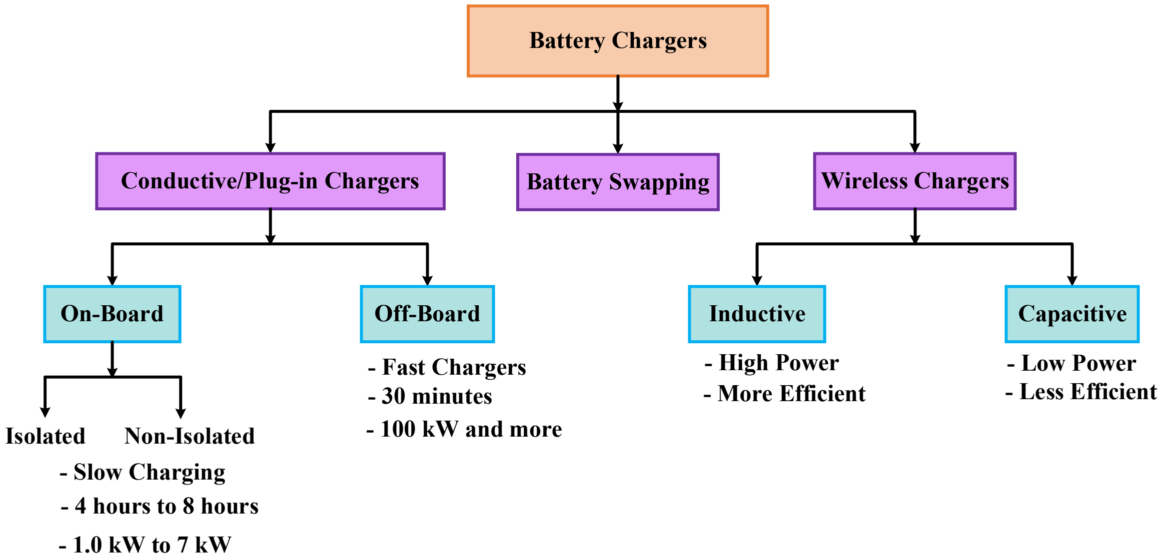

Fig. 1.8. Battery charger classification.

power plant [15]. Charging stations built with renewable energy integration minimize the cost of charging and emissions while improving utility grid coordination [16][17].

Using solar panels installed on a building's rooftop and parking lot reduce land and initial cost investment at work [18]. According to a nationwide survey, 90% of vehicles are parked for 5 to 6 hours in a parking lot, making workplace charging support vehicle-to-grid (V2G) charging [19]. Charging stations in various locations are shown in Fig. 1.7. Manufacturers of electric vehicles must meet high dependability standards regardless of the power source. Some battery technologies have a large energy capacity and potentially volatile nature, which represents a severe safety danger. The key difficulties with charging stations are reliability, availability, and maintainability, which limit large-scale commercial use of these cars [20]. A model for grid-connected charging station reliability was developed to address these issues. It aims to look into the issues of EV charging station reliability, maintainability, and availability; investigate the logical relationships between fault events, how they affect a PEV's reliability, and how proper management strategies can improve a vehicle's availability

Table 1.4: Advantages and Disadvantages of Different Charging Systems

Charging Systems	Advantages	Disadvantages
Conductive Charging	• Suitable for slow and fast-charging • High-efficiency charging • Multiple taping possible	•Need of standard connectors and cables. •Requires complex charging infrastructure
Battery Swapping	• Battery replacement takes very less time • Higher range of the vehicle	• Standardized battery size and type • Battery maintenance • Special stations required.
Wireless Charging	• No problems in standardization of connectors • Dynamic charging • Possible in all climate conditions	• Coil type needs to be standardized • High cost and complexity • Higher losses

Table 1.5: Advantages and challenges of Battery Charger

Charger Type	Advantages	Challenges
On-Board Charging	• Charging possible at any location with an electrical outlet • Simple BMS can be used	• Slower charging, less power transfer at a time • Difficult to implement forV2G applications • Weight of the charger added to the EV
Off-Board Charging	• Faster charging with higher power • Does not add to the weight of the EV	• Battery heating issue • Difficult to allocate charging locations • Cost of charging is high

[21]. A modified probabilistic index was also presented to assess the reliability of the power supply, and an integrated circuit (IC) was created to be controlled by an external BMS control unit via a serial peripheral interface (SPI), which also permitted data retrieval [22]. In addition,

1.4.1 Types of EV Charging Systems

Electric vehicle batteries can be charged through conductive coupling, wireless charging, or battery swapping. Inductive or capacitive coupling is used to charge an electric vehicle wirelessly, with the conductive coupling type utilizing an electrical outlet plug to charge the

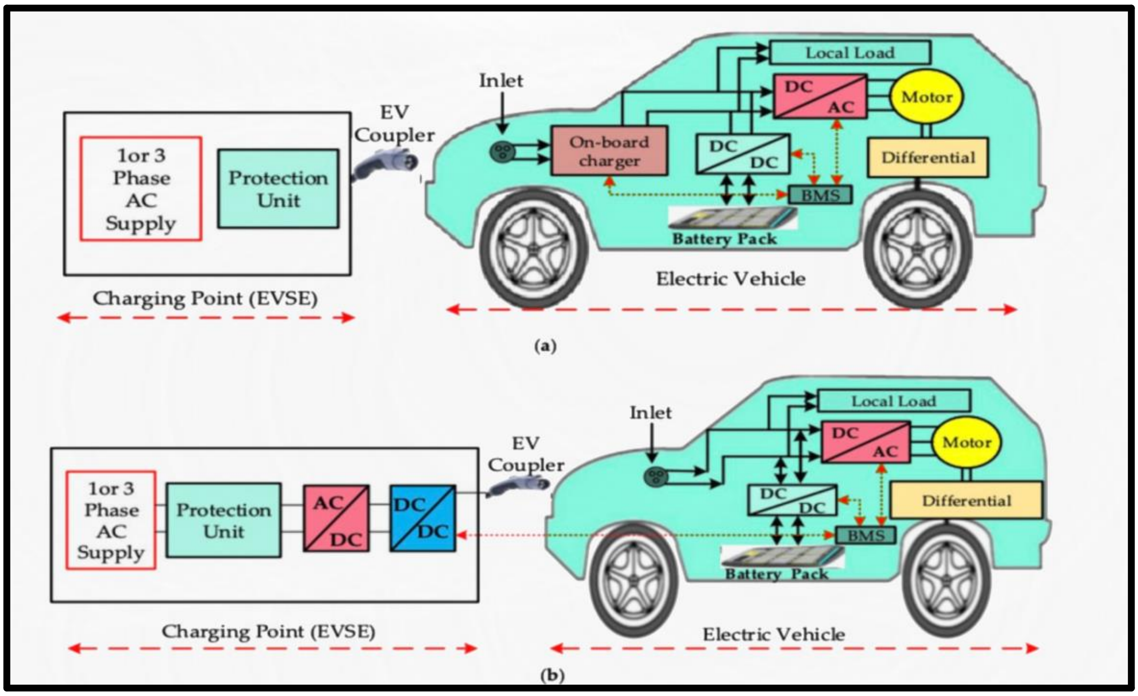

Fig. 1.9. EV Charger Schematic for (a) On-board Charger, (b) Off-board Charger [9].

vehicles [23]. For power transmission, two distinct coils are used - one is placed inside the vehicle and serves as the receiving coil, while the other is mounted on the parking slot and serves as the power transfer coil. Four capacitive plates are used in capacitive charging [24]. By designing a level-based charging station, the cost of charging can be minimized. Battery swapping technology reduces the time it takes to charge [18][25][26]. Fig. 1.8 describes the types and sub-types of EV battery chargers. Also, Table 1.4 exhibits the advantages and disadvantages of various charging methods. There are two types of electric vehicle chargers: off-board and on-board. An on-board charger is housed inside the EV, while an off-board charger is located outside the EV [27][28]. Figure 1.9 shows a block schematic of on-board and off-board types of chargers. EVs are charged from AC sources in an on-board charger; the primary challenges are power constraint and charging time [29]. Off-board chargers are used for high-power DC fast charging, and are capable of fast charging and vehicle-to-grid charging [30]. In that context, Table 1.5 shows the advantages and challenges of battery chargers.

The majority of EV charging can be done overnight at home in a garage, where the vehicle can be hooked into a convenience outlet for Level 1 (slow) charging. Level 2 charging, which is the most common technique for both private and public facilities, requires a 240 V outlet. Future advances will focus on Level 2, which provides semi-fast charging and can be used in a variety of settings. Single-phase solutions are typically employed for Levels 1 and 2, while

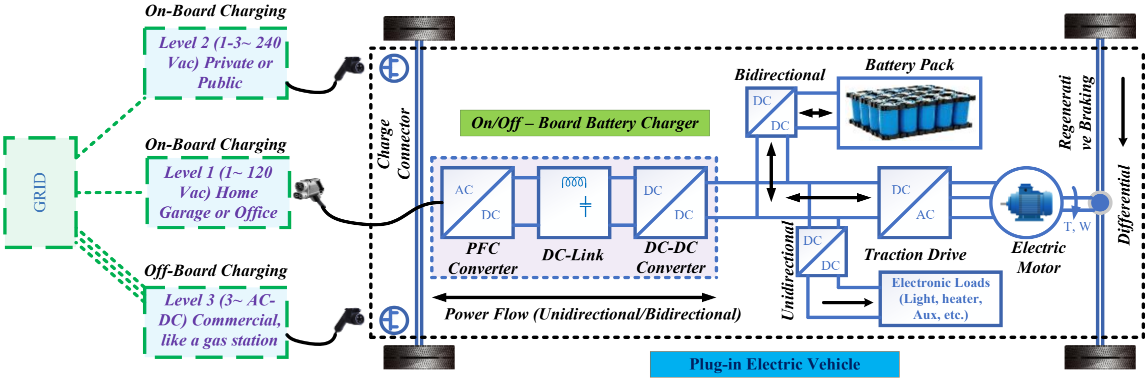

Fig. 1.10. EVSE System Schematic [9].

Level 3 and DC fast charging are designed for commercial and public use, similar to a gas-station, and three-phase systems are typically used.

On-board and off-board EV battery chargers are available with unidirectional or bidirectional power flow [9]. Because it lowers hardware needs, simplifies interconnection concerns, and tends to lessen battery degradation, unidirectional charging is a sensible initial step. Charge from the grid, battery energy injection back to the grid, and power stabilization with proper power conversion are all supported by a bidirectional charging system. Because of weight, space, and cost considerations, most onboard chargers limit high power. To circumvent these issues, they can be incorporated with the electric drive. Wireless (conductive or inductive) EV charger systems are available. Direct contact between the connector and the charge intake is used in conductive charging systems. A magnetic field is used to transfer electricity in an inductive charger. This type of charger has been explored for Levels 1 and 2 and maybe stationary or moving. An off-board battery charger is less constrained by size and weight.

1.4.2 Charging Levels, Modes, and Infrastructure

Charger power levels are based on the following factors: power, charging time and location, cost, equipment, and grid impact. The deployment of charging infrastructure and electric vehicle supply equipment (EVSE) is critical since there are numerous factors to consider, including charging time, distribution, scope, demand policies, charging station standards, and regulatory procedures. The availability of charging infrastructure can be exploited to lessen the need for and expense of onboard energy storage.

The essential components of an EVSE include EV charge cords, charge stands (residential or public), attachment plugs, power outlets, vehicle connectors, and protection (see Figure

Table 1.6: Comparison of different electric vehicle charging levels [31], [33]

Specifications	**Level 1**	**Level 2**	**Level 3**	**Ultra-Fast Charging (UFC)**
Charger Type	Onboard – Slow charging	Onboard – Semi-fast charging	Offboard – Fast charging	Offboard – Ultra-fast charging
Charging Power	1.44 - 1.9 kW	3.1 – 19.2 kW	20 – 350 kW	>350 kW
Charging Time	200 km: +/- 20 hours	200 km: +/- 5 hours	80% of 200 km: +/- 30 min	Approximately 5 min with high energy density
Charger Location	Residential	Private and Commercial	Commercial	Commercial
Power Supply	120/230 Vac, 12-16 A, 1-ϕ	208/240 Vac, 12-80 A, 1-ϕ/Split phase	208/240 Vac & 300-800 Vdc, 250-500 A, 3-ϕ	1000 Vdc and above, 400 A and higher Poly-phase
Supply Interface and Protection Type (SIPT)	Convenience outlet (Breaker in cable)	Dedicated EVSE (Braker in the cable and pilot function)	Dedicated EVSE (communication & event monitoring between EV and charging station)	Dedicated EVSE (communication & event monitoring between EV and charging station)
Standards	SAE J1772, IEC 62196-2, IEC 61851-22/23, GB/T 20234-2		IEC 61851-23/24 IEC 62196-3	IEC 62196 SAE J2836/2 & J2847/2

1.10) A specific cord set, and a wall or pedestal mounted box are the two most common options [3].

1.4.2.1 Charging Levels

Conductive charging involves an electric connection between the charging inlet and the vehicle which follows three charging levels such as Level 1, Level 2, and Level 3 depending on the power level as shown in Table 1.6. Level 1 and Level 2 charging are used in onboard

Table 1.7: Comparison of different charging modes [47]

Charge Mode	**Phase**	**Power (Max)**	**Voltage**	**Current**	**Specific Connector**	**Charging Configuration**
Mode-1	AC - 1ϕ AC - 3ϕ	3.8 kW 7.6 kW	230-250 V 480 V	16 A	No	
Mode-2	AC - 1ϕ AC - 3ϕ	7.6 kW 15.3 kW	230-250 V 480 V	32 A	No	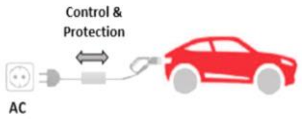
Mode-3	AC - 1ϕ AC - 3ϕ	60 kW 120 kW	230-250 V 480 V	32-250 A	Yes	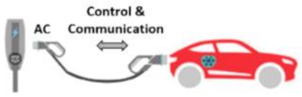
Mode-4	DC	>150 kW	600-1000 V	250-400 A	Yes	

chargers with AC power and follow the same set of standards. The Level 1 charger uses a 120 V single-phase AC power supply and has the slowest charging speed which is generally used in domestic with low power levels (up to 1.92 kW) without any additional infrastructure [31], [32]. Therefore, Level 1 charging is appropriate for long-time or overnight charging. Level 1 chargers generally require about 11-36 hours for 1.9 kW charging power for a 16-50 kWh EV battery [33]. The primary charging method for private and public facilities is Level 2 charger, as they have comparatively fast charging abilities. The charging time of Level 2 is 3 to 5 times faster than Level 1 chargers due to high power usage [34]. Level 2 charging can provide power up to 19.2 kW for both single-phase and split-phase with 208 Vac or 240 Vac voltage. Dedicated components and installations are required in Level 2 chargers for high power transfer through the onboard charger. The charging time range is 2 - 3 hours for 19.2 kW with an EV battery capacity of 30 -50 kWh [9]. Level 1 and 2 charging connectors follow the IEC62196-2 standard in Europe, SAEJ1772 and Tesla superchargers in the USA [35], [36].

The DC fast charging or Level 3 charging uses AC and DC power to deliver high voltage DC power to the EV battery. The Level 2 chargers can manage a high-power range between 20 kW to 350 kW to supply DC voltage of around 300 Vdc to 800 Vdc in offboard chargers.

DC fast chargers are directly connected to the vehicle via off-board chargers to the three-phase power grid. Charging time of 90 kW or larger Level 3 charger is range 0.2 - 0.5 hours which is faster than Level 1 and 2 [33]. CHAdeMO, Tesla superchargers and CCS combo 1, 3 connectors are considered for level 3 fast charging. However, low-power chargers including Level 1 and Level 2 have the lowest negative impact on the power network during peak time. The local distribution grid may become overloaded by the level 3 chargers due to high power usage during peak times [37].

Extrema fast charging (XFC) systems can deliver a refueling experience like ICE vehicles.

Table 1.8: Specifications of different AC charging connectors [45], [46], [47]

Specifications	**Japan**	**USA**	**Europe**		**China**		**All Markets**	
Charger Type								
	Type-1 (SAE J1772)		Type-2 (Mennekes)		Type-2 (GB/T)		Tesla	
	Level-1	Level-2	Mode-1	Mode 2-3	Mode-2	Mode-3	Mobile Connect	Wall Connect
Maximum Power	1.9 kW	19.2 kW	4 kW	22 kW	7 kW	27.7 kW	7.7 kW	11.5 kW
Input Voltage	120 V 1-ϕ	240 V Split phase	250 V 1-ϕ	480 V 3-ϕ	250 V 1-ϕ	400 V 3-ϕ	120/240 V 1-ϕ	208/250 V 1-ϕ
Current Rating	16 A	80 A	16 A	32 A	16 A	32 A	16/32 A	48 A
Standards	SAE J1772-2017 IEC 62196-2 IEC 61851-22/23		IEC 62196-2 IEC 61851-22/23		GB/T 20234-2 IEC 62196-2		IEC 62196-2	

The XFC systems can manage more than 350 kW power with 800 Vdc internal DC bus voltage and battery recharging time is approximately 5 min. The XFC stations are designed with power electronic components focusing on solid-state transformers (SST), isolated DC-DC converters, and front-end AC-DC converter stages and controllers. The installation cost of the XFC is very high and requires dedicated EVSE to deliver high power. The XFC station can be designed by combining several XFC systems to provide a chance to lower operational and capital investment to make it economically feasible. Additionally, SST provides advantages over conventional line-frequency transformers for converting medium voltage levels into low voltage levels and providing galvanic isolation in XFC stations [38].

1.4.2.2 Charging Modes

The International Electrotechnical Commission (IEC) defines 4 charging modes (IEC-62196 and 61851) for AC and DC charging systems and provides the general attributes of the safe charging process and energy supply requirements [39]. A comparison of charging modes is presented in Table 1.7 with specifications and charging configurations. The slow charging applications follow mode 1 which comprises with earthing system and circuit breaker for protection against leakage and overloading conditions. The current limit of mode 1 varies from 8 A to 16 A depending on the country. The EV is directly connected to the AC grid either 480 V in three-phase or 240 V in single-phase via a regular socket in mode 1. The charging cable is integrated with a specific EV protection device (In-cable control and protection device (IC-CPD) in mode 2 to enable control and protection. Mode 2 charger offers a moderate safety level and utilizes minimum standards. This mode delivers slow charging from a regular power socket which is ideally suited for home installation [40]. Single-phase or three-phase AC power can be used in this mode with a maximum power of 15.3 kW and 32 A current flow [2]. The mode 2 cable provides overcurrent, overheat protection, and protective earth detection. Therefore, mode 2 charging cables are more expensive than mode 1 due to high current flow and provide moderate safety for modern EVs [41].

Mode 3 is used for slow or semi-fast charging via a specific outlet with the controller. The dedicated circuit is permanently installed (on the wall) for protection, communication, and control in this mode. Public charging stations are commonly built with mode 2 and are able to facilitate integration with smart grids. Mode 3 allows a higher power level with a maximum current of 250 A which is used by fixed EVSE for single-phase or three-phase grid

Table 1.9: Specifications of different DC charging connectors [38], [44]

Specifications	**Japan**	**USA**	**Europe**	**China**	**All Markets**	
Charger Type						
	CHAdeMO	CCS-Combo 1	CCS-Combo 2	GB/T	Tesla Supercharger	CHAdeMO
Maximum Power	50-400 kW	150-300 kW	350 kW	60-237 kW	250-350 kW	50-400 kW
Input Voltage	50-1000 V	200-1000 V	200-1000 V	250-950 V	300-480 V	50-1000 V
Current Rating	400 A	500 A	500 A	250-400 A	800 A	400 A
Standards	IEC 61851-23/4, IEC 62196-3, JEVS G105	SAE J1772, IEC 61851 23/24, IEC 62196-3	IEC 61851-23/24 IEC 62196-3 DIN EN 62196-3	GB/T 20234-3, IEC 62196-3	IEC 62196-3	IEC 61851-23/4, IEC 62196-3, JEVS G105

integration. The connection cable includes an earth and control pilot to enable proper communication between the EV and the utility grid. Fast charging station uses mode 4 via fixed EVSE to deliver DC to the vehicle which is utilized in public charging stations. The installation includes control, communication and protection features [42]. Mode 4 chargers are more expensive than mode 3 and the connection includes earth and a control pilot to control a maximum of 400 A current. Off-board chargers follow mode 4 specifications with a wide range of charging capabilities over 150 kW power [38].

1.4.2.3 Charging Connectors

EV charger components (including power outlets, connectors, cords, and attached plugs) are the main components of EVSE which provide reliable charging, discharging and protection for the charging system. The configuration of the peripheral devices, power ratings, and standards of EV chargers are various in different authorities. However, governing bodies and manufacturers are attempting to ensure compatibility by developing international standards, protocols, and couplers for slow and fast charging systems to avoid conflicts and difficulties [43]. Commercially available different AC and DC connectors are shown in Tables 1.8 and 1.9 respectively by following their specifications and standards. Table 1.10 represents the basic AC charging and DC charging features. AC chargers are slow chargers which take 6 - 8 hours to fully charge EV. DC chargers are used for fast charging with a higher power range of up to 400 kW. The various connectors can be categorized into three groups according to the IEC 62196 - 2 standards.

Type 1 connectors are widely used in Japan and USA for AC single-phase charging and follow SAE J1772 standards. They have low power charging capability (maximum capacity of 19.2 kW) with a voltage of 120 V or 240 V with a maximum current of 80 A [44]. The charging cable of Type 1 connector is permanently installed to the station. Type 2 connectors are considered as standard type in all countries which support single-phase and three-phase charging by following IEC 61851-1 standards [45]. Type 2 - Mennekes connectors are utilized in Europe and Type 2 - GB/T are used in China. This connector supports mode 2 and 3 charging with higher power (22 kW) than Type 1. The detachable charging cable of the Type 2 station allows to charger of Type 1 vehicles with the correct cable [46]. Type 3 connectors are used in France and Italy that includes Type 3A and 3C depending on the physical formats. Type 3 connectors or SCAME plugs allow both single-phase and three-phase charging with shutters to prevent and follow IEC 62196-2 standards.

The DC chargers or superchargers deliver the fastest charging rate which follows the combined current system (CCS) and IEC 62196 standards. The IEC 62196-3 standard specifies four types of coupler configurations for DC fast chargers. They are configuration AA (CHAdeMO), configuration BB (GB/T), configuration EE (CCS-Combo 1), and configuration FF (CCS-Combo 2) [47]. The Combo 1 and Combo 2 connectors are extended versions of Type 1 and 2 connectors with two added DC contacts to allow high-power charging. The CCS - Combo 1 connector is based on Type 1 chargers and is used in the USA. Europe preferred CCS - Combo 2 connectors which have a Type 1 coupler configuration. CCS connectors can withstand a high-power range of up to 350 kW. The GB/T fast charging DC connectors used in China follow GB/T 20234-3 standards. It is capable of operating higher power ratings up to 237 kW with a maximum voltage of 1000 V and 400 A current.

Table 1.10: Advantages and Disadvantages of Different Charging Systems

AC Charging	• EV charging at different speed • Alternating current or alternating power • Availability in power grid • Economic transmission over long distances • Converted to DC using power electronic converter • Low cost • Found in parking lots • More prevalent
DC Charging	• Fast EV charging • Direct current or direct power • Constant • Stored in batteries • High cost • Found in highways • Less prevalent

CHAdeMO fast charging systems developed in Japan, and it competes with the supercharger network, CCS and GB/T standards. CHAdeMO connectors have ultra-fast charging and V2G integration ability for 400 kW with 1000 V maximum voltage and 400 A current [48]. Tesla offers a connector for both AC and DC charging for all the charging levels. Tesla superchargers offer excellent fast charging speeds via their own designed charging stations and connectors can supply 72 kW, 150 kW, or 250 kW electric power [49]. Type 2 connector required for AC charging with Tesla station which allowed power up to 11.5 kW and an AC voltage of 250 V single phase. Tesla superchargers are built for Tesla cars and version 3 models have a maximin power of 250 kW. The Australian standard for EV charging plugs and connectors (IEC 62196) encourages the adoption of both United State and Europe connector standards rather than imposing a single standard for EV charging systems [50].

1.5. Research Problem

EV chargers can be classified as unidirectional or bi-directional chargers depending on the possible power flow direction [51]. Unidirectional charging is an economical solution because it limits hardware requirements, simplifies interconnection issues, and reduces battery degradation. However, bidirectional battery chargers have additional advantages, such as EV batteries can be used to deliver power to the grid during peak power demand [9], [51].

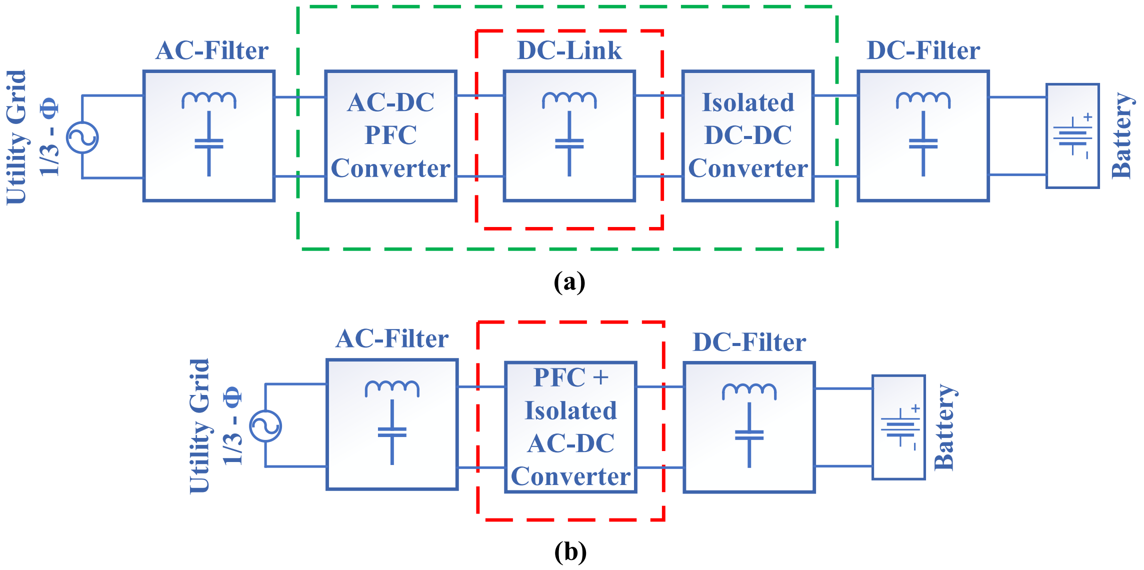

Fig. 1.11. (a) Power conversion architecture of the conventional two-stage EV charger; (b) Power

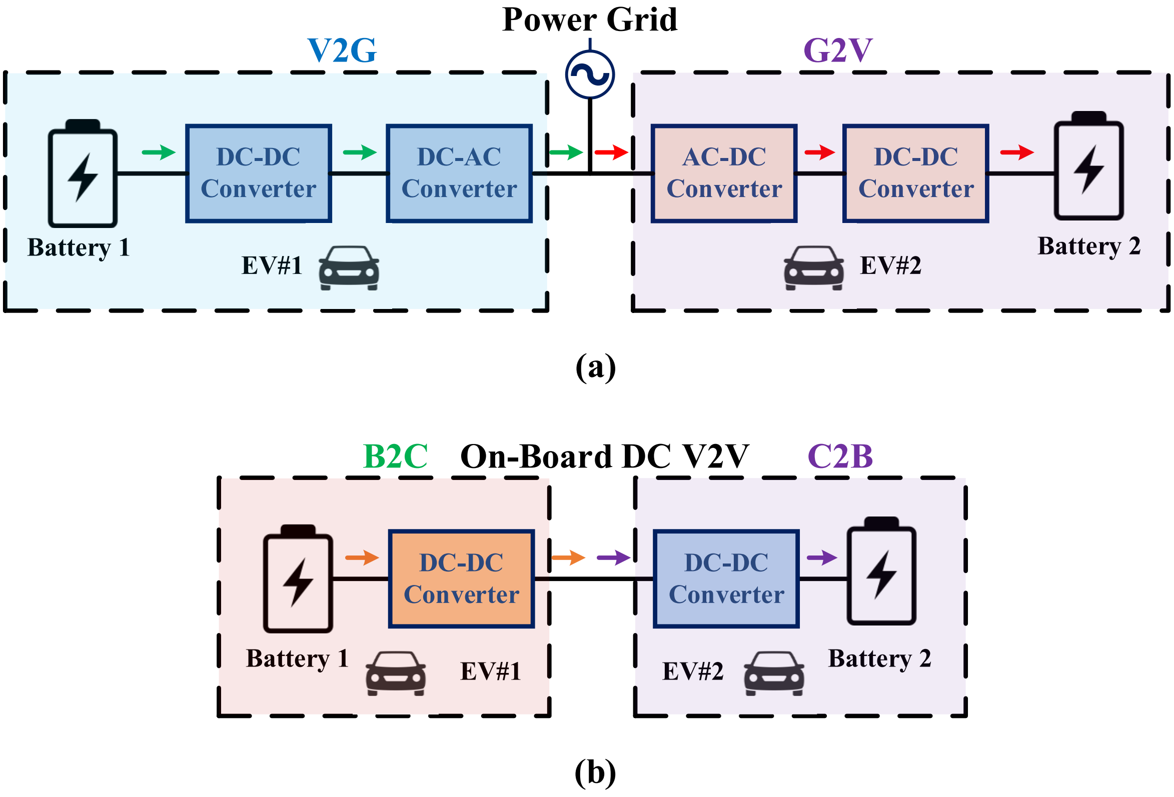

Fig. 1.12. (a) V2G operation with combination with G2V operation; (b) V2V charging using on-board DC-DC converter

The physical positioning of the EV battery charger in the vehicle is also a deciding factor for the converter topology selection [52]. For example, battery chargers are generally placed close to the internal combustion (IC) engine in the case of plugin hybrid EVs. In this scenario, the converter and the associated electronic circuits like gate drivers are exposed to high ambient temperature (more than 150^0C) [53]. Therefore, it is preferred to implement thermally more stable converters to reduce the complexity of the cooling system.

The conventional EV battery chargers are developed with two power conversion stages as depicted in Fig. 1.11 (a) [9], [51]. The first stage converts the AC voltage to a DC voltage employing power factor correction (PFC). The second stage is an isolated DC-DC converter stage, which performs the output DC voltage regulation. These two stages are interconnected by relatively large DC link capacitors. Two-stage battery charger exhibits low efficiency due to having two separate power conversion stages. Meanwhile, power density is limited by these DC link capacitors. Usually, electrolytic capacitors with higher capacitance value are utilized as DC link capacitors. These electrolytic capacitors are most susceptible to failure at high ambient temperature, thus affecting the reliability of the charger [53].

The alternative solution to improve the efficiency and power density of EV battery chargers with reliable high-temperature operation capability is to use single-stage isolated converter, as shown in Fig. 1.11 (b) that do not require any intermediate DC link capacitors [51]. In this converter, power factor correction (PFC) operation and battery voltage regulation are implemented in one stage by sharing common devices.

High-density, low cost, and light-weight are the most desirable attributes for any power electronics system. To achieve these objectives, the most prevalent ways are to use fewer conversion stages, and by increasing the converter's switching frequency leading to reduced footprint with smaller inductors and output capacitors. However, higher switching frequency causes additional switching losses that deteriorates the efficiency and thermal performance. Maintaining soft switching of the semiconductor devices for the entire range of operation is one of the key requirements to enable efficient operation at high switching frequencies. This thesis focuses on developing simple soft-switching techniques to improve the overall performance of the HF single-stage converter for EV charging application. In addition, the current-fed converters are justified to be more plausible choice for EV charging application over existing voltage-fed converters. Current-fed topologies that attracted great attention because of their evident merits over conventional voltage-fed converters as follows: 1) inherent short-circuit protection; 2) low HF turns ratio; 3) high step-up ratio; 4) low input current ripple; 5) lower duty cycle loss; 6) negligible diode ringing; 7) more accessible current control capability and 8) reduced circulating current leading to the low peak and RMS current through the switches [155].

This thesis proposes a family of current-fed single-stage isolated converter topologies with soft-switched modulation techniques for EV battery charging. These topologies, in addition to addressing the above-mentioned shortcomings of the conventional two-stage battery chargers, also provide V2G (vehicle to grid) and G2V (grid to vehicle) mode of operation.

In addition, the flexibility of the EVs can be enhanced using the vehicle-to-vehicle (V2V) charging system. This system will help in mitigating the range anxiety and also offers emergency charge transfer to another user. The energy exchange between EVs can be a viable option in an emergency situation where an EV is about to run out of charge at a location without any charging station nearby, then another EV with enough state-of-charge can transfer the energy required by the first EV. However, very few investigations from power electronics perspective on the domain of V2V charging have been reported [54]. The battery charger in each of the EV comprises front end AC-DC converter and a back-end DC-DC converter for implementing the V2G and G2V operations, the converters are bidirectional [55]. This method combines the two operational modes of V2G and G2V where both the EVs have a connection to the power grid, which is presented in Fig. 1.12 (a). EV1 is providing the energy and is operating in V2G mode where it injects the stored energy into the batteries to the power grid. EV2 works in G2V mode and recharges the batteries by accepting energy from the grid [56]. The two EVs are in connection with the power grid. The flow of power is controlled by current regulation on the AC side. The current between two EVs has 180 degrees phase-shift. The resultant current of the power grid is zero as the current requirement of EV2 is equal in amplitude to the current generated by EV1 or a set of EVs. The physical meaning is that the energy requirement for recharging EV2 batteries is completely furnished by EV1. Therefore, the power grid does not get overloaded, which represents the critical aspect of V2V operation [57]. However, this mode has a greater number of power conversion stages which leads to decrease efficiency and power density.

Therefore, the DC-DC converter for the battery chargers permits the batteries to be charged and discharged with current or voltage control. Suppose a second DC-DC converter is joined at the output of the first DC-DC converter and both the dc-dc converter can operate in bidirectional mode then a power exchange is possible between the two EVs batteries. This is outlined in Fig. 1.12 (b). The cascaded DC-DC converter permits bidirectional operation with a regulated charging current in a varied operating voltage range. There is a possibility to charge batteries having higher voltage using lower voltage batteries. Thus, the external plug that is connected to enable the V2V power transfer in DC mode do not require any additional power converters or hardware.

1.6. Research Objectives and Proposal

The prime objective of the thesis is the investigation and implementation of G2V, V2G and V2V charging techniques using a single-stage current-fed converters. The advantages of the single-stage converters in comparison to the existing ones are the reduced components count, convenient control strategy with PFC operation, compact size, higher power density, and low total harmonic distortion (THD < 5%). The AC-DC and DC-DC modes of operation are explored using the single-stage converters with primary goals to reduce components' count, improved power quality, higher reliability with robustness, flexible charging options to reduce range anxiety, and maintain overall high efficiency (> 95%). The power converter design is tested under source and load perturbations.

This overall objective is divided into the following sub-objectives:

1) A comprehensive literature overview of on-board chargers for more EVs.
2) Study of possible improvements in power converters and modulation techniques for EV charging application.
3) Proposing new snubber-less single-stage current-fed bidirectional single-stage (AC-DC and DC-DC) power converters for multifunctional plug-in EV charging (G2V, V2G, and V2V).
4) Proposing a novel soft-switching modulation scheme and reporting the detailed of steady-state performance and converter design.
5) Develop scale-down prototypes for all the proposed single-stage current-fed power converter topologies to verify mathematical analysis and simulations with experimental results.

To accomplish the above-mentioned objectives, the thesis investigates and implements different charging techniques using the single-stage current-fed topology, a brief description of the same is provided in the thesis outline next section 1.8 and the detailed description is provided in various Chapters 3 to 6.

1.7. Methodology

To achieve the objectives within the given time limit, the following methodology has been adopted:

Report a comprehensive study of existing power converters topologies for plug-in EV chargers, and identify merits and demerits

⇩

Considering the fact that an extensive study of voltage-source converter topologies has already been carried out, and feasibility of current-fed topologies received very limited attention, perform a systematic study on possible use of current-fed converters

⇩

Based on the merits and demerits of current-fed converters, propose new converter topologies, novel modulation, and modified control techniques to make it more acceptable for practical use

⇩

Perform preliminary simulation on a suitable platform to find the suitability of the proposed system

⇩

Analyse comprehensively to find out all justification of successes or failures in achieving desired results

⇩

Modify converter topology or modulation and control schemes to achieve desired results

⇩

Verify the results with the help of mathematical expressions, and also through simulation results

⇩

If the mathematical model and simulation results have acceptable agreement, then build a scale-down lab prototype and verify analytical and simulation results with experimental results

1.8. Thesis Outline

The contents of the thesis in various Chapters are organized as follow:

In Chapter 2, a comprehensive review of wide-band gap (WBG) device-based topologies of on-board chargers (OBCs) for more electric vehicles (MEVs). It reviews the current state-of-the-art solutions of OBCs, including architectures and configurations, soft-switching techniques, charging infrastructure consideration, commercially available products, and future trends with challenges. A detailed overview of the promising topologies for WBG based OBCs, including two-stage and single-stage structures, is provided. Future trends and challenges for topologies, wide bandgap technologies, thermal management, system integration, fast charging and wireless charging systems are also discussed in this chapter.

In Chapter 3, a novel zero-current assisted soft-switching bidirectional single-stage single-phase current-fed isolated power factor correction (PFC) based converter for plug-in EV charger is reported. The steady-state analysis and operation, modulation technique, control scheme, and design have been discussed. An isolated topology consists of a current-fed full-bridge converter with bidirectional switches on the AC-side that is connected with a full-bridge converter on the DC-side of a high-frequency transformer (HFT). The modulation strategy and control technique are presented for promising the soft-switching operation of all semiconductor devices where zero-current switching (ZCS) at AC-side and zero-current turn-on at DC-side throughout the range for all modes with bidirectional power flow capability. The analysis and design are validated with the simulation results from PSIM 11.4 software, and further verified with the experimental results from a 1.5 kW hardware prototype developed in the lab.

In Chapter 4, a novel isolated single-stage single-phase bidirectional current-fed PFC AC-DC converter without an intermediate DC-link for EV charging application has been investigated. The steady-state analysis and operation, modulation technique, control scheme, and design have been reported. The proposed configuration comprises a current-fed push-pull circuit on the primary side and a full-bridge circuit on the secondary side via a high-frequency transformer (HFT). The modulation strategy and control technique are presented for promising the soft-switching operation of all semiconductor devices where zero-current switching (ZCS) at AC-side and zero-current turn-on at DC-side throughout the range for all modes with bidirectional power flow capability. The performance and the analysis have been validated with the simulation results from PSIM 11.4 software, and further verified with the experimental results from a 1.5 kW hardware prototype developed in the lab.

In Chapter 5, a soft-switched single-stage single-phase current-fed full-bridge isolated DC-DC converter for vehicle-to-vehicle (V2V) energy exchange has been discussed. The detailed steady-state operation, secondary-modulation technique, and converter design have been described. A novel secondary modulation technique is proposed to naturally clamp the device voltage across the primary side eliminating the necessity for traditional active-clamp circuit or passive snubbers. The operation and performance of the converter are demonstrated with the simulation results from PSIM 11.4 software, and the experimental results from a 1.5 kW laboratory prototype. Experiment results clearly justify the soft-switching operation where zero-current switching (ZCS) of primary side devices and zero current turn-on of secondary side devices.

In Chapter 6, a snubber-less naturally clamped zero current commutated (ZCC) soft-switching single-stage single-phase current-fed push-pull configuration-based DC-DC converter for vehicle-to-vehicle (V2V) charge sharing application has been investigated. The converter steady-state analysis, secondary-modulation technique, and design of converter have been discussed. A novel secondary modulation soft-switching technique has been introduced to resolve the device turn-off voltage spike issue without the use of additional snubber circuit. The simulation results, and the experimental results from a 1.5 kW laboratory are presented in order to validate the converter analysis and the design and demonstrated the performance.

In Chapter 7, the contributions of the thesis are summarized, and guidelines for the future work are presented.

1.9. Conclusion

This chapter establishes the indispensable role and appropriateness of the EVs and their charging infrastructure. Also, the need to shift to EVs from conventional ICE vehicles owing to the strict emission restrictions and eco-friendly nature of the EVs has been explored in this chapter. The commercial aspects of EVs, FCEVs, and ICE vehicles detailing the range and refuelling time are discussed. A brief description on classification and comparison of all electric vehicles (AEVs) namely battery electric vehicles (BEVs) and fuel cell electric vehicles (FCEVs) is presented. A comprehensive review on categories of EVs along with their characteristics and classification are outlined in this Chapter. Further, different EVs charging infrastructure, types of EV charging systems, charging levels and modes with connectors are described.

Since, the plug-in EV charger system is a crucial part of electric vehicles, the next Chapter deals with a detailed review of state-of-the-art power converter topologies for EV charging application. The disadvantages of two-stage battery charger are low efficiency and poor power density due to presence of DC-link capacitors. These electrolytic capacitors are most susceptible to failure at high ambient temperature, thus affecting the efficiency, power density, reliability, and cost of the charger. The alternative solution to improve the efficiency and power density of EV battery chargers with reliable high-temperature operation capability is to use single-stage converter that do not require any intermediate DC link capacitors. These single-stage power converter topologies, in addition to addressing the above-mentioned shortcomings of the conventional two-stage battery chargers, also provide V2G (vehicle to grid), G2V (grid to vehicle), and Vehicle-to-Vehicle (V2V) mode of operation. The fundamental objective of this thesis is to study, analyse, and develop wide bandgap semiconductor based single-stage isolated power converter topologies for EV charging applications. Performance of these converters are verified with full functionality enabling V2G, G2V and V2V mode of operation.

Chapter 2: A Comprehensive Review of Wide Band-Gap (WBG) Semiconductor Based On-Board Chargers for More Electric Vehicles

2.1 Introduction

The efficiency is critical regardless of whether the charging unit is on the ground or on the EV, wired or wireless. Even a minor enhancement in converter efficiency can save substantial energy for the enormous number of vehicles on the ground. Hence, higher conversion efficiency and power density in power electronics applications lead to decreased volume and price of passive elements and cooling equipment [58]. The price and power capability are crucial factors on the roadside, while on the EV side, power density, efficiency, reliability, and price are paramount factors.

The EV charging infrastructure and advanced technologies are continually changing to enhance efficiency, power capability, power density, and lowering prices. Power converters are fundamental to the aforesaid technologies, determining and influencing the progress of all other technologies. The power density and efficiency of EV recharging infrastructure are determined mainly by their operations and properties. After decades of progress, conventional silicon-based (Si) power devices have exceeded their limitations [58]. Moreover, the power density of the OBC is currently at 3.3kW/L, and the highest efficiency is estimated over 97%. Table 2.1 shows the US Drive OBC target for 2025 [59]. It shows that the specific power and power density of the OBC are expected to reach 4kW/kg and 4.6kW/L, respectively, while a peak efficiency of 98% should be achieved.

Table 2.1: The US Drive OBC Targets

OBC Target	**PFC**	**DC/DC**	**OBC**
Specific Power (kW/kg)	4	4	4
Power Density (kW/L)	4.6	4.6	4.6
Efficiency (%)	>99	>98	98

The interest in wide bandgap (WBG) power semiconductor devices stems from outstanding features of WBG materials, power device operation at higher temperatures, larger breakdown voltages, and the ability to sustain larger switching transients than silicon (Si) devices. The WBG material, especially SiC and GaN, which has a more significant energy gap between the valence and conduction bands, is thought to be a new generation of materials that can significantly enhance the performance of power devices, as shown in Fig. 2.1. As a result, recent progress and development of converter topologies, based on WBG power devices, are well-established for power conversion system for OBCs in which classical Si-based power devices show limited operation. Currently, Si-carbide (SiC) and gallium nitride (GaN) are the most promising semiconductor materials that are being considered for the new generation of power devices. The use of new power semiconductor devices, such as GaN high electron mobility transistors (GaN HEMTs), leads to minimization of switching losses, allowing high switching frequencies (from kHz to MHz) for realizing compact power converters. The timeline of the development of SiC and GaN-based power devices with the main industrial players involved are depicted in Fig. 2.2.

The early research power device of SiC MOSFET and its capability has been beyond the hindrance of silicon devices [60,61]. WBG material-based devices have previously been used to produce a high-power-density battery charger with better efficiency [62]. WBG devices are being employed and launched in many research activities and large manufacturing. In the recent decade, OBCs have received a lot of attention due to a reduction in the conduction losses, size, and cost by increasing the voltage gain and efficiency [63].

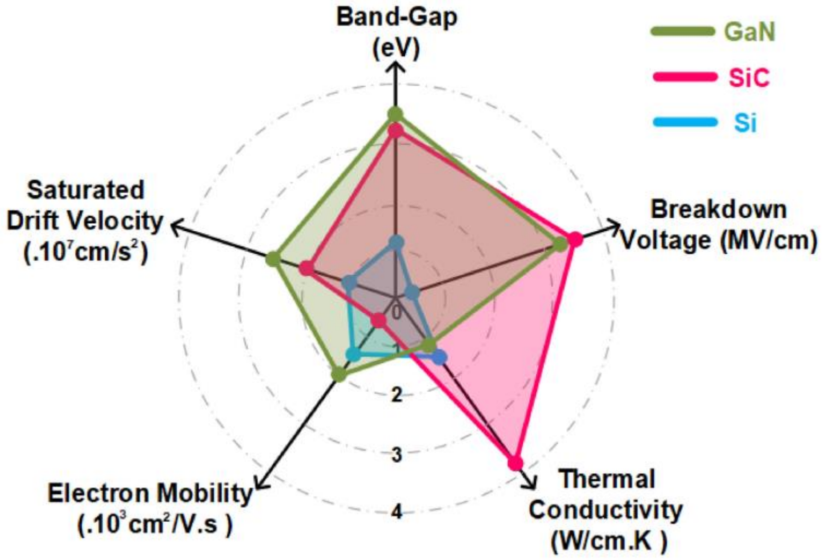

Fig. 2.1. Comparison between Si, SiC, and GaN.

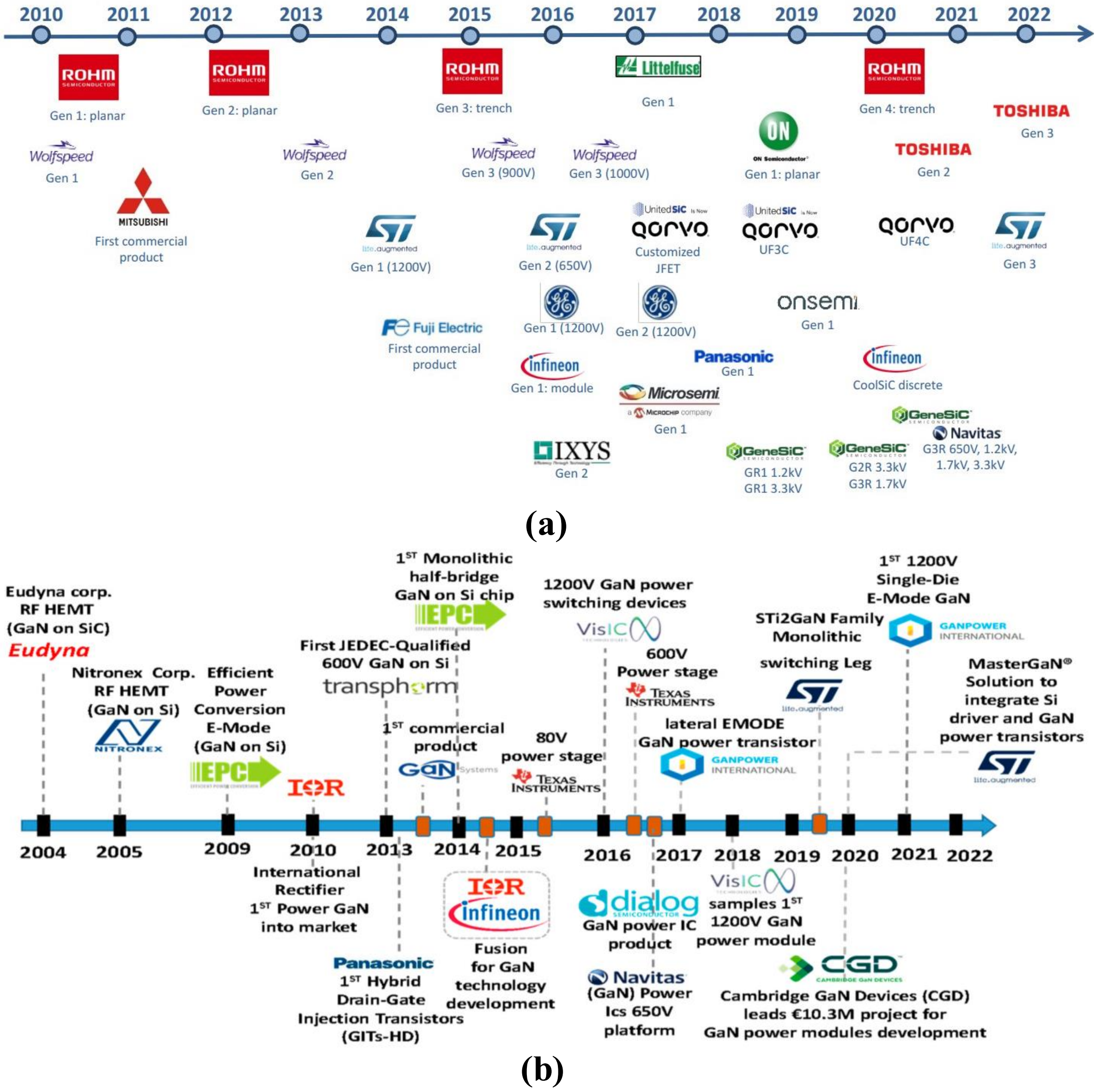

Fig. 2.2. Power electronics devices milestones and main industrial players (a) SiC-based Power Device; (b) GaN-based Power Device.

2.2 Topological Overview

The on-board chargers (OBC) system should have a high-power density, high energy utilization, small form factor, lightweight, high reliability, more efficient, economical, and grid-friendly [64]. Also, OBC can be broadly classified based on the number of power processing stages into two groups: two-stage and single-stage chargers as shown in Fig. 2.3. The OBC can be classified as unidirectional chargers and bidirectional chargers based on the power flow [64]. For the two-stage OBC architecture, an active front-end AC/DC PFC converter and an active isolated DC/DC converter are necessary. The AC/DC PFC converter is used to provide a controllable DC voltage and meet the harmonic requirements of the grid.

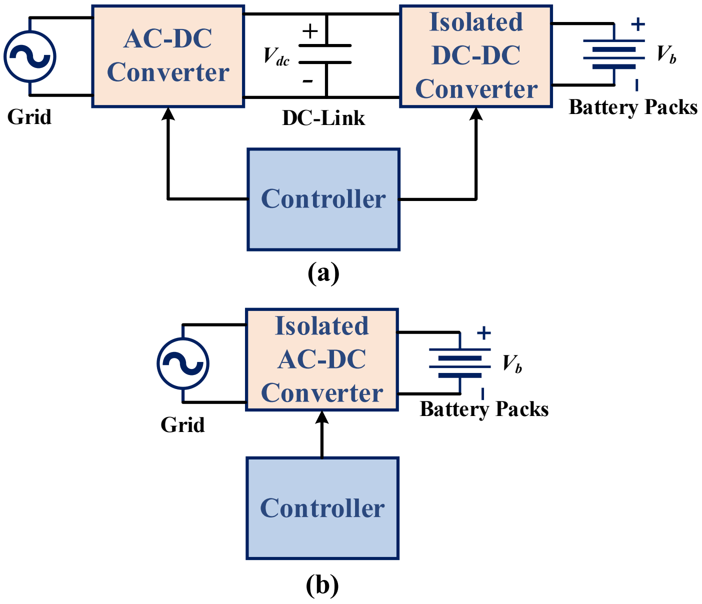

Fig. 2.3. (a) Power architecture 2-Stage battery charger; (b) Power architecture of 1-Stage battery charger.

Isolated DC/DC converters provide galvanic isolation and regulate the power delivered to the battery. Most EVs use two-stage OBCs in the automotive industry [65]. On the other hand, single-stage configurations have emerged in OBC applications as the DC-link capacitor of the two-stage OBC is voluminous and has a limited lifetime. Indeed, single-stage removes the DC-link capacitor and is comprised of solely an isolated AC/DC converter, which can provide higher power density and reduce the hardware cost [66]. This section provides a detail about the architectures and configurations of OBC.

2.2.1 Two-Stage OBC

Most commercial WBG-based OBCs used in the automotive market are two-stage architectures. This section reviews the most promising PFC AC-DC converters and DC/DC converter topologies.

2.2.1.1 PFC AC-DC Converters

Single-phase PFC converters are the most widely studied in the OBC research. As a key component of a charger system, the front-end AC–DC converter must achieve high efficiency and high-power density. Additionally, to meet the efficiency and power factor requirements and regulatory standards for the AC supply mains, power factor correction is essential. The critical comparative analysis of PFC AC-DC converters is shown in Table 2.2.

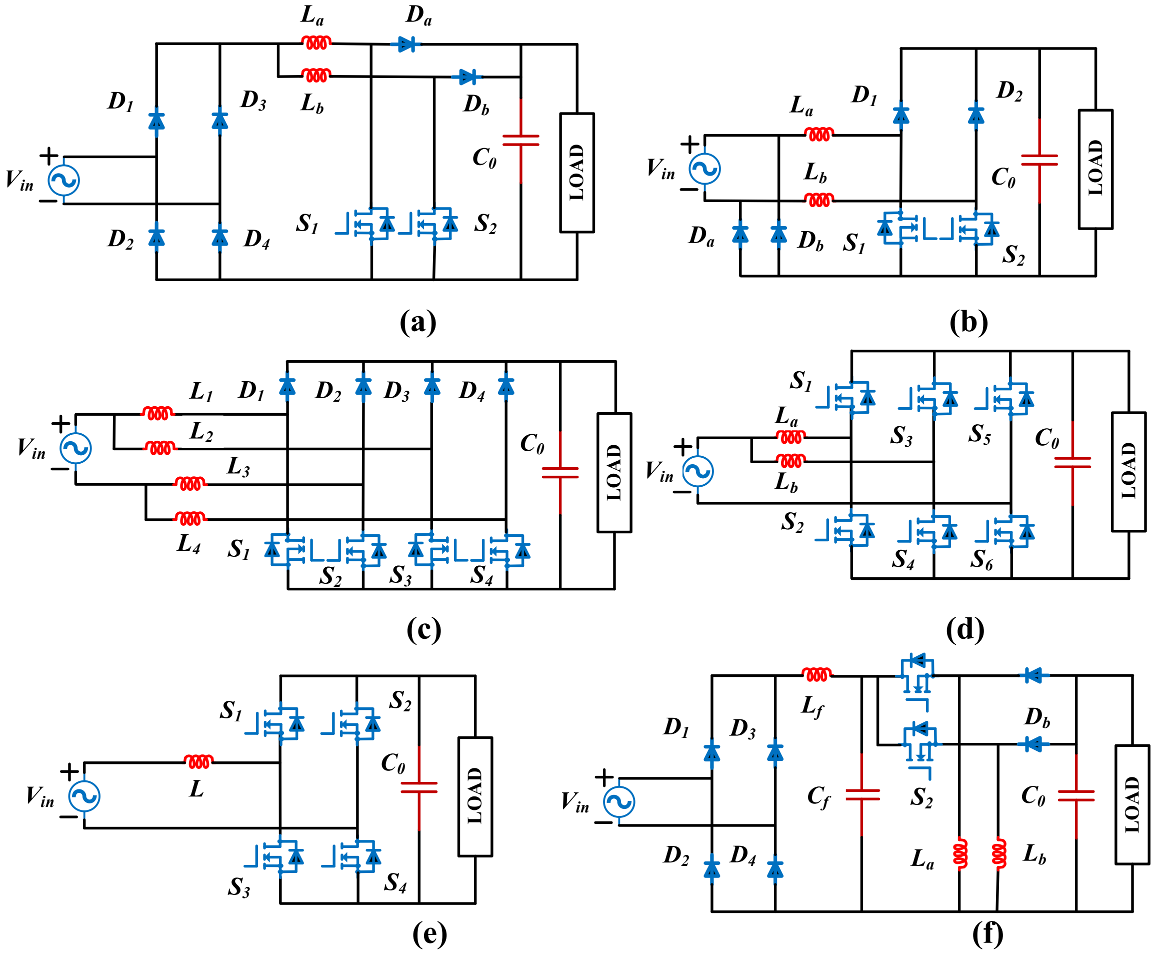

Fig. 2.4. PFC AC-DC Converters; (a) Interleaved Boost PFC; (b) Semi-Bridgeless PFC; (c) Bridgeless Interleaved PFC; (d) Interleaved Totem-pole PFC; (e) Bridgeless Totem-pole PFC; (f) Interleaved Buck-Boost PFC.

2.2.1.1.1 Interleaved Boost PFC Converter

The interleaved boost converter, illustrated in Fig. 2.4 (a), consists of two boost converters in parallel operating 180° out of phase [67]. The input current is the sum of the two input inductor currents. Because the inductors' ripple currents are out of phase, they tend to cancel each other and reduce the input ripple current caused by the boost switching action. The interleaved boost converter has the advantage of paralleled semiconductors. Furthermore, by switching 180° out of phase, it doubles the effective switching frequency and introduces smaller input current ripple, so the input EMI filter is relatively small. With ripple cancellation at the output, it also reduces stress on output capacitors.

Table 2.2: PFC AC-DC Converters with specifications

Attributes	[67]	[68]	[69]	[70]	[71]	[72]
PFC Topology	**Interleaved Boost**	**Semi-Bridgeless**	**Bridgeless Interleaved Boost**	**Interleaved Totem-Pole**	**Bridgeless Totem-Pole**	**Interleaved Buck-Boost**
Switching Device	GaN	SiC	SiC	SiC	GaN	SiC
No. of devices (Active Switches/ Diodes/ Inductors/ Capacitors)	2/6/2/1	2/4/2/1	4/4/4/1	6/0/2/1	4/0/1/1	2/4/3/3
Inductor's Place	DC-side	AC-side	AC-side	AC-side	AC-side	AC-side
Input Voltage	200	85-265	85-265	85-265	85-265	110-230
Output Voltage	400	200-430	400	300-600	280-460	400
Rated Power (kW)	3	3.3	3.3	3.3	3	1
Power Factor (PF)	---	---	0.999	0.999	0.999	0.999
Modulation Technique	---	---	CCM	CCM	CCM	DCM
Switching Frequency (kHz)	300	200	70	100	100	50
Control and Modelling Approach	Simple	Complex	Complex	Simple	Simple	Very Simple
EMI Emission	Moderate	Moderate	Low	Moderate	Low	Low
Power Density (kW/L)	---	1.13	---	---	3.9	0.04
Efficiency (%)	97.94	97.7	98	99.2	96.3	92.8

2.2.1.1.2 Semi-Bridgeless PFC Converter

Fig. 2.4 (b) exhibits the semi-bridgeless PFC topology consisting of two extra diodes at the input side to address the EMI issues. The conduction losses are very low in the converter, and it also resolves the issue of floating ground. The converter control and current sensing are complex and expensive as it requires either three current transformers or the use of Hall effect sensors and can also be measured by a differential amplifier with a noise in the signal [68].

2.2.1.1.3 Bridgeless Interleaved PFC Converter

Fig. 2.4 (c) exhibits the bridgeless interleaved boost PFC converter consisting of four diodes, four switches, and four inductors and is used for power level above 3.3 kW. The converter demonstrates a high input power factor, high efficiency, and low input current harmonics. The topology has the highest number of component count than any other bridgeless PFC topology making it costly and bulky in size for practical usage with complex control strategies [69].

2.2.1.1.4 Interleaved Totem-Pole PFC Converter

Fig. 2.4 (d) exhibits the bridgeless totem-pole topology housing six switches, large two-inductor, shutting out the need for input diode bridge. The topology is preferred where the need for higher power density and efficiency is a major concern. The converter resolves the issues of heat management at the input side but raises the concern of high electromagnetic interference (EMI). It also generates high common-mode noise than traditional other bridgeless topologies. Current sensing is challenging making the control complex [70].

2.2.1.1.5 Bridgeless Totem-Pole PFC Converter

Fig. 2.4 (e) exhibits the totem-pole PFC topology. It uses only one inductor and neither diodes nor AC return diodes are required. It has fewer components count and simpler circuit topology. It has very simple control strategy with CCM modulation. This topology has a serval advantage compared to other PFC topologies in terms of power density, thermal management, and power quality. The design of inductor and compatibility with different devices are challenging [71].

2.2.1.1.6 Interleaved Buck-Boost PFC Converter

Fig. 2.4 (f) exhibits the interleaved buck-boost PFC converter consisting of four diodes, two switches, and three inductors. The converter operated in DCM to ensure natural PFC for all operating conditions. The interleaved PFC consists of two DCM buck–boost converters in parallel, which operates at 180° out of phase. The topology has the lower control complexity by using of lower number of sensors which enhances the reliability of the system. To reduce the peak current through switches is very challenging during the higher power level [72].

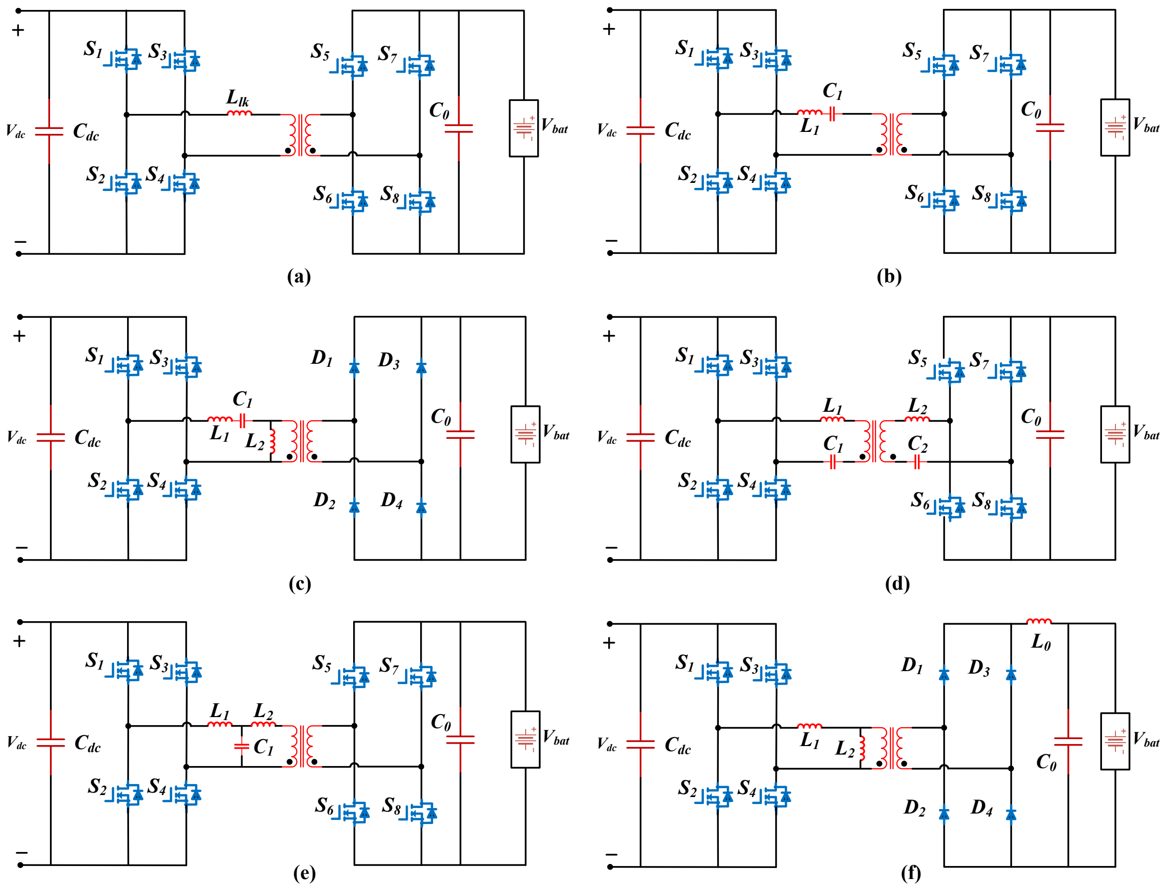

Fig. 2.5. Isolated DC-DC Converters; (a) DAB Converter; (b)Series Resonant Converter; (c) LLC Converter; (d) CLLC Converter; (e) LCL Converter; (f) PSFB Converter.

2.2.1.2 Isolated DC-DC Converters

A single-phase isolated DC-DC converters are widely used in the OBC market and research area. The DC–DC stage converts the DC bus voltage into a regulated output DC voltage for charging batteries, which is required to meet the regulation and transient requirements. In the following paragraphs, the most popular and promising WBG-based isolated DC-DC converters are presented. The comparative critical analysis with specifications is mentioned in Table 2.3.

2.2.1.2.1 Dual Active Bridge (DAB) Converter

Fig. 2.5 (a) shows the dual active bridge (DAB) converter which is commonly used for EV charging systems due to its high efficiency, reliability, bidirectional power flow, buck and boost capability, low stress on components, and small filter requirements. The converter has a fixed switching frequency and small passive components [73].

Table 2.3: Isolated DC-DC Converters with specifications

Attributes	**[73]**	**[74]**	**[75]**	**[76]**	**[77]**	**[78]**
DC-DC Topology	DAB	Series Resonant	LLC	CLLC	LCL	PSFB
Switching Device	SiC	SiC	SiC	SiC	GaN	SiC
No. of devices (Active Switches/ Diodes/ Transformers/ Inductors/ Capacitors)	8/0/1/1/1	8/0/1/1/2	4/4/1/2/2	8/0/1/2/3	8/0/1/2/2	4/4/1/3/1
Input Voltage	700-800	750	500-900	385-425	800	350
Output Voltage	380-500	400	250-450	250-450	150-950	250-400
Rated Power (kW)	10	5	10	6.6	6.6	2
Modulation Technique	PWM and PSM	SPS	Frequency	No Control DCX Mode	PSM	PSM
Switching Frequency (kHz)	500	150-190	150	500	500	500
Control and Modelling Approach	Very Simple	Simple	Complex	Complex	Complex	Very Simple
Gain Range	1.5x	2x	1.67x	1x	6x	1x
Power Density (kW/L)	5.44	1.4	4	8	7.3	5
Efficiency (%)	98.2	98.5	98.5	>96.5	>97	96.5

2.2.1.2.2 Series Resonant Converter

Fig. 2.5 (b) shows the dual active bridge (DAB) series resonant converter [74]. The LC resonant frequency is set less than the switching frequency of the converter and therefore it works in continuous current mode and may suffer from hard switching with a variation of battery voltages. The controlled switch inductor network is added in the DAB LC type converter to reduce the hard switching effects range and improve the operating battery voltage range.

2.2.1.2.3 LLC Resonant Converter

The LLC-type DC-DC converter is widely used for EV charging systems due to its wide range of voltage output, ability to control voltage output at light load states, high efficiency, power density, and soft switching control capabilities. The schematic diagram of DAB with LLC resonant tank is shown in Fig. 2.5 (c) which is included a full-bridge converter, resonant tank, and filter capacitor. The efficiency of this topology achieves more than 96 % with an extendable voltage range [75].

2.2.1.2.4 CLLC Resonant Converter

Fig. 2.5 (d) shows the schematic diagram of the DAB bidirectional CLLC resonant converter. The CLLC resonant converter has a wide range of output voltage, great soft switching, and symmetrical bidirectional power flow capabilities [76]. However, the converter has low efficiency and voltage regulation challenges under light load conditions. Compared to the DAB converter, the CLLC converter is controlled by a variable switching frequency and works with a much wider soft-switching region, especially at light load conditions. Although its control and design are more complicated, the CLLC resonant converter achieves higher efficiency.

2.2.1.2.5 LCL Resonant Converter

The LCL resonant converter is shown in Fig. 2.5 (e). The reactive power is reduced as the bridge currents are in phase and sinusoidal and therefore the efficiency of this converter is extremely high. Moreover, conduction losses are very low compared to the DAB converter as it has a soft-switching range over all switchers [77]. However, the use of a single central resonant tank may increase electric stress on the passive components and lead to an increase in current and voltage range.

2.2.1.2.6 Phase-Shifted Full Bridge (PSFB) Converter

The phase-shifted full bridge (PSFB) converter is commonly used for onboard charger due to many advantages such as low EMI, current stress on the components, soft switching capability, simple PWM control, and high-power density. In the schematic diagram of the PSFB converter shown in Fig. 2.5 (f), the secondary side active switches are replaced with the diodes for unidirectional power flow. However, the PSFB converter has conduction loss

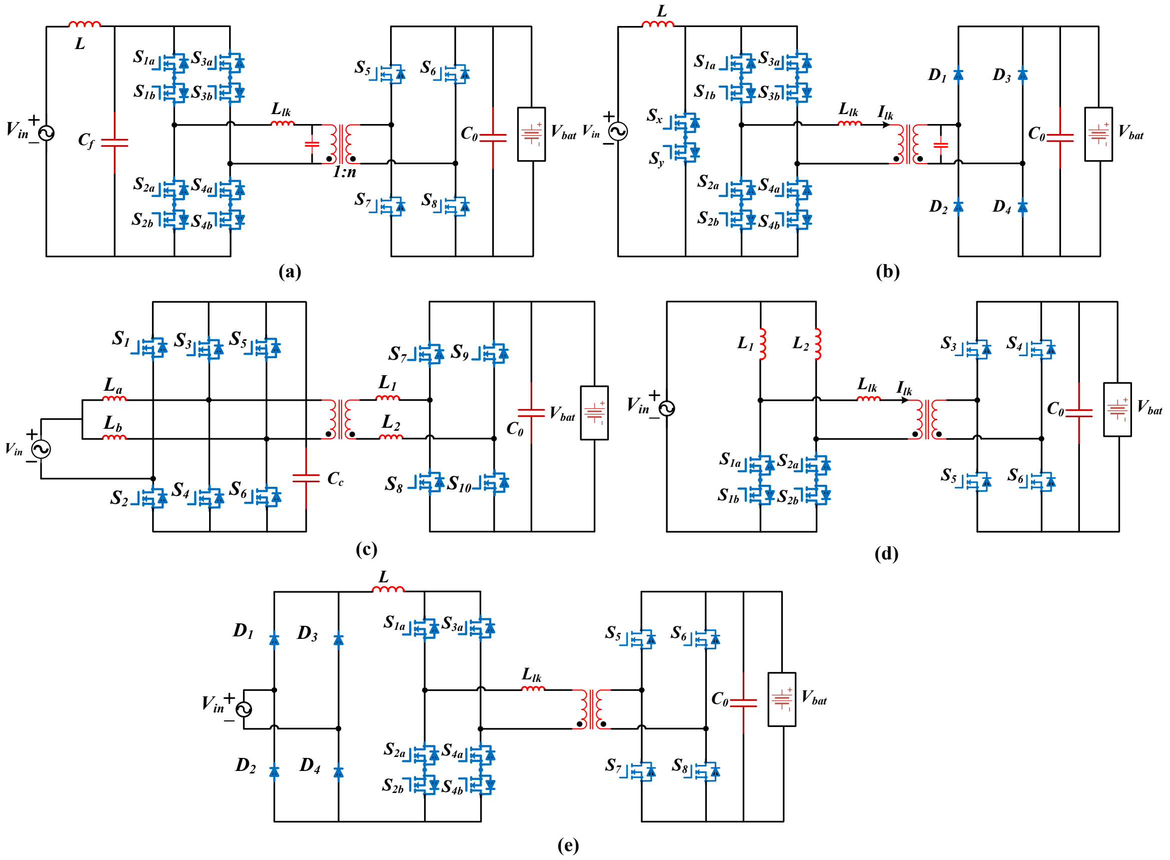

Fig. 2.6. Single-Stage OBCs; (a) DAB-Based Matrix Converter; (b) Boost-Based Matrix Converter; (c) Phase-Shifted Boost-Based Converter; (d) Current-fed Half-bridge Converter; (e) Current Source PFC Converter.

due to current circulation during the freewheeling gap, voltage overshoots across the secondary side, limited ZVS range, and duty cycle loss [78].

2.2.2 Single-Stage OBC

Single-stage OBCs combine the PFC converter with DC/DC converter without a bulky DC-link capacitor. Therefore, it has higher power density, lower cost, and higher reliability potential than the two-stage configuration. This section reviews the recent developed WBG-based single-stage isolated PFC AC-DC converter topologies. The critical comparative analysis of single-stage PFC AC-DC converters is shown in Table 2.4.

2.2.2.1 DAB-Based Matrix Converter

The DAB-based matrix converter topology is shown in Fig. 2.6 (a). It removes the DC-link capacitor, which improves reliability and power density. This OBC topology has the following merits: 1) No switching loss because of full ZVS operation of all MOSFETs of the converter; 2) open-loop input PFC without load current sensor; and 3) simple closed-loop

Table 2.4: Single-Stage OBCs with specifications

Attributes	**[79]**	**[80]**	**[81]**	**[82]**	**[83]**
Single-Stage Topology	DAB-Based Matrix Converter	Boost-Based Matrix Converter	Phase-Shifted Boost-Based Converter	Current-fed Half-Bridge Converter	Current-Source PFC Converter
Switching Device	SiC	SiC	SiC/GaN	SiC	SiC
No. of devices (Active Switches/ Diodes/ Transformers/ Inductors/ Capacitors)	12/0/1/1/1	10/4/1/2/2	10/0/1/4/2	8/0/1/3/1	10/4/1/2/1
Input Voltage	120	190-220	100-120	120	207-253
Output Voltage	300-400	400	200-240	220-330	330-470
Rated Power (kW)	1.6	3	3.8	3	3
Modulation Technique	---	Fixed Frequency	PSM	Fixed Frequency	PSM
Switching Frequency (kHz)	10	20	150	100	50
Control and Modelling Approach	Complex	Complex	Simple	Simple	Complex
Power Density (kW/L)	---	3.8	6.09	---	---
THD (%)	3.5	---	---	2.5	---
Efficiency (%)	89	94.5	96.6	96.5	95.4

control due to the fact that the phase shift is proportional to the active power [79]. The downside is that the bidirectional switch requirement doubles the switch count and gate driver demand, which increases cost. The performance of this matrix converter is similar to the traditional two-stage OBC topology. Since there are no switching losses, the switching frequency can be increased, leading to passive components with reduced volume. Therefore, this topology can be a promising solution for the OBC application because of its high-power density and low system loss.

2.2.2.2 Boost-Based Matrix Converter

Fig. 2.6 (b) shows the current-fed single-stage single-phase isolated ac–dc converter [80]. The over-voltage problem is completely eliminated by changing the position of the resonant components. Thus, lower voltage rating IGBTs can be applied. Furthermore, only one resonant capacitor is required now to realize ZCS operation. At the same time, all features such as one-stage power conversion, no dc-link capacitor, and good THD performance are inherited by the proposed converter.

2.2.2.3 Phase-Shifted Boost-Based Converter

Fig. 2.6 (c) shows the phase-shifted single-stage isolated OBC where it is operated on mixed adaptive duty cycle and phase-shift modulation strategy for achieving the soft-switching range [81]. In addition, the fourth-harmonic injection method greatly reduces the grid current THD. The converter has high reliability and power density compared to conventional single-stage converter. However, the effectiveness of the modulation technique is not able to attain full range of input voltage and battery voltage.

2.2.2.4 Current-fed Half-Bridge Converter

Fig. 2.6 (d) shows the current-fed single-stage half-bridge ac-dc converter for EV charging application [82]. The converter achieves soft-switching at primary side primary side switches and secondary side devices throughout the operation without any additional components or snubber circuit. The modulation technique and control algorithm to ensure soft switching throughout the operation range of the converter in both directions of power flow. Also, the converter has high THD suppression and low control complexity.

2.2.2.5 Current Source PFC Converter

Fig. 2.6 (e) shows the current source isolated single-stage ac-dc OBC. Development and implementation of the AC-DC modulation and a control system for the asymmetrical secondary-modulated DC-DC converter [83] (ASMC) enable PFC operation and soft-switching of the semiconductors for the whole period of the grid voltage. Other advantages include constant switching frequency and absence of clamping circuits. However, the converter is suffering from low reliability and high switching losses.

2.2.3 Unidirectional Chargers

The typical structure of a unidirectional charger is shown in Fig. 2.7 (a). To reduce system complexity, the front-end and DC-DC secondary side after isolation are typically realized using diode bridges. However, there are several unidirectional chargers that at least use an active front-end. Benefits of an active front-end power factor correction (PFC) stage in

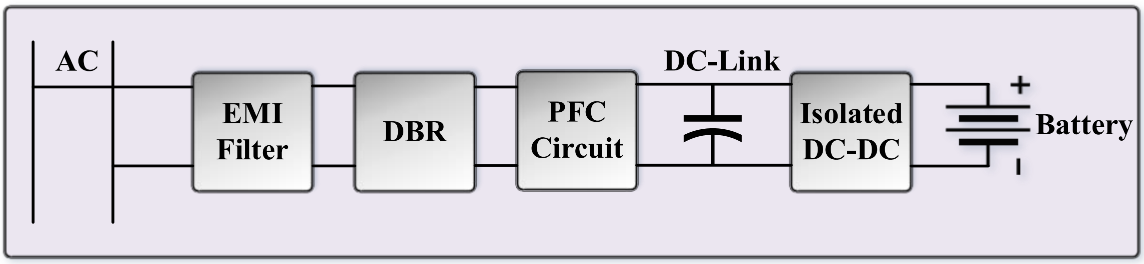

(a)

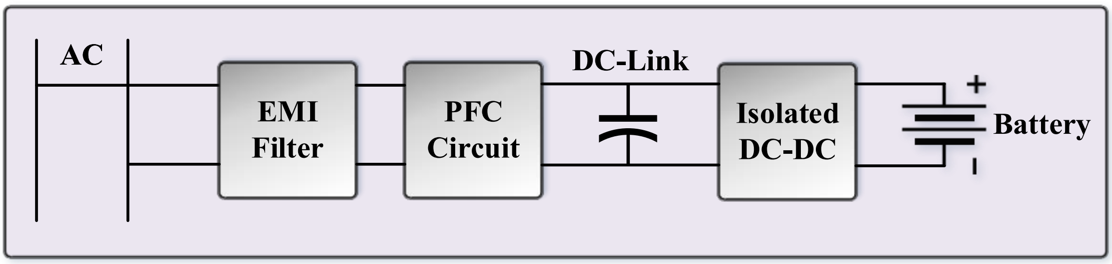

(b)

Fig. 2.7. Typical block diagram for (a) Unidirectional OBCs; (b) Bidirectional OBCs.

unidirectional chargers includes a reduction in total PFC circuit components in the conduction path leading to higher efficiency, and enhanced functionality such as adjustable power factor control. Advantages of unidirectional chargers are reduced system complexity, fewer active circuit components, thus reduced system cost, and compact size. However, their profound disadvantage lies in the inability to facilitate the future of advanced smart grid functionalities.

2.2.4 Bidirectional Chargers

The typical structure of a bidirectional charger is shown in Fig. 2.7 (b). Bidirectional chargers enable power flow control from the grid to the vehicle (G2V), as well as V2H, external load (V2L), or most commonly back to the grid (V2G). Together, V2H, V2L, and V2G power flow control will be designated as (V2x). In bidirectional OBCs, active front-end PFC stage and active DC-DC secondary side are necessary. Although bidirectional chargers can facilitate a variety of beneficial functionalities, they come at the price of more circuit components, which increases the system cost and reliability burden, and could slightly impact the power density and weight of the OBC [84].

Table 2.5: Commercial WBG-based OBCs in Market

Manufacturer	Switching Device	Input Voltage (V)	Output Voltage (V)	Power (kW)	Efficiency (%)	Power Density (kW/L)	Cooling Method
Texas Instruments [85]	SiC	208-240	250-450	6.6	97	---	---
Wolf Speed [86]	SiC	---	250-450	6.6	96.5	3.3	---
On Semiconductor [87]	SiC	90-260	250-450	6.6	95	---	---
Eaton [88]	SiC	110-240	225-500	22	>95	2	---
VisIC Technologies [89]	GaN	90-264	240-420	6.6	96	3	Liquid
Canoo [90]	SiC/GaN	---	---	7.2	98.7	---	---
Delta-q [91]	SiC/GaN	85-265	250-450	6.6	96	2.26	Liquid
Hella [92]	SiC/GaN	---	800	22	>96	4	---
Continental [93]	SiC/GaN	---	----	3	>94	---	---
BorgWarner [94]	SiC	---	400	7	---	---	---
Current Ways [95]	SiC	97-265	250-425	6.6	96	3.3	Liquid
Fraunhofer [96]	SiC	115-230	315-395	3.7	95.3	---	Air
Valeo Siemens [97]	SiC	85-265	---	3.5	94	---	---
Delta [98]	SiC/GaN	120-240	250-450	6.6	>95	0.37	Liquid
ST-Microelectronics [99]	SiC	85-265	250-450	7	---	---	---

2.3 Commercial Chargers in Market

Many manufacturers are composed of WBG-based commercial OBCs for commercial in the automotive market. Table 2.5 represents the WBG-based commercialized chargers in the market for EV charging. A 6.6kW bidirectional OBC composed of a continuous conduction-mode (CCM) totem-pole PFC and a resonant CLLC DC/DC converter was presented in. The interleaving architectures increases the power level and reduces the power loss at light load. the charger achieves a maximum efficiency of 97% utilizing Silicon Carbide (SiC) MOSFETs. Texas Instruments also developed a bidirectional 3.3kW PFC with Gallium Nitride (GaN) devices [85]. The Wolfspeed provides a bidirectional 6.6kW consists of a totem-pole PFC and an isolated CLLC DC/DC converter [86]. The bidirectional OBC demonstrates a power density of 3.3kW/L and a peak efficiency exceeding 96.5%. On Semiconductor developed SiC-based 6.6 kW OBC with higher reliability [87]. Also, the battery charger consists of interleaved boost PFC converter with LLC DC-DC converter which achieves 95% efficiency. Eaton provides a bidirectional 3kW to 22kW OBC [88]. The range of input voltage varies from 110V to 240V, and the output voltage is from 225V to 500V. It can achieve over 95% efficiency with the maximum charging rate, and a power density of 2kW/L [84]. GaN-based 6.6 kW OBC offered by Visic Technologies has a higher power density with wide input and output voltage range [89]. This charger consists of dual boost bridgeless PFC with lower size of inductor and full-bridge LLC converter with minimum power losses. It also showcases the optimal heat dissipation design with the package isolated top colling solution.

Canoo developed 7.2 kW OBC with lower switching loss and efficient thermal management [90]. This battery charger has higher power conversion efficiency at 98.7% with maximum charging rate. Delta-q provided a bidirectional 6.6 kW OBC, which uses 650 V GaN and 1200 V SiC devices achieves an efficiency above 96% and has a power density of 2.26 kW/L [91]. The OBC topology includes a totem-pole bridgeless PFC converter that operates in critical conduction mode (CRM) and downstream CLLC resonant topology as the second-end stage. Hella developed a GaN-based 22 kW EV charger with higher reliability, higher power density and decreased vehicle weight, giving more excellent driving range and opening up new diversity in structure [92]. Continental composed GaN-based 3 kW OBC, which has a higher frequency operating range, leads to compact size, great air-cooled, and design flexibility for battery charger incorporation [93]. A SiC-based 7 kW OBC is designed and developed by BorgWarner, it provides a robust design, higher power density, and low cost [94].

Current Ways also provides a 20kW modular SiC bidirectional OBC, which can achieve an efficiency higher than 97% and a power density of [95]. SiC-based 22 kW OBC offered by Fraunhofer has higher power density and efficient air-cooling system [96]. Valeo Siemens developed a bidirectional 3.5 kW OBC, which reaches an efficiency over 94% [97]. The input voltage of the totem-pole PFC varies from 85 V to 275 V, and the output voltage from 200 V to 1000 V. However, the information of the DC/DC converter is limited. Delta developed 6.6 kW SiC and GaN-based OBC, it comprises of totem-pole PFC and CLLC based DC-DC converter [98]. It has better thermal management system and higher reliability.

ST Microelectronics provides the 7kW OBC, which has wide range of input and output voltage [99]. Also, it offers dynamic power management and lower acoustic noise emissions.

2.4 EV Charging Infrastructure Consideration

EVs have not been extensively popular among public in spite of positive impact on the environment and high energy efficiency. One of the prime reasons is the lack of battery charging infrastructure, which requires a huge investment from the Government and the private sectors. The major barriers to infrastructure installations are codes and standards, costs of installation, planning of utility infrastructure, construction, knowledge of consumer, metering, role of contactor, permission procedures, etc. This section reviews the mainly infrastructure-based charging strategies and future capabilities of OBCs.

2.4.1 Infrastructure-Based Charging Strategies

Due to the year-over-year projected influx of EVs across the world, more intelligent charging of EVs will be necessary to realize EVs full benefits in the electric grid and protect potentially at-risk distribution systems. Case studies in Greece and Toronto have been carried out in [100] and [101], respectively. In Greece, large EV deployment resulted in voltage deviation violations in rural electric network lines, as well as overloading in urban electric network lines. However, smart, coordinated, charging methods were shown to alleviate these problems and enable higher EV penetration rates. In the case of Toronto, while slow EV OBCs (<6.6 kW) were not likely to cause significant overloading problems to the local electric grid, the long charging times were seen to absorb available spare capacity of transformers and negatively affect their cooling cycles. On the other hand, higher power OBCs (6.6 kW) showed significant impact on equipment capacity and margins of safe operation, and it was therefore recommended for utilities to upgrade the electrical equipment before accommodating these chargers.

2.4.1.1 Uncoordinated Charging

Uncoordinated charging is currently the predominant method of charging EVs throughout the world, as a large percentage of users charge their EVs when they return home. Uncoordinated charging designates that when a user plugs in their EV, charging begins. While this is convenient for EV owners, it may negatively impact the electric grid, for example in equipment overloading or spare capacity absorption as detailed in both of the aforementioned case studies.

2.4.1.2 Coordinated Charging

Coordinated charging is the future direction for EV charging infrastructures. This type of charging is significant for utility providers as they would be able to shape instantaneous energy consumption, in particular the EV charging load, to maintain a desirable load profile at the distribution level and thus ensure high energy efficiency and grid stability [102]. Coordinated charging can also benefit EV owners, by ensuring a reasonable SoC level at times of lower electricity cost as compared to the uncoordinated case [102], [103]. A coordinated charging pilot program was initiated by PG&E and BMW in the state of California from July 2015 to December 2016, called BMW iCharge Forward [104]. This pilot program successfully tested the feasibility of managed EV charging as a flexible grid resource, and was a success from the viewpoints of energy reduction as well as customer satisfaction [104].

2.4.2 Future Capabilities of OBCs

As EVs become more popular on a global scale, utilities will look to utilize advanced functionalities that OBCs are able to accommodate.

2.4.2.1 Peak Shaving (V2G)

One of the well-known and sought-after functionalities for EV OBCs is active V2G power flow control, deemed peak shaving. V2G enables EVs to behave as an energy storage unit that can distribute energy back to the grid whenever required by the utility, typically in a period of high electricity demand. Additionally, EVs can store energy in periods of excess grid-side generation and later deliver it back to the grid, if required [105]. One of the limitations in peak shaving is increased battery degradation, since active power is transferred in both the G2V and V2G operation modes. The effect of daily contributions from both modes has been analysed in [106]. As expected, battery degradation was pronounced in peak shaving operations primarily due to the high depth-of-discharge requested by the utility. A further limitation for V2G power flow is the power ratings of current OBCs.

2.4.2.2 Ancillary Services (G2V, V2x)

While the predominant modes of operation for EV OBCs involve simple G2V and V2G, other smart operations have been identified and investigated [9]. For instance, in [107], additional operational modes include V2H, where the EV is used as a power source for an isolated home or potentially an offline UPS for a grid-connected home, and vehicle-for-grid (V4G), where the EV provides grid support functions, such as reactive power compensation and frequency regulation. A two-stage non-isolated charger exhibiting simultaneous active and reactive power control has been shown in [108], where further it was demonstrated that neither battery lifetime nor SoC were affected by the reactive power support. The same procedure could also be applied to two-stage isolated chargers with the same conclusions, since the front-end PFC stage can take sole responsibility for generating a variable DC link voltage at the requested power factor [109]. One disadvantage is that the two-stage charger will have increased burden on the DC link capacitor, as there will be more charge and discharge cycles compared to only active power control.

Additional to reactive power compensation is grid frequency regulation. In [110], a comprehensive analysis is presented for OBCs providing frequency regulation services as well as the potential impacts on EV battery degradation. As opposed to mechanical systems that take time to react to grid disturbances, EV OBCs could provide more rapid support if controlled appropriately. While EV owners could be paid for offering this service to the grid, based on the presented cost-benefit analysis, it appeared unlikely that financial incentives would be enough, and thus the authors recommend for utilities and government to draft additional motivations. One facet of the second phase of the iCharge Forward project aims to investigate engagement strategies to incentivize drivers to participate in V2x programs [104].

While some smart charging techniques and advanced capabilities of OBCs were introduced, an additional point of reference regarding these topics can be found in [9]. Furthermore, a more recent comprehensive overview of smart microgrid control strategies utilizing distributed energy storage (ES) systems is developed in [111]. While [111] applies generally to any ES system, EVs equipped with a bidirectional OBC can be considered as a battery ES system in a smart grid network.

2.5 Future Trends and Challenges

To push the performance and adoption of OBCs, the main goals focus on low-cost, high-power density, high power level, and high efficiency. This section reviews the future research trends and potential challenges from the point of view of the topology, soft-switching techniques, advanced control techniques, thermal design, system integration, wireless charging system, and challenges.

2.5.1 Power Converter Topology

It is expected that the majority of bidirectional OBCs will be single-stage structure within the after 10 years. Due to its simple structures and controls, and high efficiency. As the power level requirement increases, a three-phase system is required where modular single-phase converters are a suitable option to achieve 22kW OBC. Three-phase full-bridge PFC is also a suitable option for bidirectional battery charging applications, in particular the three-level T-type converter, due to higher efficiency, although it has higher component number and higher complexity in control. Moreover, at high power levels, single-stage OBC converters would be preferred for bidirectional applications since they can achieve high power density and compactness, although they raise some challenges in terms of hardware design and achieving high efficiency [112]. Higher efficiency and better reliability could be achieved by an advanced control method and high-performance components.

2.5.2 Soft-Switching Techniques for WBG-Based Power Converters Topology

For EV applications, novel soft-switching approaches are being developed using unique power circuit topologies and digital control methodologies. soft-switching techniques play a cardinal role in reducing conduction losses. The goal of novel soft-switching approaches for EV power converters is to accomplish soft switching with minimum changes in power circuitry and to employ more complex modulation and control systems [113]. The study will primarily focus on employing easy and simple modulation and control techniques to improve the performance of power circuits utilizing power configuration.

2.5.3 Advanced Control Techniques

Advanced control techniques can be applied to WBG-based OBCs such as Model Predictive Control (MPC) which has a higher optimized performance level and precise tracking prediction with fast dynamics [114]. The backstepping control method has a higher signal and control stability [115]. Passivity-based control technique has more play and plug stability with accurate estimation without chattering problems [116]. The sliding mode control technique is simple in terms of implementation and higher robustness [117]. The observer technique has a precise tracking system against uncertainties and disturbances [118]. The intelligent control system has fast dynamic control and is less complicated in any system [119]. Artificial Intelligence (AI) control-based technique has higher accuracy and improves system performance [120]. Deep Learning (DL) and Machine Learning (ML)- based control methods reduce the control complexity [121]. Distance-range concerns, long-duration charging times, and significant financial pressure from off-board chargers will all be addressed in the future by increasing the size of the EV battery. The automotive industry's next step is to build a fast charger that enables high efficiency, power levels, and power density.

2.5.4 Thermal Design

The high switching frequency and integrated power electronics devices cause significant thermal management challenges due to a more compact packaging and higher eddy current and skin effect losses of passive components. These eddy current losses induced in the magnetic components have a detrimental effect on the charger's performance and reliability. The future thermal design of OBCs will likely use high-end liquid cold plates integrated into the OBC enclosure along with intelligent interfaces with the vehicle liquid cooling system like motor and DC/DC system. Hence, the thermal management engineer will have to consider the vehicle thermal design comprehensively and very early to dissipate all the heat loads efficiently, including the OBC, inverter, and battery pack. Moreover, common heat sink manufacturing process like extrusion and casting have well known limitations for heat sink designs. On the other hand, additive manufacturing technology opens up an opportunity for nonconventional geometries that can achieve higher surface density and excellent heat exchange. Additionally, heat pipes are becoming an attractive solution for automotive cooling because of its high heat transfer, low thermal resistance and low cost [122].

2.5.5 System Integration

To further increase the power density of the overall system, the OBC integration with the traction inverter is an alternative. Some production vehicles already include mechanical integration of the OBC with other vehicle power electronics modules such that they share a common housing, reducing cost and weight [123]. Beyond simple mechanical integration, there is potential to further increase the power density while simultaneously increasing the charging power capability by electrically integrating the OBC with the inverter at the topology level. This is often referred to as an integrated battery charger topology, and has received significant attention by the research community and some limited commercialization. Integrated battery charger topologies generally repurpose some combination of the traction inverter, electric motor windings, and high voltage DC/DC converter if available, to achieve battery charging functionality from the AC grid. Since the traction inverter is inherently a bidirectional DC/AC converter, integrated battery charger topologies can often have bidirectional capabilities as well, depending on how the system is configured in charging mode. Common challenges with integrated battery charger topologies include torque production in the electric machine during the charging mode, and a lack of galvanic isolation between the AC grid and the vehicle. Torque production can be eliminated by restricting it to high frequency components with a zero average [124], phase transposition in the charging mode or through flux cancellation with split winding machines [125]. Galvanic isolation is primarily required to prevent common mode currents from creating a shock hazard for the user. Renault has included a 43kW non isolated integrated charger in the Zoe [124], demonstrating the commercial viability of these solutions.

2.5.6 Wireless Charging Systems

Conductive charging techniques for EVs bring challenges such as charging time, range anxiety, charging infrastructures, and queuing time at the charging station. On the other hand, the wireless power transfer (WPT) technique is a promising trend for EV charging, since it aims to address the issues above while bringing safety and convenience for the users. Many OEMs have started to research inductive power transfer (IPT) techniques for EVs. The BMW 530e PEV features wireless charging in California, US. Honda also presented its wireless V2G concept with wireless charging specialist WiTricity in 2019, which combines the WPT and bidirectional power transfer function. Moreover, SEA 2954 offers standard guidelines of WPT industry specifications [126]. WPT theory for EVs has been widely studied in the research field. Although WPT can be applied in both on-board and off-board chargers, this paper focuses on wireless charging of OBCs.

WPT is classified as static wireless charging (SWC), dynamic wireless charging (DWC), and quasi-dynamic wireless charging (QWC). SWC avoids the shock hazard of wires and metal and can be charged at a convenient location like home garages or parking lots. The control strategies like variable frequency and fixed frequency are presented to improve the operating efficiency in [126]. Some structures and shapes of the coil are proposed in [126] for better robustness, cost-effectiveness, and minimization of the stray magnetic field. DWC charges the EV with the specific charging lane, which can prolong the EV range and reduce the battery size. Many methods are proposed like road built-in pad [127], pad array-based coupling technique [128], and segmental track strategy [129]. However, due to high maintenance costs and complicated models, they are challenging to be applied in practice. The double couple method is presented in [130], but it fails because of high-frequency transmission. SWC and DWC are combined in [131] and show promising results but are expected to also feature a high cost. QWC charges the EV when it stops for a short time, like at a traffic light, which combines the advantages of the SWC and DWC and also simplifies the complex implementation of the DWC. WPT has many challenges to be overcome, such as relatively low efficiency and power density, high cost, and manufacturing complexity. Moreover, distant charging is also a challenge at a high-power level.

2.5.7 Challenges

Due to the increasing number of active components, it is challenging to maintain the system reliability of OBCs. [132] presents a fault-tolerant system to improve reliability, but it adds additional models that cause more weight and cost. Some control methods are proposed to optimize the reliability, such as the switching function algorithm [133], the bi-objective algorithm based on efficiency and reliability [134], and the adaptive control method [135]. [136] offers a modular power converter to obtain reliable operations. The active thermal control method is also a valuable way to reduce failure [137]. Moreover, the development of bidirectional OBC also exposes challenges for the infrastructures in the related industry. Firstly, the bidirectional power flow needs to be compatible with advanced smart grid functionalities. Hence, updating the grid and infrastructures is a major concern. Secondly, although bidirectional OBC has some merits like peak shaving and frequency regulation for the grid, it has some potential impact on battery degradation because of frequent charging or discharging operations. Government or utilities need to provide additional motivation policies like financial incentives to encourage potential consumers to choose bidirectional power flow capable EV. On the other hand, safety monitoring and protection are required in the V2G and G2V modes. The smart grid should be robust and reliable to accept V2G.

2.6 Conclusion

The capacity of the EV battery will increase in the future to deal with issues such as range anxiety, long charging time, and high financial pressure of off-board chargers. Facilitating a higher-power level, higher efficiency, and higher power density is the next step in the automotive industry. This chapter presents a detailed overview and future trends of WBG-based OBCs for EVs. The current status of OBCs including architectures, power converter topologies including two-stage and single-stage, WBG-based commercial chargers in the global market, and charging infrastructure consideration have been reviewed. Two-stage and single-stage solutions have been investigated. Most high-power OBCs for commercial applications use a two-stage configuration with a DC-link capacitor because of its simple structure and excellent performance. Front-end totem-pole PFC converter and downstream CLLC DC/DC converter are widely used. Single-stage OBCs without DC-link capacitors for high power levels may be attractive because of high power density. In addition to industrial examples, this chapter reviews key promising OBC topologies. The future work of OBCs is summarized from the viewpoints of topology, soft-switching techniques, advanced control methods, thermal design, system integration, wireless charging system, and challenges. Single-stage OBC is a new trend to achieve high power density. WBG devices are of interest to OBC manufacturers due to their superior performance. Moreover, it is expected that the cost of WBG devices will further decrease, which will help broaden their use in cost-competitive applications such as the automotive industry. Research areas like gate driver design and EMI design deserve attention. The thermal design of OBCs is also projected to integrate with the thermal design of other parts of EVs. Highly integrated OBC with other electrical components like the traction inverter or motor is also a trend to improve power density. Wireless charging system will keep the popular trend. Further work is ongoing to meet the expectations in terms of efficiency, power density, reliability, and cost of OBCs.

Chapter 3: Single-Stage Bidirectional PFC Converter Based Plug-in V2G EV Charger

3.1 Introduction

Typically, in single-phase converters, the PFC with isolation is implemented using a two-stage conversion. In two-stage conversion, a single-phase ac-dc non-isolated active PFC converter is employed at first stage followed by an isolated dc-dc converter at second stage [64], [138]. The front-end active PFC converter provides sinusoidal input currents with unity power factor and low THD. The second stage DC-DC converter provides isolation and regulated output voltage according to the load requirements. This is the simplest approach, but the total power has to be processed two times, which leads to higher losses and low efficiency. In addition, the two-stage conversion requires more number of semiconductors and a bulky DC-link electrolytic capacitor, which increases the system weight and compromises the system reliability [138]. Therefore, it is not a viable option for EV charging application. The alternate option is the single-stage approach, where the power is processed only one time. The PFC and isolation stages are combined to have direct power conversion. As a single-conversion stage, it is expected to have less number of components, higher power density and reliability. Also, single-stage OBCs are potential candidates for providing power quality enhancements like reactive power compensation, power factor correction, voltage regulation, and vehicle-to-grid (V2G) functionalities, such as frequency regulation and peak shaving.

Recent studies have emphasized a new class of current-fed topologies that attracted great attention because of their evident merits over conventional voltage-fed converters as follows: 1) inherent short-circuit protection; 2) low HF turns ratio; 3) high step-up ratio; 4) low input current ripple; 5) lower duty cycle loss; 6) negligible diode ringing; 7) more accessible current control capability and 8) reduced circulating current leading to the low peak and RMS current through the switches. Usually, current-fed converters were implemented with a resistor-capacitor-diode (RCD) snubber, active clamp, or lossy regenerative snubber to avoid the voltage spike across the switched turn-off device [139]. Nevertheless, passive snubber circuits attribute to costly, bulky, and lower efficiency, while active snubber circuits need floating active devices and large HF capacitors and add peak current with less reliability.

This chapter proposes a novel topology for EV charger with soft-switched modulation technique (zero-current switching). A single-stage single-phase PFC converter comprising a current-fed full-bridge with bidirectional switches at the primary side and a full-bridge converter at the secondary with an HF transformer, as shown in Fig. 3.1 for EV charging application. Also, a current-fed converter-based novel modulation scheme has been proposed for the topology depicted that results as: 1) reduced ripple at the supply grid side and enhancing the ripple frequency to 2x switching frequency; 2) less switching loss: zero current switching at primary side switches and zero-current turn-on at secondary side switches; 3) snubber-less naturally clamped soft-switching is maintained during operating range throughout bidirectional power flow; 4) ZCS and mitigating the voltage-spike problems in semiconductor devices and limits the RMS current attribute to higher efficiency; 5) high power factor correction operation and better THD profile. Therefore, a comprehensive study of proposed steady-state operation, design, simulation results, experimental results and merits of the proposed converter with other state-of-the-art single-stage converters has been studied and analyzed in this chapter.

3.2 Proposed Converter

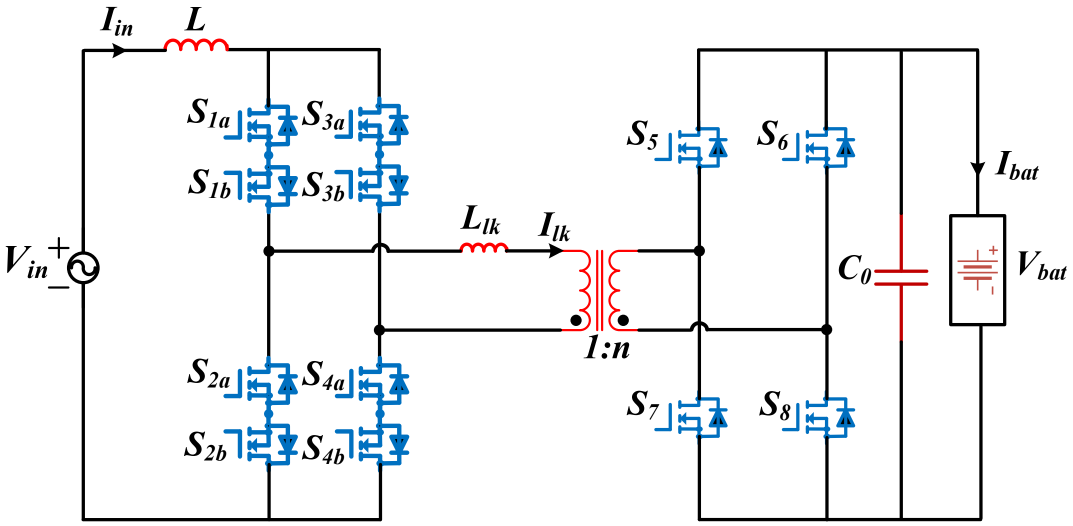

Fig. 3.1. Proposed single-stage PFC topology for Level-1 EV charger.

Fig. 3.1 shows the circuit diagram of a novel single-phase single-stage current-fed bidirectional dual active bridge PFC converter for Level-1 EV charging application. The configuration has a current-fed bidirectional full-bridge topology connected through galvanically isolated HFT to a full-bridge topology affiliated with the battery. L is the boost inductor, and L_{lk} is the series leakage inductance of the HFT. An external inductance should be connected in series if the leakage inductance is lower than necessary. C_0 is the output filter

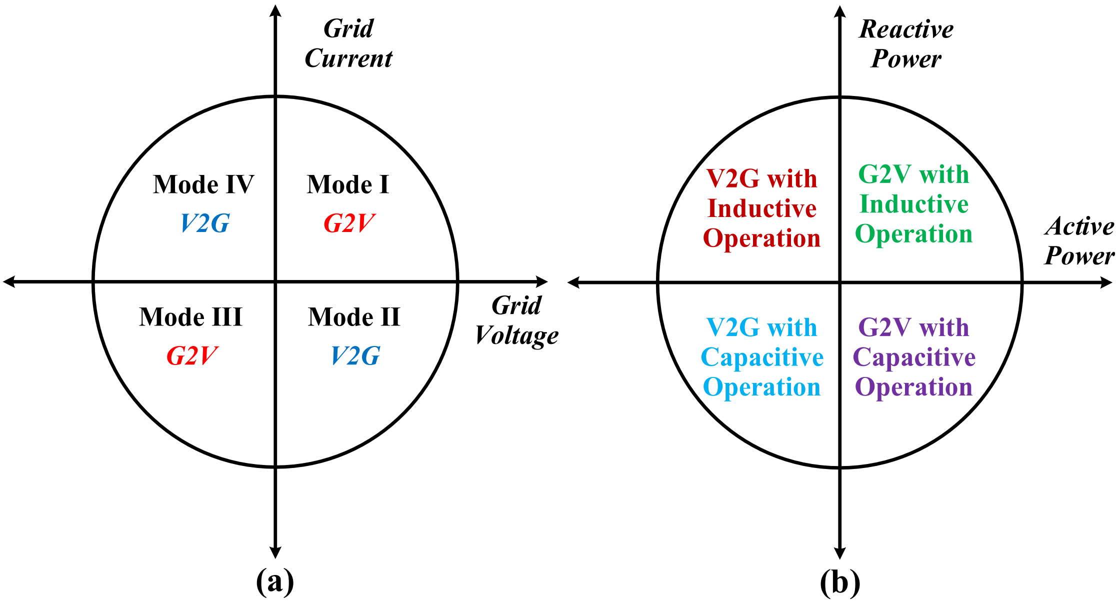

Fig. 3.2. Diagram of four modes of operation.

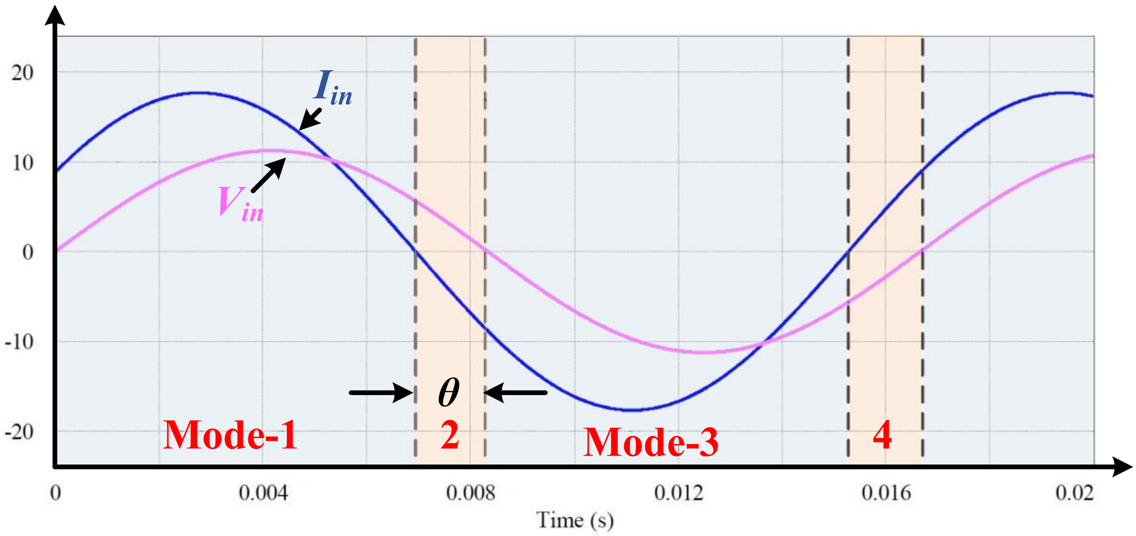

Fig. 3.3. One typical AC-line frequency cycle for different modes of operation.

capacitor. This topology can operate in four modes based on the polarity of grid voltage and grid current, as depicted in Fig. 3.2(a). Also, it can operate effectively in regions of the active and reactive power (P-Q) under the four modes of operation as shown in Fig. 3.2(b). During grid-to-vehicle battery (G2V) of Mode-I and Mode-III, the topology behaves as a full-bridge isolated boost converter (current-fed full-bridge with bidirectional switches at grid-side), and while in vehicle battery-to-grid (V2G) of Mode-II and Mode-IV, the topology behaves as a

Table 3.1: Modulation Technique for the Proposed Converter

Parameters	**Mode-I**	**Mode-II**	**Mode-III**	**Mode-IV**
Grid Voltage, V_{in}	$V_{in}>0$	$V_{in}>0$	$V_{in}<0$	$V_{in}<0$
Grid Current, I_{in}	$I_{in}>0$	$I_{in}<0$	$I_{in}<0$	$I_{in}>0$
Input Power, P_{in}	G2V	V2G	G2V	V2G
S_{1a}, S_{2a}, S_{3a}, and S_{4a}	HF at duty ratio d_1	OFF	Remained-ON	Remained-ON
S_{1b}, S_{2b}, S_{3b}, and S_{4b}	Remained-ON	Remained-ON	HF at duty ratio d_1	OFF
S_5, S_6, S_7, and S_8	Fixed duty ratio (d_2) S_5, S_8 similar S_6, S_7, similar	0.5 duty ratio d_r and PSM S_5, S_8 complementary S_6, S_7, complementary	Fixed duty ratio (d_2) S_5, S_8 similar S_6, S_7, similar	0.5 duty ratio d_r and PSM S_5, S_8 complementary S_6, S_7, complementary

where, d = duty cycle of the switch, T_s = switching period

standard voltage-fed full-bridge isolated converter with an inductive output filter L. Fig. 3.3 demonstrates the V_{in} and I_{in} with power factor angle θ in the time-domain-plot for standard operation. All modes of operation of the introduced converter are illustrated in Section III.

3.3 Converter Steady-State Analysis

The operational scheme of the proposed converter is divided into four modes based on the polarization of grid current and voltage with the handling to perform in a bidirectional way containing active and reactive power flow. Table 3.1 exhibits the modulation technique used for the proposed configuration. The detailed analysis and operation of the proposed converter in all four modes are described as follows.

3.3.1 Mode-I (Grid-to-Battery Operation)

The operational scheme of the proposed converter is divided into four modes based on the polarization of grid current and voltage with the handling to perform in a bidirectional way containing active and reactive power flow. In Mode-I, the power is transmitted from the supply grid to the vehicle battery when grid voltage and grid current are positive. Fig. 3.4

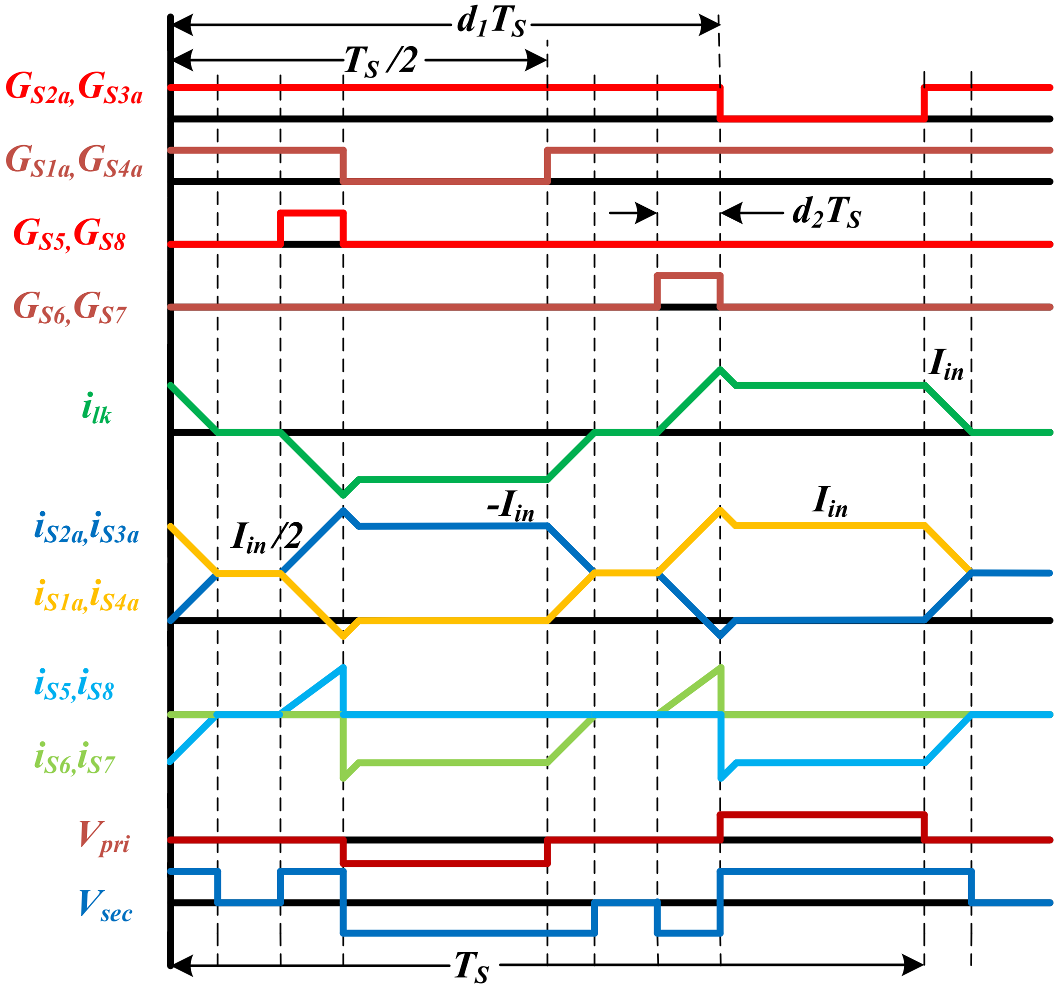

Fig. 3.4. Typical waveforms of Mode-I operation for proposed converter.

shows the gate pulses of AC-side switches S_{1a}, S_{4a}, and S_{2a}, S_{3a} of two-phases. They are phase-shifted by 180^{θ}. During mode-I, primary-side switches S_{1a}, S_{2a}, S_{3a}, and S_{4a} are operated with high-frequency duty cycle d_1 modulation, and it is maintained greater than 50% for ensuring overlap between the legs during the conduction. At the same time, other AC-side switches S_{1b}, S_{2b}, S_{3b}, and S_{4b} are continuously ON during the cycle when the grid voltage is positive in this operation. DC-side switches S_5, S_8, and S_6, and S_7 are operated with fixed duty-cycle d_2. The turned-OFF of all DC-side switches is associated with the AC-side switches as depicted in Fig. 3.4.

The grid current I_{in} flows through AC-side switches S_{1a} and S_{4a} when they are turned-ON, and S_{2a} and S_{3a} are turned-OFF. The inductor current I_L transfers through HFT from AC-side to DC-side. The current I_L is shifted from HFT to the switch linearly when S_{2a} and S_{3a} are turned-ON, followed by current via S_{1a} and S_{4a} gradually falling and reaching out at $I_{in}/2$. The

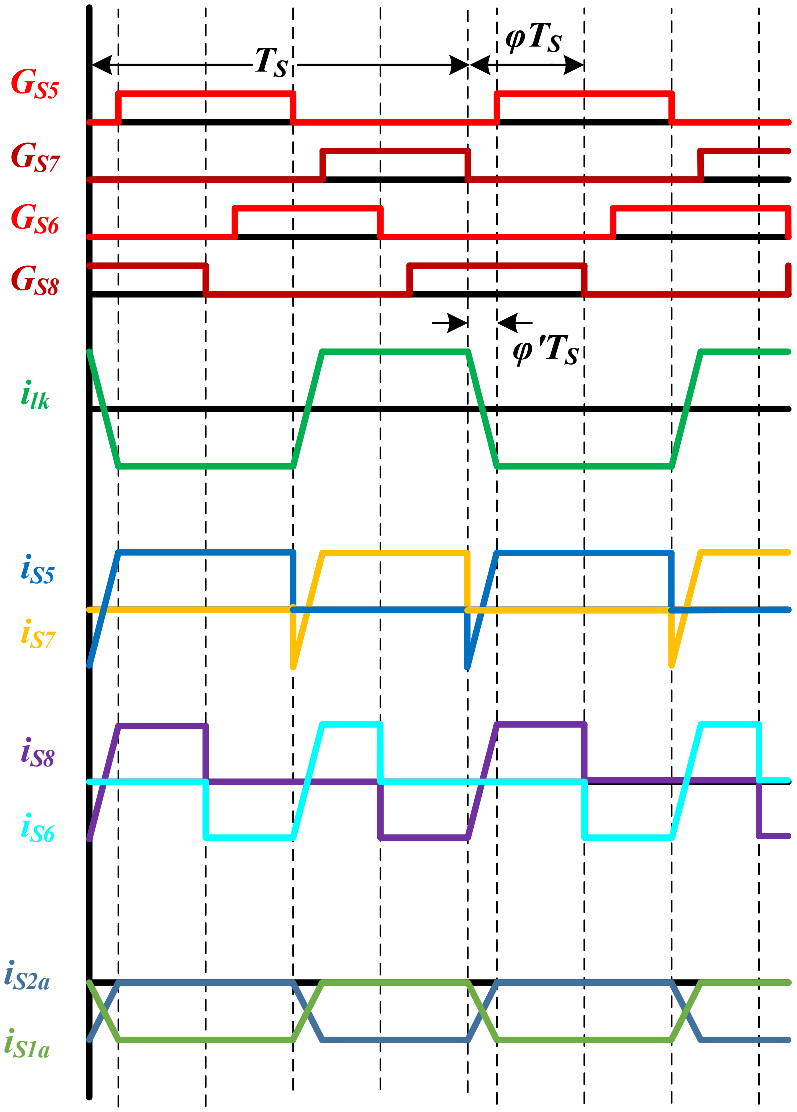

Fig. 3.5. Typical waveforms of Mode-II operation for proposed converter.

current flows through DC-side switches S_6 and S_7 until its body diodes reach zero. The DC-side switches are utilized to minimize the current at AC-side switches and naturally switched OFF to achieve ZCS. The voltage $-V_0/n$ at the AC-side of HFT is gained by gating the DC side switches S_6 and S_7 just before the turned-OFF the AC-side switches. This makes the current flow through AC-side switches reach zero naturally, regardless of load variations. The current flows through AC-side switches reaches zero before it is switched OFF by the value of duty cycle d_2, of DC-side switches. Higher peak current results from the need to deliver power to the DC-side in lesser time of $(1\text{-}d_1)\,T_s$ when d_1 is higher. For that, Under the operating conditions of grid voltage and grid current during this mode, the peak current flows through AC-side switches can be minimized by fixing the duty cycle d_2 of DC-side switches;

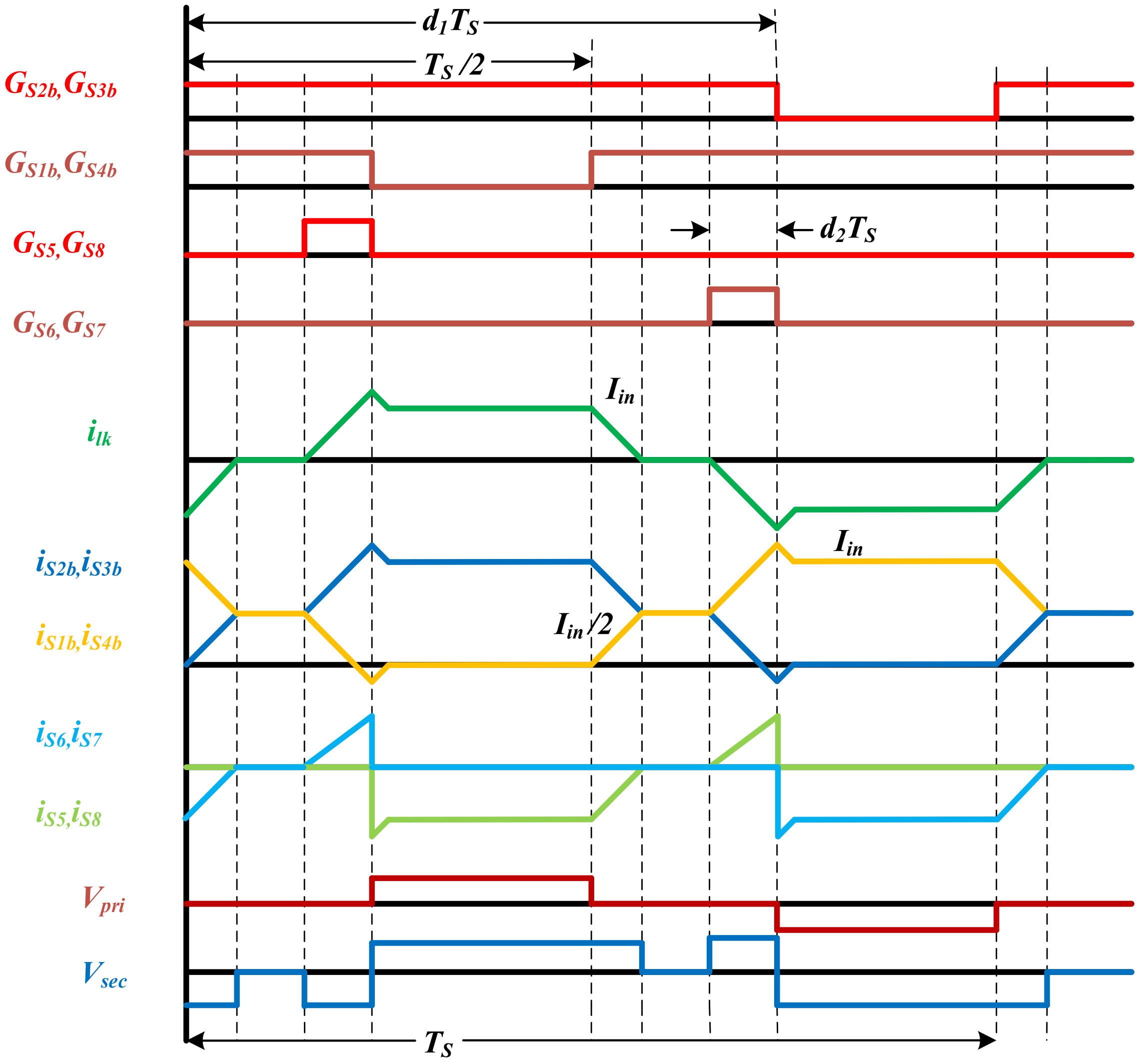

Fig. 3.6. Typical waveforms of Mode-III operation for proposed converter.

likewise, it can be reduced in the switch at another leg. Also, it minimizes the circulating current at grid side devices with the help of secondary side duty ratio d_2, resulting in lower conduction loss and increased efficiency. During this mode, it can be clearly seen that the ZCS of AC-side switches by the current flowing through HFT and semiconductor devices which is shown in Fig. 3.4. Voltage across the AC-side and DC-side of HFT is depicted in Fig. 3.4. As per the on-state and off-state of the grid side switches and DC-side switches during the mode-I, the V_{in} and V_0 a relationship is calculated as,

$$V_0 = \frac{n\,.V_{in}}{2.(1 - d_1)} \tag{3.1}$$

In [140], the full operation and analysis of this mode have been showcased in details for DC-DC applications. The limited power is being shifted by the product of switching frequency and series inductance. However, the current controller is designed to regulate the duty cycle of AC-side switches by more than 50% to follow the grid current to the reference value.

3.3.2 Mode-II (Battery-to-Grid Operation)

In Mode-II, the power is transmitted to the grid from the vehicle battery. For the negative grid current during this mode, the current flowing through diodes of of S_{1b}, S_{2b}, S_{3b}, and S_{4b} and AC-side switches S_{1a}, S_{2a}, S_{3a}, and S_{4a} are remained OFF. This configuration behaves as a standard voltage-fed full-bridge isolated converter with an inductive output filter [141]. The gate pulses of upper and lower switches at the DC-side complement each other and the phase-shifted modulation (PSM) technique by ΦT_S between two legs, as depicted in Fig. 3.5. In addition, the dead-band between upper and lower devices on the DC-side are selected to ensure the zero voltage switching (ZVS) by anti-parallel diodes are operating before turned-ON. For getting the variant efficient V_0, the phase angle can be changed from 0-50% during this mode. The V_{in} and V_0 a relationship is calculated as,

$$V_{in} = \frac{(\Phi - \Phi').V_0}{2.n} \tag{3.2}$$

where Φ is the phase angle and $\Phi' T_S$ represents the amount of time consumed by L_{lk} for transiting current from positive to negative and contrariwise, which is described in Fig. 3.5. The current flows via AC-side devices S_{1b}, S_{2b}, S_{3b}, and S_{4b} and via diodes of devices S_{1a}, S_{2a}, S_{3a}, and S_{4a} are remaining continuous with ZCS operation, which enhances the power conversion efficiency of the converter.

3.3.3 Mode-III (Grid-to-Battery Operation)

During this mode of operation, the power is transmitted from the supply grid to the vehicle battery when the negative half-cycle of grid voltage. Since the grid current in reverse polarity, the gate pulses of AC-side devices S_{1b}, S_{4b} and S_{2b}, S_{3b} are conducted with phase-shifted by 180^{θ} as shown in Fig. 3.6. During mode-III, primary-side switches S_{1b}, S_{2b}, S_{3b}, and S_{4b} are operated with high-frequency (HF) duty cycle d_1 modulation, and it is maintained greater than 50% for ensuring overlap between the legs during the operation. At the same time, other AC-side switches S_{1a}, S_{2a}, S_{3a}, and S_{4a} are continuously remained ON during the cycle due to

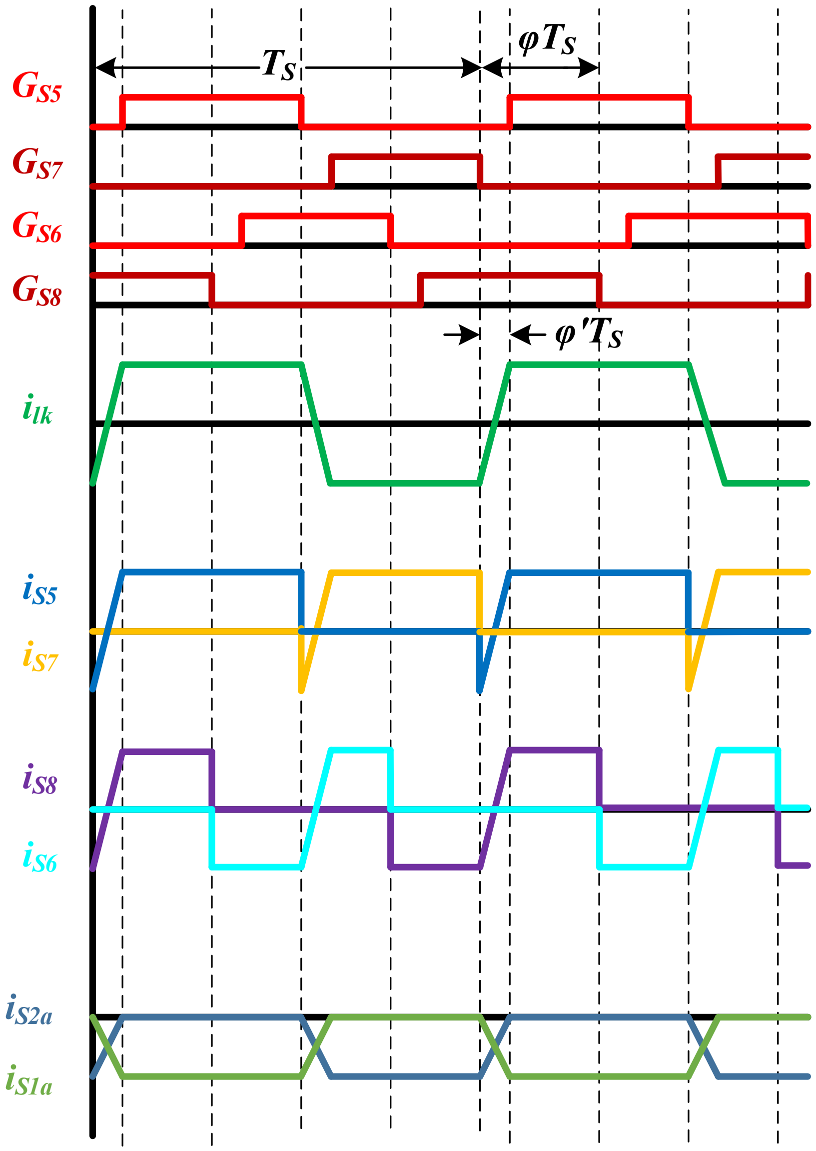

Fig. 3.7. Typical waveforms of Mode-IV operation for proposed converter.

grid voltage is in negative direction. DC-side switches S_5, S_6, S_7, and S_8 are operated with fixed duty-cycle d_2. The gate pulses are exchanged compared to the positive cycle of grid voltage and current to achieve the reverse direction of AC-side voltage across the HFT as shown in Fig. 3.6. The grid current I_{in} flows through AC-side switches S_{1b} and S_{4b} when S_{2b} and S_{3b} are turned-OFF and S_{1b} and S_{4b} are turned-ON. The turn-OFF of S_5 and S_8 are associated with turn-OFF of S_{1b} and S_{4b}. The turn-OFF of S_6 and S_7 are associated with turn-OFF of S_{2b} and S_{3b}. The current flowing through AC-side devices S_{1b} and S_{4b}, S_{2b} and S_{3b} fall to zero before turned-OFF leads to ZCS-off and also minimizing the turn-on losses during turned-ON mode of operation. The V_{in} and V_0 a relationship is calculated as,

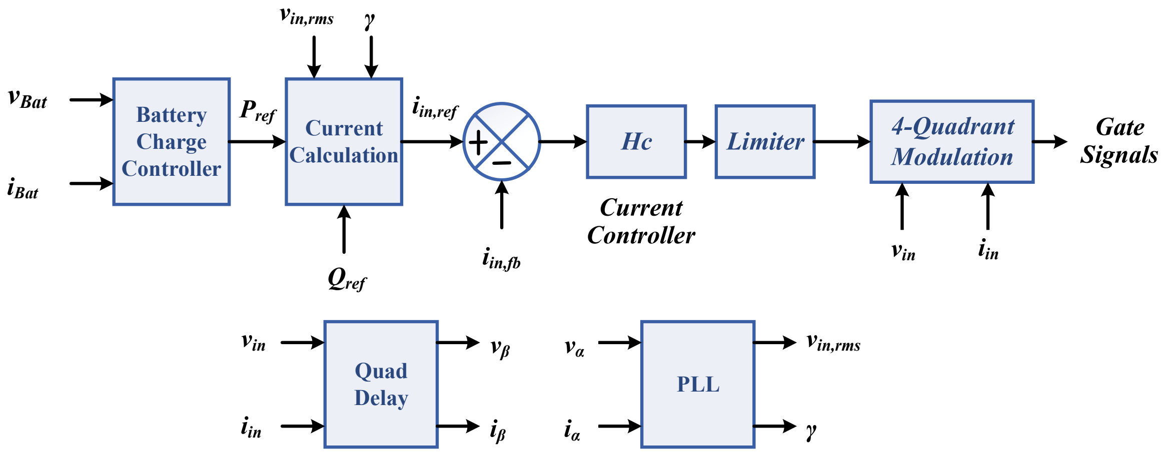

Fig. 3.8. Control scheme for proposed charger.

$$V_0 = -\frac{n \,.\, V_{in}}{2.\,(1 - d_1)} \tag{3.3}$$

3.3.4 Mode-IV (Battery-to-Grid Operation)

In Mode-IV, the power is being taken from the vehicle battery to the grid. For the positive grid current during this mode, the current is flowing through diodes of of S_{1a}, S_{2a}, S_{3a}, and S_{4a} and AC-side switches S_{1b}, S_{2b}, S_{3b}, and S_{4b} are continuously remained ON, while devices are conducted with ZVS by maintaining the PSM technique at DC-side as shown in Fig. 3.7. The V_{in} and V_0 a relationship is derived as,

$$V_{in} = -\frac{(\Phi - \Phi').\,V_0}{2.\,n} \tag{3.4}$$

3.4 Control Scheme

Fig. 3.8 exhibits the general control scheme with G2V and V2G capabilities for a plug-in EV charger. A conventional PLL is suffering from extra noise immunity due to the presence of second-order harmonic. In order to lessen the second harmonic and higher-order ripples, more feedback terms are used. A mixer phase detector creates trigonometric correlations between the sum and difference of the input and estimated frequencies in the resultant signal by multiplying two sinusoidal signals. A modified single-phase phase-locked loop (PLL) is utilized to get the phase angle and magnitude of input voltage [142]. A reference for the active power P_{ref} is calculated from the vehicle battery controller. The $i_{in,ref}$ is derived based on reactive power Q_{ref} that must be delivered to the grid. The goal of a current controller is to

Table 3.2: Converter Specifications

Parameter	**Value**
Grid Voltage, V_{in}	120V (rms)
Grid Current, $I_{in,max}$	17.76 A
Grid frequency, f_{line}	60 Hz
Output voltage, V_o	300 V
Output power, P_o	1500W
Switching frequency, f_{sw}	100 kHz

Table 3.3: Converter Design Parameters

Parameter	**Value**
Input Boost Inductor, L	170μH
Leakage Inductance of L_s	6.5μH
Turns ratio, n	1.2
Output Capacitor, C_0	$2*1200\mu$F

perfectly follow the $i_{in,ref}$ of grid frequency with the least amount of steady-state error and distortion as feasible, which can be achieved by offering high open-loop gain at grid frequency. It is known as a proportional resonant (PR) controller for providing high gain with correctly tunned grid frequency, and it is employed and designed for regulating $i_{in,ref}$. Based on the mode of operation listed in Table 3.1, a proposed four-mode modulation technique is employed to generate the gating signals for semiconductor devices of the proposed converter.

3.5 Converter Design

In this section, the proposed converter is designed according to a proposed procedure as per the given specification for Level-1 EV charging application: : Grid voltage V_{in}=120 V_{rms}, Line frequency f_s=60 Hz, Power P_o=1.5 kW, Input peak grid current $I_{in,max}$=17.1 A, switching frequency f_s=100 kHz. The vehicle battery voltage V_{Bat}=220-330 V and it utilizes

80 Li-ion batteries connections. During Mode-I and III operation, the duty ratio of AC-side switches is limited to more than 0.6 [143].

1) The maximum voltage across the AC-side switches is,

$$V_{SW,P} = \frac{V_{0,max}}{n} \tag{3.5}$$

2) The Transformer turns ratio is rated as,

$$n = \frac{2.V_{0,min}.(1 - d_{1,min})}{V_{in,max}} \tag{3.6}$$

Where, $d_{1,min}$ is the duty cycle for mode-I and III, $V_{0,min}$ is the minimum output voltage, and $V_{in,max}$ is the peak input voltage.

3) Series leakage inductance of L_{lk} is needed to verify ZCS through the operating requirements. It can be calculated as,

$$L_{lk} = \frac{V_{0,min}.(d_{1,min} - 0.5)}{2.I_{in,max} \cdot f_s . n} \tag{3.7}$$

The experimental value of $L_{lk}$is marginally low than the designing value for verifying ZCS operation is achieved during the range of operation. Also, it has primary effect on the peak current of AC-side switches, and it is merely the same as the designed calculation.

4) The input boost inductor L is calculated as per input current ripple specification,

$$L = \frac{V_{in,max} \cdot d_{1,min}}{\Delta I_L . f_s} \tag{3.8}$$

Whereas, ΔI_L demonstrates the peak-peak value in input boost inductor current. The optimal value of the boost inductor should be chosen to reduce the conduction losses to gain better converter utilization factor and converter efficiency [144].

5) The essential condition of ZCS of AC-side switches depend on the duty cycle of DC-side switches and it is derived as,

$$d_r \geq \frac{I_{in,max}.f_s . n . L_s}{V_{0,min}} \tag{3.9}$$

For ZCS soft-switching operation, the value of d_r is chosen a little more than the minimum threshold value as mentioned by equation (3.9). Nonetheless, the value of d_r should not be much higher than its minimum value for reducing the circulating and peak current through the devices.

6) The peak and RMS values of the AC-side switches are derived as,

$$I_{P,peak} = \frac{I_{in,max}}{2} + \frac{V_{0,max} \cdot d_r}{L_s \,.\, f_s \,.\, n} \tag{3.10}$$

$$I_{P,RMS} = I_{in,max} \sqrt{\frac{9 + 4.\, d_r - 6.\, d_{1,min}}{12}} \tag{3.11}$$

By accounting the full-AC cycle during the mode of operation, the RMS current can be measured.

7) The peak and RMS values of the DC-side switches are derived as,

$$I_{s,peak} = \frac{V_{0,max} \cdot d_r}{n^2 L_s \,.\, f_s} \tag{3.12}$$

$$I_{s,RMS} = \frac{I_{in,max}}{n} \sqrt{\frac{9 + 4.\, d_r - 6.\, d_{1,min}}{12}} \tag{3.13}$$

The RMS current can be measured by considering the full-AC cycle during the mode of operation. Additionally, the maximum voltage of DC-side switches should be more than the maximum voltage at output as, $V_{SW,S} \geq V_{0,max}$.

8) The peak and RMS values of the AC-side high frequency transformer (HFT) are given as,

$$I_{PT,peak} = \frac{V_{0,max} \cdot d_r}{L_s \,.\, f_s \,.\, n} \tag{3.14}$$

$$I_{PT,RMS} = I_{in,max} \sqrt{\left[\frac{1 - d_{1,min}}{2} + \frac{d_r}{3}\right]} \tag{3.15}$$

By accounting the full-HF over AC-cycle with fluctuations of $I_{in,max}$ and $d_{1,min}$ during the mode of operation, the RMS current can be measured.

9) The RMS and peak values of the DC-side high frequency transformer (HFT) are given as,

$$I_{ST,peak} = \frac{V_{0,max} \cdot d_r}{L_s \cdot f_s \cdot n^2} \tag{3.16}$$

$$I_{ST,RMS} = \frac{I_{in,max}}{n} \sqrt{\left[\frac{1 - d_{1,min}}{2} + \frac{d_r}{3}\right]} \tag{3.17}$$

The RMS current can be measured by considering the full-HF over AC-cycle with fluctuations of $I_{in,max}$ and $d_{1,min}$ during the mode of operation.

10) The primary and secondary turns of transformer are calculated as,

$$N_P = \frac{V_{0,max} \cdot (1 - d_{1,min})}{2. A_C . f_s . n. B_m} \tag{3.18}$$

$$N_S = \frac{V_{0,max} \cdot (1 - d_{1,min})}{2. A_C . f_s . B_m} \tag{3.19}$$

Whereas, B_m denotes as maximum magnetic flux density of core and A_C is the cross-sectional area of core. For the HFT,

$$A_f . J_f . K_f = N_P . I_{PT,RMS} + N_S . I_{ST,RMS} \tag{3.20}$$

Whereas, A_f is the cross-sectional area of frame-winding, K_f is the frame-windownutilization ratio, and J_f is the frame-current denstity. From eauations (3.17) to (3.20), the product of core-area of HFT is derived as,

$$A_f . A_C = \frac{2. V_{0,max} \cdot \left(1 - d_{1,min}\right) . I_{PT,RMS}}{K_f . J_f . f_s . n. B_m} \tag{3.21}$$

11) The output capacitor is designed by considering to imbibe the fluctuation in power related to 2x the grid frequency [145]. The designed equation of output capacitance C_0 is given by,

$$C_0 = \frac{2.\ P_0}{V_{0,min} \cdot \omega. \Delta V_0} \tag{3.22}$$

Whereas, ΔV_0 is the output voltage ripple range and $\omega = 2. \pi. f\ rad/sec$ is the grid frequency.

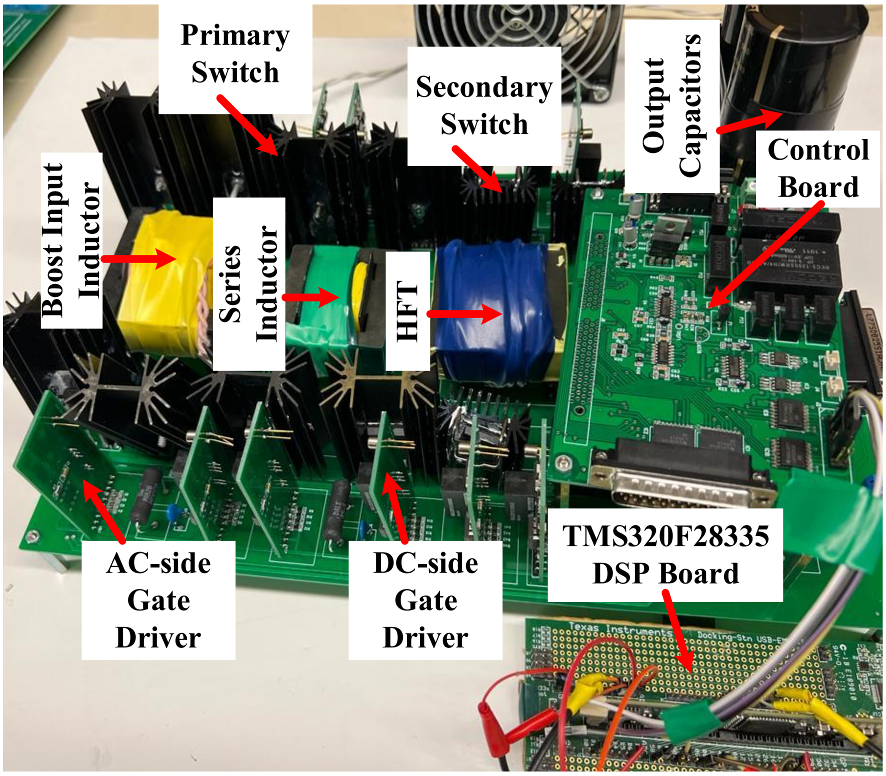

Fig. 3.9. A 1.5 kW proof-of-concept experimental prototype of the proposed converter.

3.6 Results and Discussion

In this section, the proposed converter is designed according to a proposed procedure as per the given specification for Level-1 EV charging application. In this section, the proposed converter analysis and designed expressions are verified through simulation and experimental results. The proposed configuration as shown in Fig. 3.1. is simulated in PSIM 11.04 software. Table 3.2 and Table 3.3 represent the converter input specifications and design parameters, respectively. To corroborate the analysis and design of the proposed configuration for EV charger, a 1.5-kW proof-of-concept experimental laboratory prototype is established as shown in Fig. 3.9.

3.6.1 Simulation Results

Fig. 3.10 presents the simulation results of the proposed configuration which is examined in all four modes of operation of power direction. From the converter design calculation in Section 3.5 and above-given topology requirements, the values of devices and components are selected. Fig. 3.10(a) demonstrates the power flowing bidirectionally via grid voltage V_{in}, grid current I_{in}, and input boost inductor current I_L. In the beginning, P_{ref}=1.50 kW is

Table 3.4: Component Specifications of the Laboratory Prototype

Component	**Specifications**
AC-side switches	CREE-SiC MOSFET, C3M0032120D, 1.2 kV, 63A, 32mΩ
DC-side switches	CREE-SiC MOSFET, C3M0021120D, 1.2 kV, 81A, 21mΩ
Boost Inductor	55 x 28 x 21 EE ferrite Core, 170μH
High Frequency Transformer (HFT)	EE ferrite core, Primary turns, N_1=26, secondary turns N_2=30, L_{lk1}= 1.65μH
Series Inductance	EE ferrite core, 4.85μH
Output Capacitor	2*1200μF 450V electrolytic capacitor
Gate Driver IC	IC-IXYS-IXDN609SI
DSP Board	TMS320F28335
Power Source	California Instruments AST1503
Voltage Sensor	Broadcom-ACPL-C79
Current Sensor	Allegro ACS714

instructed to the control system to shifting the I_{in}=17.7A at t =0.07s. The grid current and grid voltage are in phase with unity power factor (UPF) mode. Afterward, P_{ref} is altered to -1.5kW at t =0.10s, grid current moves 180^{0} phase-shifted regarding grid voltage forthwith exhibiting the rugged and dynamic execution design of the controller. Furthermore, interposing the reactive power to the converter is presented in Fig. 3.10(b) and (c) which are showcased that the ability to perform the converter in all different modes of power flow to offer the flexibleness to command over the P_{ref} and Q_{ref} in both the ways. In which, P_{ref}=1.3 kW at t =0.07s maintaining the Q_{ref}=0 kVAr. Q_{ref}= -0.7 kVAr is changed at t =0.10s with the converter working at 1.5-kW Fig. 3.10(c) provides information on the ideal concept of transferring reactive power in the absence of battery charging or discharging, in which case the power converter can be used to compensate for reactive power. It is clearly seen that this topology is operated in all modes of operation and offering the flexibleness to control the bidirectional flow of active and reactive power. Fig. 3.10(d) represents the primary-side voltage HFT during the mode-I and mode-III. operated in all modes of operation

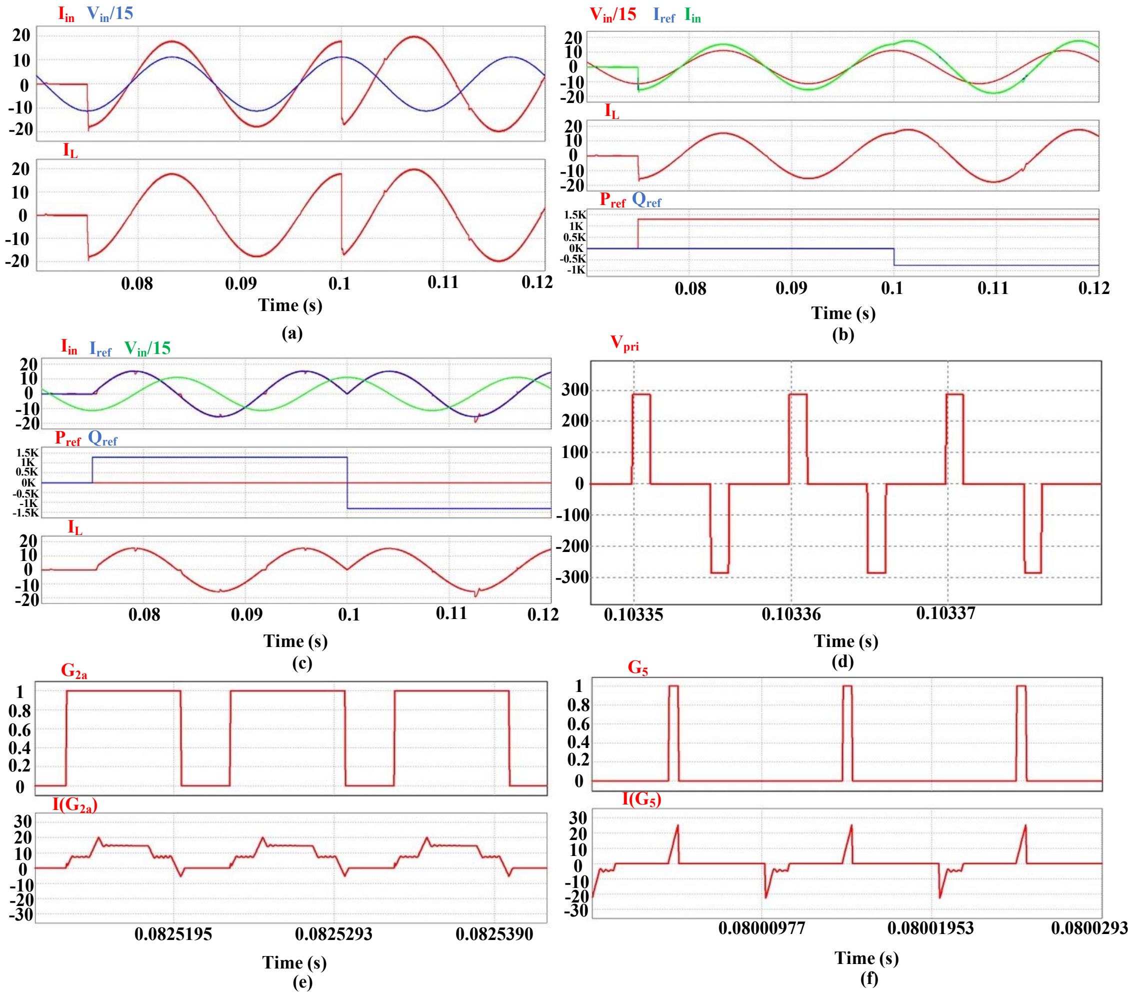

Fig. 3.10. Simulation results at rated output power P_o=1.5 kW (a) Transient operation and grid synchronized; (b) Reactive power shifting; (c) Reactive power compensation; (d) Primary-side voltage across HFT (e) Zero Current Switching (ZCS) of AC-side switches; (f) Zero Current turn-ON Switching (ZCS-turn ON) of DC-side switches.

and offering the flexibleness to control the bidirectional flow of active and reactive power. Fig. 3.10(d) represents the primary-side voltage HFT during the mode-I and mode-III. During the mode-I and III, the gating pulses and current through AC-side switches are shown in Fig. 3.10(e).

From Fig. 3.10(e), it is clearly denoted that primary switches achieve naturally zero current switching (ZCS) during the operation of the converter in G2V mode, the primary switch current attains zero without any extra components, snubber circuit, or active clamped before taking out the gate pulse reaching ZCS. These results are verified through given load and voltage range of converter. When the gate pulse is turned on, current begins to conduct from zero with a positive slope to attain the ZCS turn-ON of the DC-side as shown in Fig. 3.10(f).

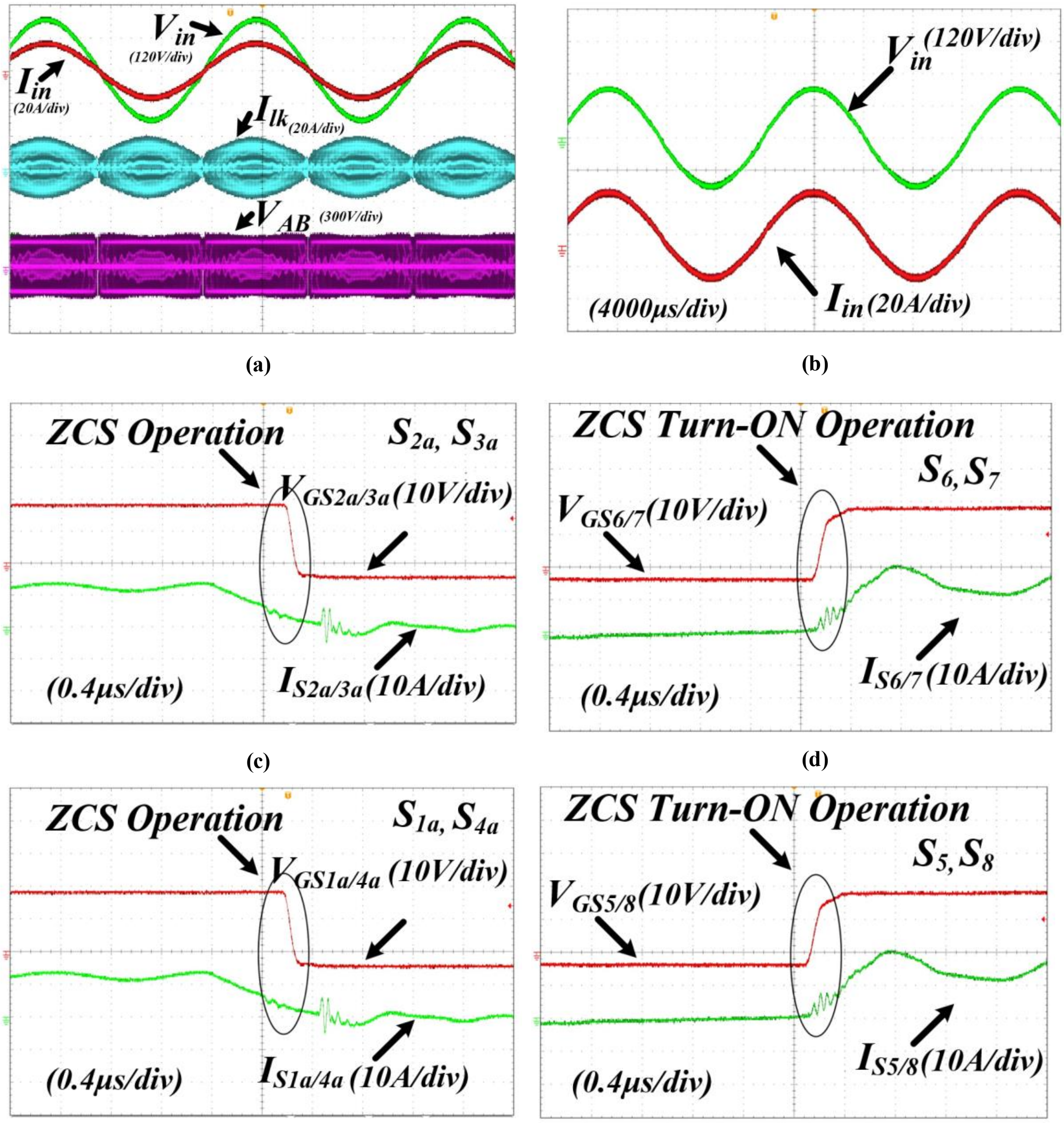

(a) **(b)**

(c) **(d)**

(e) **(f)**

Fig. 3.11. Experimental results for G2V mode; (a) G2V operation at with Input Current, Input Voltage, Primary HFT Current, and Primary HFT Voltage. (b) PFC opratrion at 1.5kW. (c) ZCS operation at AC-side switch S_{2a} and S_{3a}. (d) ZCS Turn-ON operation at DC-side switch S_6 and S_7. (e) ZCS operation at AC-side switch S_{1a} and S_{4a}. (f) ZCS Turn-ON operation at DC-side switch S_5 and S_8.

3.6.2 Experimental Results

In this section, the proposed converter is designed according to a proposed procedure as per the given specification for Level-1 EV charging application. 1.5 kW experimental prototype is established for validating the performance and design as shown in Fig. 3.9. for converter specifications given in Table 3.2 and 3.3. The components specifications are required to build

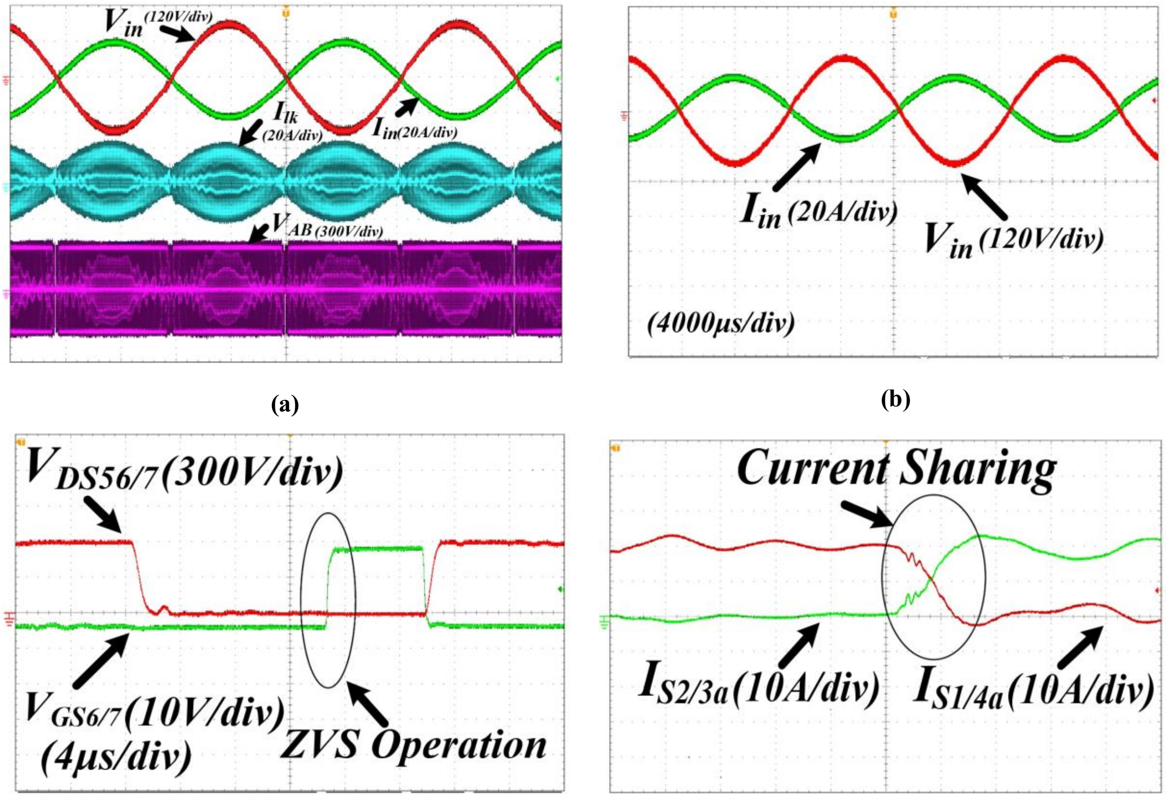

(a) (b)

(c) (d)

Fig. 3.12. Experimental results for V2G mode; (a) V2G operation at with Input Current, Input Voltage, Primary HFT Current, and Voltage. (b) Input Volatge and Current are out of phase at 1.5kW. (c) ZVS Turn-ON operation at DC-side switch S_6 and S_7. (d) Current Sharing at AC-side switch S_{2a}, S_{3a} and S_{1a}, S_{4a}

the laboratory hardware and it is listed in Table 3.4. The measurements of the proposed topology are 7.5*9.5*0.40 in^3 (l*b*h) resulting in power density of 52.63 W/in^3. The proposed converter grid voltage of 120V rms is considered from California Instruments AST1503. The gating signals for the primary and secondary switches were generated by using the TI DSP TMS320F28335 Board. By using gate driver IC IXYS-IXDN609SI and Broadcom-ACPL4800 optocoupler, the isolated gate-driver circuits are designed for the semiconductor devices. The experimental results are observed very closely and it is estimated as per digital simulation results. SiC-MOSFETs based PFC converter has been built, tested and performed with different operating conditions. Fig. 13.11. exhibits the experimental results at rated 1.5 kW for AC-DC power conversion, where the power is transmitted from grid to battery during mode-I and III. The value of primary HFT current and voltage are illustrated in Fig. 3.11(a) and it is within the anticipated boundaries. Fig. 3.11(a) and (b) demonstrates the grid current is purely sinusoidal and follow in both phase and shape with grid-voltage. Also, it should be observed that the grid current is nearly unity power factor

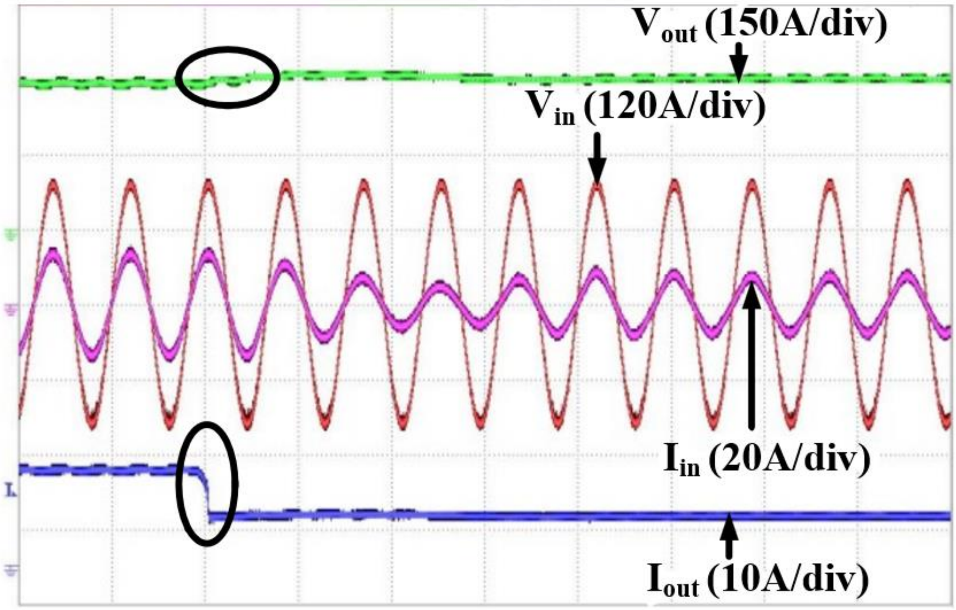

Fig. 3.13. Dynamic response of the converter at load change from 100% to 50%.

(PF) operation (0.99) and THD of 2.55% (< 5% as per IEEE Standard 519-2014) [146] is maintained during mode of operation. The current falls to zero naturally and anti-parallel diodes are operated across the AC-side semiconductor devices, which shows the negative current resulting into ZCS turn-off operation. Fig. 3.11(c) and (e) depicts the primary switches S_{2a}, S_{3a} and S_{1a}, S_{4a} are achieved the ZCS turn-off soft switching operation at different time-interval. Similar waveforms have been observed in the other switches to ensure the soft-switching during mode-III. Along with, DC-side switches S_6, S_7 and S_5, S_8 are operated with ZCS turn-ON at different time-interval and it can be seen from Fig. 3.11(d) and (f), in which the current goes from zero to positive when switch turned-ON results into ZCS turn-ON operation. Similarly, other switches of secondary-side achieved the soft-switching during mode-III. Fig. 3.12(a). represents the experimental outcomes of V2G mode of operation, where power is converted from dc to ac. The grid voltage and current are out of phase and that indicates the negative power flow as shown in Fig. 3.12(b). Fig. 3.12(c) presents the anti-parallel diodes of DC-side switches are operating before the turned-ON the switches resulting in ZVS-turn-ON operation during mode-II and IV. The current is mutually sharing with diodes of primary switches which enhances the efficiency of converter as shown in Fig. 3.12(d) during mode-II and IV. The experimental results and digital simulation results are proved that the design and mathematical analysis of the proposed converter is accurate. Fig. 3.13 describes that the proposed converter has better dynamic response when the load

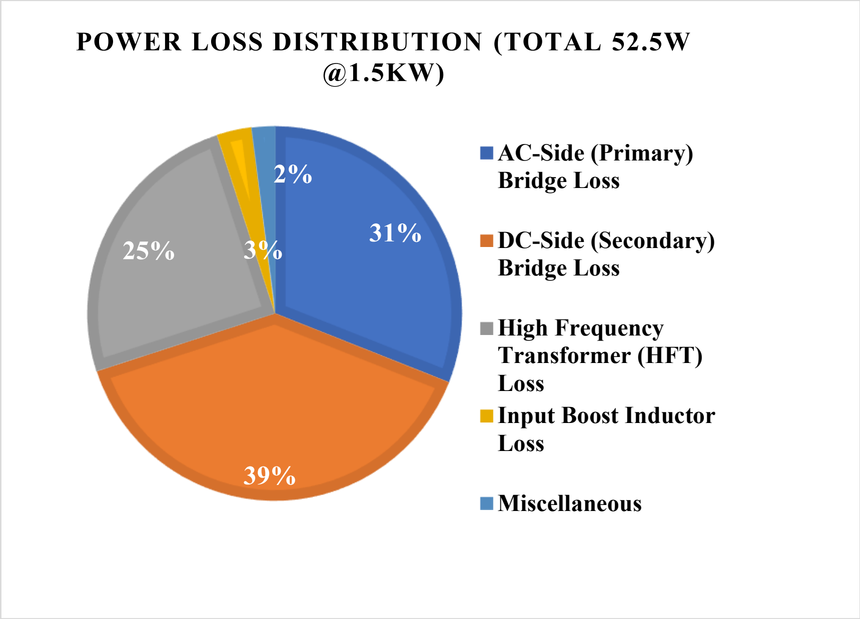

Fig. 3.14. Power loss distribution at 1.5kW.

changes from 100% to 50% which can be examined as mode differ from constant current (CC) to constant voltage (CV). It is clear that a battery functions as a current sink throughout the charging process, with CC mode representing a large load for the charger and CV mode representing a small load. As a result, a battery charger must maintain high efficiency over the whole power-range. The output voltage is shown to follow the reference voltage accurately and to settle in less than 60 rms. Fig. 3.14 describes the total power distribution at 1.5 kW. More than 70% losses of primary and secondary side semiconductor switches contribute to the total losses. HFT losses depicts the total losses of HFT and series inductor. Also, it shows that the selecting a SiC-MOSFET with lower on-state resistance is operating for achieving the high efficiency with significantly reduced the switching losses. The measured power factor (PF) is 0.9996, while the input current THD is 2.55% at full-load condition. Table 3.5 represents the information on the input current THD (%) of the converter and PF at various output power levels. It is noted that the input current THD (%) is under 3% and the converter PF is 0.999 (almost unity).

From Table 3.6 elucidates the comparative and efficiency analysis of the proposed converter with other existing topologies for EV chargers. In [147], Barbosa *et al.* proposed three-state switching cells (3SSCs) based bidirectional ac-dc converter. The higher number of active devices and magnetic components leads to higher costs, is voluminous, and suffers from poor efficiency with lower reliability. The current-fed ZCS-enabled single-stage PFC

Table 3.5: Power Factor and Input Current THD (%) of the Proposed Converter at different power levels

P_o, kW	PF	THD (%)
0.5	0.9992	3.56
0.7	0.9993	3.37
0.9	0.9993	3.05
1.1	0.9994	2.91
1.3	0.9996	2.67
1.5	0.9996	2.55

converter is presented in [154]. However, owing to resonant circuit design limits, maximum power is reduced at the output voltage range boundaries. However, this topology has higher efficiency and reliability. In [83], Zinchenko *et al.* proposed an ac-dc current source OBC, but the transformer has a higher RMS current and requires additional snubber circuits and HF capacitors than previous ones. Nevertheless, this configuration has higher reliability and lifespan with better efficiency at full load. A high-gain dc-ac HFL inverter with a quasi-resonant modulation technique is presented in [150]. This topology has better efficiency and performance at a low cost. However, the design, modeling, and control approach of this configuration is very tricky and complex. The peak efficiency of the proposed converter is 96.7%, which is higher than other single-stage isolated AC/DC with PFC topologies. At 50% of full-load, the converter achieves around efficiency of 95.5% as compared to 94.3% in [83], and 91.1% in [148] respectively. Also, converter provides efficiency of 94.7% at light-load conditions which comparatively higher than 93.3% in [147], 92.1% in [149], and 94.1% in [150]. The proposed converter has lower conduction and switching losses, simple control technique, and snubber-free circuits leads to better power quality and higher efficiency. Due to absence of DC-link capacitor, the proposed converter has higher-temperature operation capability and power density which ultimately enhances the reliability and lifespan of the converter.

Table 3.6: Comparison of the proposed converter with other state-of-the-art topologies for EV chargers

Description	**[151]**	**[152]**	**[147]**	**[148]**	**[153]**	**[149]**	**[154]**	**[83]**	**[150]**	**Proposed**
Switches (S)	6	11	16	6	16	5	10	10	12	12
Diodes (D)	9	14	0	20	0	13	4	4	0	0
Total = S+D	15	25	16	26	16	18	14	14	12	12
Inductors (I)	1	2	1	2	3	4	4	2	3	2
Capacitors (C)	2	3	1	5	4	3	2	1	2	1
Total = I+C	3	5	2	7	7	7	6	3	5	3
DBR	Y	N	N	Y	N	N	N	Y	N	N
Transformer	1	0	4	2	1	1	1	1	1	1
Circuit Complexity	**	*	***	***	***	*	*	*	**	*
CMA	**	+	+	***	***	+	+	+	***	+
Soft-Switching	N	Y	N	Y	Y	Y	Y	Y	Y	Y
Bidirectional Operation Method	N	Y	N	N	Y	N	N	N	Y	Y
Efficiency	**	**	**	*	**	**	***	**	**	***

*DBR= Diode Bridge Rectifier, CMA= Control and Modelling Approach, N=No, Y=Yes, * =Low, ** =Moderate, *** =High, + =Simple

3.7 Conclusion

A novel zero-current-switching assisted current-fed full bridge (CFFB) based bidirectional single-stage single-phase isolated power factor correction-based converter is proposed for plug-in EV charger. The isolated converter offers a simple solution towards compact design and lightweight. A novel modulation technique and control strategy has been formulated, where ac-side CFFBA with bidirectional switch that attains the ZCS which is connected with a full-bridge converter at the secondary side that attains zero current turned-ON through high-frequency (HF) transformer offers safety and galvanic isolation towards the design of the converter with a wide range of battery voltages and grid voltages. Soft-switching is accomplished throughout all modes of operation without any additional passive components, active clamped or snubber circuits which leads to cost-effective, compact size, reliable, robust design, lightweight, and higher efficiency and it establishes for all the switches during the working of the power converter in all different modes with active and reactive power flow balancing in both directions. Steady-state operation for all modes and design procedures with equations are given in detail. Also, the simulation and experiment results of the proposed converter have been demonstrated for a 1.5 kW EV charger which is closely matched with theoretical waveforms.

Chapter 4: High-Efficiency Single-Stage PFC Converter Based Bidirectional Plug-in G2V EV Charger

4.1 Introduction

In Chapter 3, a single-stage matrix based bidirectional AC-DC PFC converter has been proposed for EV charging. It provides merits like higher reliability, robust design, and high-power density. The main issue with this PFC topology is higher number of devices with associated gate driving requirements and higher chances of false switching compromising reliability. In this chapter, a novel current-fed push-pull (CFPP) bidirectional single-phase PFC converter with novel modulation technique of zero current communication is investigated for plug-in EV charger.

This chapter introduces a single inductor topology with two 4-quadrant switches is derived from the CFPP DC-DC converter topology [155]. A single-stage single-phase HFL bidirectional CFPP PFC AC-DC topology is studied as shown in Fig. 2. The proposed modulation for AC-DC conversion is a modified technique than that of used in dc/dc conversion discussed in [155]. It is a variable duty cycle modulation with duty cycle > 0.5 for grid-side devices (overlap in conduction time of the switches in two legs) while duty cycle < 0.5 for battery-side devices. The revised modulation is also implemented, keeping PFC requirements in mind. Natural voltage clamping (NVC) across the grid side switches, at battery voltage transmitted to the grid side. Additionally, zero current switching (ZCS) turn-on at DC-side semiconductor devices is accomplished, which minimizes the switching losses. The proposed soft-switching converter effectively solves the historical problem of voltage spike across the switching devices at their turn-off and thus, eliminates the requirement of the snubber or the clamping circuit across them. This reduces the hardware complexity while making the converter snubber-less, compact, and cost-effective. Soft switching is achieved in the proposed configuration without the need for any snubber or resonant circuit, and it is maintained throughout the full operating range in both directions of power flow. Due to minimizing the switching losses, the proposed converter can be performed with higher frequency, attaining better power density and efficiency. Also, Push-pull topology is advantageous by virtue of having only four switching devices with common ground with the

Table 4.1: Comparison of the proposed topology with other state-of-the-art topologies for EV chargers

Description	**[5]**	**[12]**	**[14]**	**[15]**	**[20]**	**[21]**	**[22]**	**[23]**	**[24]**	**Proposed**
Switches (S)	16	12	2	8	2	2	2	6	5	8
Diodes (D)	0	0	8	0	2	2	4	16	13	0
Total = S+D	16	12	10	8	4	4	6	22	18	8
Inductors (I)	1	3	2	4	1	2	3	2	2	1
Capacitors (C)	1	3	4	6	1	3	2	5	3	1
Total = I+C	2	6	6	10	2	5	5	7	5	2
DBR	N	N	Y	N	N	N	N	Y	Y	N
Transformer	4	1	1	1	0	0	0	2	1	1
Circuit Complexity	**	*	**	**	**	**	**	***	*	*
CMA	**	++	+	**	+	+	++	++	**	+
Soft-Switching	N	Y	Y	Y	N	N	N	Y	Y	Y
Bidirectional Operation Method	N	Y	N	Y	N	N	N	N	N	Y
Efficiency	**	**	***	**	**	**	***	*	**	***

*DBR= Diode Bridge Rectifier, CMA= Control and Modelling Approach, N=No, Y=Yes, * =Low, ** =Moderate, *** =High, + =Simple

source simplifying the gate driving requirements to cater cost and control limitations. In addition, this configuration utilizes single boost inductor with relatively less components.

Table 4.1 demonstrates the merits of the proposed soft-switching topology with other single-stage topologies. The proposed topology is competent in high-density owing to the reduced number of components and less magnetics, the objectives of this paper are accomplished in different sections as follows. The description of the proposed converter, steady-state operation with novel modulation technique, and control strategy are explicated in Section 4.2, 4.3, and 4.4 respectively. In Section 4.5, the detailed design procedure of the converter is explicated. Simulation results from PSIM 11.04 software, hardware prototype components details, and experimental results are illustrated in Section 4.6. Section 4.7 describes the key features of the proposed EV charger.

4.2 Proposed Topology

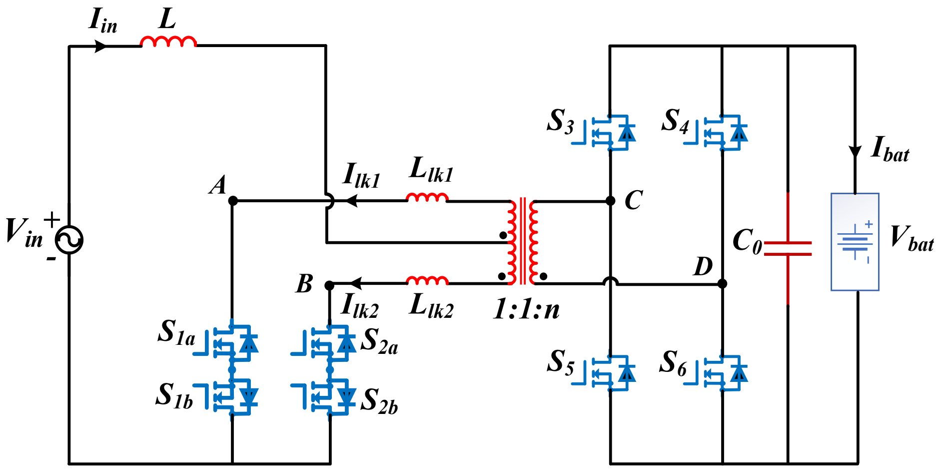

Fig. 4.1. Proposed single-stage bidirectional PFC-based converter.

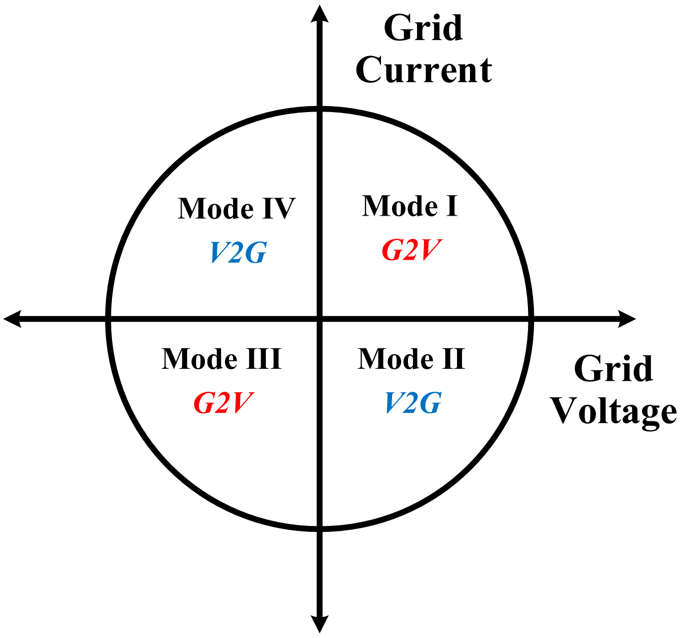

Fig. 4.2. Operation area of Plug-in EV charger.

The proposed single-stage isolated bidirectional PFC-based configuration has a current-fed bidirectional push-pull topology at the grid side with a boost inductor L and full-bridge topology at the battery side with output filter capacitor C_0, through HFT as per shown in Fig. 4.1. The topology is derived from current-fed push-pull DC-DC converter by replacing the primary side switches with 4-quadrant switches [155] to perform AC-DC conversion. It is operated with fixed-frequency pulse-width modulation and maintains ZCS at switches of the primary side and ZCS turn-on at switches of the secondary side. The design takes into account the boost inductor (L) and the HFT's series leakage inductances (L_{lk1} and L_{lk2}). An external inductance must be coupled in series if the L_{lk1} and L_{lk2} are less than required. From Fig. 4.2., the proposed converter can work in four modes of operation based on the polarity of the grid voltage (V_{in}) and grid current (I_{in}). During the grid-to-vehicle (G2V) charging mode of I and III, the topology behaves as an isolated boost converter (current-fed bidirectional push-pull topology at the grid-side). In contrast, the converter behaves as a typical voltage-fed converter with an inductive output filter when power is being transmitted from the vehicle-to-grid (V2G) mode of II and IV.

4.3 Operation Principal Analysis

The operation of the proposed configuration is divided into four different modes depending upon the polarity of grid voltage and grid current with the ability to handle power flow bidirectionally, including active and reactive power flow. In order to investigate the operation and analysis of the converter, some presumptions are as follows:

1. In a switching cycle, the boost inductor L is high enough to keep constant current through it.
2. All the components are assumed ideal and parasitic PCB is neglected.
3. Transformer magnetizing inductance is infinitely large.
4. The ac-line frequency is much lower than the switching frequency, and the grid inductor current is deemed as stiff at HF mode.

The following description explains the operation of the proposed converter in all four different modes.

4.3.1 Mode-I (G2V Operation)

The instantaneous power flows from the ac grid to the battery. The grid voltage and grid current are in a positive half-cycle during this mode. In Fig. 4.3., the grid side upper switches

Table 4.2: Modulation Technique for the Proposed Converter

Parameters	**Mode-I**	**Mode-II**	**Mode-III**	**Mode-IV**
Grid Voltage, V_{in}	$V_{in}>0$	$V_{in}>0$	$V_{in}<0$	$V_{in}<0$
Grid Current, I_{in}	$I_{in}>0$	$I_{in}<0$	$I_{in}<0$	$I_{in}>0$
Input Power, P_{in}	G2V	V2G	G2V	V2G
S_{1a} and S_{2a}	HF at duty ratio d_1	OFF	Remained-ON	Remained-ON
S_{1b} and S_{2b}	Remained-ON	Remained-ON	HF at duty ratio d_1	OFF
S_3, S_4, S_5, and S_6	Fixed duty ratio (d_2) S_3, S_6 similar S_4, S_5 similar	0.5 duty ratio d_r and PSM S_3, S_5 complementary S_4, S_6 complementary	Fixed duty ratio (d_2) S_3, S_6 similar S_4, S_5 similar	0.5 duty ratio d_r and PSM S_3, S_5 complementary S_4, S_6 complementary

where, d = duty cycle of the switch, T_s = switching period

S_{1a} and S_{2a} are operated at high-frequency (HF) with duty cycle modulation and identical gate signals phase-shifted with 180^0. The duty cycle d_1 associated with primary switches is always considered more than 0.6 for promising overlay operation between primary switches of S_{1a} and S_{2a}. The grid side lower side switches S_{1b} and S_{2b} remained in ON-position throughout this mode due to the grid voltage and current being positive during this cycle. The secondary side switches S_3, S_4, S_5, and S_6 are fixed with duty-cycle d_r, and their turn-OFF is associated with the turn-OFF of grid side switches. The current is flowing through S_{1a} when S_{1a} is in ON condition, and S_{2a} is in OFF state.

The power is exchanged from the primary to the secondary side through the inductor current I_L via HFT. At t_1, the current is transmitted linearly from HFT to the switch when switch S_{2a} is turned-ON. Likewise, the current flowing through device S_{1a} declines till it attains $I_{in}/2$. At t_2, the current flows through the battery side devices S_4 and S_5 till its body diode achieves null. The battery side devices are utilized to decline the current at the grid side devices and inherently switched OFF to plausibly attain zero current switching (ZCS) operation. At t_3, the voltage $-2.V_0/n$ at on the primary side of the transformer is obtained by

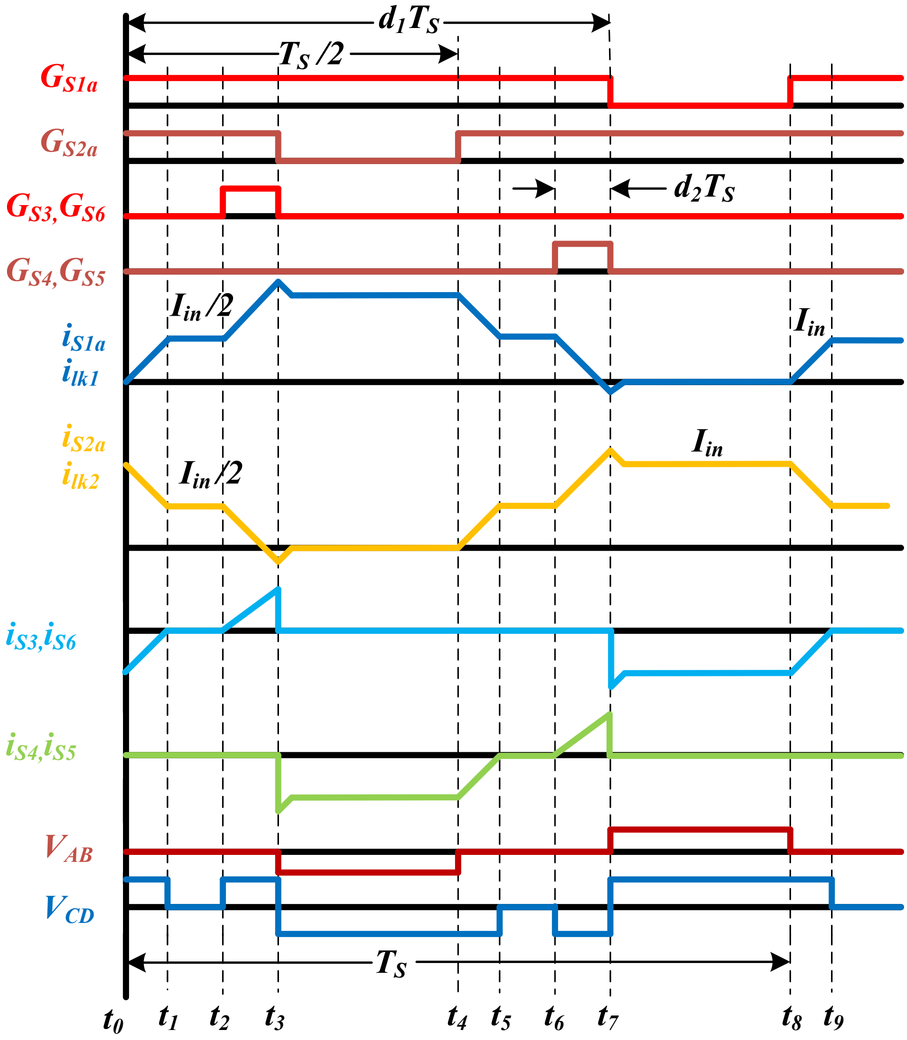

Fig. 4.3. G2V (Mode-I) operational waveform for proposed converter.

gating pulses at the secondary side devices S_4 and S_5 just before the turned-OFF at the primary side devices. With similar at t_4 -t_6, it makes the current going through primary side devices attain inherently zero independent of changes in load characteristics. At t_7, the current flows via the gid side switches attain zero just before it is turned OFF with the duty cycle d_r, of the battery side switches. The peak current through switches on the grid side can be reduced by adjusting the duty cycle of battery side switches during this mode; similarly, it can be decreased in the switch on other leg. In this mode, the current flows through the HFT and switches of the grid side with achieving ZCS as shown in Fig. 4.3. The voltages of HFT across the grid side and battery side are shown in Fig. 4.3. The V_{in} and V_0 a relationship is determined as,

$$V_0 = \frac{n\,.V_{in}}{2.\,(1-d_1)} \tag{4.1}$$

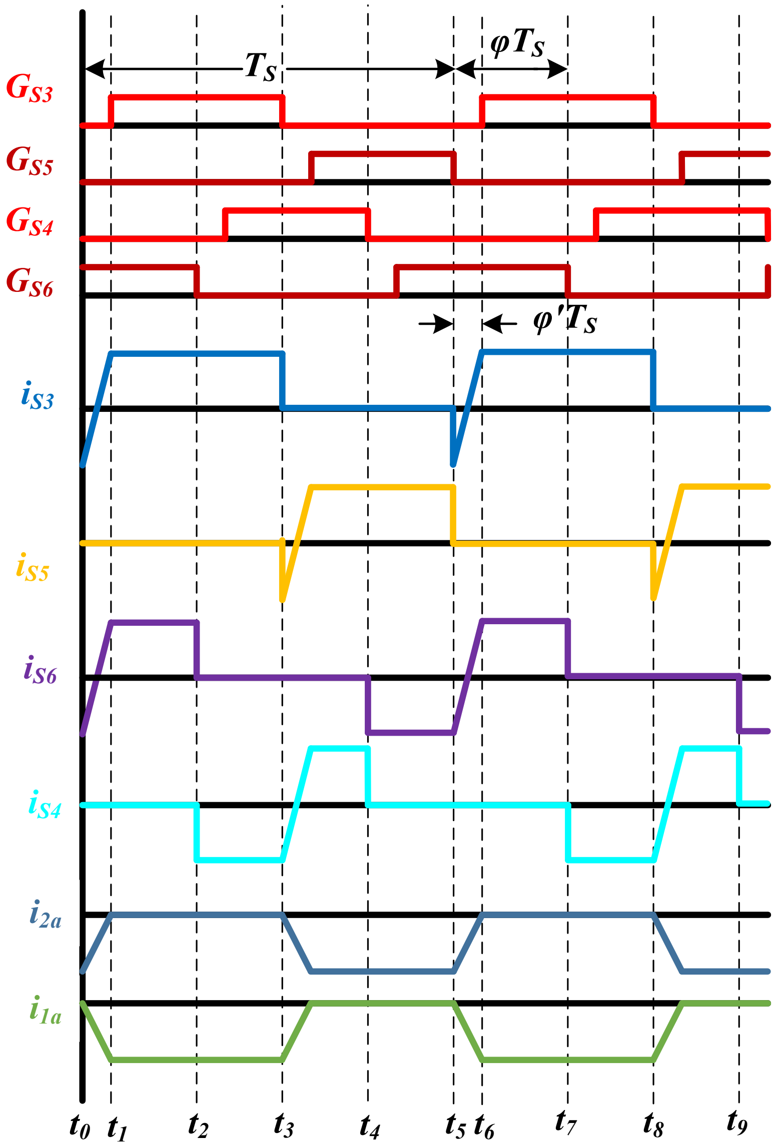

Fig. 4.4. V2G (Mode-II) operational waveform for proposed converter.

The analysis and design of this mode have been discussed in detail for dc-dc application of fuel-cell vehicles (FCVs) [155]. The power of switching frequency and series inductances shift the restricted power. However, the duty cycle of the grid-side switches is adjusted by more than 0.6 using the current controller to ensure that the grid current tracks the reference value.

4.3.2 Mode-II (V2G Operation)

The power is transmitted to the grid side from the vehicle battery during mode-II. The grid side switches S_{1a} and S_{2a} are continuous ON state and the current flows via diodes of S_{1b} and S_{2b} devices. The proposed converter mimics as a standard full-bridge voltage-fed topology

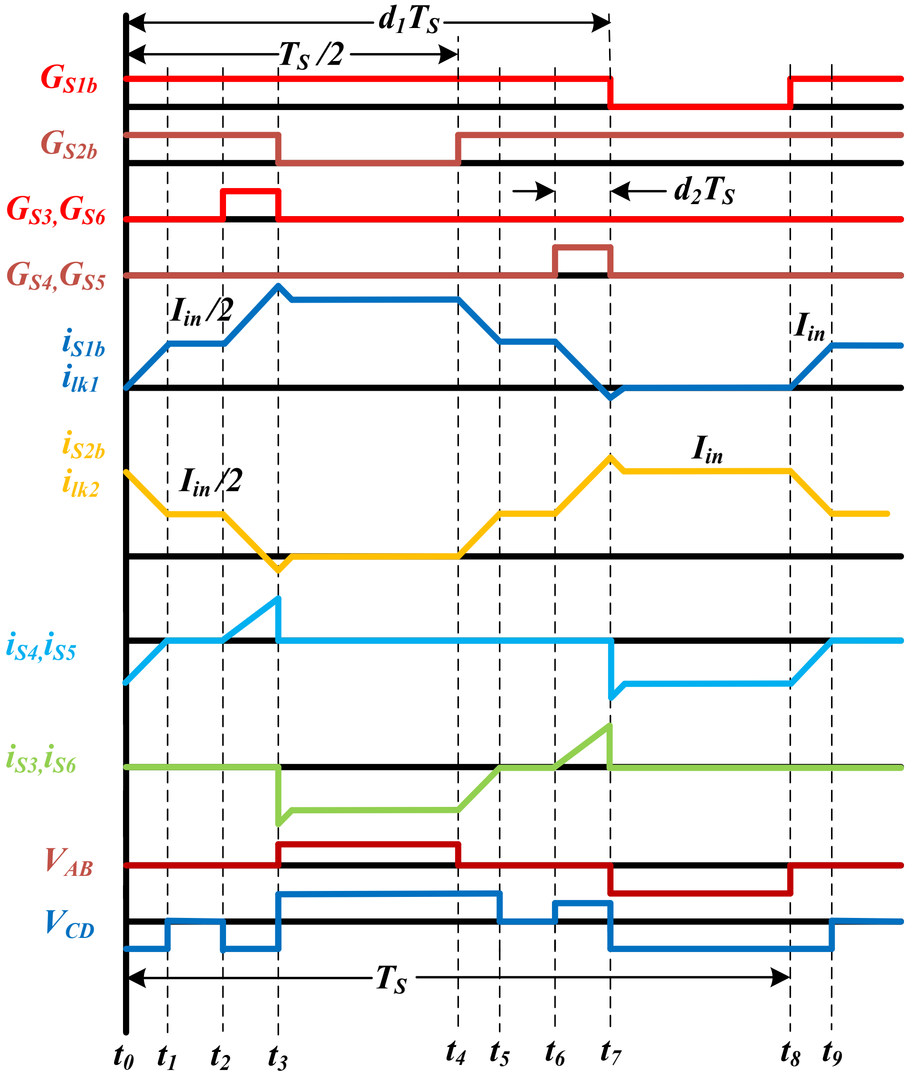

Fig. 4.5. G2V (Mode-III) operational waveform for proposed converter.

with an inductive output filter [156]. The phase shifted modulation (PSM) method is utilized by ΦT_S between two legs, and the gate pulses are applied to the top (t_1 -t_3) and bottom switches (t_3 -t_5) complement to each other at the battery side, as shown in Fig. 4.4. Furthermore, in order to achieve zero voltage switching (ZVS) operation, a dead band gap is implemented between the top and bottom devices on the battery side, ensuring that anti-parallel diodes are activated before it is turned ON condition. During this mode, the phase angle is varied from 0 to 50% for acquiring the effective output voltage, which is determined by,

$$V_{in} = \frac{(\Phi - \Phi').V_0}{2.n} \tag{4.2}$$

While Φ denotes the phase angle, $\Phi' T_S$ refers to the time required (t_5 -t_6) by L_{lk} to transfer current from positive to negative and vice versa, which is illustrated in Fig. 4.4. With zero current switching (ZCS) operation, the current flows through the diodes of the grid-side switches S_{1a} and S_{2a}, through switches S_{1b} and S_{2b}, thereby improving the efficiency of the proposed converter.

4.3.3 Mode-III (G2V Operation)

During this mode, if the grid voltage is in the negative half-cycle, the power is being drawn from the supply grid to the vehicle battery. The gate pulses of grid side switches S_{1b} and S_{2b}

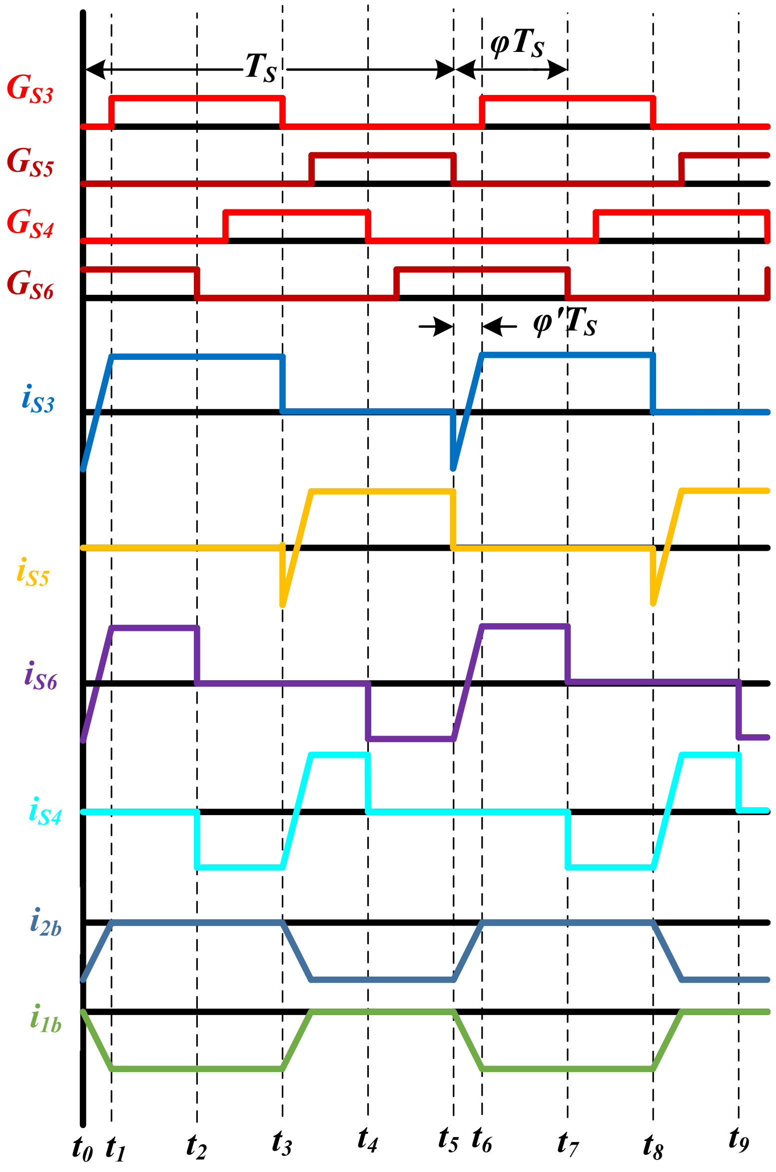

Fig. 4.6. V2G (Mode-IV) operational waveform for proposed converter.

are conducted with a 180^{θ} phase shift because the grid current is in the positive half-cycle, as illustrated in Fig. 4.5. High-frequency duty cycle d_1 modulation is utilized in mode-III to operate the primary side devices S_{1b} and S_{2b}, and d_1 is held above 0.6 to guarantee overlap among the converter legs. At the same time, the grid-side devices S_{1a} and S_{2a} are held in the ON state condition whilst the battery-side devices S_3, S_4, S_5, and S_6 are set to a duty-cycle of d_r when the grid voltage is in the negative cycle. The gate pulses are reversed in relation to the positive half-cycle of the grid current and voltage to attain the reverse direction of the grid-side voltage at HFT, as illustrated in Fig. 4.5. As similar mode-I operation with S_b switches, during the turn-OFF condition of S_{2b}, the current in the grid flows through S_{1b} as it is turned-ON mode. The turn-OFF of S_{2b} is related to S_4 and S_5, whilst the turn-OFF mode of S_{1b} device is associated with S_6 and S_7. The current that passes through the grid side devices S_{1b} and S_{2b} decreases to zero just before their turn-OFF, which leads to ZCS-off operation, reducing the turn-ON losses while in operation condition. The V_{in} and V_0 a relationship is calculated as,

$$V_0 = -\frac{n \, . V_{in}}{2.(1 - d_1)} \tag{4.3}$$

4.3.4 Mode-IV (V2G Operation)

The power is transferred to the vehicle battery from the supply grid during mode-IV. As similar mode-I operation with S_b switches, the power is passing via primary side devices S_{1b} and S_{2b}, and diodes of devices S_{1a} and S_{2a}. The devices S_{1b} and S_{2b} are remained-ON in

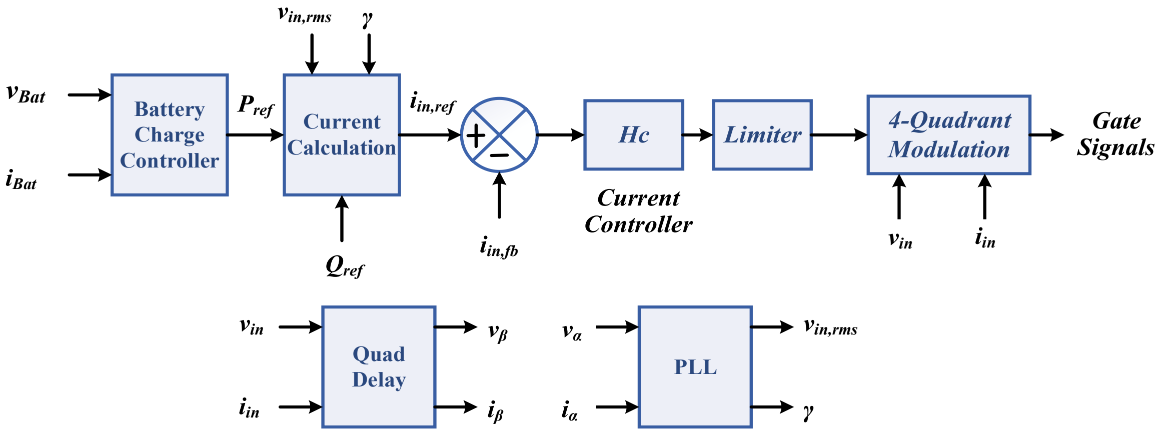

Fig. 4.7. Control scheme for proposed charger.

condition during the switches are operated with ZVS by regulation of the PSM method at the battery side as illustrated in Fig. 4.6. The output voltage is given as,

$$V_{in} = -\frac{(\Phi - \Phi').V_0}{2.n} \tag{4.4}$$

4.4 Control Technique

The control architecture of the Plug-in EV charger with G2V and V2G capabilities is shown in Fig. 4.7. To determine the magnitude of grid voltage and the phase angle, an effectuated single-phase phase-locked loop (PLL) is used [142]. In order to supply the required reactive power Q_{ref} to the grid, the vehicle battery controller calculates the active power reference P_{ref}, and the current controller achieves accurate tracking of the grid frequency $i_{in,ref}$ with low steady-state error and distortion by providing high open-loop gain at grid frequency. The $i_{in,ref}$ is controlled using a Proportional Resonant (PR) controller which is optimized for high gain at the grid frequency. The gating pulses for the switches of the proposed converter are generated using a specified novel modulation approach based on the mode of operation as shown in Table 4.2.

4.5 Design of the Proposed Converter

This section describes the proposed converter is designed and validated as per the following specifications: V_{in}=120 V_{rms}; $I_{in,max}$=17.1 A; f_{line}=60 Hz; f_s=100 kHz; P_o=1.5 kVA and V_{Bat}=220-330 V employs 80 Li-ion batteries. The duty cycle at grid-side switches during G2V mode of operation is restricted above 0.6 [143]. The duty cycle at battery-side switches during is restricted at 0.05. The designed parameters are outlined in Table 4.3 and 4.4.

12) Maximum voltage across SiC-MOSFETs at grid-side is,

$$V_{SW,P} = \frac{2.V_{0,max}}{n} \tag{4.5}$$

13) The Transformer turns ratio is rated as,

$$n = \frac{2.V_{0,min}.(1 - d_{1,min})}{V_{in,max}} \tag{4.6}$$

Table 4.3: Converter Specifications

Parameter	**Value**
Grid Voltage, V_{in}	120V (rms)
Grid Current, $I_{in,max}$	17.76 A
Grid frequency, f_{line}	60 Hz
Output voltage, V_o	300 V
Output power, P_o	1500W
Switching frequency, f_{sw}	100 kHz

Table 4.4: Converter Design Parameters

Parameter	**Value**
Input Boost Inductor, L	170μH
Leakage Inductance of L_s	7.2μH
Turns ratio, n	1.1
Output Capacitor, C_0	$2*1200\mu$F

The transformer turn ratio is selected to achieve low conduction losses in primary switches and secondary switches because converter efficiency primarily depends upon losses in primary and secondary switches due to conduction of higher current compared to other components in the converter. Losses in the HF transformer like core loss and copper loss in windings are also considered while selecting the turn ratio. The primary and secondary windings of the transformer are tested for various turn ratios, ensuring that the maximum flux density in the core remains constant across all cases. Using the primary and secondary winding currents, the gauge of the windings is selected, and the winding resistances are calculated. The duty cycle for G2V mode is denoted as $d_{1,min}$, while the minimum output voltage is represented by $V_{0,min}$, and the maximum input voltage is designated as $V_{in,max}$.

14) To ensure ZCS mode at operating conditions, the selection of total series leakage inductance of L_{lk_T} is validated. It can be derived as,

$$L_{lk\_T} = L_{lk1} + L_{lk2} = \frac{2.V_{0,min}.(d_{1,min} - 0.5)}{I_{in,max} \cdot f_s \cdot n} \tag{4.7}$$

In the experimental validation of ZCS operation, the total series leakage inductance L_{lk_T} is set to be lower than the designed value. Nonetheless, the effect of L_{lk_T} on the peak current of the grid side switches was not significantly different from the design calculation.

15) To meet the input current ripple (ΔI_L) specification, the input boost inductor L is calculated as,

$$L = \frac{V_{in,max} \cdot d_{1,min}}{\Delta I_L \cdot f_s} \tag{4.8}$$

The value of the input boost inductor L is determined according to the input current ripple specification, with ΔI_L indicating the peak-to-peak value of the inductor current. To achieve high converter efficiency and utilization factor, an appropriate boost inductor value that minimizes conduction losses must be selected, as described in [144].

If $L_{lk1}$and L_{lk2} are not equal then equation (4.8) is modified as follows,

$$L = \frac{(V_{in,max} + \frac{V_{0,min}}{n} - \frac{2.V_{0,min}.L_{lk\_T\_min}}{L_{lk\_T} \cdot n}).d_{1,min}}{\Delta I_L \cdot f_s} \tag{4.9}$$

Whereas, $L_{lk\_T\_min}$ is the minimum value of L_{lk1} and L_{lk2}.

16) To achieve zero current switching (ZCS) condition in the primary side switches, it is necessary to determine the duty cycle of the battery side and it is computed by,

$$d_r \geq \frac{I_{in,max}.f_s \cdot n \cdot L_{lk\_T}}{2.V_{0,min}} \tag{4.10}$$

The duty cycle value of d_r is selected to maintain ZCS condition, but it should not exceed its least value by a significant amount to prevent excessive current flow through the devices.

17) The RMS and peak current of the primary side switches can be determined by,

$$I_{P,peak} = I_{in,max} + \frac{2.V_{0,max}.d_r}{L_{lk\_T} \cdot f_s \cdot n} \tag{4.11}$$

$$I_{P,RMS} = I_{in,max}\sqrt{\frac{9 + 4.d_r - 6.d_{1,min}}{12}} \tag{4.12}$$

In order to determine the RMS current at the primary side, it is essential to account for the complete the grid cycle while the system is under operational mode.

18) The RMS and peak current of the secondary side switches can be determined by,

$$I_{s,peak} = \frac{2.V_{0,max}.d_r}{n^2 L_{lk\_T} \cdot f_s} \tag{4.13}$$

$$I_{s,RMS} = \frac{I_{in,max}}{2.n}\sqrt{\frac{2.d_r - 3.d_{1,min} + 5}{6}} \tag{4.14}$$

When measuring the RMS current during operation at the secondary side, it is important to consider the entire grid cycle. Additionally, the voltage at the secondary side switches should exceed the maximum voltage at the battery side as, $V_{SW,S} \geq V_{0,max}$.

19) The RMS and peak current of the primary side HFT can be computed as,

$$I_{PT,peak} = \frac{2.V_{0,max}.d_r}{L_{lk\_T} \cdot f_s \cdot n} \tag{4.15}$$

$$I_{PT,RMS} = I_{in,max}\sqrt{\left[\frac{1 - d_{1,min}}{2} + \frac{d_r}{3}\right]} \tag{4.16}$$

The RMS current can be determined by considering the complete HF over grid cycle, which fluctuates with $I_{in,max}$ and $d_{1,min}$ during the mode of operation.

20) The peak and RMS current of the secondary side HFT can be given as,

$$I_{ST,peak} = \frac{2.V_{0,max}.d_r}{L_{lk\_T} \cdot f_s \cdot n^2} \tag{4.17}$$

$$I_{ST,RMS} = \frac{I_{in,max}}{2.n}\sqrt{\left[\frac{1 - d_{1,min}}{2} + \frac{d_r}{3}\right]} \tag{4.18}$$

In order to determine the RMS current during operational mode, it is considered the complete HF over a grid cycle, taking into account the variations in both $I_{in,max}$ and $d_{1,min}$.

21) To account for power fluctuations related to twice of the grid frequency, the output capacitor is designed. The output capacitance C_0 is calculated as,

$$C_0 = \frac{2.\ P_0}{V_{0,min}.\ \omega.\ \Delta V_0} \tag{4.19}$$

Whereas, the range of output voltage ripple is represented by ΔV_0, while grid frequency is denoted by $\omega = 2.\pi.f\ rad/sec.$

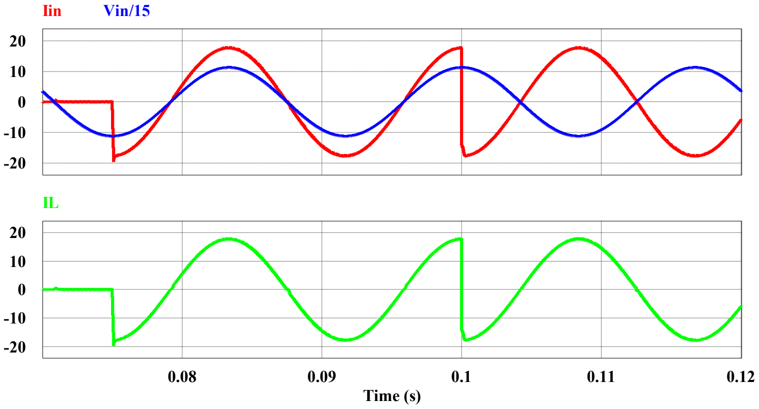

Fig. 4.8. Transient operation and grid synchronized converter.

4.6 Results and Discussion

Simulation and experimental results, loss analysis, efficiency performance, and comparison between proposed topology with conventional two-stage topology are discussed in this section and it is used to validate the proposed topology from the analysis and designed expressions from previous sections.

4.6.1 Simulation Results

The proposed topology is depicted in Fig. 4.1 is simulated using PSIM 11.04 software, and Tables 4.3 and 4.4 provide the input specifications and design parameters of the converter, respectively. The values of devices and components are selected based on the converter design calculation in Section 4.5 and the topology requirements. The circulating power flowing through source current I_{in}, source voltage V_{in}, and source inductor current I_L in both directions is illustrated in Fig. 4.8. The control algorithm is to transfer the I_{in}=17.7A at t =0.07s at initially by usage of P_{ref}=1.50 kVA. The source voltage and source current are synchronized in the unity power factor (UPF) mode. When P_{ref} is changed to -1.5 kVA at t

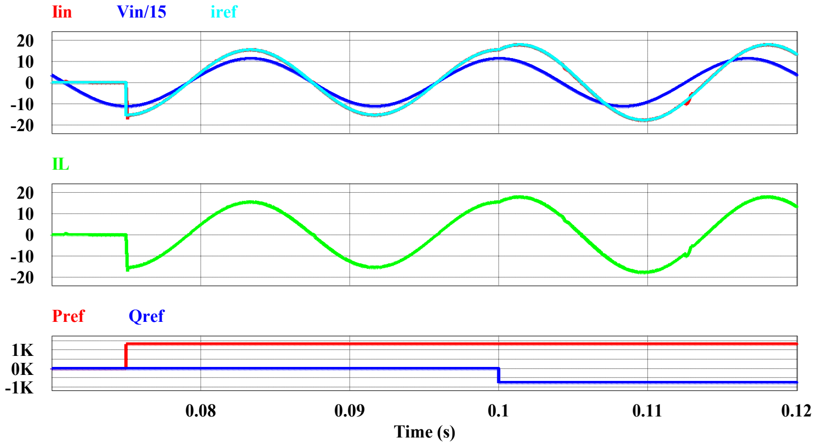

Fig. 4.9. Reactive power shifting converter.

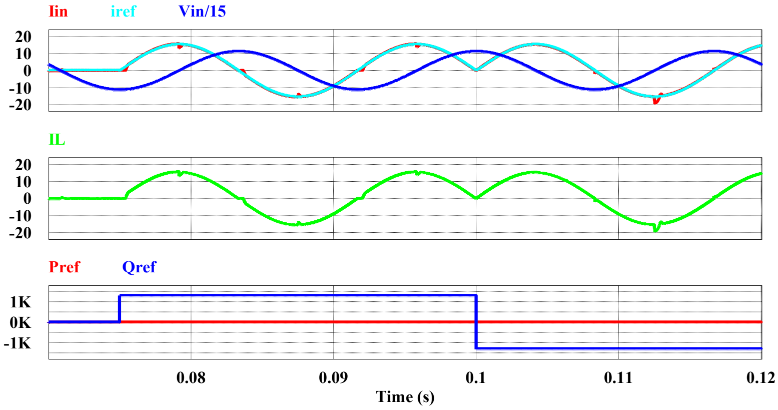

Fig. 4.10. Reactive power compensation.

=0.10s, the source current immediately changes 180^{0} phase-shifted with respect to the source voltage, demonstrating the controller's robust and dynamic execution architecture.

The capacity of the proposed converter to operate in a variety of modes with power flow to provide the flexibility to control the P_{ref} and Q_{ref} in bidirectionally is shown in Fig. 4.9 and 4.10, which interpose reactive power to the converter. In that case, the Q_{ref}=0 kVAr and P_{ref}=1.3 kVA at t =0.07s has to be set. At 1.5 kVA operation, Q_{ref} is changed to -0.7 kVAr at t=0.10s. The proposed topology is utilized for compensating reactive power without charging or discharging the battery, and Fig. 4.10 shows the transfer of reactive power. The proposed topology is employed in all operating modes and offers the flexibility to control the flow of active and reactive power in both directions. Fig. 4.11 illustrates the gate pulses and current flowing through the primary side switches during mode-I and III. It can be clearly observed that zero current switching (ZCS) is achieved by the grid-side switches during G2V

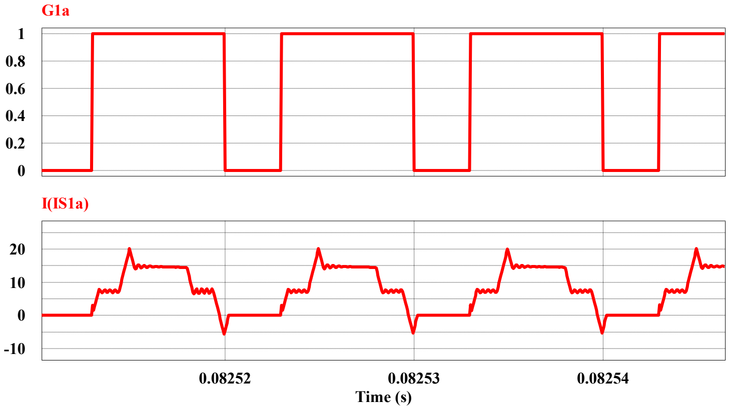

Fig. 4.11. Zero Current Switching (ZCS) of grid side switches.

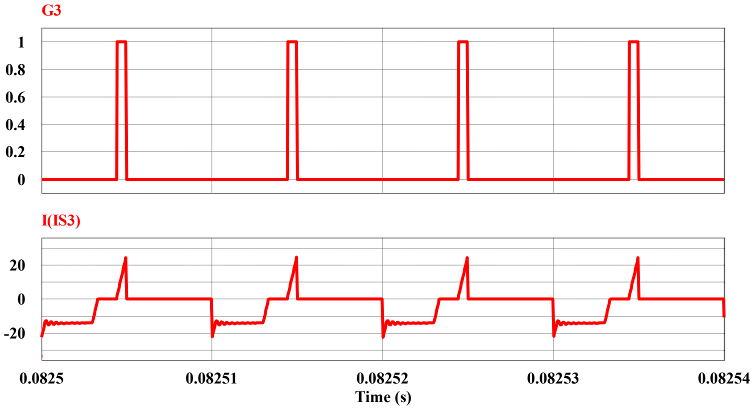

Fig. 4.12. Zero Current turn-ON Switching (ZCS-turn ON) of battery side switches.

mode operation. The grid side switch current reaches zero without the aid of any snubber circuit, additional circuitry, or active clamp just before the gate pulse reaches ZCS. Across the full range of voltage and specified load condition of the proposed converter, the simulation results are verified. Fig. 4.12 demonstrates that the current starts conducting from zero with a positive slope and reaches the ZCS turn-ON of the battery side when the gate pulses is switched-ON.

4.6.2 Experimental Results

An experimental laboratory prototype with a power rating of 1.5 kVA is established to verify the analysis and design of the proposed topology for single-stage EV charger, as shown in Fig. 4.13. The laboratory prototype is constructed using the converter specifications described in Tables 4.3 and 4.4, as well as the component specifications listed in Table 4.5. The gating pulses for the grid side and battery side switches in the proposed topology are

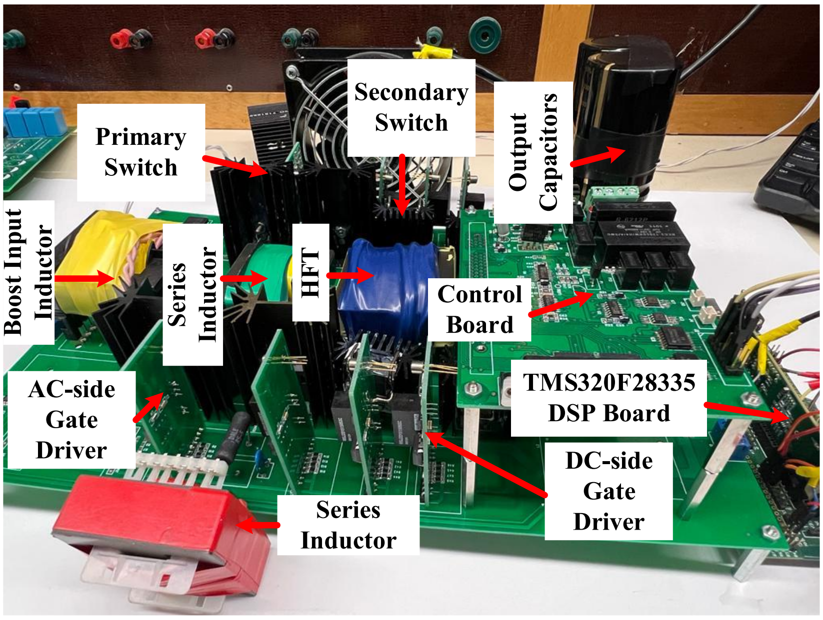

Fig. 4.13. Fabricated hardware prototype demonstration of the proposed topology with 1.5 kW.

Table 4.5: Component Specifications of the Laboratory Prototype

Component	**Specifications**
AC-side switches	CREE-SiC MOSFET, C3M0032120D, 1.2 kV, 63A, 32mΩ
DC-side switches	CREE-SiC MOSFET, C3M0021120D, 1.2 kV, 81A, 21mΩ
Boost Inductor	55 x 28 x 21 EE ferrite Core, 170μH
High Frequency Transformer (HFT)	EE ferrite core, Primary turns, N_1=26, secondary turns N_2=30, L_{lk1}= 1.65μH
Series Inductance	EE ferrite core, L_{lk1} = 13μH, L_{lk1} = 12μH
Output Capacitor	2*1200μF 450V electrolytic capacitor
Gate Driver IC	IC-IXYS-IXDN609SI
DSP Board	TMS320F28335
Power Source	California Instruments AST1503
Voltage Sensor	Broadcom-ACPL-C79
Current Sensor	Allegro ACS714

generated using the TI DSP TMS320F28335 Board, with a 120V rms grid voltage sourced

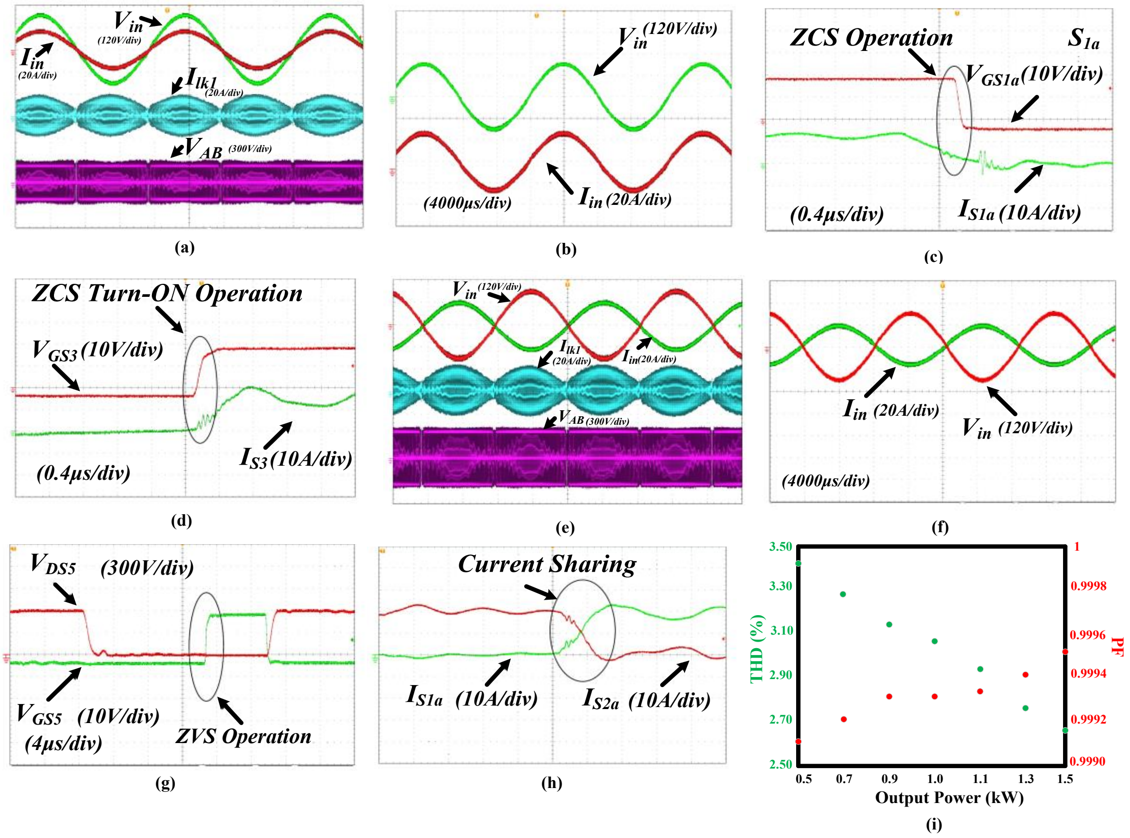

Fig. 4.14. Experimental results at 1.5 kVA (a) Source Current, Source Voltage, HFT Current, HFT Voltage at the primary side with G2V mode of operation; (b) PFC operation at 1.5 kVA; (c) ZCS operation at source side switch S_{1a}; (d) ZCS Turn-ON operation at battery side switch S_3; (e) Source Current, Source Voltage, HFT Current, HFT Voltage at the primary side with V2G mode of operation; (f) Source Current and Source Voltage are out of phase; (g) ZVS turn-ON performance at battery side switch S_5; (h) Sharable current at grid side switches S_{1a} and S_{2a}; (i) The input current THD (%) and power factor at various power levels.

and generated from California Instruments AST1503. The isolated gate-driver circuits for the semiconductor devices are designed with the gate driver IC IXYS-IXDN609SI and Broadcom-ACPL4800 optocoupler. The results of the experiment were carefully analyzed and compared to the digital simulation results.

The proposed isolated ac-dc topology, which is based on wide-band gap (WBG) technology, has been developed, tested, and executed in different modes to recharge the battery application. The experimental results of the high-frequency link isolated AC-DC converter topology at 1.5 kVA have been illustrated in Fig. 4.14. Fig. 4.14(a) and (b) represent the source current and source voltage are completely sinusoidal with each other during the power is exchanged from grid to the vehicle battery of mode-I and mode-III, which includes a high-frequency transformer (HFT) voltage and current within expected ranges. In addition, it ought to be noted that the source current or grid current is closely operates with a power factor to unity (0.999), and that the operating mode maintains a THD of 2.67% (<5% as per IEC 6100-2-2 standard).

In order to demonstrate the negative current that results in the ZCS turn-off operating condition, anti-parallel diodes are driven at the source side switches as the current inherently goes to zero. The grid side switch S_{1a} is shown in Fig. 4.14(c) as being accomplished via ZCS turn-off operation. Likewise, for assuring soft-switching with a mode-III operating conditions, identical experimental waveforms have been observed in the other devices as

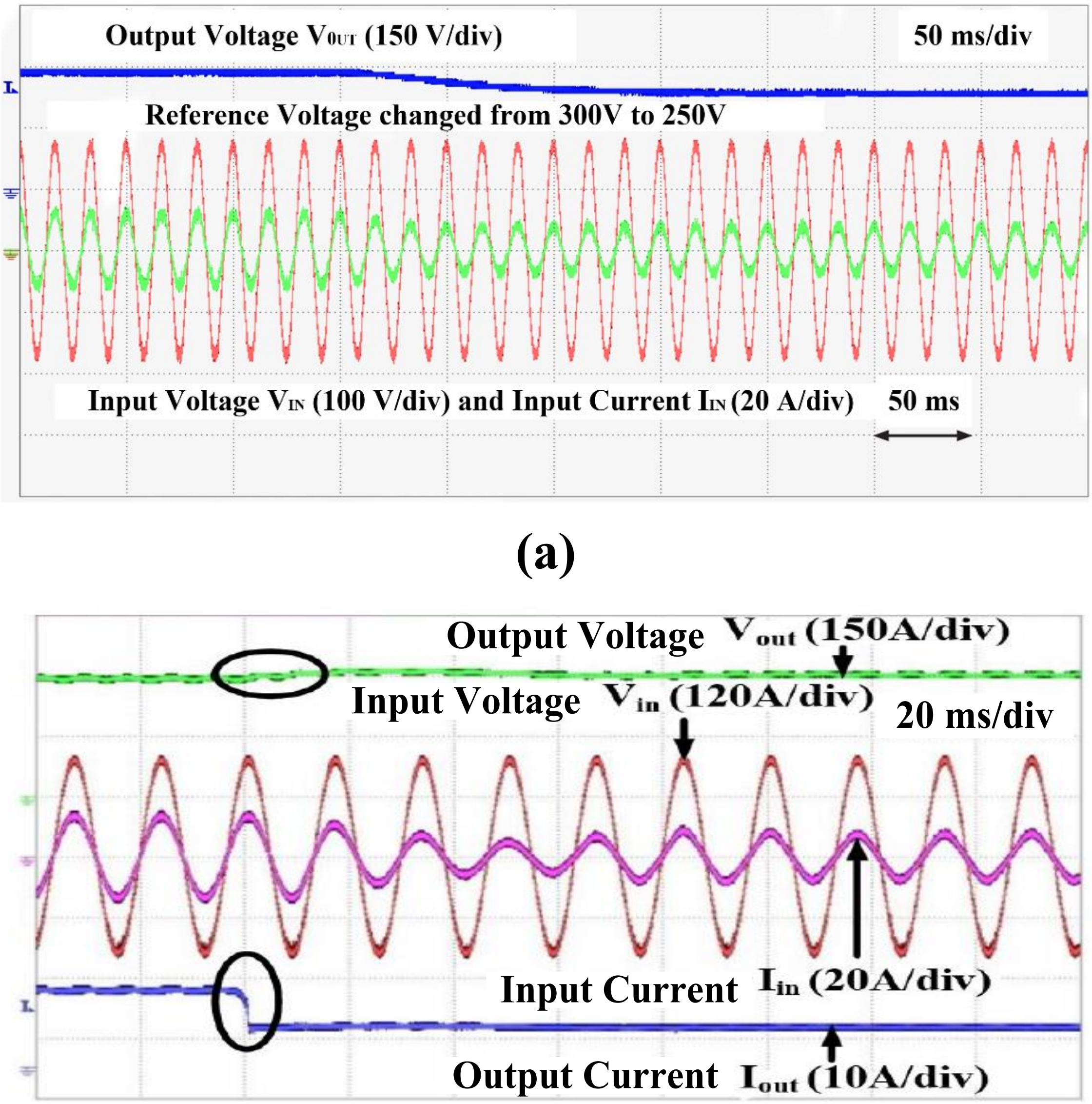

(a)

(b)

Fig. 4.15. Dynamic response of the converter at load change from 100% to 50%.

well. Moreover, the output DC side switch S_3 is triggered when ZCS is turned-ON as shown in Fig. 4.14(d). ZCS turn-ON operation is shown in Fig. 4.14(d), where the current changes from zero to positive when the switch is switched-ON. However, others battery side switches are also accomplished during the operation of mode-III. The experimental results of the vehicle battery to grid (V2G) operational modes are shown in Fig. 4.14(e). Fig. 4.14(e) and (f) exhibit that the source current, and source voltage are out of phase, showing the negative flow of power. In Fig. 4.14(g), it is clearly seen that the output side switches' anti-parallel diodes are operating before the switches are ON condition, causing ZVS turn-ON functioning in mode-II and IV. As illustrated in Fig. 4.14(h), the current is shared across the diodes of source side switches while operation of modes II and IV, which increases the efficiency of the converter. During full-load testing, the proposed topology had a power factor (PF) of 0.9995 and a grid current THD of 2.67%. Fig. 4.14(i) demonstrates the information regarding on the grid current THD (%) and PF of the proposed topology at various output power levels. Both experimental and digital simulation results have depicted the accuracy the design and mathematical analysis of the proposed EV charger.

Fig. 4.15(a) represents the system robustness and dynamic response while changing the output voltage from 300V to 250V with harmonics-free rectifications. In Fig. 4.15(b), the proposed converter has a superior dynamic response when the load is reduced from 100% to 50%, which can be evaluated when the mode alters from constant current (CC) to constant

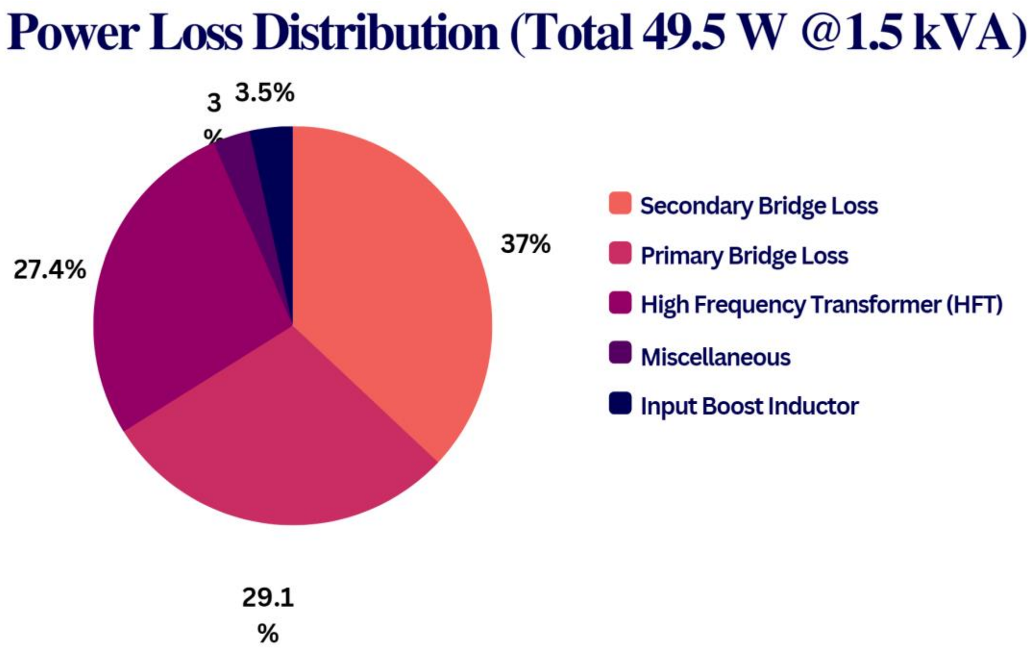

Fig. 4.16. Total power distribution losses at 1.5 kVA.

voltage (CV). Throughout the charging process, a battery operates as a current sink, with CC mode indicating a big load for the charger and CV mode representing a small load. As a result, a battery charger has higher efficiency over the full power range. Due to presence of inherent parasitic elements such as resistance, capacitance, and inductance in the inductors and capacitors of the proposed converter, it causes temporary deviations from the constant current behaviours during transient when the grid voltage zero-crossing, followed by grid-current will also zero-crossing. However, a small damping resistor which is 2.4* V_0/n has been utilized at the grid side switches to alleviate this deviation and the resonance.

A new generation wide band gap (WBG) silicon carbide (SiC) based semiconductor device has been used in the proposed converter. Also, SiC MOSFET has higher electron mobility which results in faster switching and reduced energy losses compared to silicon devices. In addition, SiC MOSFET can operate at high-temperature which allows for a more compact and efficient thermal design, reducing the need for additional cooling requirements. Thence, the selection of a SiC MOSFET with lower on-state resistance can effectively reduce the switching losses which enhances the conversion efficiency in the proposed EV charger topology. A digital control system in power conversion plays a crucial role in optimizing the power transfer between the AC grid and the EV battery. Unlike analog control systems, digital control utilizes TI DSP TMS320F28335 advanced digital signal processor with 32-bit static CMOS high-performance technology for monitoring precisely and adjusting various parameters in real-time with efficient power management and lower power losses, leading to improved efficiency. Also, it provides a faster and more accurate control mechanism with changing operating conditions, flexible adaptive control to achieve optimal efficiency in dynamic EV charging, and to detect and respond to abnormal conditions which prevent system damage. Also, the pie chart in Fig. 4.16 shows the total power distribution at 1.5 kVA for identifying the percentage of losses occurring in various converter components. It is clearly visible that the primary causes of power loss are due to the power semiconductor devices which accounting for over 70% of the total losses. The losses are computed using all information from different components datasheet.

4.7 Conclusion

This chapter studied and investigated on an isolated single-stage bidirectional current-fed push-pull AC-DC converter with PFC for a plug-in EV charging application. With single-inductor and two 4-quadrant switches PFC along with soft-switching is obtained while doing efficient AC-DC conversion. Natural commutation or ZCS is very crucial in current-fed devices to eliminate the turn-off device voltage spike and snubbers associated with voltage clamping. The ZCS turn-off of the grid-side devices is obtained making the topology snubber-less. The implemented modulation is a modified technique, used in current-fed push-pull DC-DC converter, to attain PFC and AC-DC conversion. The developed modulation ensures soft-switching of all semiconductor devices during G2V and V2G modes of operation with active and reactive power flow. The analysis and design of the proposed converter are validated with simulation results from PSIM 11.04. A proof-of-concept hardware prototype of 1.5 kVA is developed and tested to demonstrate the converter performance and the modified modulation. The developed prototype has demonstrated an impressive efficiency of 96.7%, PF of 0.99, and a low THD of 2.67%, which is in good agreement with the analysis.

Chapter 5: Single-Stage Current-fed Derived Isolated DC-DC Converter for Vehicle-to-Vehicle Energy Exchange

5.1 Introduction

Widespread electric vehicle (EV) adoption is critically challenged by the limited range of driving, longer charging duration, and non-availability of charging stations everywhere [157]. The flexibility of the EVs can be enhanced using the vehicle-to-vehicle (V2V) charging system. This system will help in mitigating the range anxiety and also offers emergency charge transfer to another user. According to a report released by Idaho National Laboratory (INL) [158], about 85 % EV owners recharge the EV batteries at their residence. The main reason behind this is the nonavailability of battery charging stations at different locations at present as well as cost. Development of new charging stations involves extra cost and the EVs are limited to locations close to grid infrastructure.

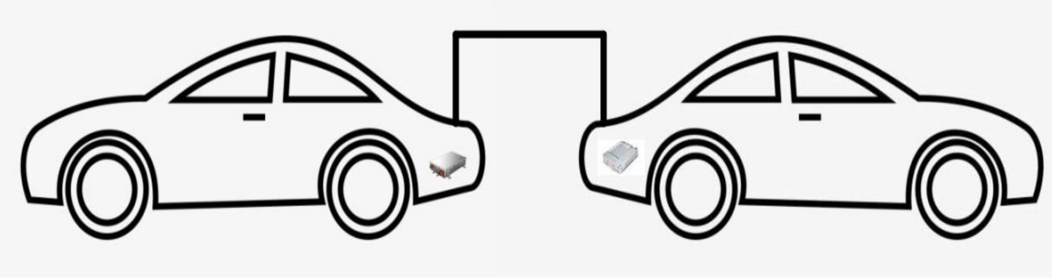

Fig. 5.1. Vehicle-to-Vehicle (V2V) Charging using On-board Chargers.

The energy exchange between EVs can be a viable option in an emergency situation where an EV is about to run out of charge at a location without any charging station nearby, then another EV with enough state-of-charge can transfer the energy required by the first EV. The V2V charging operation is represented in Fig. 5.1. Different EV charging techniques have been reported in literature [159]-[161]. However, very few investigations from power electronics perspective on the domain of V2V charging have been reported.

5.2 Different Vehicle to Vehicle Charging Techniques

This section describes the various charging modes for the V2V power transfer between two EVs [162]-[165].

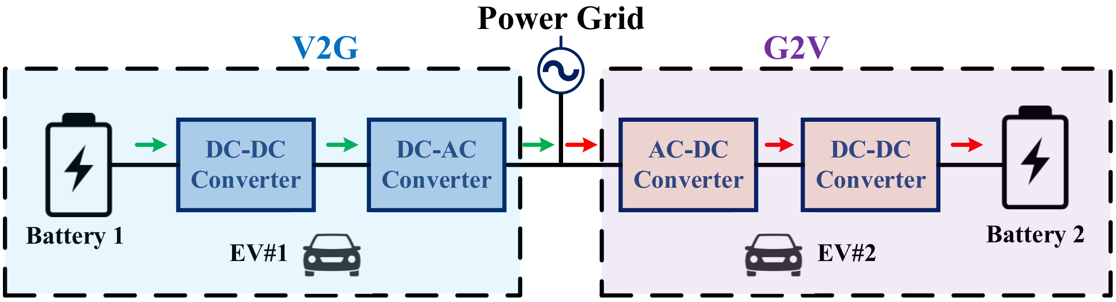

Fig. 5.2. V2G Operation in Combination with G2V Operation.

5.2.1 V2V Power Transfer in AC Mode

The power transfer in AC mode for the V2V charging operation are described below:

(a) Indirect Traditional Approach: In this method, the power grid is used as an intermediate point. Here the V2G operation is combined with G2V

(b) Direct Approach: In this method, the connection to the power grid is not necessary. Here the V2H operation is combined with the G2V operation.

The power transfer takes place between two EVs where EV1 is transmitting power to EV2 in all the considered cases. The battery charger in each of the EV comprises front end AC-DC converter and a back-end DC-DC converter for implementing the V2G and G2V operations, the converters are bidirectional.

5.2.1.1 V2G Operation in Combination with G2V Operation

This method combines the two operational modes of V2G and G2V where both the EVs have a connection to the power grid, which is presented in Fig. 5.2. EV1 is providing the energy and is operating in V2G mode where it injects the stored energy into the batteries to the power grid. EV2 works in G2V mode and recharges the batteries by accepting energy from the grid. The two EVs are in connection with the power grid. The flow of power is controlled by current regulation on the AC side. The current between two EVs has 180 degrees phase-shift. The resultant current of the power grid is zero as the current requirement of EV2 is equal in amplitude to the current generated by EV1 or a set of EVs. The physical meaning is that the energy requirement for recharging EV2 batteries is completely furnished by EV1. Therefore, the power grid does not get overloaded, which represents the critical aspect of V2V operation.

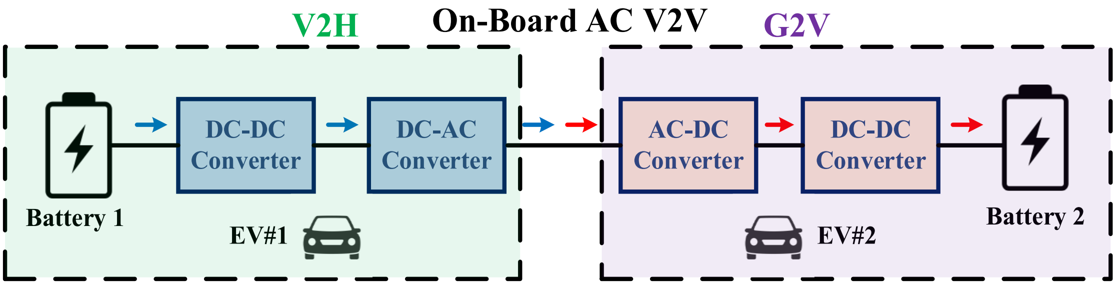

Fig. 5.3. V2H Operation in combination with G2V Operation.

5.2.1.2 V2H Operation in Combination with G2V Operation

On the contrary to the previous case, there is a possibility of direct V2V transfer of power utilizing AC power. The V2H mode of operation is an aspect of isolated systems in which there is no connection to the power grid. In this case, an EV is regulated to generate AC voltage to give energy to the electrical loads. The method can be utilized for V2V power transfer where EV1 acts as the AC voltage source work in V2H mode as depicted in Fig. 5.3 and the EV is feeding from it working in G2V mode where the current and voltage are in-phase. The difference between the traditional and direct method is that in the latter there is no power grid connection. As there is no grid connection in the second method, it is considered as direct method because the two EVs are only connected to each other and there is a direct V2V power transfer between them. This approach is a good option when the batteries of the EVs are completely discharged and there is no possibility to move.

5.2.2 V2V Power Transfer in DC Mode

This section describes the methods of DC mode V2V power transfer. There are several advantages to the direct V2V power transfer in AC mode, which combines the V2H and G2V modes. But there are four power conversion stages in AC V2V power transfer irrespective of direct or traditional method. As the batteries are charged using DC power, there is an advantage in connecting the EVs using the DC terminals. This can be implemented using the following methods:

(a) On-board DC-DC converter: In this method, both the EVs will have on-board DC-DC converter and the power will be transferred by establishing a back-to-back connection between them.

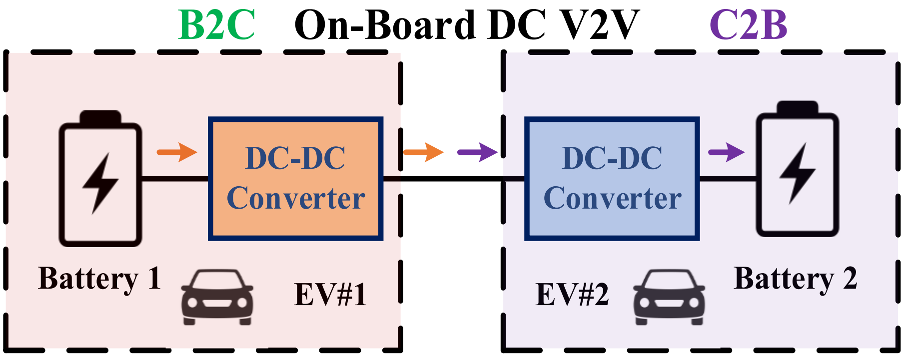

Fig. 5.4. V2V Charging using On-board DC-DC Converter.

(b) Off-board DC-DC converter: In this method, an external DC-DC converter is used to connect the battery terminals in both the EVs.

5.2.2.1 V2V Charging using On-board DC-DC Converter

A bidirectional power flow is allowed in the on-board EV battery charger so that the V2G and G2V operations can be implemented. Therefore, the DC-DC converter for the battery chargers permits the batteries to be charged and discharged with current or voltage control. Suppose a second DC-DC converter is joined at the output of the first DC-DC converter and both the dc-dc converter can operate in bidirectional mode then a power exchange is possible between the two EVs batteries. This is outlined in Fig. 5.4. The cascaded DC-DC converter permits bidirectional operation with a regulated charging current in a varied operating voltage range. There is a possibility to charge batteries having higher voltage using lower voltage batteries. The EV connections should be using the DC links for such condition. The DC link nodes are common to both the DC-DC and AC-DC converters for each charger. Thus, the external plug that is connected to enable the V2V power transfer in DC mode do not require any additional power converters or hardware.

5.2.2.2 V2V Charging using Off-board DC-DC Converter

The V2V power transfer is possible using an off-board DC-DC converter instead of an onboard charger. This is a useful method when there is a need of galvanic isolation or in situations when there is a significant voltage difference in EV batteries. In such cases, the EVs should be interfaced directly to the batteries and is shown in Fig. 5.5. The on-board battery charger operation is not required in such a case because as the off-board DC-DC converters permit the operation using regulated current or voltage. An off-board charger does not require a power source as each of the terminals are connected to the batteries of each EV.

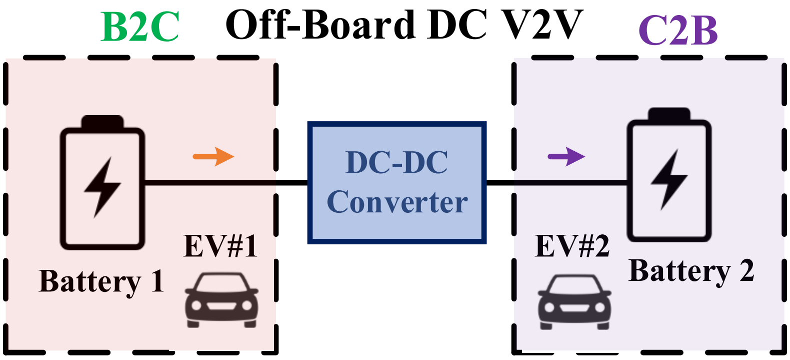

Fig. 5.5. V2V Charging using Off-board DC-DC Converter.

Thus, to enable this mode of operation, the power plug must comprise of power semiconductors and high frequency transformer. Though there is no requirement to use the on-board EV chargers, which is an advantage to the EVs but the external DC-DC converter for off-board V2V EV charging comprises extra cost in comparison to the on-board charging solution. Therefore, this Chapter presents a novel V2V charge transfer using the proposed converter where only the on-board charger of the EV to be charged is utilized for charging the EV battery.

5.3 Proposed Converter Working in DC Charging Mode

In this chapter, a novel zero current switched secondary-modulation enabled single-phase single-stage naturally clamped snubber-less isolated DC-DC converter is utilized for V2V DC charge transfer technique as per shown in Fig. 5.6. When compared to existing AC and DC charging procedures, this method uses a smaller number of power conversion stages because it just uses the on-board charger of the EV that needs to be charged to the EV battery. Additionally, this method only uses one on-board charger with single-stage, which gives it an advantage over other V2V charging techniques that normally use two-stage. The charger satisfies the requirements for an on-board charger by being compact in size, high power density, and lower cost. Also, this converter has more advantageous than other V2V DC chargers are, such as lower duty cycle loss, lower high-frequency (HF) transformer turns ratio, lower current ripple, less circulating current which leads to low RMS and peak current, and snubber-free or without active-clamp or snubber circuits. Also, a novel modulation technique has been proposed for this configuration which gives results as: 1) lower switching losses: zero current turn-on at the secondary or output side switches and zero current at the primary or input side switches; 2) Alleviating the traditional voltage-spike problems in primary and secondary switches with ZCS method and limiting the RMS current which leads

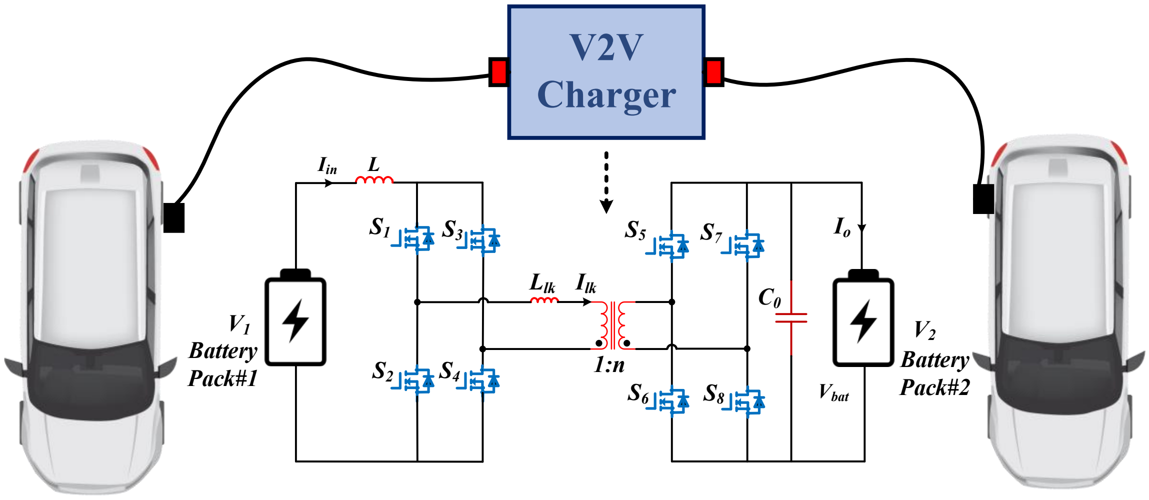

Fig. 5.6. Single-Stage Single-Phase V2V EV Charger.

to higher efficiency; 3) Snubber-less inherently clamped soft-switching is tracked and maintained during the full operation.

The article is organized as follows: V2V DC-DC converter configuration and steady state analysis in DC charging mode is proposed in Section 5.4. Section 5.5 describes the design of the converter for V2V charge transfer. In Section 5.6, the simulation results are demonstrated. The hardware laboratory prototype has been developed and experimental results are reported in section 5.7. Section 5.8 concludes this paper.

5.4 Converter Steady-State Analysis and Operation for V2V DC Charge Transfer

The detailed steady-state analysis and operation of the ZCS concept are explained and articulated in this section. Two diagonal switches of the output side (secondary side) are turned-ON just before taking out the gating pulses of the input side (primary side) switches, and the reflected output voltage V_0/n visible at the primary side of HFT. As a result of this, the current is redirected from the input side switches to the HFT which lead to the current of the HFT is to rise and the input side switches current to fall until it becomes null. The gating pulses are withdrawn once the current drops below null, and the body diodes at the switches commences conducting, resulting in ZCS turn-off operation. To ensure output voltage stability and power exchange control, fixed-frequency duty-cycle (FFDC) modulation technique is adopted.

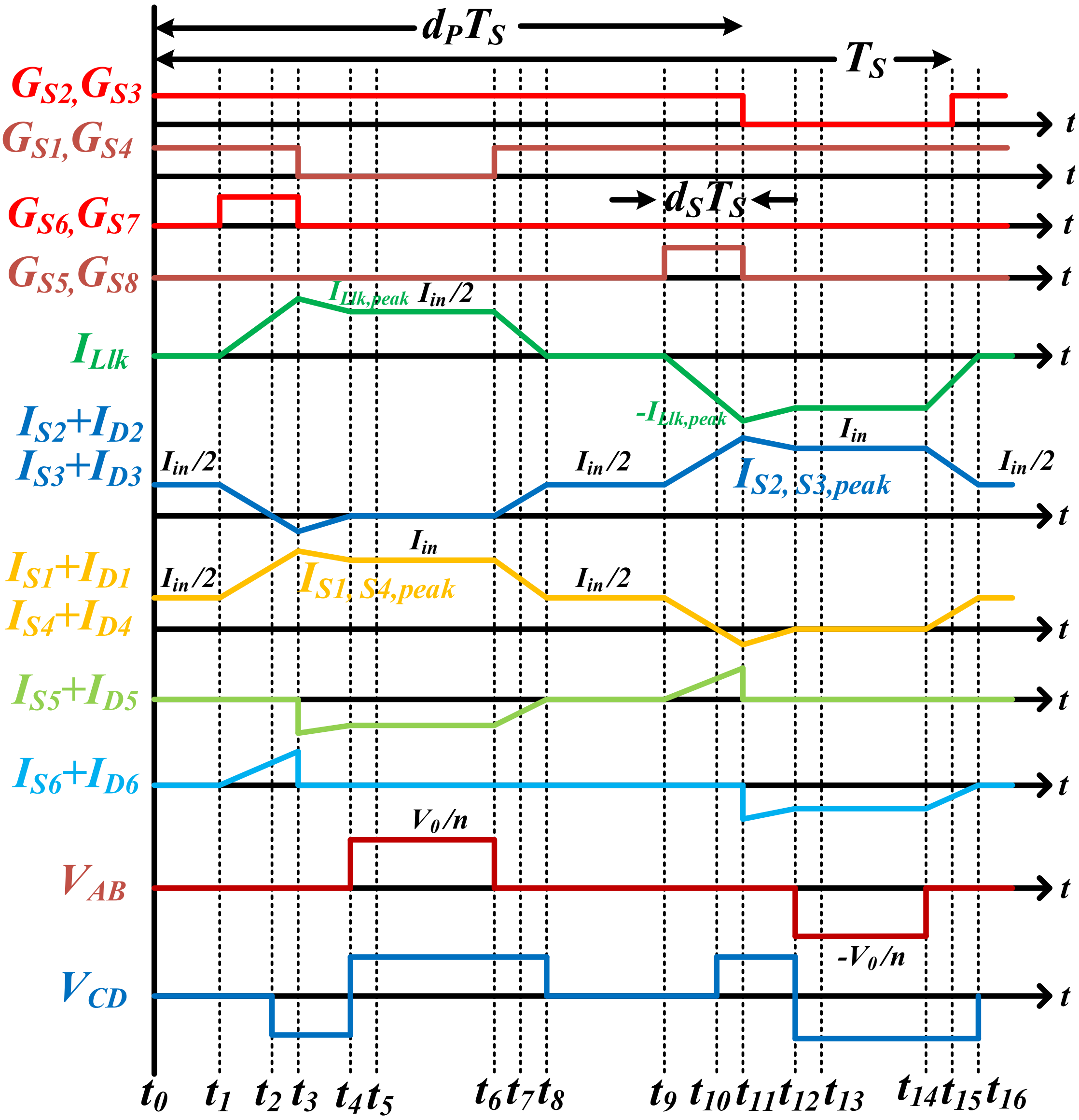

Fig. 5.7. Operational waveforms-I of the DC-DC converter for V2V charging.

The operating waveforms of V2V charger in steady-state are displayed in Fig. 5.7. The gating signals are used to control the input side switches S_1, S_4 and S_2, S_3 and are phase-shifted by 180^0 with an overlap across the legs at the conduction time. The d_P (should be > 0.5) and d_S (should be < 0.5) are the duty ratios of the input side and output side devices, respectively. The amount of overlap in the gating pulses changes based on the value of duty ratio, which is determined by the input voltage and load characteristics. As depicted in Fig. 5.7, the duty cycle of the secondary side devices S_5 and S_8 is d_S, and they are switched-off synchronously with devices of the primary side S_1 and S_4. Likewise, the turn-off of the device

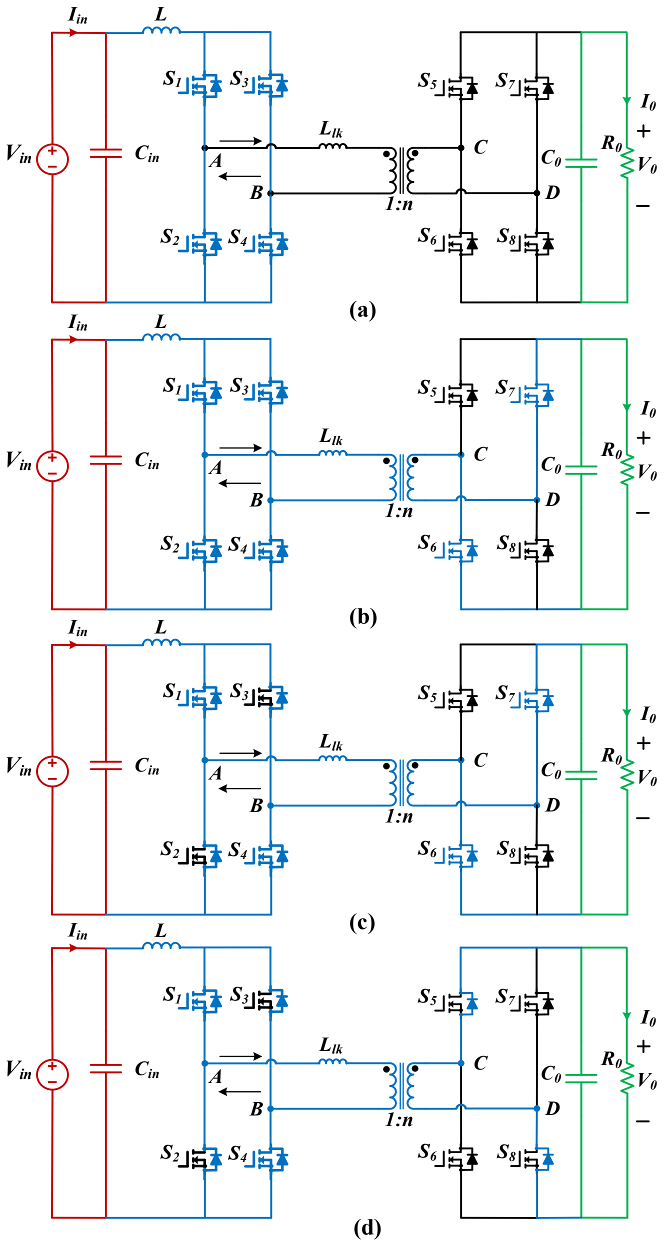

Fig. 5.8. Equivalent circuits while various intervals of operation of the converter-I.

S_2 and S_3 are synchronized with the turn-off with the devices of S_6 and S_7. A few assumptions have been made to make the analysis more easy and under-stable of V2V charger, which are exhibited as below:

(a) Input boost inductor (L) with a big enough value to guarantee that the input ripple current (I_L) remains as minimum.

(b) All the semiconductor devices are lossless and ideal.

(c) The HFT has a large magnetizing inductance (L_{lk}).

(d) Throughout one switching cycle of the converter, the input voltages (V_{in}) and output voltages (V_0) are presumed to remain constant.

(e) The output voltage is regulated by capacitor in the output filter (C_0), which have a high capacitance value.

By using equivalent circuits of the proposed V2V charger shown in Fig. 5.8 and 5.9, the operation of the converter throughout different intervals in a half high frequency (HF) cycle can be elucidated.

Mode-1: ($t_0 < t < t_1$)

In Mode-1, the input current (I_{in}) is flowing through the input side switches S_1, S_4 and S_2, S_3 as they conduct simultaneously which is shown in Fig. 5.8(a). The output capacitor is responsible for supplying power to the load. By utilizing the given equations as follows, one can ascertain the currents passing through different primary side components.

$$I_L = I_{\text{in}} \tag{5.1}$$

$$I_{S1} = I_{S2} = I_{S3} = I_{S4} = \frac{I_{\text{in}}}{2} \tag{5.2}$$

Mode-2: ($t_1 < t < t_2$)

In Mode-2, the activation of output side switches S_6 and S_7 occurs at $t = t_1$ which is shown in Fig. 5.8(b). This conduction causes the voltage V_0/n to emerge across the input side of HFT, initiating the buildup of leakage inductor current I_{Llk} of HFT. Consequently, the input boost inductor current I_L, which was originally passing through devices of S_2 and S_3, is redirected towards the primary winding of HFT. Consequently, there is a linear decline in the current of the input side switches S_2 and S_3, whilst the current I_{Llk} is gradually increases. The following provided equations offer insight into the currents that traverse various elements in the converter.

At the completion of this mode, the current in the devices of S_2 and S_3 diminish to zero, resulting in its ZCS turn-off condition, despite the ongoing gating pulses. Meanwhile, the currents of devices S_1, S_4, and L_{lk} attain values of I_{in}.

$$I_{Llk} = \frac{V_o}{n \cdot L_{lk}}(t - t_2) \tag{5.3}$$

$$I_{S2} = I_{S3} = I_{in} - \frac{V_o}{2.n \cdot L_{lk}}(t - t_2) \tag{5.4}$$

$$I_{S1} = I_{S4} = I_{in} + \frac{V_o}{2.n \cdot L_S}(t - t_2) \tag{5.5}$$

$$I_{S6} = I_{S7} = \frac{I_{in}}{n} + \frac{V_o}{n^2 \cdot L_{lk}}(t - t_2) \tag{5.6}$$

Mode-3: ($t_2 < t < t_3$)

With commencing at $t = t_2$, the antiparallel diodes D_2 and D_3 of devices S_2 and S_3 becomes conductive as demonstrated in Fig. 5.8(c). Consequently, the currents passing through the HFT, as well as switches S_1, S_4, S_6, and S_7 progressively increase at the same rate. At the culmination of this mode, denoted by $t = t_3$, both I_{Llk} and the currents of devices S_1 and S_4 achieve their peak magnitudes. It is worth mentioning that the magnitude of these peaks depends on the duration of the gating pulses G_6 and G_7 applied to the output side devices.

Mode-4: ($t_3 < t < t_4$)

When $t = t_3$, output side devices S_6 and S_7 are deactivated. This prompts the current on the output side to be taken over by antiparallel diodes D_5 and D_8, which are positioned across output side devices S_5 and S_8, respectively. As a result, a negative voltage of $-V_0/n$ materializes across the input side of the HFT, causing the current I_{Llk} to commence a decline from its peak level as shown in Fig. 5.8(d).

$$I_{\text{lk}} = I_{\text{lk,peak}} - \frac{V_o}{n \cdot L_{\text{lk}}} \cdot (t - t_4) \tag{5.7}$$

$$I_{S1} = I_{S4} = I_{\text{sw,peak}} - \frac{V_o}{2.n \cdot L_{\text{lk}}} \cdot (t - t_4) \tag{5.8}$$

$$I_{D2} = I_{D3} = I_{D2\text{,peak}} - \frac{V_o}{2.n \cdot L_{\text{lk}}} \cdot (t - t_4) \tag{5.9}$$

$$I_{D5} = I_{D8} = \frac{I_{\text{lk,peak}}}{n} - \frac{V_o}{n^2 \cdot L_{\text{lk}}} \cdot (t - t_4) \tag{5.10}$$

At $t = t_4$, the current passing through diodes D_2 and D_3 inherently drops down to null. Meanwhile, the current I_{Llk} and currents through devices S_2 and S_3 reach levels of I_{in}.

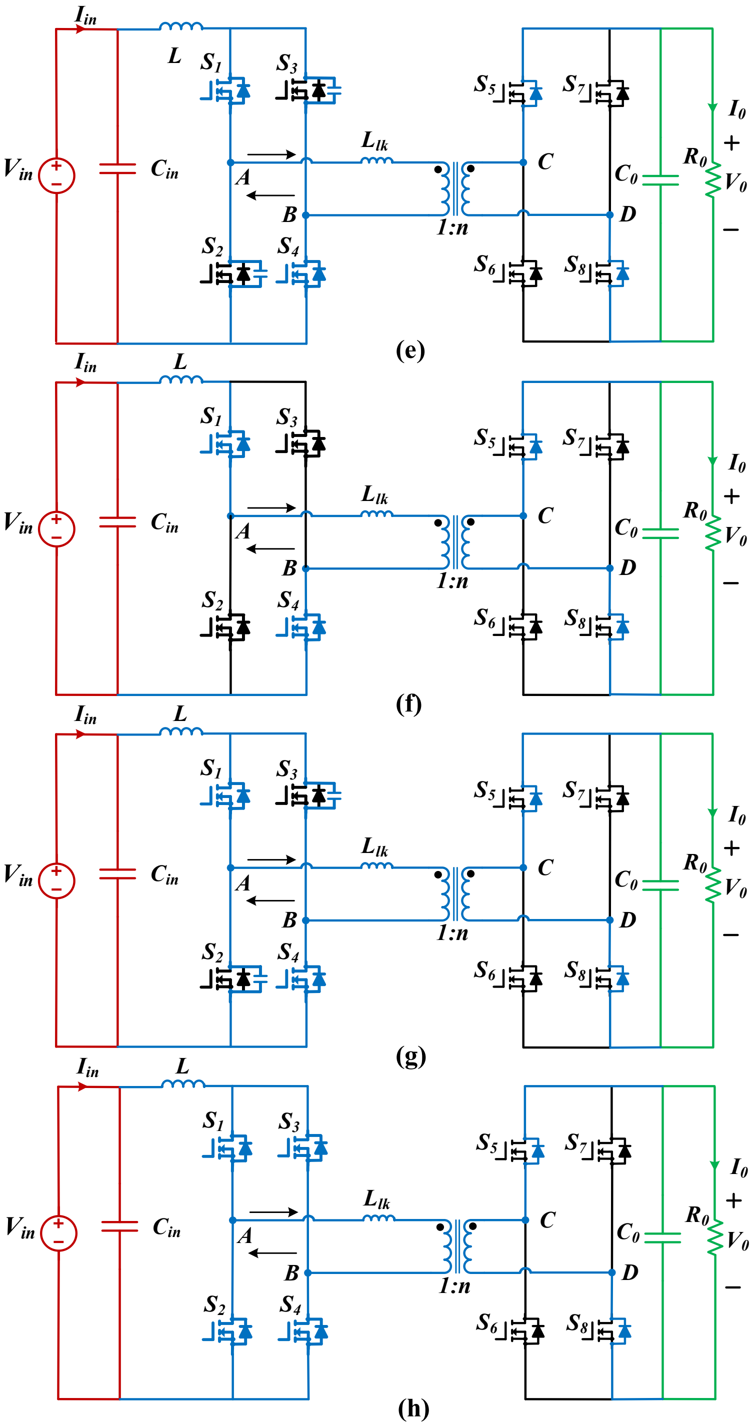

(e)

(f)

(g)

(h)

Fig. 5.9. Equivalent circuits while various intervals of operation of the converter-II.

Mode-5: ($t_4 < t < t_5$)

From Fig. 5.9(e), during this mode, the snubber capacitor across the input side devices S_2 and S_3 rapidly accumulate charge and reaches the voltage level of V_0/n. This phase is small, and the rate of charging is controlled by the series snubber resistance.

Mode-6: ($t_5 < t < t_6$)

In this mode, the input voltage of the HFT remains at zero, causing a consistent current of I_{in} to flow through its input side winding. The semiconductor devices S_1 and S_4 handle the entire input current I_{in}, while the antiparallel diodes D_5 and D_8 enable the charging of the output capacitor C_0 with a constant current of I_{in}/n as per Fig. 5.9(f). The gating pulses G_1-G_8 are assigned to devices S_1-S_8 in the given order.

Mode-7: ($t_6 < t < t_7$)

At $t = t_6$, the input side devices S_2 and S_3 are switched ON condition, leading to the discharge of the snubber capacitor through the series snubber resistance which is shown in Fig. 5.9(g). This discharge process causes the switch voltage to progressively diminish and eventually reach null within a short duration.

Mode-8: ($t_6 < t < t_7$)

A negative voltage of $-V_0/n$ becomes present across the input side of the HFT, leading to a descent in the input side current from its initial value of I_{in} during this mode which can shown in Fig. 5.9(h). The initiation of an increase in current through devices S_2 and S_3 indicate the transfer of current I_{Llk} from the HFT. This moment denotes the zero-current turn-on operation of devices S_2 and S_3. When t reaches t_8, the I_{Llk} current reduces to null, and the current of devices current S_2 and S_3 rises to I_{in}. The current flowing through elements can be determined using the following equations.

$$I_{\text{lk}} = -I_{\text{in}} + \frac{V_o}{n \cdot L_{\text{lk}}} \cdot (t - t_7) \tag{5.11}$$

$$I_{S1} = I_{S4} = \frac{V_o}{2n \cdot L_{\text{lk}}} \cdot (t - t_7) \tag{5.12}$$

$$I_{S2} = I_{S3} = I_{\text{in}} - \frac{V_o}{2n \cdot L_{\text{lk}}} \cdot (t - t_7) \tag{5.13}$$

$$I_{D6} = I_{D7} = \frac{I_{\text{in}}}{n} - \frac{V_o}{n^2 \cdot L_{\text{lk}}} \cdot (t - t_7) \tag{5.14}$$

The end of this interval signifies the completion of a half high-frequency (HF) switching cycle. The intervals are repeated in a similar fashion in next half cycle, with other symmetrical switches taking turns to conduct and complete the full HF cycle.

Table 5.1: Converter Specifications

Parameter	**Value**
Input Voltage, V_{in}	170V (rms)
Input Current, I_{in}	17.76 A
Output voltage, V_o	300 V
Output power, P_o	1500W
Switching frequency, f_{sw}	100 kHz

5.5 Design of the Converter

This section describes the procedure for designing of the proposed single-phase single-stage current-fed DC-DC converter for vehicle-to-vehicle charging application. The parameters include: Input voltage V_{in}=170 V, Output voltage V_0=220-330 V, Output power P_o=1.5 kW, nominal output voltage = 300 V, and switching frequency f_s=100 kHz. The following presented design equations assist in determining the ratings of the components used in the proposed converter. This information is beneficial in the selection process of components and estimating the performance of the converter as theoretically and practically.

22) The input current I_{in} is calculated by,

$$I_{in} = \frac{P_o}{n.V_{in}} \tag{5.15}$$

Presuming an ideal efficiency η=100%.

23) The maximum allowable voltage across at the switches of the primary side is,

$$V_{SW,P} = \frac{V_0}{n} \tag{5.16}$$

Where n is the high-frequency transformer (HFT) turns-ratio.

24) The high-frequency transformer (HFT) turns ratio is given by,

$$n = \frac{2.V_0.(1 - d_P)}{V_{in}} \tag{5.17}$$

Where d_P is the duty cycle of the primary side switches.

Table 5.2: Converter Design Parameters

Parameter	**Value**
Input Boost Inductor, L	170μH
Leakage Inductance of L_s	6.5μH
Turns ratio, n	1.2
Output Capacitor, C_0	$2*1200\mu$F

25) The leakage series inductance L_{lk} of HFT is required to yield ZCS with operating requirements necessities and it can be computed as,

$$L_{lk} = \frac{V_0 . (d_P - 0.5)}{2. I_{in} . f_s . n} \tag{5.18}$$

Where f_s is the switching frequency of the converter. Although the experimental value of L_{lk} is slightly lower than the design value, it is still enough to ensure ZCS operation within the boundary of operation. Additionally, this has a substantial effect on the peak current of the primary side switches, but it matches the designed calculation as well.

26) The input boost inductor L can be calculated according to the specification for input current ripple,

$$L = \frac{V_{in} . d_P}{\Delta I_L . f_s} \tag{5.19}$$

The peak-to-peak current value of the input boost inductor is denoted by ΔI_L, where ΔI_L=1. To achieve maximum converter efficiency and utilization factor, it is critical to choose the ideal boost inductor value that minimizes conduction losses.

27) The relationship between input voltage V_{in} and output voltage V_0 is given as,

$$V_0 = \frac{n. V_{in}}{2. (1 - d_P)} \tag{5.20}$$

28) The duty cycle of the secondary side switches d_S is a crucial factor that determines the zero-current-switching (ZCS) condition of the primary side switches, and it can be expressed as follow,

$$d_S \geq \frac{I_{in} . f_S . n . L_{lk}}{V_0} \tag{5.21}$$

The peak-to-peak current value of the input boost inductor is denoted by ΔI_L, where ΔI_L=1. To achieve maximum converter efficiency and utilization factor, it is critical to choose the ideal boost inductor value that minimizes conduction losses.

29) For determining the RMS and peak values of the primary side switches, the following equation is used and calculated as,

$$I_{P,peak} = \frac{I_{in}}{2} + \frac{V_0 . d_S}{L_{lk} . f_s . n} \tag{5.22}$$

$$I_{P,RMS} = I_{in}\sqrt{\frac{9 + 4. d_S - 6. d_P}{12}} \tag{5.23}$$

30) The RMS and peak values of the secondary side switches can be obtained as,

$$I_{s,peak} = \frac{V_0 . d_S}{n^2 L_{lk} . f_s} \tag{5.24}$$

$$I_{s,RMS} = \frac{I_{in}}{n}\sqrt{\frac{9 + 4. d_S - 6. d_P}{12}} \tag{5.25}$$

In order to achieve reliable operation, it is important for the maximum voltage of the secondary side switches to exceed the maximum output voltage, which is indicated by $V_{SW,S} \geq V_{0,max}$.

31) The primary side of the high frequency transformer (HFT) has peak and RMS values that can be expressed as,

$$I_{PT,peak} = \frac{V_0 . d_S}{L_{lk} . f_s . n} \tag{5.26}$$

$$I_{PT,RMS} = I_{in}\sqrt{\left[\frac{1 - d_P}{2} + \frac{d_S}{3}\right]} \tag{5.27}$$

32) The secondary side of the high frequency transformer (HFT) has peak and RMS values that can be calculated as,

$$I_{ST,peak} = \frac{V_0 . d_S}{L_{lk} . f_s . n^2} \tag{5.28}$$

$$I_{ST,RMS} = \frac{I_{in}}{n}\sqrt{\left[\frac{1-d_P}{2}+\frac{d_S}{3}\right]} \tag{5.29}$$

33) The calculation of primary and secondary turns of the HFT is carried out by,

$$N_P = \frac{V_0.(1-d_P)}{2.A_C.f_s.n.B_m} \tag{5.30}$$

$$N_S = \frac{V_0.(1-d_P)}{2.A_C.f_s.B_m} \tag{5.31}$$

The maximum magnetic flux density of the core is indicated by B_m, and the cross-sectional area of the core is denoted by A_C, both of which are important factors for the HFT.

$$A_f.J_f.K_f = N_P.I_{PT,RMS} + N_S.I_{ST,RMS} \tag{5.32}$$

The core area of the HFT can be determined using equations (5.29) to (5.32), which incorporate the frame winding's cross-sectional area A_f, frame winding utilization ratio K_f, and frame current density J_f. It is computed as,

$$A_f.A_C = \frac{2.V_0.(1-d_P).I_{PT,RMS}}{K_f.J_f.f_s.n.B_m} \tag{5.33}$$

34) The output capacitor C_0 is obtained as,

$$C_0 = \frac{I_0.(1-d_P)}{\Delta V_0.f_s} \tag{5.34}$$

Whereas, ΔV_0 is the output voltage ripple range.

5.6 Simulation Results of V2V Charger

The proposed V2V charger has been designed and simulated as per specifications of Table 5.1 and 5.2 using PSIM 11.04 software to ensure that it meets the desired performance and theoretical analysis. The steady-state behavior of the converter with the specified parameters and design characteristics, which are rated for 1.5 kW power. Fig. 5.10 and 5.11 exhibit the simulation results of the proposed converter in DC charging strategy.

The DC input voltage V_{in} and input current I_{in} are depicted in Fig. 5.10(a). Also, Fig. 5.10(b) affirms the DC output current I_0 and the DC output voltage V_0 at rated output power

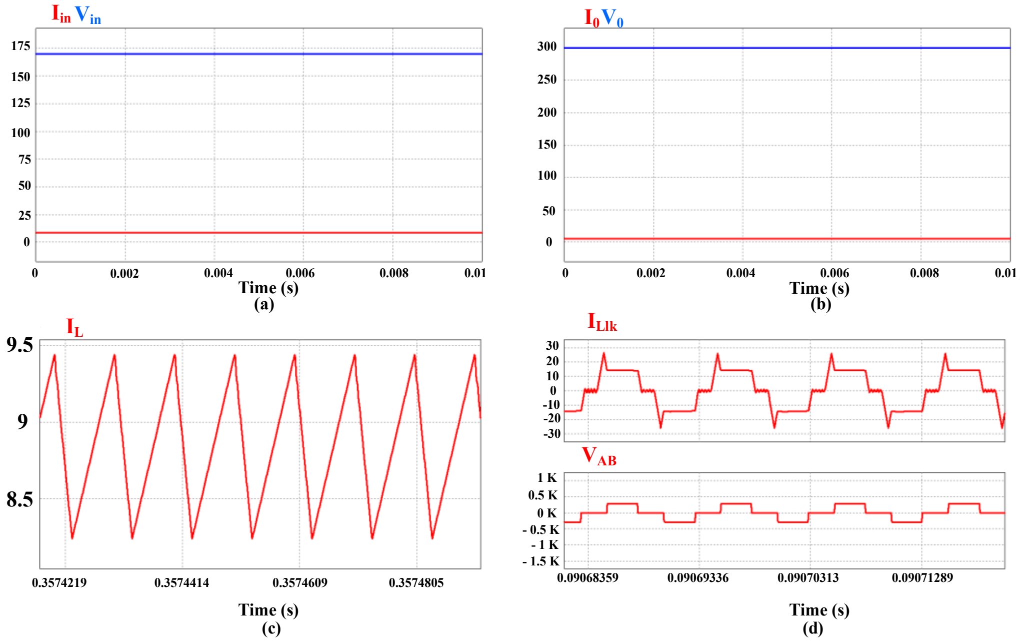

Fig. 5.10. Simulation results of V2V chargers from PSIM 11.04 Software at P_o=1.5 kW; (a) DC input voltage V_{in} and DC input current I_{in}. (b) DC output current I_0 and the DC output voltage V_0. (c) Input boost inductor current I_L. (d) Leakage series inductor current waveform I_{Llk} and voltage waveform V_{AB} at primary side.

1.5 kW. The output voltage V_0 is clearly observed to stabilize precisely at 300V in Fig. 5.10(b). Fig. 5.10(c) shows the current waveform for the input boost inductor L. The input boost inductor current I_L ripple frequency is twice of device switching frequency f_s, leading to a smaller in size. Moreover, the peak current I_{Llk} through inductor L_{lk} above the constant value is due to the extended enable of the anti-parallel body diodes of the corresponding primary semiconductor devices, which ensures ZCS turnoff operation as shown in Fig. 5.10(d). The continuous current has the lower peak value. Furthermore, according to the voltage waveform V_{AB}, the voltage across the main devices is inherently capped at low voltage, $V_0/\ n$.

The current through the primary and secondary switches and its corresponding gate signals while the operation of the converter during the DC charging mode is shown in Fig. 5.11. The primary switch current reaches zero inherently without requiring any external circuitry before removing the gate signal, thereby achieving ZCS turn-off operation as shown in Fig. 5.11(a). This is applicable and accurate for all voltage and load ranges configurations, as discussed in the converter design section 5.2. The current through the secondary side devices during V2V charging is depicted in Fig. 5.11(b) along with its gate signal. The gate signal enables the

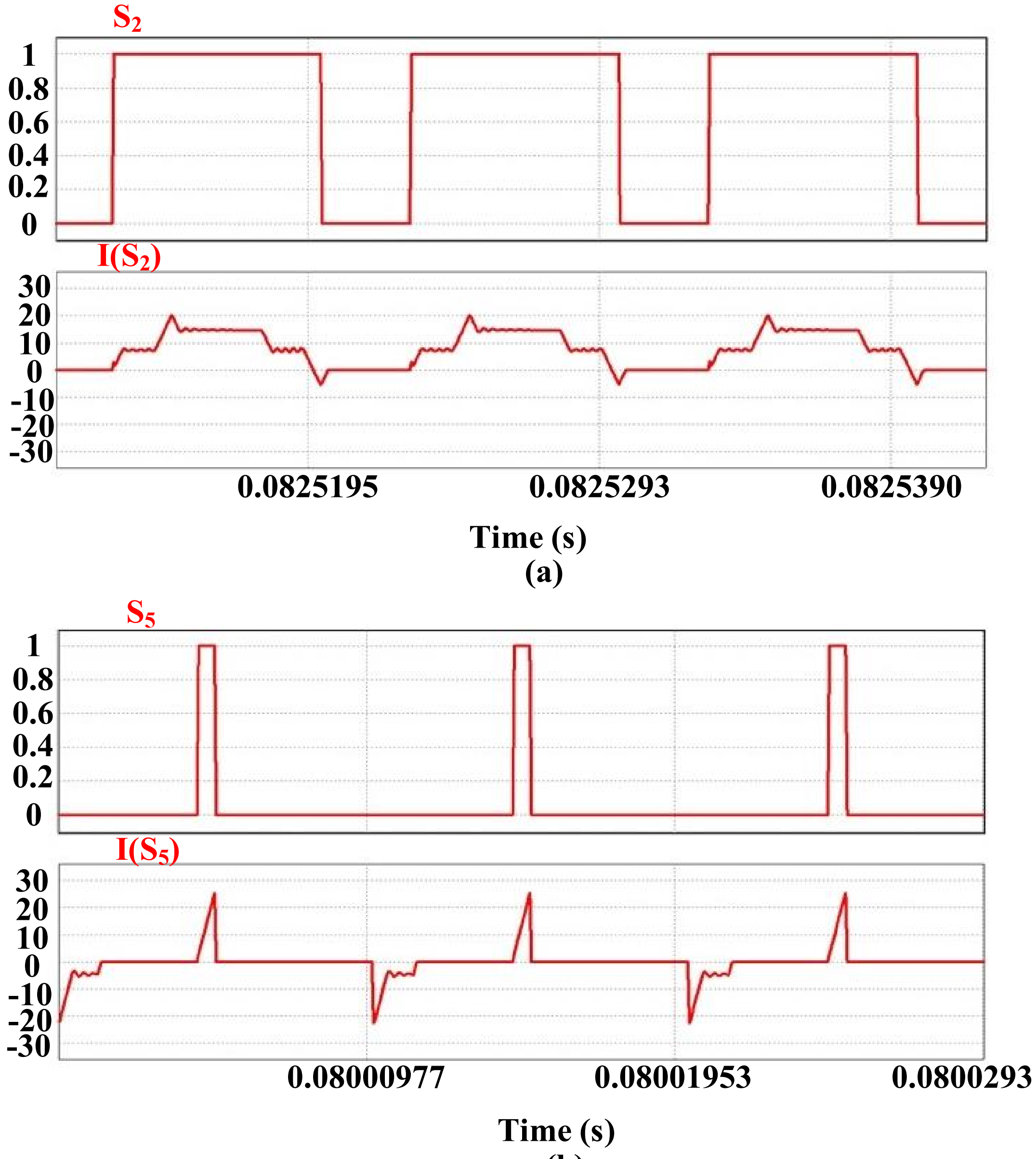

(a)

(b)

Fig. 5.11. (a) Simulation results of ZCS operation at primary side devices. (b) Simulation results of ZCS turn-on operation at secondary side devices.

devices to turn-on gradually until achieving zero current turn-on (ZCS turn-on) condition. The waveforms displayed in Figs. 5.10 and 5.11 which are precisely match with the expected results predicted by theoretical analysis, demonstrating to verification of the accuracy of the proposed secondary side modulation strategy and the steady-state operation with its design of the converter as discussed in Section 5.1 and Section 5.2.

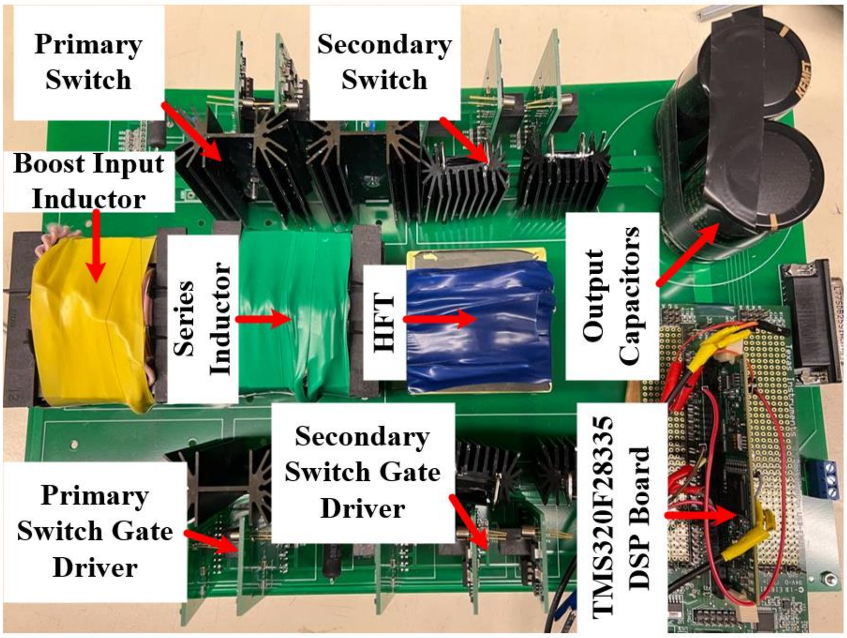

Fig. 5.12. V2V Charger laboratory hardware prototype.

Table 5.3: Hardware Components Specifications

Component	Specifications
Primary-side switches	CREE-SiC MOSFET, C3M0045065D
Secondary-side switches	CREE-SiC MOSFET, C3M0025065D
Boost Inductor	55 x 28 x 21 EE ferrite Core, 170 μH
High Frequency Transformer (HFT)	EE ferrite core, Primary turns, N_1=26, secondary turns N_2=30, L_{lk1}= 1.65μH
Series Inductance	EE ferrite core, 4.85 μH
Output Capacitor	2*1200μF 450V electrolytic capacitor
Gate Driver IC	IC-IXYS-IXDN609SI
DSP Board	TMS320F28335

5.7 Experimental Results

To validate the performance and design, a laboratory prototype of the proposed V2V DC-DC power exchange converter rated at 1.5 kW is developed, as shown in Fig. 5.12., utilizing the converter specifications outlined in Tables 5.1 and 5.2. The laboratory hardware necessitates specific component specifications, which are detailed in Table 5.3. The gating

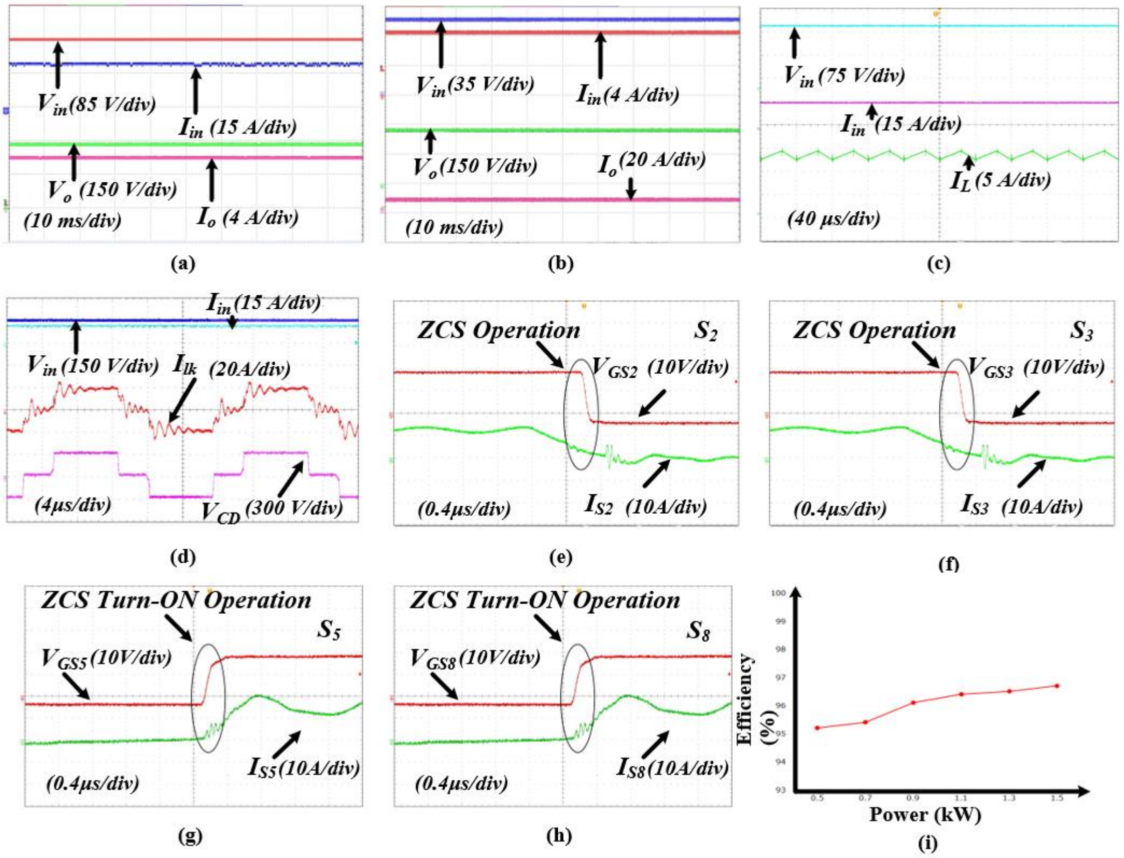

(a) (b) (c)

(d) (e) (f)

(g) (h) (i)

Fig. 5.13. Experimental results of DC-DC Converter for V2V Charger; (a) DC input voltage V_{in}, DC input current I_{in}, DC output current I_0 and the DC output voltage V_0 at 1500 W; (b) DC input voltage V_{in}, DC input current I_{in}, DC output current I_0 and the DC output voltage V_0 at 750 W; (c) DC input voltage V_{in}, DC input current I_{in}, Input boost inductor current I_L; (d) DC input voltage V_{in}, DC input current I_{in}, Primary HFT I_{Llk}, Secondary HFT V_{CD}; (e) ZCS operation at primary side switch S_2; (f) ZCS operation at primary side switch S_3; (g) ZCS Turn-ON operation at secondary side switch S_5; (h) ZCS Turn-ON operation at secondary side switch S_8; (i) Efficiency analysis at different power level.

signals for SiC MOSFETs are generated by code using the TI-DSP-TMS320F28335 Board. The dimensions of the proposed topology measure 7.59.50.40 in^3 (length * width * height), resulting in a power density of 52.63 W/in3. The isolated gate-driver circuits for the semiconductor switches are designed using the gate driver IC IXYS-IXDN609SI and Broadcom-ACPL4800 optocoupler. The experimental results closely align with the digital simulation results, validating their accuracy and design of the DC-DC converter for V2V charger. A DC-DC converter for V2V charger based on SiC-MOSFETs is constructed, tested, and evaluated under diverse operating conditions.

Experimental results in the steady-state of the DC-DC converter for V2V charger operating in DC-DC mode are presented in Fig. 5.13. Fig. 5.13(a) displays the DC input current and voltage, as well as the DC output current and voltage at power levels of 1500W. The waveforms of DC input current and voltage and the DC output current and voltage at half-load shown in Fig. 5.13(b). The input boost inductor current waveform which is shown in Fig. 5.13(c) with lower ripple magnitude and twice of the semiconductor device switching frequency, also with input DC current and voltage. In Fig. 5.13(d), the experimental results for a single high-frequency switching cycle are presented, highlighting the complete absence of voltage and current in the high-frequency transformer (HFT) after the active state ends with secondary side voltage at HFT. Additionally, the low voltage is clamped at low voltage semiconductor devices. Unlike traditional hard-switching and active-clamped converters, the primary current in the dc-dc converter maintains a continuous flow. As predicted, this characteristic results in a low peak value for the primary current, corroborating the findings outlined in the analysis and simulation results. Through the utilization of anti-parallel diodes across the primary side semiconductor devices, the current naturally diminishes to zero, leading to ZCS turn-off operation.

Fig. 5.13(e) and (f) demonstrate the experimental results of the ZCS turn-off soft-switching operation achieved by primary switches S_2 and S_3 at different time intervals. Furthermore, secondary side devices S_5 and S_8 exhibit ZCS turn-on at different time intervals, as depicted in Fig. 5.13(g) and (h). These figures demonstrate that the current transitions from zero to a positive value upon switch turn-on, resulting in ZCS turn-on operation. Similarly, the remaining switches at primary side S_1 and S_4 and S_6 and S_7 on the secondary side achieve

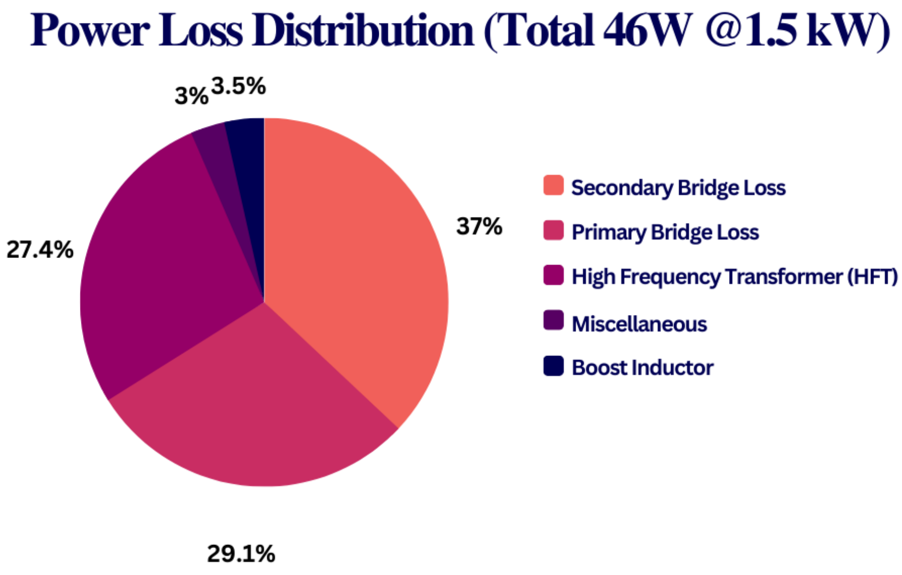

Fig. 5.14. Power loss distribution at 1.5 kW.

soft-switching during other mode. The experimentation conducted on the hardware prototype as part of the proof-of-concept demonstrates exceptional efficiency, achieving a remarkable 96.7% efficiency level at full-load. Also, efficiency evaluation is analyzed at different power levels in Fig. 5.13(i). The distribution of power losses in the converter is also shown graphically in Fig. 5.14., using a pie chart to show the proportional percentages that each component contributed. Secondary side switches and capacitor, which account for 37% of the converter's overall loss, are the main cause of the power loss. SiC-MOSFETS are main responsible for 29.1% of the overall loss at primary-bridge. 27.4% of the total loss is accounted for by HFT, while the remaining 3.5% is caused by input boost inductor. Surprisingly, the observed efficiency from the experiment using the proof-of-concept hardware prototype nearly matches the theoretically predicted efficiency.

5.8 Conclusion

This chapter presents a novel zero-current-switching enabled current-fed full bridge (CFFB) based dc-dc converter for V2V charging application. The incorporation of an isolated dc-dc converter showcases a simple solution for achieving a compact and lightweight design. A novel modulation technique has been proposed, utilizing at primary side devices with zero current switching (ZCS) and zero current turn-on at secondary side devices. Soft-switching is maintained throughout the operation, eliminating the need for additional passive components, active clamped circuits, or snubber circuits. This results in high power density, cost-effective, compact in size, robust and reliable solution. The main benefit of this method is that it uses just one power conversion stage, which is more less than other V2V charging techniques that have been demonstrated in this chapter. A thorough analysis of steady-state functioning over one switching cycle is given, and design calculation for the converter in DC charging mode are also obtained. PSIM 11.04 simulations are used to confirm the viability of the proposed V2V charge transfer method employing with power converter in DC charging mode. Additionally, a hardware prototype with a 1.5 kW power rating is built and put through testing to confirm the effectiveness of the analysis and design of the proposed converter for V2V charger. The experimental set-up produces a remarkable V2V power transfer efficiency with 96.7%.

Chapter 6: Electric Vehicle-to-Vehicle (V2V) Energy Transfer Using Current-Fed DC-DC Converter

6.1 Introduction

Electric vehicle-to-electric vehicle (V2V) charging technology is proposed to offer solutions to the increased energy demand. It is considered as a new way of transferring energy between vehicles without directly relying on the utility grid. Some car manufacturers, such as Rivian, Tata Motors and Hyundai, announced to include this feature in their new EV models [16]-[18]. In chapter 5, the propose a V2V charge sharing using current-fed isolated dual active bridge (DAB). It provides the merits of modularity, scalability, high reliability, fault tolerance, and reduced filter requirements. The primary issue with this is the increased number of devices and gate driving needs, as well as false switching endangering dependability.

This Chapter introduces and investigates in detail, the concept of V2V charging using current-fed push-pull (CFPP) converter topology to achieve zero-current switching (ZCS) of the semiconductor switches. The proposed soft-switching converter effectively solves the historical problem of voltage spike across the switching devices at their turn-off and thus, eliminates the requirement of the snubber or the clamping circuit across them. This reduces the hardware complexity while making the converter snubber-less, compact, and cost-effective. Also, Push-pull topology is advantageous by virtue of having only two switching devices with common ground with the source simplifying the gate driving requirements to cater cost and control limitations. Push-pull configuration utilizes single boost inductor with relatively less components. Table 6.1 corroborates the merits of the proposed converter for V2V charging compared to the existing V2V chargers. The distinct attributes of the proposed converter configuration presented in this chapter are elaborated as 1) lower switching losses: zero current turn-on at the secondary or output side switches and zero current at the primary or input side switches; 2) Alleviating the traditional voltage-spike problems in primary and secondary switches with ZCS method and limiting the RMS current which leads to higher efficiency, and allow the high switching frequency operating with higher converter density; 3) Snubber-less inherently clamped soft-switching is tracked and maintained during the full operation.

The layout of this Chapter is as follows: Section 6.2 explains the steady-state operation of the proposed converter. Section 6.3 describes the steady-state analysis and mathematical

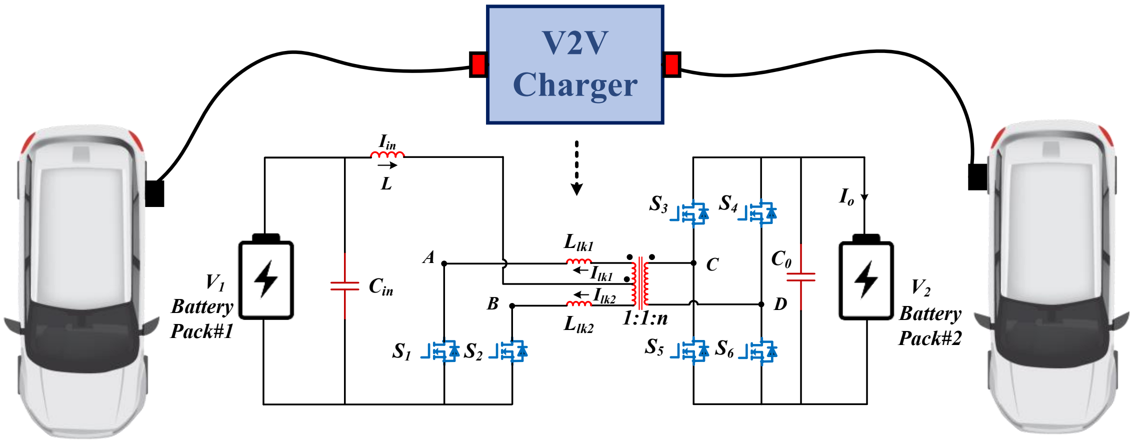

Fig. 6.1. Single-Stage Single-Phase V2V EV Charger.

expressions for each mode of converter operation. Section 6.4 illustrates the converter design procedure to determine the desired attributes with appropriate selection of the various component ratings for the given specifications. Section 6.5 shows simulation and experimental results. Concluding remarks are presented in Section 6.6.

6.2 Proposed Converter Topology

Fig. 6.1. illustrates the schematic of high frequency isolated current fed push-pull converter for V2V charging application. Push-pull topology features a pair of symmetrical switches S_1 and S_2 operated with gating signals phase shifted by 180º with duty ratio $D > 0.5$ which then periodically reverses the current polarity in the transformer primary. Therefore, continuous current is drawn from the source in both halves of the switching cycle resulting in steady input current with significantly low noise. Two diagonal switches of the output side (secondary side) are turned-ON just before taking out the gating pulses of the input side (primary side) switches, and the reflected output voltage $2.V_0/n$ visible at the primary side of HFT. As a result of this, the current is redirected from the input side switches to the HFT which lead to the current of the HFT is to rise and the input side switches current to fall until it becomes null. The gating pulses are withdrawn once the current drops below null, and the body diodes at the switches commences conducting, resulting in ZCS turn-off operation. To ensure output voltage stability and power exchange control, fixed-frequency duty-cycle (FFDC) modulation technique is adopted.

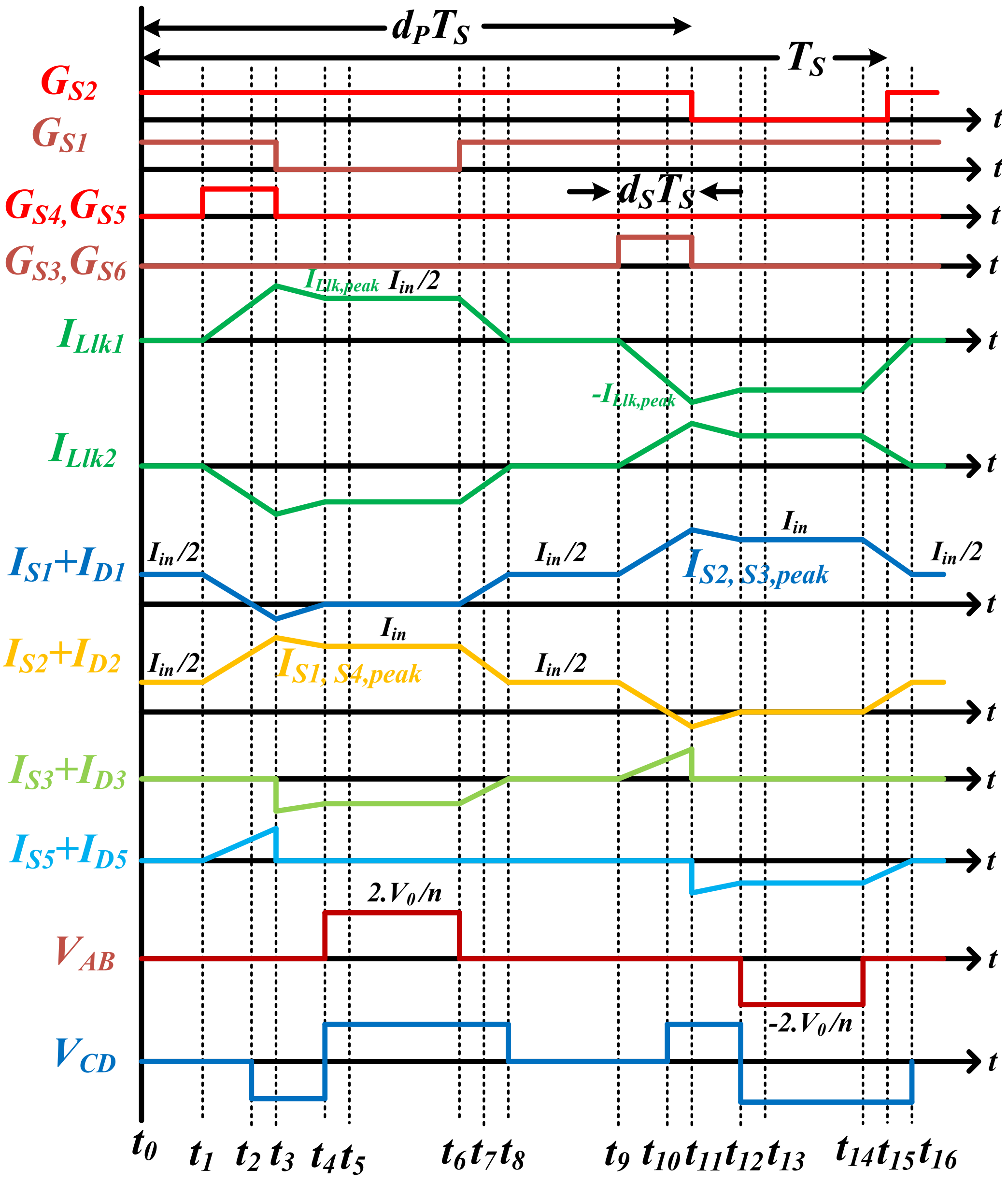

Fig. 6.2. Operational waveforms of the DC-DC converter for V2V charging.

6.3 Steady State Operation of the Converter

The detailed steady-state analysis and operation of the ZCS concept are explained and articulated in this section. The operating waveforms of V2V charger in steady-state are displayed in Fig. 6.2. The gating signals are used to control the input side switches S_1 and S_2 are phase-shifted by 180^{θ} with an overlap across the legs at the conduction time. The d_P (should be > 0.5) and d_S (should be < 0.5) are the duty ratios of the input side and output side devices, respectively. The amount of overlap in the gating pulses changes based on the value of duty ratio, which is determined by the input voltage and load characteristics. As depicted in Fig. 6.2, the duty cycle of the secondary side devices S_3 and S_6 is d_S, and they are switched-

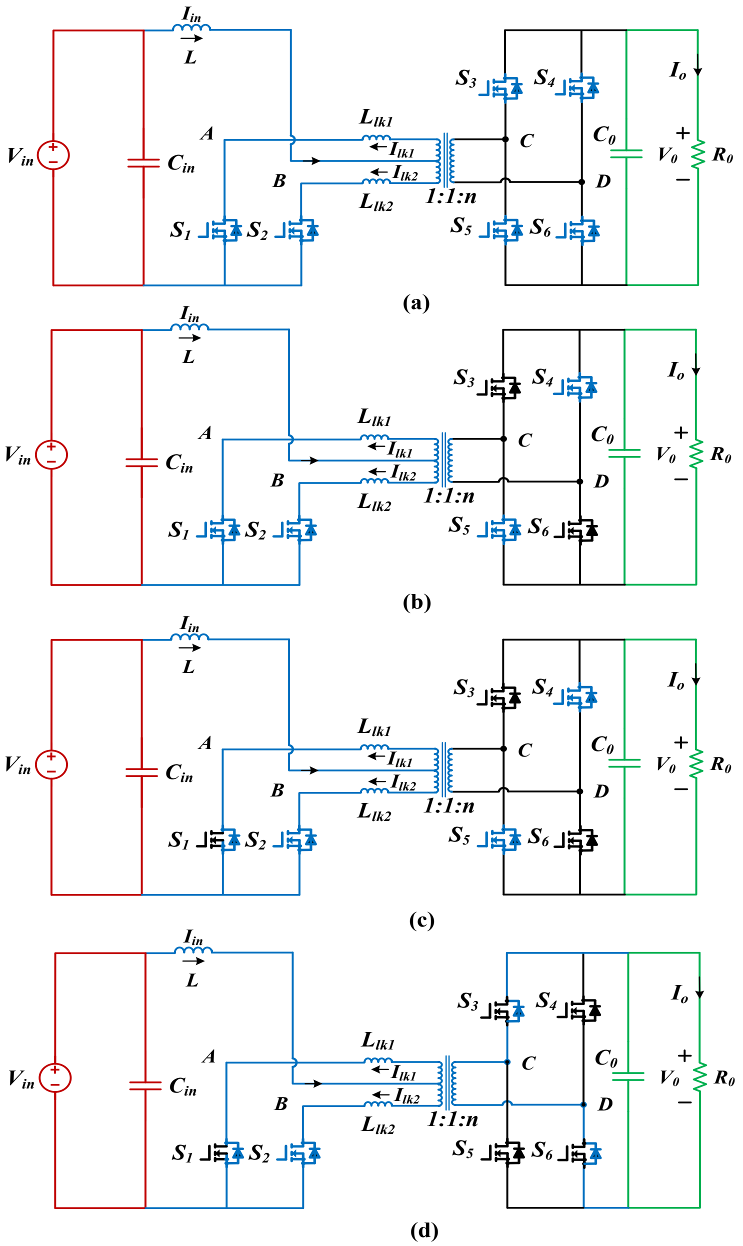

Fig. 6.3. Equivalent circuits while various intervals of operation of the converter-I.

off synchronously with devices of the primary side S_1. Likewise, the turn-off of the device S_2 is synchronized with the turn-off with the devices of S_4 and S_5. A few assumptions have been made to make the analysis more easy and under-stable of V2V charger, which are exhibited as below:

a) Sufficiently large boost inductor is assumed to maintain constant current.

b) All the semiconductor devices are ideal and lossless.

c) The output filter is large enough to maintain the constant output voltage.

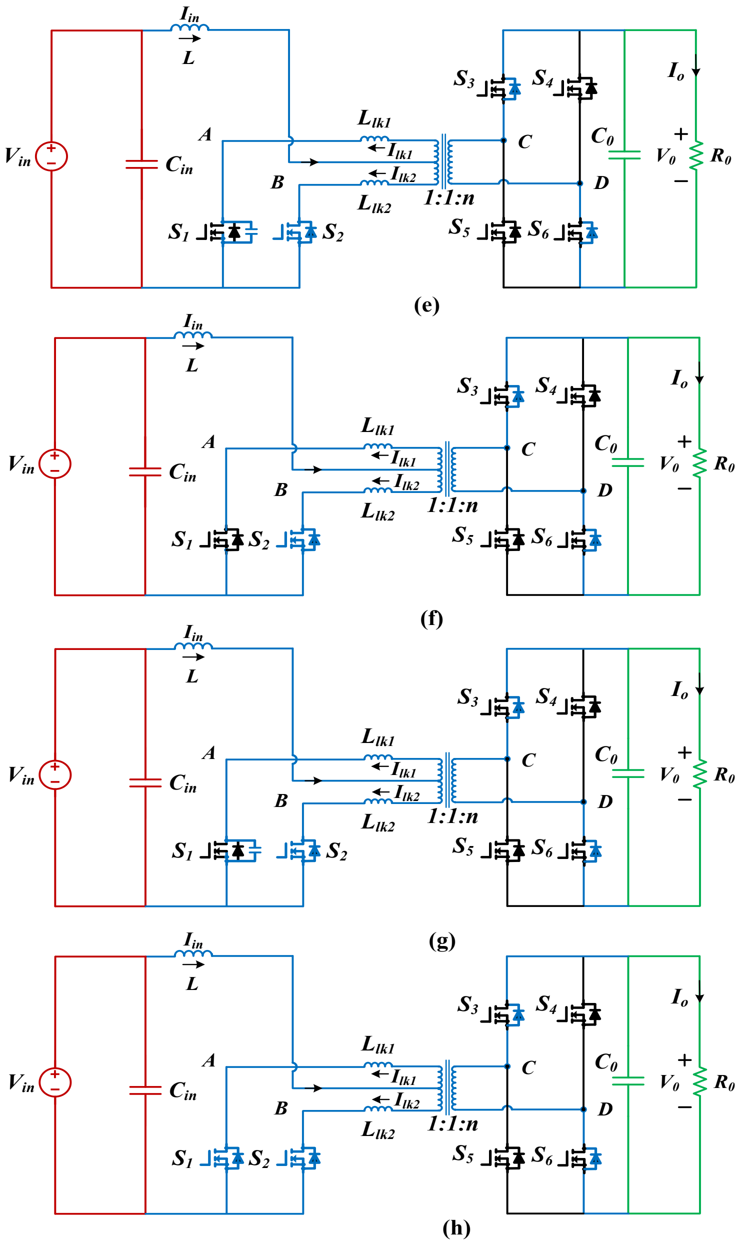

(e) (f) (g) (h)

Fig. 6.4. Equivalent circuits while various intervals of operation of the converter-II.

d) Infinitely large magnetizing inductance of HF transformer is assumed.

By using equivalent circuits of the proposed V2V charger shown in Fig. 6.3 and 6.4, the operation of the converter throughout different intervals in a half high frequency (HF) cycle can be elucidated.

Mode-1: ($t_0 < t < t_1$)

During this interval, both the primary-side switches S_1 and S_2 are conducting and sharing 50% each of the input current. Power is fed to the load by the output capacitor.

$$I_{S1} = I_{S2} = I_L = \frac{I_{in}}{n} \tag{6.1}$$

Mode-2: ($t_1 < t < t_2$)

In this interval, secondary-side switches S_4 and S_5 are turned on at $t=t_1$. It causes voltage $2.V_0/n$ to appear across the primary of the transformer. In this interval, the leakage inductance current I_{lk1} increases further; hence, the inductor current I_L, which was earlier flowing through switch S_1, is diverted to the transformer primary. Therefore, current i_{S1} through switch S_1 starts decreasing linearly, and current i_{lk1} starts increasing. The currents through the several components are given by,

$$I_{Llk1} = \frac{2.V_o}{n \cdot L_{lk\_T}}(t - t_2) \tag{6.2}$$

$$I_{S1} = I_{Llk2} = I_{in} - \frac{2.V_o}{n \cdot L_{lk\_T}}(t - t_2) \tag{6.3}$$

$$I_{S2} = I_{in} + \frac{2.V_o}{n \cdot L_{lk\_T}}(t - t_2) \tag{6.4}$$

$$I_{S4} = I_{S5} = \frac{4.V_o}{n^2 \cdot L_{lk\_T}}(t - t_2) \tag{6.5}$$

At the end of this interval, switch S_1 current reduces to zero, causing its ZCS turn-off since the gating signal has not been removed yet.

Mode-3: ($t_2 < t < t_3$)

In this interval, antiparallel diode D_1 of the switch S_1 starts conducting at $t=t_2$. The currents through the transformer and the switches S_2, S_4, and S_5 are increasing with the same slope. At the end of this interval at $t=t_3$, currents i_{lk1} and i_{S2} reach their peak values. The peak value depends upon the pulse width of the gating signal (G_4 and G_5 shown in Fig. 6.3) applied to secondary switches.

Mode-4: ($t_3 < t < t_4$)

Secondary switches S_4, and S_5 are turned off at $t=t_3$. The current on the secondary side is taken over by antiparallel diodes D_3, and D_6 across secondary switches S_3, and S_6, respectively. A negative voltage of -$2.V_0/n$ appears across the transformer primary, and its current i_{lk1} starts decreasing from its peak value and i_{lk2} starts increasing. At *t=t₄*, the current through diode D_1 naturally reaches zero.

$$I_{Llk1} = I_{in} - \frac{2.V_o}{n \cdot L_{lk\_T}}(t - t_3) \tag{6.6}$$

$$I_{S2} = I_{S2,peak} - \frac{2.V_o}{n \cdot L_{lk\_T}}(t - t_3) \tag{6.7}$$

$$I_{Llk1} = I_{in} + \frac{2.V_o}{n \cdot L_{lk\_T}}(t - t_3) \tag{6.8}$$

Mode-5: ($t_4 < t < t_5$)

During this interval, the snubber capacitor across the primary switch S_1 charges to voltage $2.V_0/n$. This interval is very short. Series snubber resistance controls the charging rate.

Mode-6: ($t_5 < t < t_6$)

In this interval, the transformer primary voltage is zero; therefore, a constant current I_{in}/n flows through its primary. Switch S_2 conducts full input current Iin. Output capacitor C_0 is charged by constant current I_{in}/n through the antiparallel diodes D_3 and D_6. $G_1{-}G_6$ are the gating signals for the switches $S_1 - S_6$, respectively.

Mode-7: ($t_6 < t < t_7$)

At $t{=}t_6$, primary switch S_1 is turned on. The snubber capacitor across it discharges through the series snubber resistance, and switch voltage reduces to zero at the end of this interval. This interval is very short.

Mode-8: ($t_7 < t < t_8$)

During this interval, a negative voltage -$2.V_0/n$ appears across the transformer primary, and its primary current starts falling from I_{in}/n. Switch S_1 current starts increasing. It is the zero-current turn-on of switch S_1. At the end of this interval at $t{=}t_8$, current i_{lk1} reduces to zero, and switch current i_{S1} increases to I_{in}/n. Their mathematical expressions are given as follows:

$$I_{S1} = \frac{2.V_o}{n \cdot L_{lk\_T}}(t - t_7) \tag{6.9}$$

$$I_{Llk1} = I_{in} - \frac{2.V_o}{n \cdot L_{lk\_T}}(t - t_7) \tag{6.10}$$

$$I_{Llk2} = I_{in} + \frac{2.V_o}{n \cdot L_{lk\_T}}(t - t_7) \tag{6.11}$$

A half HF switching cycle terminates at the end of this interval. For the next half HF cycle, the intervals are repeated in a similar sequence with other symmetrical devices conducting to complete the full HF cycle.

Table 6.1: Converter Specifications

Parameter	**Value**
Input Voltage, V_{in}	170V (rms)
Input Current, I_{in}	17.76 A
Output voltage, V_o	300 V
Output power, P_o	1500W
Switching frequency, f_{sw}	100 kHz

6.4 Design of the Converter

This section describes the procedure for designing of the proposed single-phase single-stage current-fed DC-DC converter for vehicle-to-vehicle charging application. The parameters include: Input voltage V_{in}=170 V, Output voltage V_0=220-330 V, Output power P_o=1.5 kW, nominal output voltage = 300 V, and switching frequency f_s=100 kHz. The following presented design equations assist in determining the ratings of the components used in the proposed converter. This information is beneficial in the selection process of components and estimating the performance of the converter as theoretically and practically.

35) The input current I_{in} is calculated by,

$$I_{in} = \frac{P_o}{n.V_{in}} \tag{6.12}$$

Table 6.2: Converter Design Parameters

Parameter	**Value**
Input Boost Inductor, L	170μH
Leakage Inductance of L_{lk_T}	7.2μH
Turns ratio, n	1.1
Output Capacitor, C_0	2*1200μF

Presuming an ideal efficiency η=100%.

36) The maximum allowable voltage across at the switches of the primary side is,

$$V_{SW,P} = \frac{2.V_0}{n} \tag{6.13}$$

Where n is the high-frequency transformer (HFT) turns-ratio.

37) The high-frequency transformer (HFT) turns ratio is given by,

$$n = \frac{2.V_0.(1 - d_P)}{V_{in}} \tag{6.14}$$

Where d_P is the duty cycle of the primary side switches.

38) The leakage series inductance L_{lk_T} of HFT is required to yield ZCS with operating requirements necessities and it can be computed as,

$$L_{lk\_T} = L_{lk1} + L_{lk2} = \frac{2.V_0.(d_P - 0.5)}{I_{in} \cdot f_s \cdot n} \tag{6.15}$$

Where f_s is the switching frequency of the converter. Although the experimental value of L_{lk_T} is slightly lower than the design value, it is still enough to ensure ZCS operation within the boundary of operation. Additionally, this has a substantial effect on the peak current of the primary side switches, but it matches the designed calculation as well.

39) The relationship between input voltage V_{in} and output voltage V_0 is given as,

$$V_0 = \frac{n.V_{in}}{2.(1 - d_P)} \tag{6.16}$$

40) The duty cycle of the secondary side switches d_S is a crucial factor that determines the zero-current-switching (ZCS) condition of the primary side switches, and it can be expressed as follow,

$$d_S \geq \frac{I_{in}.f_s\,.n\,.L_{lk}}{2.V_0} \tag{6.17}$$

The peak-to-peak current value of the input boost inductor is denoted by ΔI_L, where ΔI_L=1. To achieve maximum converter efficiency and utilization factor, it is critical to choose the ideal boost inductor value that minimizes conduction losses.

41) To meet the input current ripple (ΔI_L) specification, the input boost inductor L is calculated as,

$$L = \frac{V_{in}\,.d_P}{\Delta I_L \cdot f_s} \tag{6.18}$$

The value of the input boost inductor L is determined according to the input current ripple specification, with ΔI_L indicating the peak-to-peak value of the inductor current. To achieve high converter efficiency and utilization factor, an appropriate boost inductor value that minimizes conduction losses must be selected, as described in [144].

If $L_{lk1}$and L_{lk2} are not equal then equation (4.8) is modified as follows,

$$L = \frac{(V_{in} + \frac{V_0}{n} - \frac{2.V_0.L_{lk\_T}}{L_{lk\_T}\,.n}).\,d_P}{\Delta I_L \cdot f_s} \tag{6.19}$$

Whereas, L_{lk_T} is the minimum value of L_{lk1} and L_{lk2}.

42) The RMS and peak current of the primary side HFT can be computed as,

$$I_{PT,peak} = \frac{2.V_0.d_S}{L_{lk\_T} \cdot f_s\,.n} \tag{6.20}$$

$$I_{PT,RMS} = I_{in}\sqrt{\left[\frac{1-d_P}{2} + \frac{d_S}{3}\right]} \tag{6.21}$$

The RMS current can be determined by considering the complete HF over grid cycle, which fluctuates with I_{in} and d_P during the mode of operation.

43) The peak and RMS current of the secondary side HFT can be given as,

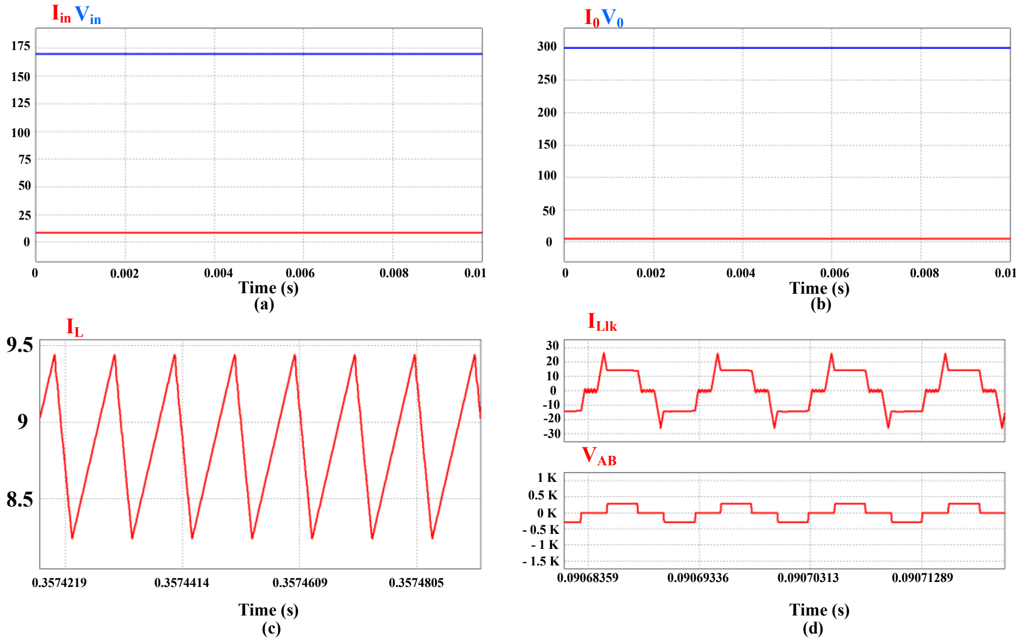

Fig. 6.5. Simulation results of V2V chargers from PSIM 11.04 Software at P_0=1.5 kW; (a) DC input voltage V_{in} and DC input current I_{in}. (b) DC output current I_0 and the DC output voltage V_0. (c) Input boost inductor current I_L. (d) Lekage series inductor current waveform I_{Llk} and voltage waveform V_{AB} at primary side.

$$I_{ST,peak} = \frac{2.V_0.d_S}{L_{lk\_T}\,.f_s\,.n^2} \tag{6.22}$$

$$I_{ST,RMS} = \frac{I_{in}}{2.n}\sqrt{\left[\frac{1-d_P}{2}+\frac{d_S}{3}\right]} \tag{6.23}$$

In order to determine the RMS current during operational mode, it is considered the complete HF over a grid cycle, taking into account the variations in both I_{in} and d_P.

44) The output capacitor C_0 is obtained as,

$$C_0 = \frac{I_0.(1-d_P)}{\Delta V_0.f_s} \tag{6.24}$$

Whereas, ΔV_0 is the output voltage ripple range.

6.5 Simulation Results of V2V Charger

The proposed V2V charger has been designed and simulated as per specifications of Table 6.1 and 6.2 using PSIM 11.04 software to ensure that it meets the desired performance and

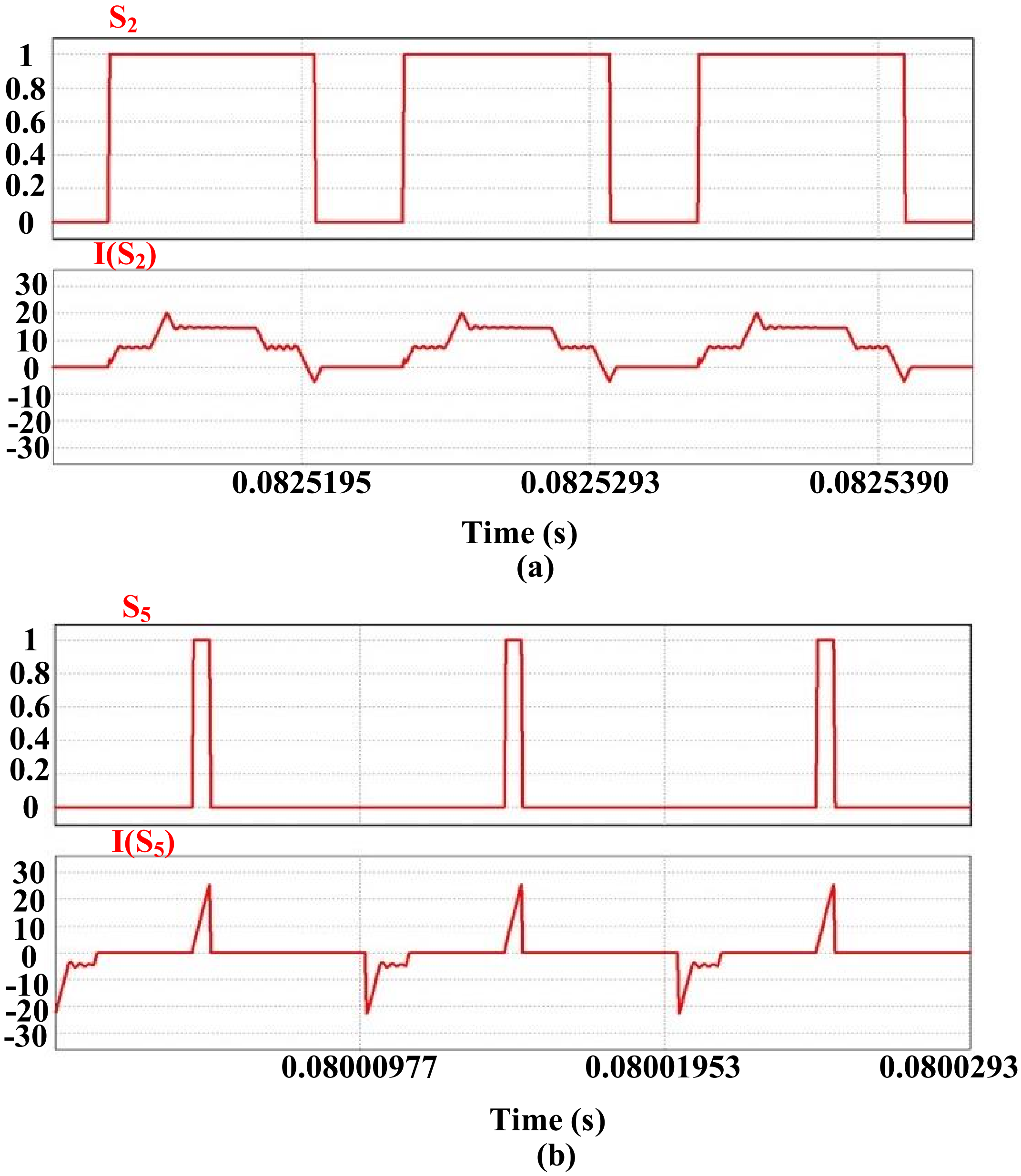

Fig. 6.6. (a) Simulation results of ZCS operation at primary side devices. (b) Simulation results of ZCS turn-on operation at secondary side devices.

theoretical analysis. The steady-state behavior of the converter with the specified parameters and design characteristics, which are rated for 1.5 kW power. Fig. 5.10 and 5.11 exhibit the simulation results of the proposed converter in DC charging strategy.

The DC input voltage V_{in} and input current I_{in} are depicted in Fig. 6.5(a). Also, Fig. 6.5(b) affirms the DC output current I_0 and the DC output voltage V_0 at rated output power 1.5 kW. The output voltage V_0 is clearly observed to stabilize precisely at 300V in Fig. 6.5(b). Fig. 6.5(c) shows the current waveform for the input boost inductor L. The input boost inductor

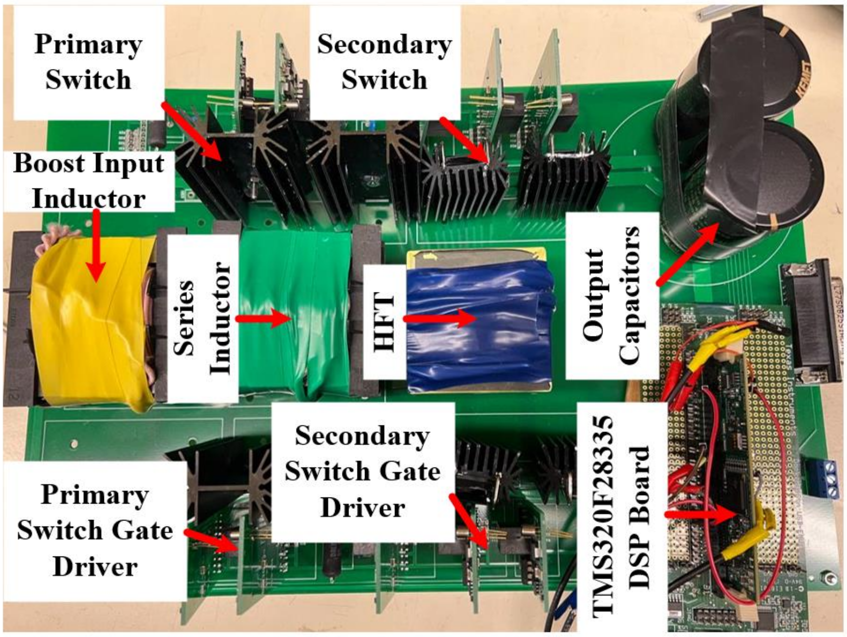

Fig. 6.7. V2V Charger laboratory hardware prototype.

current I_L ripple frequency is twice of device switching frequency f_s, leading to a smaller in size. Moreover, the peak current I_{Llk} through inductor L_{lk} above the constant value is due to the extended enable of the anti-parallel body diodes of the corresponding primary semiconductor devices, which ensures ZCS turnoff operation as shown in Fig. 6.5(d). The continuous current has the lower peak value. Furthermore, according to the voltage waveform V_{AB}, the voltage across the main devices is inherently capped at low voltage, V_0/ n.

The current through the primary and secondary switches and its corresponding gate signals while the operation of the converter during the DC charging mode is shown in Fig. 6.6. The primary switch current reaches zero inherently without requiring any external circuitry before removing the gate signal, thereby achieving ZCS turn-off operation as shown in Fig. 6.6(a). This is applicable and accurate for all voltage and load ranges configurations, as discussed in the converter design section 6.4. The current through the secondary side devices during V2V charging is depicted in Fig. 6.6(b) along with its gate signal. The gate signal enables the devices to turn-on gradually until achieving zero current turn-on (ZCS turn-on) condition. The waveforms displayed in Figs. 6.5 and 6.6 which are precisely match with the expected results predicted by theoretical analysis, demonstrating to verification of the accuracy of the proposed secondary side modulation strategy and the steady-state operation with its design of the converter as discussed in Section 6.2 and Section 6.4.

Table 6.3: Component Specifications of the Laboratory Prototype

Component	**Specifications**
Primary-side switches	CREE-SiC MOSFET, C3M0045065D
Secondary-side switches	CREE-SiC MOSFET, C3M0025065D
Boost Inductor	55 x 28 x 21 EE ferrite Core, 170 μH
High Frequency Transformer (HFT)	EE ferrite core, Primary turns, N_1=26, secondary turns N_2=30, L_{lk1}= 1.65μH
Series Inductance	EE ferrite core, L_{lk1} = 13μH, L_{lk1} = 12μH
Output Capacitor	2*1200μF 450V electrolytic capacitor
Gate Driver IC	IC-IXYS-IXDN609SI
DSP Board	TMS320F28335

6.6 Experimental Results

To validate the performance and design, a laboratory prototype of the proposed V2V DC-DC power exchange converter rated at 1.5 kW is developed, as shown in Fig. 6.7., utilizing the converter specifications outlined in Tables 6.1 and 6.2. The laboratory hardware necessitates specific component specifications, which are detailed in Table 6.3. The gating signals for SiC-MOSFETs are generated by code using the TI-DSP-TMS320F28335 Board. The dimensions of the proposed topology measure 7.59.50.40 in^3 (length * width * height), resulting in a power density of 52.63 W/in3. The isolated gate-driver circuits for the semiconductor switches are designed using the gate driver IC IXYS-IXDN609SI and Broadcom-ACPL4800 optocoupler. The experimental results closely align with the digital simulation results, validating their accuracy and design of the DC-DC converter for V2V charger. A DC-DC converter for V2V charger based on SiC-MOSFETs is constructed, tested, and evaluated under diverse operating conditions.

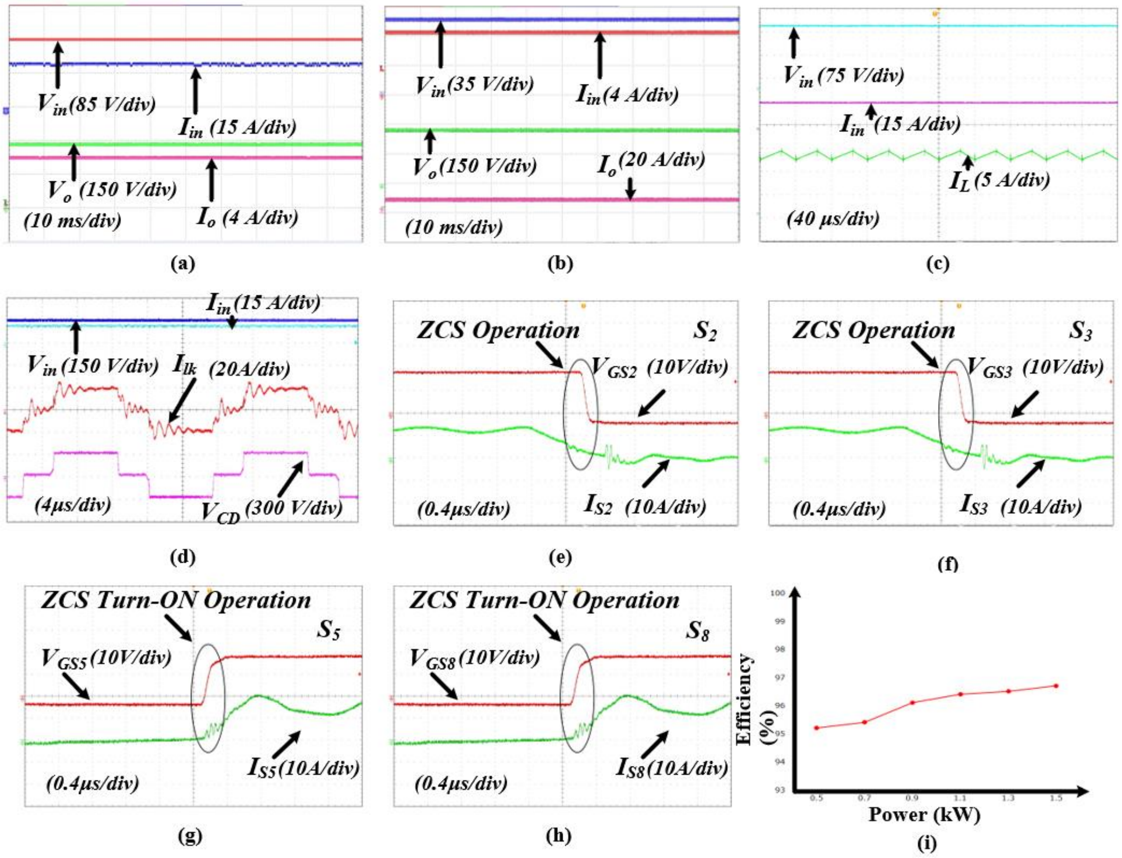

Fig. 6.8. Experimental results of DC-DC Converter for V2V Charger; (a) DC input voltage V_{in}, DC input current I_{in}, DC output current I_0 and the DC output voltage V_0 at 1500 W; (b) DC input voltage V_{in}, DC input current I_{in}, DC output current I_0 and the DC output voltage V_0 at 750 W; (c) DC input voltage V_{in}, DC input current I_{in}, Input boost inductor current I_L; (d) DC input voltage V_{in}, DC input current I_{in}, Primary HFT I_{Llk}, Secondary HFT V_{CD}; (e) ZCS operation at primary side switch S_2; (f) ZCS operation at primary side switch S_3; (g) ZCS Turn-ON operation at secondary side switch S_5; (h) ZCS Turn-ON operation at secondary side switch S_8; (i) Efficiency analysis at different power level.

Experimental results in the steady-state of the DC-DC converter for V2V charger operating in DC-DC mode are presented in Fig. 6.8. Fig. 6.8(a) displays the DC input current and voltage, as well as the DC output current and voltage at power levels of 1500W. The waveforms of DC input current and voltage and the DC output current and voltage at half-load shown in Fig. 6.8(b). The input boost inductor current waveform which is shown in Fig. 6.8(c) with lower ripple magnitude and twice of the semiconductor device switching frequency, also with input DC current and voltage. In Fig. 6.8(d), the experimental results for a single high-frequency switching cycle are presented, highlighting the complete absence of voltage and current in the high-frequency transformer (HFT) after the active state ends with secondary side voltage at HFT. Additionally, the low voltage is clamped at low voltage semiconductor devices. Unlike traditional hard-switching and active-clamped converters, the primary current in the DC-DC converter maintains a continuous flow. As predicted, this characteristic results in a low peak value for the primary current, corroborating the findings outlined in the analysis and simulation results. Through the utilization of anti-parallel diodes across the primary side semiconductor devices, the current naturally diminishes to zero, leading to ZCS turn-off operation.

Fig. 6.8(e) and (f) demonstrate the experimental results of the ZCS turn-off soft-switching operation achieved by primary switch S_2 at different time intervals. Furthermore, secondary side devices S_3 and S_6 exhibit ZCS turn-on at different time intervals, as depicted in Fig. 6.8(g) and (h). These figures demonstrate that the current transitions from zero to a positive value upon switch turn-on, resulting in ZCS turn-on operation. Similarly, the remaining switches at primary side S_1 and S_4, S_5 on the secondary side achieve soft-switching during other mode. The experimentation conducted on the hardware prototype as part of the proof-of-concept demonstrates exceptional efficiency, achieving a remarkable 96.7% efficiency level at full-load. Also, efficiency evaluation is analyzed at different power levels in Fig. 6.8(i). The distribution of power losses in the converter is also shown graphically in Fig. 6.9., using a pie chart to show the proportional percentages that each component contributed. Secondary side switches and capacitor, which account for 37% of the converter's overall loss, are the main cause of the power loss. SiC-MOSFETS are main responsible for 29.1% of the overall loss at primary-bridge. 27.4% of the total loss is accounted for by HFT, while the remaining 3.5% is caused by input boost inductor. Surprisingly, the observed efficiency from

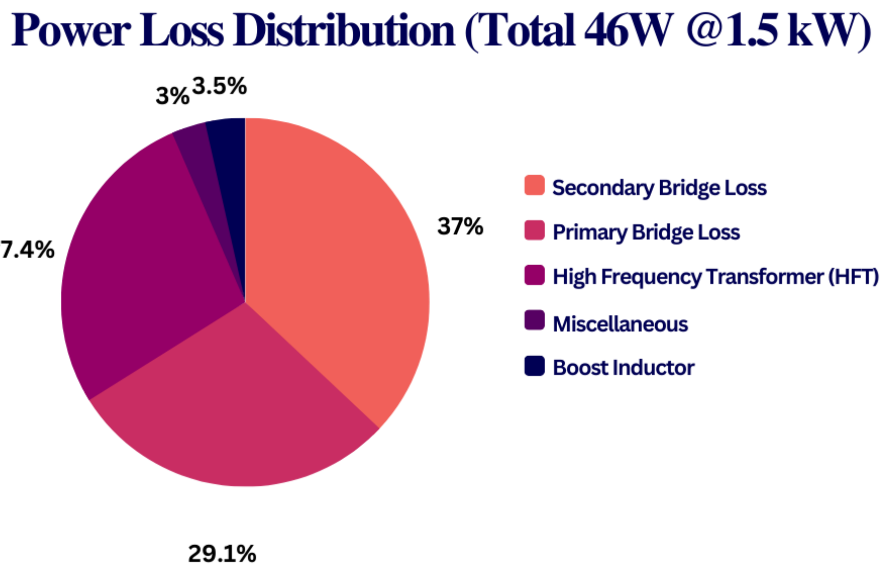

Fig. 6.9. Power loss distribution at 1.5 kW.

the experiment using the proof-of-concept hardware prototype nearly matches the theoretically predicted efficiency.

6.7 Conclusion

This chapter presents a novel zero-current-switching enabled current-fed push-pull (CFPP) based DC-DC converter for V2V charging application. The incorporation of an isolated DC-DC converter showcases a simple solution for achieving a compact and lightweight design. A novel modulation technique has been proposed, utilizing at primary side devices with zero current switching (ZCS) and zero current turn-on at secondary side devices. Soft-switching is maintained throughout the operation, eliminating the need for additional passive components, active clamped circuits, or snubber circuits. This results in high power density, cost-effective, compact in size, robust and reliable solution. The main benefit of this method is that it uses just one power conversion stage, which is more less than other V2V charging techniques that have been demonstrated in this chapter. A thorough analysis of steady-state functioning over one switching cycle is given, and design calculation for the converter in DC charging mode are also obtained. PSIM 11.04 simulations are used to confirm the viability of the proposed V2V charge transfer method employing with power converter in DC charging mode. Additionally, a hardware prototype with a 1.5 kW power rating is built and put through testing to confirm the effectiveness of the analysis and design of the proposed converter for V2V charger. The experimental set-up produces a remarkable V2V power transfer efficiency with 96.7%.

Chapter 7: Conclusion and Future Research

This chapter concludes the thesis and highlights the research contributions of the thesis in Section 7.1 and 7.2, respectively. Recommendations and brief description for the future scope of research has been discussed in Section 7.3.

7.1 Conclusion

The conventional EV battery chargers are developed with two cascaded power conversion stages. The first stage is an AC-DC converter, which performs power factor correction (PFC). The second stage is an isolated DC-DC converter stage, which regulates the battery voltage. These two stages are integrated by DC-link capacitors. This two-stage battery charger suffers from low overall efficiency due to two separate power conversion stages. The converter power density is also limited due to the inevitable presence of the intermediate DC-link capacitors. Generally, electrolytic capacitors with higher μF rating are selected for the intermediate DC link. More importantly, the battery charger is placed close to the internal combustion engine under the hood in the case of plug-in hybrid EV (PHEV), where the ambient temperature is more than 150^0C. The electrolytic capacitors are most susceptible to failure at high ambient temperature, thus the reliability of the conventional two-stage EV battery charger is low in the high-temperature environment.

An alternative solution to improve the efficiency and power density of EV battery chargers with reliable high-temperature operation capability is to eliminate the intermediate DC link capacitors. This approach leads to the development of single-stage AC-DC converters, where the PFC operation and battery voltage regulation are accomplished in only one-stage.

This dissertation proposes a family of novel isolated single-stage bi-directional AC-DC converter topologies with novel soft-switching modulation techniques for Level-1 battery charging application to address the shortcomings of the conventional two-stage battery chargers. The proposed converters achieve PFC and DC voltage regulation in one-stage, thus provides higher efficiency. At the same time, the converter power density and reliability are also improved due to the elimination of intermediate DC-link capacitors. The performance of the proposed converters is evaluated in the developed converter prototypes enabling G2V and V2G mode of operation. In addition, this dissertation also proposes a novel low-cost high-temperature gate driver for the SiC MOSFETs. The proposed high-temperature gate driver is used in the battery chargers of PHEVs, where the ambient temperature is more than 150^0C.

Further, to mitigate the range anxiety battery chargers incorporating flexible charging options such as V2V power transfer becomes meritorious. In order to reduce the size of the passive components, high frequency operation of the power converter is crucial. Usually, these EV chargers are separate for AC and DC charging so, they are unable to incorporate the option of flexible charging. This thesis puts forward a single-phase current-fed derived battery charger for V2V battery charging operations.

7.2 Thesis Contributions

The thesis contributions have been explained and summarized as follows:

i. In chapter 2, a comprehensive review of wide-band gap (WBG) device-based topologies of on-board chargers (OBCs) for more electric vehicles (MEVs). It examines the current state-of-the-art solutions for OBCs, encompassing architectures, configurations, soft-switching techniques, charging infrastructure, commercially available products, and future trends with challenges. Additionally, a detailed overview of promising topology options for WBG based OBCs, including two-stage and single-stage structures, is provided. Furthermore, this chapter discusses future trends and challenges for WBG technologies, thermal management, system integration, fast charging, and wireless charging systems.

ii. In Chapter 3, a novel bidirectional single-stage single-phase isolated power factor correction (PFC) converter for plug-in EV chargers that employs zero-current assisted soft-switching technology is presented. The converter's steady-state analysis, operation, modulation technique, control scheme, and design are discussed in detail. The converter consists of a current-fed full-bridge converter with bidirectional switches on the AC-side, connected to a full-bridge converter on the DC-side of a high-frequency transformer (HFT). A novel modulation strategy and control technique are proposed to ensure soft-switching operations of all semiconductor devices, with zero-current switching (ZCS) at the AC-side and zero-current turn-on at the DC-side throughout the range for all modes, even during bidirectional power flow. The design and analysis of the converter are validated through simulation results from the PSIM 11.4 software, and further verified through experimental results from a 1.5 kW hardware prototype developed in the lab.

iii. In Chapter 4, a novel single-stage single-phase bidirectional PFC AC-DC converter for EV charging application has been examined. The converter operates without an intermediate DC-link, and its steady-state analysis, operation, modulation technique, control scheme, and design have been reported. The proposed configuration incorporates a current-fed push-pull circuit on the primary side and a full-bridge circuit on the secondary side, which is controlled by a high-frequency transformer (HFT). Additionally, a modulation strategy and control technique have been presented to ensure soft-switching operation for all semiconductor devices, including zero-current switching (ZCS) at the AC-side and zero-current turn-on at the DC-side throughout the range, even when bidirectional power flow is present. The performance and analysis of the proposed configuration have been validated through simulation results from PSIM 11.4 software and further confirmed with experimental results from a 1.5 kW hardware prototype developed in the lab.

iv. In Chapter 5, a single-stage single-phase current-fed full-bridge converter for V2V energy exchange was discussed. The steady-state operation, secondary modulation technique, and design of the converter were described in detail. A novel secondary modulation technique was proposed to eliminate the need for traditional active-clamp or passive snubber circuits. The operation and performance of the converter were verified through simulation and experimental results from a 1.5 kW laboratory prototype. The simulation results showed that the converter operated with soft-switching (ZCS of primary side devices and zero current turn-on of secondary side devices).

v. In Chapter 6, a DC-DC converter for vehicle-to-vehicle (V2V) charge sharing has been proposed. This converter is a naturally clamped zero current commutated (ZCC) push-pull configuration that is single-stage and single-phase. The design and analysis of the converter, including the steady-state analysis and secondary modulation technique, have been discussed. A novel soft-switching technique has been introduced to address the issue of device turn-off voltage spikes, without the need for an additional snubber circuit. The performance of the converter has been validated through simulation and experimental results from a 1.5 kW laboratory setup.

7.3 Future Scope of Research

Based on the research done in this thesis, the recommendations for future research are as follows:

7.3.1 Modular Three-Phase Matrix-Based Electrolytic Capacitor-less Single-Stage Isolated AC-DC PFC Bidirectional Converter for EV Charging

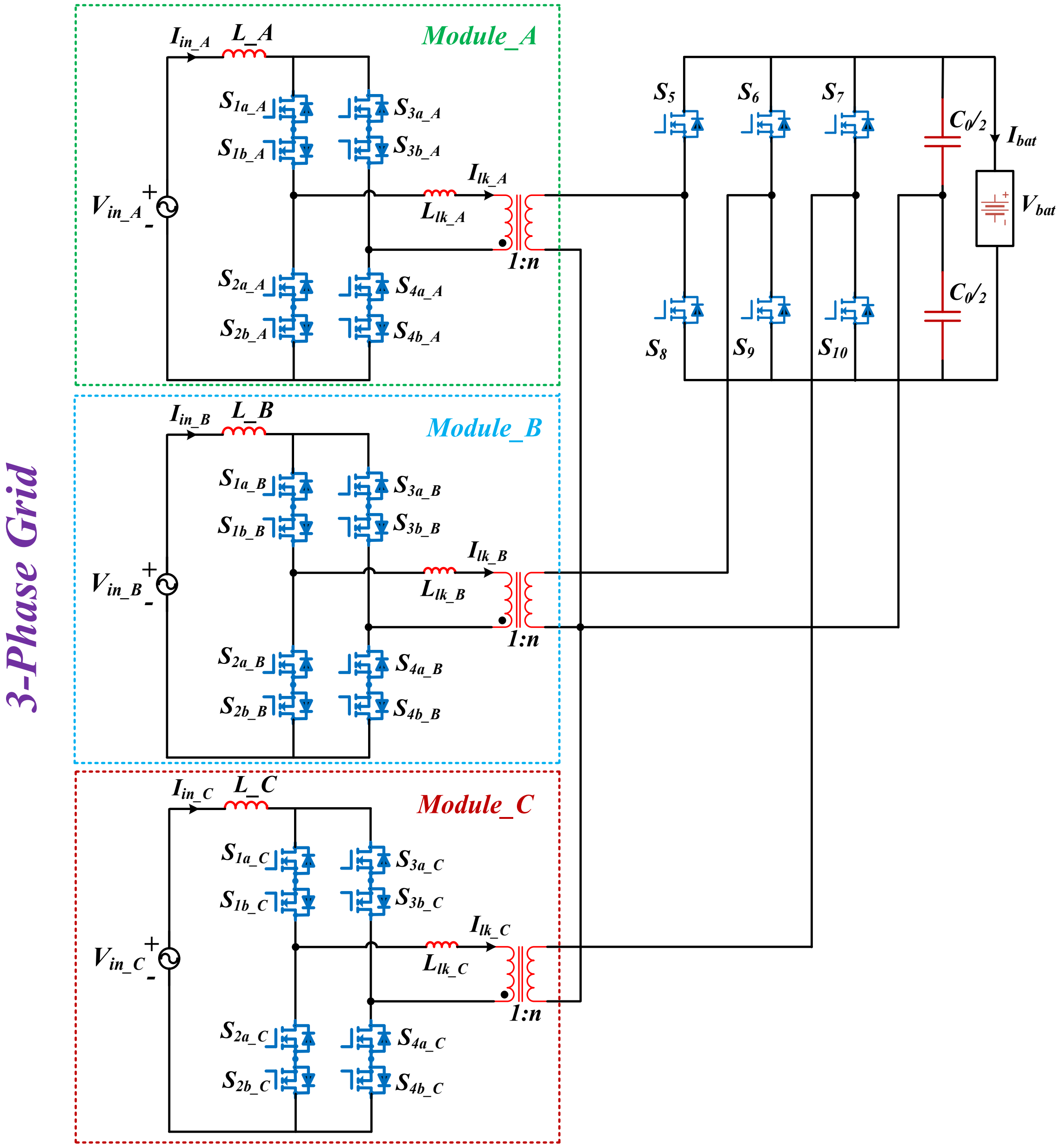

Fig. 7.1 Schematic of single-stage three-phase EV onboard charger

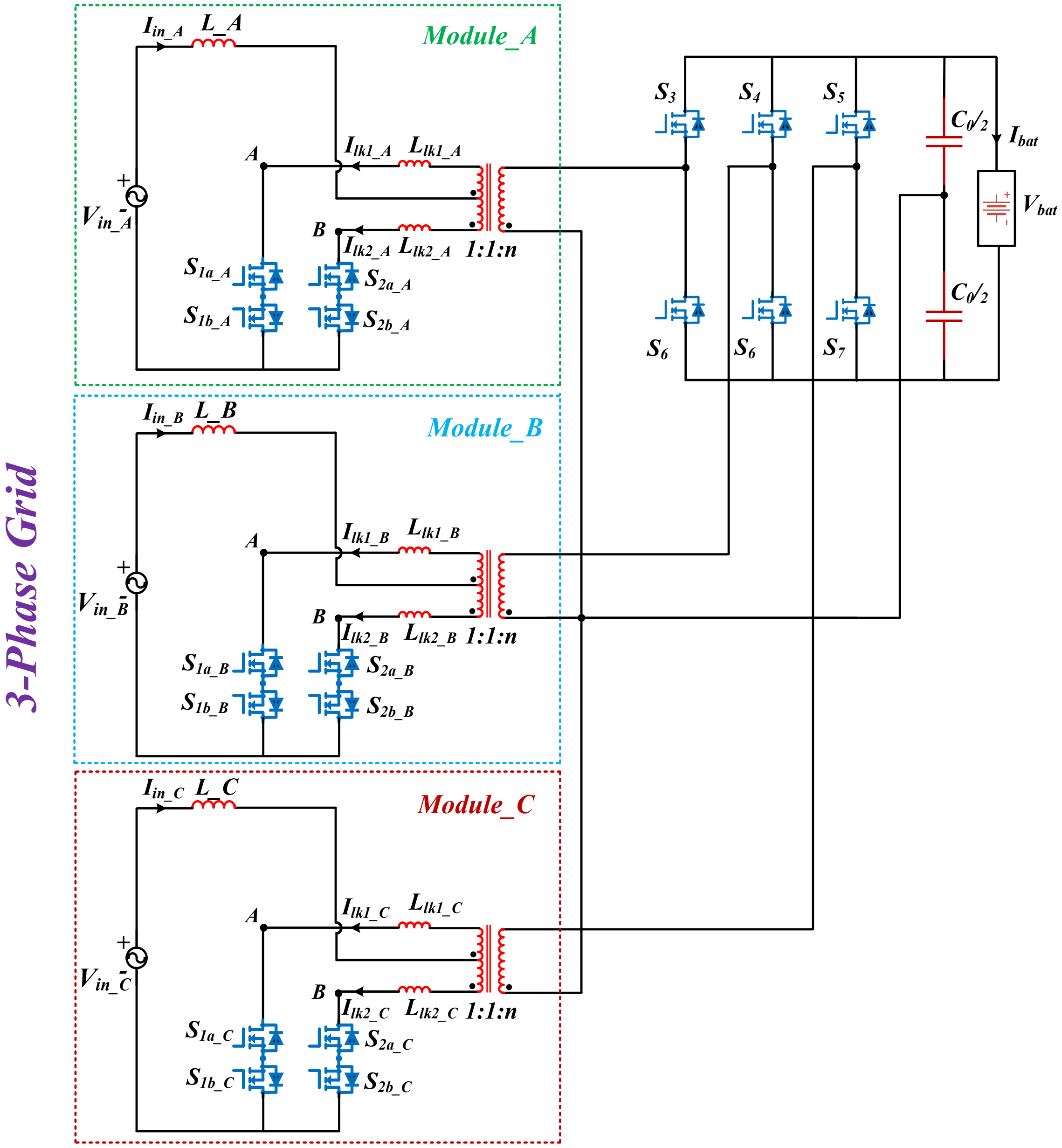

Fig. 7.2. Schematic of single-stage three-inductor-based three-phase EV onboard charger.

In this thesis, current-fed matrix-based single-stage single-phase topology was proposed and studied in Chapter 3. The same can be extended to other current fed three-phase circuits, is shown in Fig. 7.1. One potential converter configuration is a three-inductor modular three-phase current-fed topology for Level-2 EV charging (>10 kW). Various converter modules can be configured in such way to supply high power levels while reducing the current stresses on the individual components. The benefits with modular architecture include: lower component's ratings, scalability, design flexibility and higher fault-tolerant capability. In addition, a current-fed push-pull based single-stage PFC converter proposed in Chapter 4. The same topology can be extended in three-phase mode which is shown in Fig. 7.2. The

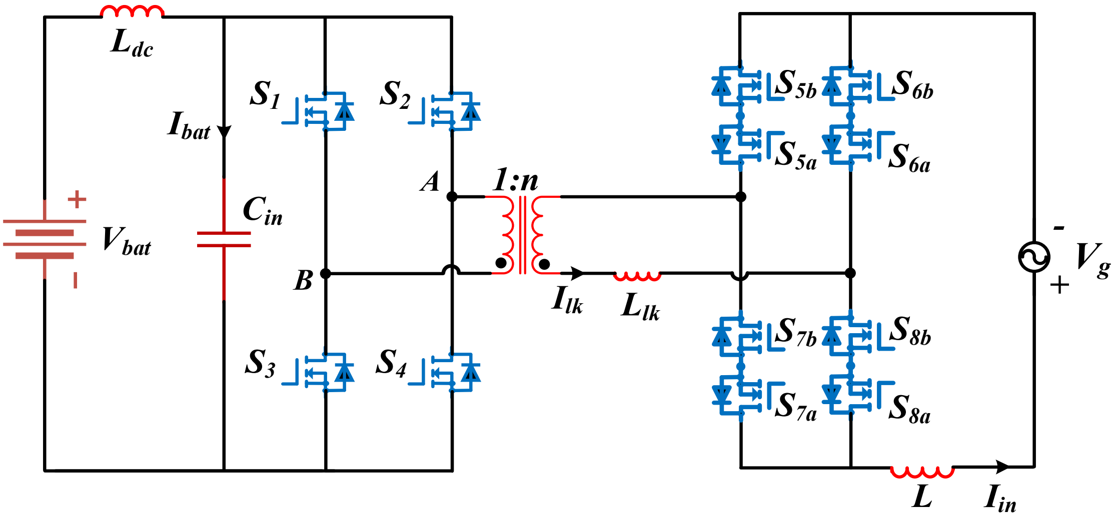

Fig. 7.3. Single-stage L-type current-fed bidirectional converter for V2H operation.

operation, analysis, design, and feasibility of this topology can be considered as the extension of this research work.

7.3.2 Current-Fed Bidirectional Onboard Chargers for V2H Operational Mode

A modification to the single-phase single-stage current-fed PFC converter proposed in chapter 3 and chapter 4 for G2V and V2G application in order to charging vehicle-to-home (V2H) application, which is shown in Fig. 7.3, and Fig. 7.4. The modulation technique and control method have been modified in this topology. The examination, assessment, creation, and evaluation of the feasibility of this topology can be viewed as future scope of research.

7.3.3 Single-Stage Universal Topology with V2G Capability

In this thesis, bidirectional and single-stage power converter topologies are addressed. However, if universal, bidirectional, and single-stage, all these possibilities are combined in a single converter, then that system will be very suitable for practical use. This will increase flexibility, and reduce cost of the charger. Two-stage chargers will be quite expensive, especially due to increase of the power conversion stages and number of components. Therefore, a universal single-stage charger with V2G capability will not only reduce manufacturing cost due to mass production, but also increases flexibility by accepting power both from ac grid and solar PV. To explain this concept, Fig. 7.5 is included, where input to the charger is either ac grid or solar PV. Also, it will be able to participate in V2G, thereby

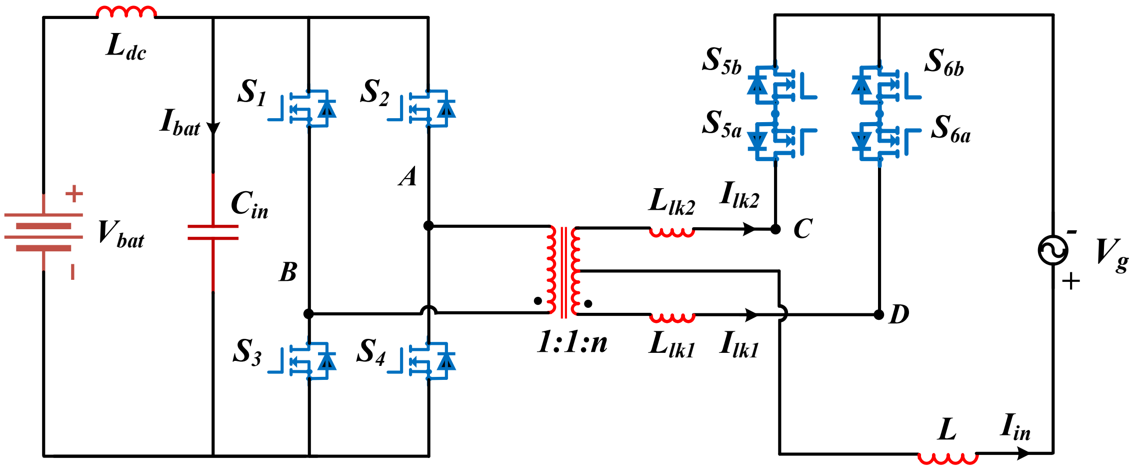

Fig. 7.4. Current-fed single-stage bidirectional topology for vehicle-to-home (V2H) charging application.

making it a single charger solution. Although, voltage-fed technology is most popular in the single-stage topology. But, VSI may not be a preferred choice. However, current-fed technology can easily perform those tasks, and this is briefly described in this thesis.

Grid to vehicle (G2V) operation: This part is clearly explained in Chapter 4 that due to boost derived structure of current-fed ac-dc converter is the most suitable solution to meet all the control goals.

Solar to vehicle (S2V) operation: A single-stage S2V power converter requires maximum power point tracking from solar PV. Traditionally, this is done using boost or boost derived converters. Again, due to buck derived structure of VSI at dc-side, it will not be preferred a choice. Therefore, the current-fed converter will be the appropriate choice.

Vehicle to grid (V2G) operation: During this operation, the vehicle side converter acts as inverter and grid side converter act as a rectifier. If the vehicle side converter is built with active devices to enable inversion mode, then selection of voltage-fed topology in vehicle side will ensure this operation. The primary side converter can be either current-fed or voltage-fed type. With these considerations, a possible power converter structure to achieve all the operating modes can be derived as shown in Fig. 7.5. However, detailed converter analysis, design, closed-loop control, and experimental verification can be taken as future research work.

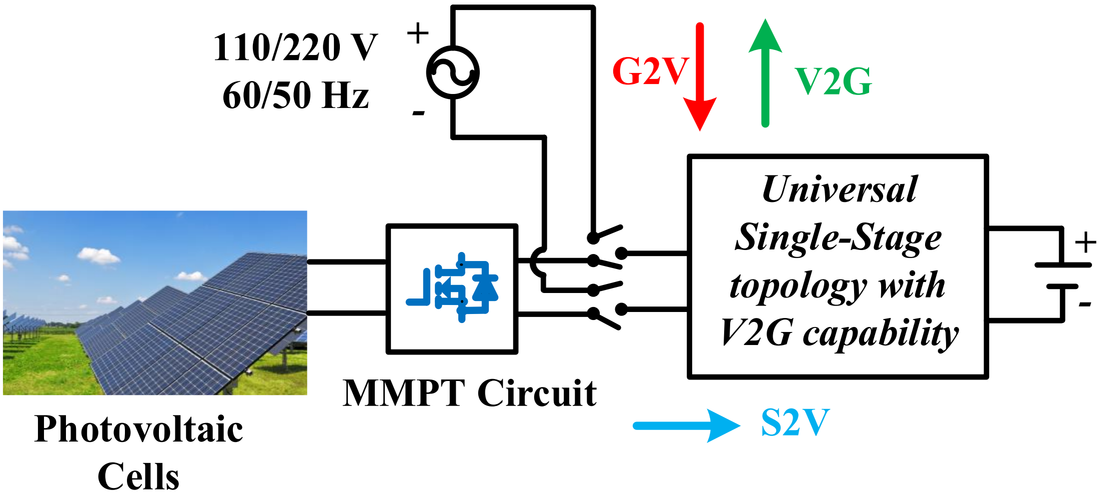

Fig. 7.5. Universal single-stage charger with V2G capability.

7.3.4 Dynamic Model and Control of Bidirectional EV Charger

In Chapter 3 and Chapter 4, steady-state analysis and performance of a current-fed single-stage topology is proposed. The converter control is carried out through duty-cycle modulation of CSI during G2V operation, and through fixed-frequency modulation of VSI during V2G operation. However, detailed closed-loop control and performances are not addressed. Therefore, this part can be taken as possible future research work.

7.3.5 Use of GaN-based Devices

The current hardware setup contains Silicon Carbide (SiC) based components. To improve the efficiency and power density of the converter, the possibility is to use devices Gallium Nitrate (GaN) switches. The cost of converter increases, it is a trade-off between the cost and efficiency.

Bibliography

[1] A. Emadi, Y. J. Lee, and K. Rajashekara, “Power electronics and motor drives in electric, hybrid electric, and plug-in hybrid electric vehicles,” IEEE Trans. Ind. Electron., vol. 55, no. 6, pp. 2237–2245, Jun. 2008, doi: 10.1109/TIE.2008.922768

[2] S. S. Williamson, A. K. Rathore, and F. Musavi, “Industrial electronics for electric transportation: Current state-of-the-art and future challenges,” IEEE Trans. Ind. Electron., vol. 62, no. 5, pp. 3021–3032, May 2015, doi: 10.1109/TIE.2015.2409052.

[3] A. Khaligh and Z. Li, "Battery, Ultracapacitor, Fuel Cell, and Hybrid Energy Storage Systems for Electric, Hybrid Electric, Fuel Cell, and Plug-In Hybrid Electric Vehicles: State of the Art," in IEEE Transactions on Vehicular Technology, vol. 59, no. 6, pp. 2806-2814, July 2010, doi: 10.1109/TVT.2010.2047877.

[4] C. C. Chan and K. T. Chau, “An overview of power electronics in electric vehicles,” IEEE Trans. Ind. Electron., vol. 44, no. 1, pp. 3–13, Feb. 1997, doi: 10.1109/41.557493.

[5] A. Khaligh and M. D'Antonio, "Global Trends in High-Power On-Board Chargers for Electric Vehicles," in IEEE Transactions on Vehicular Technology, vol. 68, no. 4, pp. 3306-3324, April 2019, doi: 10.1109/TVT.2019.2897050.

[6] M. Pahlevani and P. K. Jain, "Soft-Switching Power Electronics Technology for Electric Vehicles: A Technology Review," in IEEE Journal of Emerging and Selected Topics in Industrial Electronics, vol. 1, no. 1, pp. 80-90, July 2020, doi: 10.1109/JESTIE.2020.2999590.

[7] International Energy Agency. (2023). *Global EV Outlook 2023*. [Online]. Available: https://www.iea.org/reports/global-ev-outlook-2023

[8] “Global BEV & PHEV Sales for 2023” [Online]. Available: https://www.evvolumes.com/

[9] M. Yilmaz and P. T. Krein, “Review of battery charger topologies, charging power levels, and infrastructure for plug-in electric and hybrid vehicles,” IEEE Trans. Power Electron., vol. 28, no. 5, pp. 2151–2169, May 2013.

[10] *Limits for Harmonic Current Emissions (Equipment Input Current <16A Per Phase)*, IEC/EN61000-3-2, 1995.

[11] A. Emadi, S. S. Williamson and A. Khaligh, "Power electronics intensive solutions for advanced electric, hybrid electric, and fuel cell vehicular power systems," in IEEE Transactions on Power Electronics, vol. 21, no. 3, pp. 567-577, May 2006, doi: 10.1109/TPEL.2006.872378.

[12] Lasseter, R.; Paigi, P. Microgrid: A conceptual solution. In Proceedings of the 2004 IEEE 35th Annual Power Electronics Specialists Conference (IEEE Cat. No.04CH37551), Aachen, Germany, 20–25 June 2004; Volume 6, pp. 4285–4290.

[13] Schroeder, A.; Traber, T. The economics of fast charging infrastructure for electric vehicles. Energy Policy 2012, 43, 136–144.

[14] Richardson, P.; Flynn, D.; Keane, A. Local Versus Centralized Charging Strategies for Electric Vehicles in Low Voltage Distribution Systems. IEEE Trans. Smart Grid 2012, 3, 1020–1028.

[15] Liu, L.; Kong, F.; Liu, X.; Peng, Y.; Wang, Q. A review on electric vehicles interacting with renewable energy in smart grid. Renew. Sustain. Energy Rev. 2015, 51, 648–661.

[16] Savio Abraham D, Verma R, Kanagaraj L, Giri Thulasi Raman SR, Rajamanickam N, Chokkalingam B, Marimuthu Sekar K, Mihet-Popa L. Electric Vehicles Charging Stations’ Architectures, Criteria, Power Converters, and Control Strategies in Microgrids. Electronics. 2021; 10(16):1895.

[17] Kempton, W.; Tomi´c, J. Vehicle-to-grid power implementation: From stabilizing the grid to supporting large-scale renewable energy. J. Power Sources 2005, 144, 280–294.

[18] Mak, H.-Y.; Rong, Y.; Shen, Z.-J.M. Infrastructure Planning for Electric Vehicles with Battery Swapping. Manag. Sci. 2013, 59, 1557–1575.

[19] Van Haaren, R. Assessment of Electric Cars’ Range Requirements and Usage Patterns Based on Driving Behavior Recorded in the National Household Travel Survey of 2009; Earth and Environmental Engineering Department, Columbia University; Fu Foundation School of Engineering and Applied Science: New York, NY, USA, 2009; Volume 51, p. 53.

[20] M. Ghavami and C. Singh, "Reliability evaluation of electric vehicle charging systems including the impact of repair," 2017 IEEE Industry Applications Society Annual Meeting, 2017, pp. 1-9, doi: 10.1109/IAS.2017.8101865.

[21] Talukdar, B.; Deka, B. An Approach to Reliability, Availability and Maintainability Analysis of a Plug-In Electric Vehicle. World Electr. Veh. J. 2021, 12, 34.

[22] Xu, G.; Du, X.; Li, Z.; Zhang, X.; Zheng, M.; Miao, Y.; Gao, Y.; Liu, Q. Reliability design of battery management system for power battery. Microelectron. Reliab. 2018, 88–90, 1286–1292.

[23] McDonough, M. Integration of Inductively Coupled Power Transfer and Hybrid Energy Storage System: A Multiport Power Electronics Interface for Battery Powered Electric Vehicles. IEEE Trans. Power Electron. 2015, 30, 6423–6433.

[24] Park, M.; Nguyen, V.T.; Yu, S.-D.; Yim, S.-W.; Park, K.; Min, B.D.; Kim, S.-D.; Cho, J.G. A study of wireless power transfer topologies for 3.3 kW and 6.6 kW electric vehicle charging infrastructure. In Proceedings of the 2016 IEEE Transportation Electrification Conference and Expo, Asia-Pacific (ITEC Asia-Pacific), Busan, Korea, 1–4 June 2016; pp. 689–692.

[25] Chittoor, P.K.; Chokkalingam, B.; Mihet-Popa, L. A Review on UAV Wireless Charging: Fundamentals, Applications, Charging Techniques and Standards. IEEE Access 2021, 9, 69235–69266.

[26] Krishnamoorthy, R.; Krishnan, K.; Chokkalingam, B.; Padmanaban, S.; Leonowicz, Z.; Holm-Nielsen, J.B.; Mitolo, M. Systematic Approach for State-of-the-Art Architectures and System-on-chip Selection for Heterogeneous IoT Applications. IEEE Access 2021, 9, 25594–25622.

[27] V. Monteiro, J. C. Ferreira, A. A. Nogueiras Meléndez, C. Couto and J. L. Afonso, "Experimental Validation of a Novel Architecture Based on a Dual-Stage Converter for Off-Board Fast Battery Chargers of Electric Vehicles," in IEEE Transactions on Vehicular Technology, vol. 67, no. 2, pp. 1000-1011, Feb. 2018, doi: 10.1109/TVT.2017.2755545.

[28] Rahman, I.; Vasant, P.M.; Singh, B.S.M.; Abdullah-Al-Wadud, M.; Adnan, N. Review of recent trends in optimization techniques for plug-in hybrid, and electric vehicle charging infrastructures. Renew. Sustain. Energy Rev. 2016, 58, 1039–1047.

[29] Kisacikoglu, M.C.; Kesler, M.; Tolbert, L. Single-Phase On-Board Bidirectional PEV Charger for V2G Reactive Power Operation. IEEE Trans. Smart Grid 2015, 6, 767–775.

[30] Furiya, K.; Omura, N.; Nagano, H.; Nishimura, K.; Ueda, A.; Tokura, S. Parallel connected bilayer coil for a 3.3-kW electric vehicle wireless charging system. In Proceedings of the 2017 IEEE Wireless Power Transfer Conference (WPTC), Taipei, Taiwan, 10–12 May 2017.

[31] M. Safayatullah, M. T. Elrais, S. Ghosh, R. Rezaii, and I. Batarseh, ‘‘A comprehensive review of power converter topologies and control methods for electric vehicle fast charging applications,’’ IEEE Access, vol. 10, pp. 40753–40793, 2022.

[32] *Electric Vehicle Inductive Coupling Recommended Practice*, Standard SAE 5-1773, Feb. 1995.

[33] M. Shahjalal, T. Shams, M. N. Tasnim, M. R. Ahmed, M. Ahsan, and J. Haider, ‘‘A critical review on charging technologies of electric vehicles,’’ Energies, vol. 15, no. 21, p. 8239, Nov. 2022.

[34] PNW. (2020). *Charging Your Electric Vehicle*. [Online]. Available: https://www.pnm.com/ev-charging

[35] *SAE Electric Vehicle and Plug in Hybrid Electric Vehicle Conductive Charge Coupler*, Standard J1772, SAE, 2017.

[36] IEC. (2021). *Plugs, Socket-Outlets, Vehicle Connectors and Vehicle Inlets—Conductive Charging of Electric Vehicles*. [Online]. Available: https://webstore.iec.ch/publication/6582

[37] S. Bae and A. Kwasinski, ‘‘Spatial and temporal model of electric vehicle charging demand,’’ IEEE Trans. Smart Grid, vol. 3, no. 1, pp. 394–403, Mar. 2012.

[38] H. Tu, H. Feng, S. Srdic, and S. Lukic, ‘‘Extreme fast charging of electric vehicles: A technology overview,’’ IEEE Trans. Transport. Electrific., vol. 5, no. 4, pp. 861–878, Dec. 2019.

[39] IEEE Guide—Adoption of IEC/TR 61000-3-7:2008, Electromagnetic Compatibility (EMC)—Limits—Assessment of Emission Limits for the Connection of Fluctuating Installations to MV, HV and EHV Power Systems, Standard 1453.1-2012, 2012.

[40] PLC. (2022). *Electric Vehicle Charging—Domestic Electric Vehicle Charging Solution*. [Online]. Available: https://www.farnell.com/ datasheets/2813749.pdf

[41] T. Brünl. (2020). *EV Charging Standards*. The University of Western Australia. [Online]. Available: http://www.therevproject.com/doc/2012- EVcharging-s.pdf

[42] A. Kersten, A. Rodionov, M. Kuder, T. Hammarström, A. Lesnicar, and T. Thiringer, ‘‘Review of technical design and safety requirements for vehicle chargers and their infrastructure according to national Swedish and harmonized European standards,’’ Energies, vol. 14, no. 11, p. 3301, Jun. 2021.

[43] (2020). *EV Charging Standards in China and Japan*. [Online]. Available: https://ihsmarkit.com/research-analysis/ev-charging-standards-inchina-and-japan.html

[44] D. K. Ronanki and A. Williamson, ‘‘Extreme fast charging technology prospects to enhance sustainable electric transportation,’’ Energies, vol. 12, no. 9, p. 3721, Dec. 2019.

[45] Wikipedia. (2022). *IEC 61851*. [Online]. Available: https://en.wikipedia.org/wiki/IEC_61851

[46] *IEC 62196 Electric Vehicle Charge Connector Assembly (Type 2 for Mode 2 and 3)*, Standard IEC 62196, 2016. [Online]. Available: https://www.dalroad.com/wp-content/uploads/2016/08/Type-IIconnector-product-spec.pdf

[47] *Plugs, Socket-Outlets and Couplers for Industrial and Similar Applications, and for Electric Vehicles*. [Online]. Available: https://www.iec.ch/ords/f?p=103:38:516082676922542::FSP_ORG_ID,FSP_APEX_PAGE, FSP_PROJECT_ID:1426,20,22301.

[48] CHAdeMO. (2022). *What is CHAdeMO?* [Online]. Available: https://www.chademo.com/about-us/what-is-chademo

[49] K. Field. (2022). *CARS*. [Online]. Available: https://cleantechnica.com/2019/07/01/teslas-nanochargers-deliver-250-kw-charging-1722- km-hr-today/

[50] E. D. Queensland. (2018). *Electric Vehicle (EV) Charging Infrastructure*. [Online]. Available: https://www.statedevelopment.qld.gov.au/_data/assets/pdf_file/0016/18142/practice-note-electric-vehicle-charging.pdf

[51] G. E. Sfakianakis, J. Everts and E. A. Lomonova, “Overview of the requirements and implementations of bidirectional isolated AC-DC converters for automotive battery charging applications," 2015 Tenth International Conference on Ecological Vehicles and Renewable Energies (EVER), Monte Carlo, 2015, pp. 1-12.

[52] A. Emadi, K. Rajashekara, S. S. Williamson and S. M. Lukic, “Topological overview of hybrid electric and fuel cell vehicular power system architectures and configurations," in IEEE Transactions on Vehicular Technology, vol. 54, no. 3, pp. 763-770, May 2005.

[53] R. W. Johnson, J. L. Evans, P. Jacobsen, J. R. Thompson and M. Christopher,"The changing automotive environment: high-temperature electronics," in IEEE Transactions on Electronics Packaging Manufacturing, vol. 27, no. 3, pp. 164-176, July 2004.

[54] T. J. C. Sousa, V. Monteiro, J. C. A. Fernandes, C. Couto, A. A. N. Meléndez and J. L. Afonso, "New Perspectives for Vehicle-to-Vehicle (V2V) Power Transfer," IECON 2018 - 44th Annual Conference of the IEEE Industrial Electronics Society, 2018, pp. 5183-5188.

[55] C. Liu, K. T. Chau, D. Wu, and S. Gao, "Opportunities and challenges of vehicle-to-home, vehicle-to-vehicle, and vehicle-to-grid technologies," Proceedings of the IEEE, vol. 101, no. 11, pp. 2409–2427, 2013.

[56] R. Alvaro, J. Gonzalez, C. Gamallo, J. Fraile-Ardanuy, and L. Knapen, "Vehicle to vehicle energy exchange in smart grid applications," IEEE Conference on Connected Vehicles and Expo, pp. 1–7, 2014.

[57] P. You and Z. Yang, "Efficient optimal scheduling of charging station with multiple electric vehicles via V2V," in 2014 IEEE International Conference on Smart Grid Communications (SmartGridComm), 2014, pp. 716–721.

[58] S. Li, S. Lu and C. C. Mi, "Revolution of Electric Vehicle Charging Technologies Accelerated by Wide Bandgap Devices," in Proceedings of the IEEE, vol. 109, no. 6, pp. 985-1003, June 2021, doi: 10.1109/JPROC.2021.3071977.

[59] J. Yuan, L. Dorn-Gomba, A. D. Callegaro, J. Reimers and A. Emadi, "A Review of Bidirectional On-Board Chargers for Electric Vehicles," in IEEE Access, vol. 9, pp. 51501-51518, 2021, doi: 10.1109/ACCESS.2021.3069448.

[60] M. Hoshi, "Electric vehicles and expectations for wide bandgap power devices," *Proc. Int. Symp. Power Semicond. Devices ICs*, vol. 2016, July, pp. 5–8, Jul. 2016, doi: 10.1109/ISPSD.2016.7520765.

[61] Y. Berube, A. Ghazanfari, H. F. Blanchette, C. Perreault and K. Zaghib, “Recent advances in wide bandgap devices for automotive industry,” *IECON Proc.(Industrial Electron. Conf.*, vol. 2020, October, pp. 2557–2564, Oct. 2020, doi: 10.1109/IECON43393.2020.9254478.

[62] Y. Zhang *et al.*, “Development of a WBG-based transformerless electric vehicle charger with semiconductor isolation,” *2018 IEEE 4th South. Power Electron. Conf. SPEC 2018*, Feb. 2019, doi: 10.1109/SPEC.2018.8636011.

[63] S. Bhattacharya, “Wide-band Gap (WBG) WBG devices enabled MV power converters for utility applications - Opportunities and challenges,” *2nd IEEE Work. Wide Bandgap Power Devices Appl. WiPDA 2014*, Nov. 2014, doi: 10.1109/WIPDA.2014.6964611.

[64] A. Khaligh and M. D'Antonio, "Global Trends in High-Power On-Board Chargers for Electric Vehicles," in IEEE Transactions on Vehicular Technology, vol. 68, no. 4, pp. 3306-3324, April 2019, doi: 10.1109/TVT.2019.2897050.

[65] D. C. Erb, O. C. Onar and A. Khaligh, "Bi-directional charging topologies for plug-in hybrid electric vehicles," 2010 Twenty-Fifth Annual IEEE Applied Power Electronics Conference and Exposition (APEC), Palm Springs, CA, USA, 2010, pp. 2066-2072, doi: 10.1109/APEC.2010.5433520.

[66] S. S. Williamson, A. K. Rathore and F. Musavi, "Industrial Electronics for Electric Transportation: Current State-of-the-Art and Future Challenges," in IEEE Transactions on Industrial Electronics, vol. 62, no. 5, pp. 3021-3032, May 2015, doi: 10.1109/TIE.2015.2409052.

[67] Jinhaeng Jang, S. K. Pidaparthy, Seungjun Lee and Byungcho Choi, "Performance of an interleaved boundary conduction mode boost PFC converter with wide band-gap switching devices," 2015 IEEE 2nd International Future Energy Electronics Conference (IFEEC), Taipei, Taiwan, 2015, pp. 1-6, doi: 10.1109/IFEEC.2015.7361498.

[68] R. Pandey and B. Singh, "Bridgeless PFC Converter Based EV Charger," 2020 IEEE International Conference on Computing, Power and Communication Technologies (GUCON), Greater Noida, India, 2020, pp. 290-295, doi: 10.1109/GUCON48875.2020.9231266.

[69] M. Ancuti, M. Svoboda, S. Musuroi, A. Hedes, N. Olarescu, and M. Wienmann, “Boost interleaved PFC versus bridgeless boost interleaved PFC converter performance/efficiency analysis,” in Proc. Int. Conf. Appl. Theor. Electricity, Craiova, Romania, 2014, pp. 1–6.

[70] Y. Tang, W. Ding and A. Khaligh, "A bridgeless totem-pole interleaved PFC converter for plug-in electric vehicles," 2016 IEEE Applied Power Electronics Conference and Exposition (APEC), Long Beach, CA, USA, 2016, pp. 440-445, doi: 10.1109/APEC.2016.7467909.

[71] M. Jia and H. Sun, "GaN-based High-Frequency, High-Power-Density, 2-in-1 Bi-directional OBC Design for EV Applications," PCIM Europe 2023; International Exhibition and Conference for Power Electronics, Intelligent Motion, Renewable Energy and Energy Management, Nuremberg, Germany, 2023, pp. 1-10, doi: 10.30420/566091148.

[72] A. Dixit, K. Pande, S. Gangavarapu and A. K. Rathore, "DCM-Based Bridgeless PFC Converter for EV Charging Application," in IEEE Journal of Emerging and Selected Topics in Industrial Electronics, vol. 1, no. 1, pp. 57-66, July 2020, doi: 10.1109/JESTIE.2020.2999595.

[73] Y. Park, S. Chakraborty and A. Khaligh, "DAB Converter for EV Onboard Chargers Using Bare-Die SiC MOSFETs and Leakage-Integrated Planar Transformer," in IEEE Transactions on Transportation Electrification, vol. 8, no. 1, pp. 209-224, March 2022, doi: 10.1109/TTE.2021.3121172.

[74] J. -W. Kim and P. Barbosa, "PWM-Controlled Series Resonant Converter for Universal Electric Vehicle Charger," in IEEE Transactions on Power Electronics, vol. 36, no. 12, pp. 13578-13588, Dec. 2021, doi: 10.1109/TPEL.2021.3072991.

[75] P. He and A. Khaligh, "Comprehensive Analyses and Comparison of 1 kW Isolated DC–DC Converters for Bidirectional EV Charging Systems," in IEEE Transactions on Transportation Electrification, vol. 3, no. 1, pp. 147-156, March 2017, doi: 10.1109/TTE.2016.2630927.

[76] B. Li, Q. Li and F. C. Lee, "High-Frequency PCB Winding Transformer With Integrated Inductors for a Bi-Directional Resonant Converter," in IEEE Transactions on Power Electronics, vol. 34, no. 7, pp. 6123-6135, July 2019, doi: 10.1109/TPEL.2018.2874806.

[77] S. Mukherjee, J. M. Ruiz and P. Barbosa, "A High Power Density Wide Range DC–DC Converter for Universal Electric Vehicle Charging," in IEEE Transactions on Power Electronics, vol. 38, no. 2, pp. 1998-2012, Feb. 2023, doi: 10.1109/TPEL.2022.3217092.

[78] B. Whitaker et al., "A High-Density, High-Efficiency, Isolated On-Board Vehicle Battery Charger Utilizing Silicon Carbide Power Devices," in IEEE Transactions on Power Electronics, vol. 29, no. 5, pp. 2606-2617, May 2014, doi: 10.1109/TPEL.2013.2279950.

[79] N. D. Weise, G. Castelino, K. Basu and N. Mohan, "A Single-Stage Dual-Active-Bridge-Based Soft Switched AC–DC Converter With Open-Loop Power Factor Correction and Other Advanced Features," in IEEE Transactions on Power Electronics, vol. 29, no. 8, pp. 4007-4016, Aug. 2014, doi: 10.1109/TPEL.2013.2293112.

[80] C. Li and D. Xu, "Family of Enhanced ZCS Single-Stage Single-Phase Isolated AC–DC Converter for High-Power High-Voltage DC Supply," in IEEE Transactions on Industrial Electronics, vol. 64, no. 5, pp. 3629-3639, May 2017, doi: 10.1109/TIE.2017.2652374.

[81] H. Kim, J. Park, J. Lee and S. Choi, "A Simple Modulation Strategy for Full ZVS of Single-Stage Electrolytic Capacitor-Less EV Charger With Universal Input," in IEEE Transactions on Power Electronics, vol. 37, no. 10, pp. 12030-12040, Oct. 2022, doi: 10.1109/TPEL.2022.3165182.

[82] U. R. Prasanna, A. K. Singh and K. Rajashekara, "Novel Bidirectional Single-phase Single-Stage Isolated AC–DC Converter With PFC for Charging of Electric Vehicles," in IEEE Transactions on Transportation Electrification, vol. 3, no. 3, pp. 536-544, Sept. 2017, doi: 10.1109/TTE.2017.2691327.

[83] D. Zinchenko, A. Blinov, A. Chub, D. Vinnikov, I. Verbytskyi and S. Bayhan, "High-Efficiency Single-Stage On-Board Charger for Electrical Vehicles," in IEEE Transactions on Vehicular Technology, vol. 70, no. 12, pp. 12581-12592, Dec. 2021, doi: 10.1109/TVT.2021.3118392.

[84] R. Pradhan, N. Keshmiri and A. Emadi, "On-Board Chargers for High-Voltage Electric Vehicle Powertrains: Future Trends and Challenges," in IEEE Open Journal of Power Electronics, vol. 4, pp. 189-207, 2023, doi: 10.1109/OJPEL.2023.3251992.

[85] T. Instruments, ‘‘Designing 6.6 kw bidirectional hev/ev on-board charger with SiC and embedded technologies,’’ TI Training, Tech. Rep., Apr. 2019.

[86] 6.6 kw High Power Density Bi-Directional EV on-Board Charger, Cree Power Applications, Durham, CA, USA, Jan. 2020.

[87] On Semiconductor, ‘‘Designing 6.6 kw SiC-based On-board Chargers,”, Tech. Rep., 2020.

[88] On-Board Charger Specifications Eaton, Eaton, Dublin, Ireland, 2013.

[89] “VisIC’s smallest 6.7 kW on-board-charger reference design best power density of 3kW/L and lightweight of 4.5kg.”.

[90] “CANOO | GaN systems.” https://gansystems.com/gan-applications/canoo/ (accessed Dec. 18, 2020).

[91] Z. Liu, B. Li, F. C. Lee, and Q. Li, ‘‘High-efficiency high-density critical mode rectifier/inverter for WBG-device-based on-board charger,’’ *IEEE Trans. Ind. Electron.*, vol. 64, no. 11, pp. 9114–9123, Nov. 2017.

[92] “HELLA | GaN systems.” https://gansystems.com/gan-applications/hella-22-kw-evonboard-charger/ (accessed Dec. 18, 2020).

[93] “CONTINENTAL GaN systems.” https://gansystems.com/gan-applications/continental-3-kw-ev-onboard-charger/ (accessed Dec. 18, 2020).

[94] Borg Warner, ‘‘Designing 7 kw SiC-based On-board Chargers,”, Tech. Rep., 2021.

[95] K. Bai, ‘‘Applying wide-bandgap devices to EV battery chargers—PDF free download,’’ Eaton, Tech. Rep., Oct. 2019.

[96] “22 kW 900 V bidirectional DC-DC converter.” [Online]. Available: www.iisb.fraunhofer.de

[97] S. W. Johannessen, ‘‘Power factor correction for a bidirectional onboard charger for electric vehicles and plug-in hybrid electric vehiclesa fundamental study of the bidirectional totem-pole PFC,’’ M.S. thesis, Dept. Electr. Power Eng., NTNU, Trondheim, Norway, Jun. 2018.

[98] On-Board Charger Specifications Delta, Delta Americas, 2017.

[99] ST Microelectronics, ‘‘Designing 7 kw SiC-based On-board Chargers,”, Tech. Rep., 2020.

[100] E. Voumvoulakis, E. Leonidaki, G. Papoutsis, and N. Hatziargyriou, “Evaluation of the impact of plug-in electric vehicles in Greek distribution network,” *CIRED - Open Access Proc. J.*, vol. 2017, no. 1, pp. 2270–2274, 2017.

[101] M. A. Awadallah, B. N. Singh, and B. Venkatesh, “Impact of EV charger load on distribution network capacity: A case study in Toronto,” *Can. J. Elect. Comput. Eng.*, vol. 39, no. 4, pp. 268–273, 2016.

[102] B. Sun, Z. Huang, X. Tan, and D. H. K. Tsang, “Optimal scheduling for electric vehicle charging with discrete charging levels in distribution grid,” *IEEE Trans. Smart Grid*, vol. 9, no. 2, pp. 624–634, Mar. 2018.

[103] A. Ahmadian, M. Sedghi, B. Mohammadi-ivatloo, A. Elkamel, M. Aliakbar Golkar, and M. Fowler, “Cost-benefit analysis of V2G implementation in distribution networks considering PEVs battery degradation,” *IEEE Trans. Sustain. Energy*, vol. 9, no. 2, pp. 961–970, Apr. 2018.

[104] S. Kaluza, D. Almeida, and P. Mullen, “BMW i ChargeForward: PG&E’s electric vehicle smart charging pilot,” Dec. 2016.

[105] F. Un-Noor, P. Sanjeevikumar, L. Mihet-Popa, and E. Hossain, “A comprehensive study of key electric vehicle (EV) components, technologies, challenges, impacts, and future direction of development,” *Energies*, vol. 10, no. 8, Aug. 2017, Art. no. 1217.

[106] M. Jafari, A. Gauchia, S. Zhao, K. Zhang, and L. Gauchia, “Electric vehicle battery cycle aging evaluation in real-world daily driving and vehicle-to-grid services,” *IEEE Trans. Transp. Electrific.*, vol. 4, no. 1, pp. 122–134, Mar. 2018.

[107] V. Monteiro, J. G. Pinto, and J. L. Afonso, “Operation modes for the electric vehicle in smart grids and smart homes: Present and proposed modes,” *IEEE Trans. Veh. Technol.*, vol. 65, no. 3, pp. 1007–1020, Mar. 2016.

[108] M. C. Kisacikoglu, M. Kesler, and L. M. Tolbert, “Single-phase onboard bidirectional PEV charger for V2G reactive power operation,” *IEEE Trans. Smart Grid*, vol. 6, no. 2, pp. 767–775, Mar. 2015.

[109] M. Restrepo, J. Morris, M. Kazerani, and C. A. Canizares, “Model- ˜ ing and testing of a bidirectional smart charger for distribution system EV integration,” *IEEE Trans. Smart Grid*, vol. 9, no. 1, pp. 152–162, Jan. 2018.

[110] A. O. David and I. Al-Anbagi, “EVs for frequency regulation: Cost benefit analysis in a smart grid environment,” *IET Elect. Syst. Transp.*, vol. 7, no. 4, pp. 310–317, 2017.

[111] T. Morstyn, B. Hredzak, and V. G. Agelidis, “Control strategies for microgrids with distributed energy storage systems: An overview,” *IEEE Trans. Smart Grid*, vol. 9, no. 4, pp. 3652–3666, Jul. 2018.

[112] D. Varajão, L. M. Miranda, R. E. Araújo, and J. P. Lopes, “Power transformer for a single-stage bidirectional and isolated ac-dc matrix converter for energy storage systems,” in IECON 2016-42nd Annual Conference of the IEEE Industrial Electronics Society, pp. 1149–1155, Florence, Italy, Oct. 2016.

[113] M. Tissieres, I. Askarian, M. Pahlevani, A. Rotzetta, A. Knight and I. Preda, “A digital robust control scheme for dual Half-Bridge DC-DC converters,” Conf. Proc. – IEEE Appl. Power Electron. Conf. Expo. –APEC, vol. 2018, March, pp. 311–315, Apr. 2018, doi: 10.1109/APEC.2018.8341028.

[114] L. Chen, S. Shao, Q. Xiao, L. Tarisciotti, P. W. Wheeler and T. Dragičević, “Model predictive control for dual-active-bridge converters supplying pulsed power loads in naval DC micro-grids,” IEEE Trans. Power Electron., vol. 35, no. 2, pp. 1957–1966, Feb. 2020, doi: 10.1109/TPEL.2019.2917450.

[115] A. Hernández-Méndez, J. Linares-Flores, H. Sira-Ramírez, J. F. GuerreroCastellanos and G. Mino-Aguilar, “A backstepping approach to decentralized active disturbance rejection control of interacting boost converters,” *IEEE Trans. Ind. Appl.*, vol. 53, no. 4, pp. 4063–4072, Jul. 2017, doi: 10.1109/TIA.2017.2683441.

[116] M. A. Hassan, E. P. Li, X. Li, T. Li, C. Duan and S. Chi, “Adaptive passivity-based control of DC-DC buck power converter with constant power load in DC microgrid systems,” *IEEE J. Emerg. Sel. Top. Power Electron.*, vol. 7, no. 3, pp. 2029–2040, Sep. 2019, doi: 10.1109/JESTPE.2018.287444.

[117] S. Dutta, S. Hazra and S. Bhattacharya, “A digital predictive current-mode controller for a single-phase high-frequency transformer-isolated dual-active bridge DC-to-DC converter,” *IEEE Trans. Ind. Electron.*, vol. 63, no. 9, pp. 5943–5952, Sep. 2016, doi: 10.1109/TIE.2016.2551201.

[118] H. Yuan and Y. Kim, “Equivalent input disturbance observer-based ripple-free deadbeat control for voltage regulation of a DC–DC buck converter,” *IET Power Electron.*, vol. 12, no. 12, pp. 3272–3279, Oct. 2019, doi: 10.1049/IET-PEL.2019.0652.

[119] J. Wang, W. Luo, J. Liu and L. Wu, “Adaptive type-2 FNN-based dynamic sliding mode control of DC-DC boost converters,” *IEEE Trans. Syst. Man, Cybern. Syst.*, vol. 51, no. 4, pp. 2246–2257, Apr. 2021, doi: 10.1109/TSMC.2019.2911721.

[120] X. Shi, N. Chen, T. Wei, J. Wu and P. Xiao, “A reinforcement learning-based online-training AI controller for DC-DC switching converters,” *2021 6th Int. Conf. Integr. Circuits Microsystems, ICICM 2021*, pp. 435–438, 2021, doi: 10.1109/ICICM54364.2021.9660319.

[121] M. S. M. Gardezi and A. Hasan, “Machine learning based adaptive prediction horizon in finite control set model predictive control,” *IEEE Access*, vol. 6, pp. 32392–32400, May 2018, doi: 10.1109/ACCESS.2018.2839519.

[122] S. G. Kandlikar and C. N. Hayner, “Liquid cooled cold plates for industrial high-power electronic devices—thermal design and manufacturing considerations,” Heat transfer engineering, vol. 30, pp. 918–930, Jul. 2009.

[123] J. Reimers, L. Dorn-Gomba, C. Mak, and A. Emadi, “Automotive traction inverters: Current status and future trends,” IEEE Transactions on Vehicular Technology, vol. 68, pp. 3337–3350, Feb. 2019.

[124] I. Subotic and E. Levi, “An integrated battery charger for evs based on a symmetrical six-phase machine,” in 2014 IEEE 23rd International Symposium on Industrial Electronics (ISIE), pp. 2074–2079, Istanbul, Turkey, Jun. 2014.

[125] J. Gao, W. Sun, Y. Zhang, D. Jiang, and R. Qu, “Improved operation and control of single-phase integrated on-board charger system,” IEEE Transactions on Power Electronics, vol. 36, pp. 4752–4765, Sep. 2020.

[126] Y. Zhang, W. Perdikakis, Y. Cong, X. Li, M. Elshaer, Y. Abdullah, J. Wang, K. Zou, Z. Xu, and C. Chen, “Leakage current mitigation of non-isolated integrated chargers for electric vehicles,” in 2019 IEEE Energy Conversion Congress and Exposition (ECCE), pp. 1195–1201, Baltimore, MD, USA, Sep. 2019.

[127] A. N. Azad, A. Echols, V. A. Kulyukin, R. Zane, and Z. Pantic, “Analysis, optimization, and demonstration of a vehicular detection system intended for dynamic wireless charging applications,” IEEE Transactions on Transportation Electrification, vol. 5, no. 1, pp. 147–161, Sep, 2018.

[128] G. Elliott, J. Boys, and G. Covic, “A design methodology for flat pick-up icpt systems,” in 2006 1ST IEEE Conference on Industrial Electronics and Applications, pp. 1–7, Singapore, May 2006.

[129] G. A. Covic and J. T. Boys, “Modern trends in inductive power transfer for transportation applications,” IEEE Journal of Emerging and Selected topics in power electronics, vol. 1, no. 1, pp. 28–41, May 2013.

[130] J. Kim, D.-H. Kim, and Y.-J. Park, “Analysis of capacitive impedance matching networks for simultaneous wireless power transfer to multiple devices,” IEEE Transactions on Industrial Electronics, vol. 62, no. 5, pp. 2807–2813, Oct. 2014.

[131] M. Adil, J. Ali, Q. T. H. Ta, M. Attique, and T.-S. Chung, “A reliable sensor network infrastructure for electric vehicles to enable dynamic wireless charging based on machine learning technique,” IEEE Access, vol. 8, pp. 187933–187947, Oct. 2020.

[132] A. A. Mohamed, C. R. Lashway, and O. Mohammed, “Modeling and feasibility analysis of quasi-dynamic wpt system for ev applications,” IEEE transactions on transportation electrification, vol. 3, no. 2, pp. 343– 353, Mar. 2017.

[133] M. Alharbi, S. Bhattacharya, and N. Yousefpoor, “Reliability comparison of fault-tolerant hvdc based modular multilevel converters,” in 2017 IEEE Power & Energy Society General Meeting, pp. 1–5, Chicago, IL, USA. Feb. 2017.

[134] S. Kwak and H. A. Toliyat, “Remedial switching function approach to improve reliability for ac–ac converters,” IEEE Transactions on Energy Conversion, vol. 22, pp. 541–543, May 2007.

[135] J. Sakly, A. B.-B. Abdelghani, I. Slama-Belkhodja, and H. Sammoud, “Reconfigurable dc/dc converter for efficiency and reliability optimization,” IEEE

Journal of Emerging and Selected Topics in Power Electronics, vol. 5, pp. 1216–1224, Feb. 2017.

[136] G. Chen and X. Cai, “Adaptive control strategy for improving the efficiency and reliability of parallel wind power converters by optimizing power allocation,” IEEE Access, vol. 6, pp. 6138–6148, Jan. 2018.

[137] V. Raveendran, M. Andresen, and M. Liserre, “Improving onboard converter reliability for more electric aircraft with lifetime-based control,” IEEE Transactions on Industrial Electronics, vol. 66, pp. 5787–5796, Jul. 2019.

[138] A. Khaligh and S. Dusmez, ‘‘Comprehensive topological analysis of conductive and inductive charging solutions for plug-in electric vehicles,’’ IEEE Trans. Veh. Technol., vol. 61, no. 8, pp. 3475–3489, Oct. 2012.

[139] L. Zhu, “A novel soft-commutating isolated boost full-bridge ZVS-PWM DC–DC converter for bi-directional high power applications,” IEEE Trans. Power Electron., vol. 21, no. 2, pp. 422–429, Mar. 2006.

[140] U. R. Prasanna, A. K. Rathore, and S. K. Mazumder, “Novel zerocurrent-switching current-fed half-bridge isolated DC/DC converter for fuel-cell-based applications,” IEEE Trans. Ind. Appl., vol. 49, no. 4, pp. 1658–1668, Jul. 2013.

[141] I. O. Lee, S. Y. Cho, and G. W. Moon, “Phase-shifted dual H-bridge converter with a wide ZVS range and reduced output filter,” in Proc. 38th IEEE IECON, 2012, pp. 656–661.

[142] Thacker, and Timothy, "Phase-locked loop noise reduction via phase detector implementation for single-phase systems." IEEE Transactions on Industrial Electronics 58.6 (2011): 2482-2490.

[143] H. Chen and D. Divan, “Soft-switching solid state transformer (S4T),” in Proc. IEEE Energy Convers. Congr. Expo. (ECCE), Sep. 2016, pp. 1–10.

[144] S. Abdel-Rahman, F. Stuckler, and K. Siu, “PFC boost converter design guide,” Infineon, Neubiberg, Germany, Appl. Note, Feb. 2016.

[145] Texas Instruments PFC With >98% Efficiency Based Reference Design, https://www.ti.com

[146] IEEE Recommended Practice and Requirements for Harmonic Control in Electric Power Systems, IEEE Standard 519-2014, Revised IEEE Stanard 519-1992, 2014.

[147] S. G. Barbosa, L. H. S. C. Barreto and D. d. S. Oliveira, "A Single-Stage Bidirectional AC-DC Converter Feasible for Onboard Battery Chargers," in IEEE Journal of Emerging and Selected Topics in Power Electronics, doi: 10.1109/JESTPE.2021.3108958.

[148] S. Li, J. Deng and C. C. Mi, "Single-Stage Resonant Battery Charger With Inherent Power Factor Correction for Electric Vehicles," in IEEE Transactions on Vehicular Technology, vol. 62, no. 9, pp. 4336-4344, Nov. 2013, doi: 10.1109/TVT.2013.2265704.

[149] Y. Zhang, C. Li, Z. Cao, and D. Xu, “Soft-switching single-stage current-fed full-bridge isolated converter for high power ac/dc applications,” in Proc. 9th Int. Conf. Power Electron. ECCE Asia, 2015, pp. 48–53.

[150] A. Blinov et al., "High Gain DC–AC High-Frequency Link Inverter With Improved Quasi-Resonant Modulation," in IEEE Transactions on Industrial Electronics, vol. 69, no. 2, pp. 1465-1476, Feb. 2022, doi: 10.1109/TIE.2021.3060657.

[151] Y.-J. Lee, A. Khaligh, and A. Emadi, “Advanced integrated bidirectional AC/DC and DC/DC converter for plug-in hybrid electric vehicles,” IEEE Trans. Veh. Technol., vol. 58, no. 8, pp. 3970–3980, Oct. 2009.

[152] D. C. Erb, O. C. Onar, and A. Khaligh, “An integrated bi-directional power electronic converter with multi-level AC-DC/DC-AC converter and non-inverted buck-boost converter for PHEVs with minimal grid level disruptions,” in Proc. IEEE Veh. Power Propuls. Conf. (VPPC), Sep. 2010, pp. 1–6.

[153] D. Sal y Rosas, D. Frey, J. -L. Schanen and J. -P. Ferrieux, "Isolated single stage bidirectional AC-DC converter with power decoupling and reactive power control to

interface battery with the single phase grid," 2018 IEEE Applied Power Electronics Conference and Exposition (APEC), 2018, pp. 631-636, doi: 10.1109/APEC.2018.8341078.

[154] C. Li, Y. Zhang, and D. Xu, “Soft-switching single stage isolated ac-dc converter for single-phase high power PFC applications,” in Proc. 9th Int. Conf. Power Electron. ECCE Asia, 2015, pp. 1103–1108.

[155] P. Xuewei and A. K. Rathore, "Naturally Clamped Zero-Current Commutated Soft-Switching Current-Fed Push–Pull DC/DC Converter: Analysis, Design, and Experimental Results," in IEEE Transactions on Power Electronics, vol. 30, no. 3, pp. 1318-1327, March 2015, doi: 10.1109/TPEL.2014.2315834.

[156] P. Xuewei and A. K. Rathore, "Current-Fed Soft-Switching Push–Pull Front-End Converter-Based Bidirectional Inverter for Residential Photovoltaic Power System," in IEEE Transactions on Power Electronics, vol. 29, no. 11, pp. 6041-6051, Nov. 2014, doi: 10.1109/TPEL.2014.2301495.

[157] E. Bulut and M. C. Kisacikoglu, "Mitigating Range Anxiety via Vehicle-to-VehicleSocial Charging System," 2017 IEEE 85th Vehicular Technology Conference(VTC Spring), 2017, pp. 1-5, doi: 10.1109/VTCSpring.2017.8108288.

[158] I. N. L. (INL), “Plugged in: How americans charge their electric vehicles,” 2015.[Online]. Available: http://avt.inel.gov/pdf/ arra/SummaryReport.pdf

[159] D. P. Tuttle and R. Baldick, "The Evolution of Plug-In Electric Vehicle-Grid Interactions," in IEEE Transactions on Smart Grid, vol. 3, no. 1, pp. 500-505, March 2012, doi: 10.1109/TSG.2011.2168430.

[160] M. Brenna, F. Foiadelli and M. Longo, "The Exploitation of Vehicle-to-Grid Function for Power Quality Improvement in a Smart Grid," in IEEE Transactions on Intelligent Transportation Systems, vol. 15, no. 5, pp. 2169-2177, Oct. 2014, doi: 10.1109/TITS.2014.2312206.

[161] N. Z. Xu and C. Y. Chung, "Reliability Evaluation of Distribution Systems Including Vehicle-to-Home and Vehicle-to-Grid," in IEEE Transactions on Power Systems, vol. 31, no. 1, pp. 759-768, Jan. 2016, doi: 10.1109/TPWRS.2015.2396524.

[162] T. J. C. Sousa, L. Machado, D. Pedrosa, C. Martins, V. Monteiro and J. L. Afonso, "Comparative Analysis of Vehicle-to-Vehicle (V2V) Power Transfer Configurations without Additional Power Converters," 2020 IEEE 14th International Conference on Compatibility, Power Electronics and Power Engineering (CPE-POWERENG), Setubal, Portugal, 2020, pp. 88-93, doi: 10.1109/CPE-POWERENG48600.2020.9161697.

[163] T. J. C. Sousa, V. Monteiro, J. C. A. Fernandes, C. Couto, A. A. N. Meléndez and J. L. Afonso, "New Perspectives for Vehicle-to-Vehicle (V2V) Power Transfer," IECON 2018 - 44th Annual Conference of the IEEE Industrial Electronics Society, Washington, DC, USA, 2018, pp. 5183-5188, doi: 10.1109/IECON.2018.8591209.

[164] C. Liu, K. T. Chau, D. Wu and S. Gao, "Opportunities and Challenges of Vehicle-to-Home, Vehicle-to-Vehicle, and Vehicle-to-Grid Technologies," in Proceedings of the IEEE, vol. 101, no. 11, pp. 2409-2427, Nov. 2013, doi: 10.1109/JPROC.2013.2271951.

[165] R. Alvaro-Hermana, J. Fraile-Ardanuy, P. J. Zufiria, L. Knapen and D. Janssens, "Peer to Peer Energy Trading with Electric Vehicles," in IEEE Intelligent Transportation Systems Magazine, vol. 8, no. 3, pp. 33-44, Fall 2016, doi: 10.1109/MITS.2016.2573178.

List of Publications

Journal papers

1. **N. Patel**, L. A. C. Lopes, A. Rathore and V. Khadkikar, "A Soft-Switched Single-Stage Single-Phase PFC Converter for Bidirectional Plug-In EV Charger," in ***IEEE Transactions on Industry Applications***, vol. 59, no. 4, pp. 5123-5135, July-Aug. 2023, doi: 10.1109/TIA.2023.3270387.
2. **N. Patel**, L. A. C. Lopes, A. K. Rathore and V. Khadkikar, "High-Efficiency Single-Stage Single-Phase Bidirectional PFC Converter for Plug-in EV Charger," in ***IEEE Transactions on Transportation Electrification***, doi: 10.1109/TTE.2023.3324358.

Conference papers

1. **N. Patel**, L. A. C. Lopes and A. K. Rathore, "Analysis and Design of Soft-Switching Single-Stage Single-Phase PFC Converter for Bidirectional Plug-in EV Charger," *2022 IEEE Energy Conversion Congress and Exposition (ECCE)*, Detroit, MI, USA, 2022, pp. 1-7, doi: 10.1109/ECCE50734.2022.9947730.
2. **N. Patel**, L. A. C. Lopes and A. K. Rathore, "Single-Stage Bidirectional PFC Based Plug-in G2V EV Charger," *2022 IEEE International Conference on Power Electronics, Drives and Energy Systems (PEDES)*, Jaipur, India, 2022, pp. 1-6, doi: 10.1109/PEDES56012.2022.10080548.
3. **N. Patel**, L. A. C. Lopes and A. K. Rathore, "Modeling and Control of Single-Stage Bidirectional Isolated AC-DC Converter with PFC for EV Battery Charging," *2022 IEEE International Conference on Power Electronics, Drives and Energy Systems (PEDES)*, Jaipur, India, 2022, pp. 1-6, doi: 10.1109/PEDES56012.2022.10080477.
4. **N. Patel**, L. A. C. Lopes and A. K. Rathore, "An Accurate Loss Model of Single-Stage Single-Phase Isolated PFC Converter for Bidirectional Plug-in EV Charger," *2023 IEEE Applied Power Electronics Conference and Exposition (APEC)*, Orlando, FL, USA, 2023, pp. 1896-1901, doi: 10.1109/APEC43580.2023.10131495.